Universidade Católica Portuguesa

Faculdade de Engenharia

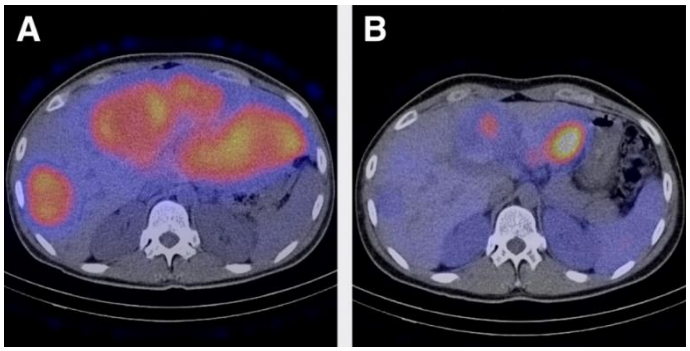

Radionuclide Therapy in Nuclear Medicine: Applying Monte Carlo Simulation to Investigate Bremsstrahlung Imaging with a Gamma Camera

Catarina Ramos de Mendonça

Dissertation Submitted for the Degree of Master of Science in Clinical Engineering

Júri

Prof. Doutor Manuel José Martinho Barata Marques (Presidente)

Prof. Doutor José Pedro Miragaia Trancoso Vaz

Prof. Doutor Rui Jorge Correia Mendes Alves Pires (Co-Orientador)

Prof. Doutor Ian Cullum (Orientador)

September 2013

Universidade Católica Portuguesa

Faculdade de Engenharia

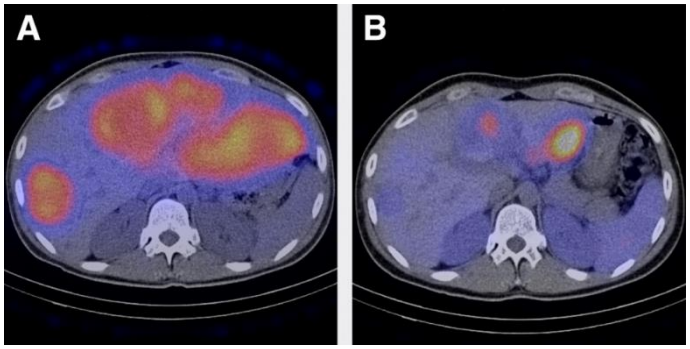

Radionuclide Therapy in Nuclear Medicine: Applying Monte Carlo Simulation to Investigate Bremsstrahlung Imaging with a Gamma Camera

Catarina Ramos de Mendonça

Dissertation Submitted for the Degree of Master of Science in Clinical Engineering

Orientador: Prof. Doutor Ian Cullum

Co-Orientador: Prof. Doutor Rui Jorge Correia Mendes Alves Pires

September 2013

ABSTRACT

Radionuclide therapy is an innovative treatment in nuclear medicine that uses unsealed sources to treat some specific tumours in the human body. With an increasing interest in this modality, some efforts have been done to improve this field in nuclear medicine, such as the radiopharmaceuticals administered or the components of the imaging equipment.

Pure beta emitters are the radionuclides most used in radionuclide therapy. They are described to have extremely high potential in the treatment of malignant and non-malignant disorders. The energy of these radionuclides is absorbed close to the target site due to its low range (few mm in tissue). The problem is the impossibility of imaging their uptake in the interest places since there are no gamma rays emissions and the beta radiation is impossible to detect externally. As a result, the only radiation capable to be perceived by the gamma camera is the bremsstrahlung photons produced when an accelerate beta particle passes close to the atomic nucleus and is deflected towards it. The detection of these photons is relevant for dosimetric purposes, in order to detect the real uptake of the radionuclide and hence to know the absorbed dose in the patient.

Thus, the current dissertation reports a study about bremsstrahlung characteristics by using a Monte Carlo simulation. The study attempts to realise in what way the bremsstrahlung photons are produced in different types of biological materials, using different beta particles energies.

The simulator used was the EGSnrc (Electron Gamma Shower) system (V4 2.3.2), a package for Monte Carlo simulations. The programs were written in Mortran language and compiled to Fortran. With this study, an additional aim was to obtain a strong knowledge on EGSnrc system and to be able to modify and produce a wide range of different simulations in different physical conditions. In order to understand the bremsstrahlung photons several simulations were performed, in different media and with different energies of beta particles emissions.

Future work should be necessary in order to relate the bremsstrahlung photons understanding with the gamma camera components. The aim will be to improve the bremsstrahlung imaging and hence gathering realistic dosimetric data for the pure beta emitters.

Keywords: Radionuclide Therapy; Bremsstrahlung photons; Monte Carlo Simulation; EGSnrc.

RESUMO

A terapia com radionuclídeos é um tratamento inovador em medicina nuclear, o qual utiliza fontes não seladas para tratar tumores específicos no corpo humano. Com o crescente interesse por esta especialidade terapêutica, alguns esforços têm sido feitos para melhorar este campo da medicine nuclear, nomeadamente através dos radiofármacos administrados ou na tecnologia dos equipamentos de imagiologia.

Os emissores beta puros (electrões) são os radionuclídeos mais utlizados nesta terapia. São descritos na literatura como os que apresentam um elevado potencial no tratamento de doenças malignas e benignas, uma vez que a energia destes radionuclídeos é absorvida perto do local alvo (poucos mm de alcance nos tecidos). O problema da utilização de beta puros reside na impossibilidade de se formar uma imagem médica, uma vez que estes radionuclídeos não emitem qualquer radiação gama. Como resultado, a única radiação capaz de ser detectada pela câmara gama são os fotões bremsstrahlung (radiação de travagem), produzidos quando ocorre uma desaceleração e deflexão dos electrões acelerados quando estes passam perto dos núcleos atómicos. A detecção de bremsstrahlung é muito importante para fins dosimétricos, dado que permite conhecer a verdadeira dose absorvida pelo paciente.

A presente dissertação tem como principal objectivo estudar as características dos fotões bremsstrahlung, através da utilização de um simulador Monte Carlo - EGSnrc (Electron Gamma Shower). Pretende-se compreender de que forma os fotões bremsstrahlung são produzidos no interior de diferentes tipos de materiais biológicos, utilizando partículas beta de diferentes energias. Os códigos foram programados em linguagem Mortran e compilados para Fortran. Pretende-se também obter um forte conhecimento sobre o sistema usado, de forma a ser possível produzir qualquer tipo de simulação para diferentes condições físicas.

Torna-se necessário prosseguir este trabalho, a fim de se relacionar as características dos fotões bremsstrahlung com os componentes da câmara gama. O objectivo será melhorar as imagens criadas por fotões bremsstrahlung e, portanto, reunir dados dosimétricos realistas para os emissores beta puros.

Palavras-chave: Terapia com radionuclideos; Fotões Bremsstrahlung; Simulação de Monte Carlo; EGSnrc.

FRAMEWORK

The present dissertation encompasses a research work developed at the Institute of Nuclear Medicine (INM) of the University College London Hospital (UCLH), with a contribution of the Institute of Cancer Research (ICR) and the Department of Nuclear Medicine in Cambridge Biomedical Campus (Addenbrooke's Hospital). The work developed in UCLH was undertaken from February to November 2012, within the framework of an Erasmus exchange program.

The Institute of Nuclear Medicine (INM), actually included within the new UCL Hospital NHS Foundation Trust building, was founded in 1961 by Professor E.S. Williams (director of the institute 1963-1985) and by Professor P.J. Ell (currently consultant physician). This institute is the only academic department of nuclear medicine in the UK and its physics research group is internationally recognised. The INM is responsible for the nuclear medicine service of UCL Hospitals NHS Trust. In addition, the institute also offers the full range of nuclear medicine diagnostic, laboratory based and therapy procedures, which currently performs approximately 15,000 patient studies every year. The INM has a unique technology platform in the UK and it comprises an extensive range of state-of-the-art imaging equipment, image processing, IT systems and radiopharmacy/radiochemistry facilities. The institute is equipped with two PET-CT systems (a 16-slice system and a 64-slice system), two SPECT-CT systems, two SPECT gamma camera systems, a cardiac camera (D-SPECT) and DEXA (dual-energy x-ray absorptiometry) bone densitometry. Currently, it possesses the first fully integrated 3T PET/MR in the UK, as well as a full range of supporting nuclear medicine instrumentation. Particular areas of expertise include nuclear cardiology, PET-CT and SPECT-CT imaging in oncology and radiotherapy, the sentinel lymph node technique - the application of nuclear medicine to neurology and psychiatry, and radionuclide therapy (UCLH NHS Foundation Trust & UCL, 2011).

ACKNOWLEDGMENTS

The current thesis would not have been possible without the contribute, help and support of many people who followed me in different ways, both in this phase as along to many years during which transmitted me the necessary knowledge to achieve this step.

First, I am truly thankful to my supervisor Dr. Ian Cullum, for his continuous and valuable guidance, support, understanding and help throughout this study. Thank you for all your advices, for the patience in answering all my questions and for being a good mentor.

I am also thankful to INM for the opportunity to conduct the research, as well as to Prof. Robert Speller, from University College of London (Department of Medical Physics) to have advised me to participate in this project.

I would like to take the opportunity to thank all my teachers in FEUCP for all the academic knowledge transmitted, for have guided, inspired and helped us during our academic formation and education. A special thank you to Prof. Manuel Barata Marques, Prof. Pedro Encarnação, Prof. Rui Pires, Prof. Rui Assis, and Prof. Ana Pascoal who accompanied and guided me unconditionally throughout my whole MSc course, supported and motivated me to go further on without ever giving up.

A special thanks to all my friends who supported and encouraged me. Thank you Simone, for have made my life far away from home not so lonely. Thanks very much Nanas for being there when I needed. Gonçalo, to you I am really thankful for having followed my work so closely and for have given me the strength to carry on, sharing all the tough moments, not forgetting a big thank you for providing me the huge amount of computers to undertake my simulations.

Finally, and most importantly, I would like to thanks all my family. Mother/Father/Mano thank you so much for allowing me the opportunity to fulfil my dreams, for the support, encouragement, patience and love and for having made of me what I am today. Thank you!

CONTENTS

LIST OF FIGURES

LIST OF TABLES

LIST OF APPENDICES

LIST OF ABBREVIATIONS AND ACRONYMS

ADC	Analog-to-Digital Converters
ACHRE	Advisory Committee on Human Radiation Experiments
AE	Lower Electron Energy
AP	Lower Photon Energy
BNMS	British Nuclear Medicine Society
CT	Computer Tomography
CRT	Cathode Ray Tube
DPK	Dose Point Kernels
EANM	European Association of Nuclear Medicine
EC	Electron Capture
ECUT	Electron Cut-off Energy
EGS	Electron Gamma Shower
FOV	Field of view
FWHM	Full Width at Half Maximum
HEGP	High-Energy, General-Purpose
HSS	Health, Safety and Security
IAEA	Institute Atomic Energy Agency
IC	Internal Conversion
ICR	Institute of Cancer Research
ICRP	International Commission on Radiological Protection
INM	Institute of Nuclear Medicine
IRS	Ionizing Radiation Standards
IT	Internal Transition
LCD	Liquid Crystal Display
LEGP	Low Energy General Purpose
LEHR	Low-Energy, High-Resolution

LET	Linear Energy Transfer
LSF	Line Spread Function
MCA	Multi-Channel Analyser
MEGP	Medium Energy General Purpose
MR	Magnetic Resonance
NaI(Tl)	Thallium-doped Sodium Iodine Crystal
NRC	National Research Council
NEMA	National Electrical Manufactures Association
NIST	National Institute of Standards and Technology
PCUT	Photon Cut-off Energy
PFD	Probability Distribution Functions
PHA	Pulse-Height Analyser
PET	Positron Emission Tomography
PMT	Photomultipliers Tubes
SCA	Single-Channel Analyser
ROI	Region of Interest
RIT	Radioimmunotherapy
RNG	Random Number Generators
SLAC	Stanford Linear Accelerator Centre
SNMMI	Society of Nuclear Medicine and Molecular Imaging
SPECT	Single Photon Emission Computed Tomography
TRT	Targeted Radionuclide Therapy
UE	Upper Electron Energy
UP	Upper Photon Energy

CHAPTER 1.

INTRODUCTION

1. INTRODUCTION

1.1. Dissertation Context

Nuclear medicine is one of the most dynamic fields in medicine. It is defined by the British Nuclear Medicine Society (BNMS) and the Society of Nuclear Medicine and Molecular Imaging (SNMMI) as "*a medical specialty that embracing all applications that leads with unsealed radioactive materials for diagnosis, therapy and research purposes*". This scientific and clinical discipline is a painless and cost-effective technique. It uses a radiopharmaceutical, a chemical or molecular agent labelled with a small amount of a radioactive material (called radionuclide, radioisotope or unsealed source), to image the patient's body or treat diseases. Nuclear medicine is used by many medical specialties, such as paediatry, cardiology, psychiatry, angiology, and so forth, which resort to this field both to diagnostic and therapeutic purposes (Britton, 1995; SNMMI, 2004; BNMS, 2010)

The origins of nuclear medicine stem from many scientific discoveries, as the discovery of radioactivity from uranium, in 1896 by Henri Bequerel, and the finding, in 1898, of other natural radioactive compounds, as radium and polonium, by Marie Curie. But it was in 1913 that was born the real biological fundamentals to this speciality, when Georg de Hevesy developed the principles of the tracer approach, forming the first radiopharmaceutical. This event, amongst the fact of Alexander Graham Bell, in 1903, having suggested to place sources containing radium in or near tumours, which became to be the pioneering activities for the birth of radionuclide therapy (Wheat *et al.*, 2011).

After these, the growth of the nuclear medicine history was astonishing. The "artificial radioactivity" was found with the invention of cyclotron; Lawrence made the first clinical therapeutic application to treat leukaemia with phosphorus-32 (^{32}P) and the radioactive iodine-131 (^{131}I) was firstly applied in the treatment of the thyroid cancer (News Medical, 2012a).

The advent of technology has enabled further the progression of this multidisciplinary medical specialty. In 1958, the first gamma camera was developed by Hal Anger - an imaging device that detects photons (γ- and x-rays) from the isotope decay, creating images reflecting the distribution of the radiopharmaceutical in the human body. The development of a generator system to produce technetium-99m (^{99m}Tc) in the 1960s was a landmark event. Today, ^{99m}Tc is the most widely used radionuclide in the nuclear medicine (Cherry *et al.*, 2003; Graham & Metter, 2007).

The computational progress, together with the mathematics innovations to reconstruct tomographic images from a set of angular views around the patient, allowed the emergence of others image equipment, as the Single Photon Emission Computed Tomography (SPECT),

developed by David E. Kuhl, and the Positron Emission Tomography (PET), developed by Gordon (Graham & Metter, 2007).

This revolutionized the whole field of medical imaging, as it replaced the two-dimensional representation by a true three-dimensional representation of the radioactivity distribution (Cherry *et al.*, 2003), giving to the nuclear medicine a unique property to provide information about the function of an organ (SNMMI, 2004). All these events led to the nuclear medicine as we know it today.

As previously stated, the ^{99m}Tc is the most used radionuclide in imaging diagnostic. Consequently, the actual gamma cameras are designed to image low activities of low-energy gamma emitters produced by ^{99m}Tc. Contrasting to diagnostic, therapeutic radionuclides have high activities and high energies since the objective is to destroy malignant cells. Thus, the ideal mode of decay for radioisotopes used in radionuclide therapy is the beta-minus emission (β^-, also known as electrons). Beta emitters have a high linear energy transfer (LET) and just a few millimetres of tissue range enabling the tumour's destruction and reducing the likelihood of damaging healthy tissue (Sprawls, 1993).

The radionuclides used in diagnostic decay by emission of gamma rays. This radiation provides the ability to image the biodistribution *in vivo* of the radiopharmaceutical and consequently indicating the tumour localization and the non-target uptake and retention (Stanciu, 2012). There are some radionuclides used in the radionuclide therapy that emit both beta and gamma rays, as lutetium-177 (^{177}Lu) or rhenium-188 (^{188}Re) and therefore these ones enable simultaneously the treatment and uptake's visualization of the radiopharmaceutical that delivers the treatment *in vivo* (Flux, 2006; Stanciu, 2012), giving them a "bifunctional" property.

However, there are a few radioisotopes used in the radionuclide therapy that do not emit gamma rays. Those are the pure beta emitters, as yttrium-90 (^{90}Y) and phosphorus-32 (^{32}P), and their detection relies on the bremsstrahlung photons released when the electrons interact in the tissue (Heard, 2007). ^{90}Y also does produce 511keV gamma rays by a very low probability of internal pair production followed by annihilation, so it can be imaged on a PET scanner.

Imaging pure beta emitters, used in radionuclide therapy, are useful to assess the uptake and the distribution of the radiopharmaceutical for each tumour under treatment. However, the beta emissions are completely stopped inside the tissue (a few millimetres of range) and do not emit gamma rays. For this reason, it is not possible to detect them with gamma cameras.

Nowadays, for dosimetry purposes, surrogate radionuclides with gamma rays emissions and similar chemical properties, as the radionuclides used in radionuclide therapy, are typically used for treatment planning (Minarik *et al.*, 2009; Rong *et al.*, 2012). In the case of ^{90}Y, the pre-therapy dosimetry is performed by imaging the indium-111 (^{111}In) to predict the ^{90}Y activity

required for the treatment (Minarik *et al.*, 2010). However, imaging the therapeutic radionuclide biodistribution is essential to confirm its uptake and estimate the absorbed dose. Therefore, imaging pure beta emitters depends on the bremsstrahlung radiation produced in the patient (Walrand *et al.*, 2011). Problems, such as the low bremsstrahlung production efficiency, particularly in the low atomic number (low-Z) areas, such as tissue, and the continuous bremsstrahlung spectrum, prevent the easy formation of the bremsstrahlung imaging. According to Martin (2006), when beta particles are absorbed in the tissue (with a low-*Z*), less than 2% of the interactions produce bremsstrahlung and many of those might escape from the tissue medium, since the probability of interaction in media with low-Z is also small.

Problems related to bremsstrahlung imaging are a challenge to overcome, in order to allow a patient-specific dosimetry planning. There have been studies in this area to try to exceed the complexities and the challenges in detecting the bremsstrahlung photons, particularly in selection of the acquisition parameters of the gamma camera, such as the collimator or energy window.

1.2. Dissertation Aim

Since there is a great potential in imaging bremsstrahlung photons, created by pure beta emitters used in radionuclide therapy, and still is a challenge to do it because of all difficulties related to their emission and detection, the present investigation aims to study and understand the behaviour of the bremsstrahlung photons.

This dissertation comprises an understanding of the physical principles involved in the therapeutic process with unsealed sources when pure beta emitters are injected. The study attempts to realise the characteristics of the bremsstrahlung photons, when they are produced in different types of biological materials using different energies, *i.e.*, aims to recognize the relationship between bremsstrahlung photons, biological materials and different energies of beta particles.

For this purpose, a Monte Carlo simulation was used to simulate realistic events. Among some coding systems that use Monte Carlo simulation, for the present work the simulation's software called EGSnrc (Electron Gamma Shower) was chosen. EGSnrc was chosen due to its advantages with respect to electrons transport. The programs created in EGSnrc were written in Mortran language and compiled to Fortran.

A Mortran code using a point source of photons was used to validate the code model developed. The photons behaviour can be easily understood, making easier the full understanding of the EGSnrc system. The accuracy of the code may be validated by comparison of the results

obtained with the theoretical and published data. Another Mortran code was created to simulate the pure beta particles emission and hence the production of bremsstrahlung *in vivo*. Realistic events using beta particles source in different homogeneous media and for different energies emitted were simulated and the bremsstrahlung photons formed were recorded and studied. Also with the present study, one intends to obtain a strong knowledge of the EGSnrc system in order to be able to modify and produce a wide range of different simulations in different physical conditions.

Particular limitations in this study arise from the lack of published information in specific results, such as the bremsstrahlung spectra for different media, and the nonexistence of proved and validated evidences of imaging bremsstrahlung in patients treated with some pure beta emitters.

The results obtained may be a support tool that could be useful in future works as experimental evidence, mostly for dosimetric purposes. Due to the fact that this is an emerging area and in great development, further studies are required in order to establish and confirm the benefits of the practice, namely in the dosimetry field, to understand the real uptake of radionuclides in the patients treated by radionuclide therapy.

1.3. Dissertation Structure

The present dissertation is comprised of 5 main chapters. The second chapter presents the physics behind the nuclear medicine and all the concepts that will be drawn on throughout this study. The chapter is then divided into 3 different sections: section 2.1. summarises the general concepts of nuclear physics; section 2.2. provides an overview of the gamma camera components, imaging techniques and performance characteristics, and the last section reviews the concepts and the current practice of radionuclide therapy, the dosimetry undertaken in the treatments, as well as, it explains the difficulty in imaging bremsstrahlung photons. In chapter 3 it is clarified the methodology used in the investigation: section 3.1. summarises the general principles of Monte Carlo simulation, how EGSnrc works and likewise it described the models created in EGSnrc to achieve the proposed aim and in section 3.2. are presented the measurements undertaken. In chapter 4 all the results are described, as well as the discussion of one of them. Each simulation is properly explained in addition to the method used in each one of them. Section 4.1. refers to the validation of the Mortran code created, section 4.2. explains and discusses the bremsstrahlung results and section 4.3., mentions the validation of a program to decode the list mode data. Ultimately, the conclusions are referred in the followed chapters, along with the bibliography needed for the development of this study. The Mortran and Matlab codes developed are presented in the appendices.

CHAPTER 2.

GENERAL BACKGROUND

2. GENERAL BACKGROUND

Nuclear medicine is a medical speciality used both in diagnosis and therapy of a wide range of diseases. In each one of these situations, the goals are achieved throughout the energy release and uptake. This "*energy in transit*" or radiation (Cherry *et al.*, 2003) is obtained by the radionuclide decay. The radionuclide is linked to a pharmaceutical, forming the radiopharmaceutical administered to the patients. For diagnosis, the pharmaceutical is labelled with a gamma ray-emitting radionuclide or positron-emitting radionuclide, whereas in therapy the radiopharmaceutical ideally has a pure negative beta-emitting radionuclide or an alpha-emitting radionuclide.

After the radionuclide decay, the radiation interacts with the body tissues by several mechanisms, being scattered and attenuated. However, a significant fraction of the photons (gamma and x-rays) that outcome from the decay and tissues interactions can be externally detected by a sensitive gamma camera, forming an image of the distribution of the radiopharmaceutical in the body. A single photon imaging (Gamma Camera or SPECT) is used when the radionuclide decay by gamma ray emission, whilst a positron imaging (PET scanner) is used when there is a positron emission.

Due to the fact that the present study involves all the processes described above, a general physical approach will be summarised in this chapter as an introductory course of all physical mechanisms underlying in this project.

2.1. General Concepts of Nuclear Physics

All matter is composed of atoms. Each one of them contains a collection of protons and neutrons (nucleons) in the atomic nucleus and shells of electrons, with discrete energy levels, orbit the nucleus. An atom is completely identified by the formula ${}^{A}_{Z}X$, where *A* stands for the mass number, *i.e.*, number of nucleons, *Z* represents the atomic number, *i.e.*, number of electrons, (equal to the number of protons for stable atomic species), and *X* is the symbol for a certain chemical element. The number of neutrons is usually represented by *N (A-Z)*.

Besides the number and organization of the orbital electrons, which defines the atomic specie or chemical element, the composition of the atomic nuclei also determines the properties of atoms (Khan, 2003). An atomic specie, characterized by a specific nuclear constitution, is called a nuclide (Turner, 2007). Nuclides with the same number of protons constitute a chemical element and each nuclide with a different number of neutrons is called an isotope of that element. A given element may have many isotopes and some of them have unstable nuclear

combinations, by excess of protons or neutrons, or even both. In the nuclei of the unstable isotopes, called radioisotopes or radionuclides, the Coulomb force (repulsive) starts to gain ground relatively to the nuclear force (attractive) and they tend to break apart, being transformed into a more stable nucleus throughout a process called radioactive disintegration or radioactive decay (Bushberg *et al.*, 2002).

Consequently, when the neutron-proton ratio is slightly above or below the ratio of nuclear stability, the radionuclides attempt to reach stability by emitting radiation. This emission can be in the form of particles (changing the number of protons or neutrons within the nucleus) and/or photons.

The radioactive decay is a spontaneous process that continues until a stable nuclide is reached. This process results in the conversion of mass into energy and energy into mass, according to Einstein's equation:

$$E = mc^2 \qquad \text{Eq. (2.1)}$$

Where *m* represents the nuclear rest mass (in atomic mass units, *u*, with an energy equivalent of 931.5 MeV) and *c* stands for the speed of light. Therefore, the total mass-energy conversion, or the transition energy (*Q*) is equal to the net decrease in the rest mass of the stable atom, from the initial (or parent, which will be represent by *X*) to the final (or daughter, which will be represent by *Y*) atomic specie. Total energy, momentum and electric charge are conserved during the process (Cherry, *et al.*, 2003; Attix, 2004).

2.1.1. Radioactive Disintegration Processes

The three main disintegration processes in nuclear medicine are: alpha decay (α), beta decay (β), which encompasses three beta decays (β^-, β^+ and electron capture, EC) and gamma (γ) decay, which incorporates two processes (isomeric transition (IT) and internal conversion(IC)).

ALPHA DECAY (α)

Usually α-decay occurs naturally in heavy nuclides with $Z \geq 83$ (Turner, 2007). In this process the unstable nucleus emits an α-particle consisting on two neutrons and two protons. This results in a decrease of *A* by four, due to a reduction of both *Z* and *N* by two. This disintegration is often followed by gamma and characteristic x-ray emission, since the α-particle captures two electrons from its surroundings to become a neutral $^4_2$He atom. The general equation of α-decay can be written as:

$$ {}^{A}_{Z}X \xrightarrow{\alpha} {}^{A-4}_{Z-2}Y + Q_{\alpha} \qquad \text{Eq. (2.2)} $$

Where the $Q\alpha$ is the difference in mass-energy between the parent and formed products, daughter and α-particle, and shared between the α-particle and the daughter. However, since the nuclear rest mass of the daughter is much higher than that of the α-particle, the energy released in the decay is almost all transferred to the α-particle in the form of kinetic energy.

Due to their considerable higher mass (four times heavier than the proton) and electrical charge (twice than a proton), α-particles are not used in diagnostic medical imaging. The reason is that their ranges are limited to approximately 1cm/MeV in the air and typically less than 100μm in tissue (Bushberg *et al.*, 2002). However, they are used in radionuclide therapy or radioimmunotherapy (RIT) and the increasing of their effectiveness is being a subject of study by researchers (*e.g.* see Abbas *et al.*, 2011 and Kratochwil *et al.*, 2011).

POSITIVE BETA DECAY (B^+) AND ELECTRON CAPTURE (EC)

When the radionuclide has an excess of protons in the nucleus, *i.e.*, neutron deficit (low *N/Z* ratio), there is a high probability to occur a beta plus emission where the radionuclide decays to a stable level. As a result, a proton is converted into a neutron, ejecting a positron (β^+, which is the antiparticle of the electron) and a neutrino (ν) from the nucleus. The atomic number *Z* of the daughter nuclide decreases by one and *N* increases by one, whilst the mass number *A* remains constant since there is only a conversion of particles inside the nucleus. Schematically, the process of proton conversion and the positron emission equation could be represented, respectively, by:

$$ p \rightarrow n + \beta^+ + \nu \qquad \text{Eq. (2.3)} $$

$$ {}^{A}_{Z}X \xrightarrow{\beta^+} {}^{A}_{Z-1}Y + \beta^+ + \nu + Q_{\beta^+} \qquad \text{Eq. (2.4)} $$

The energy released in the decay, Q_{β^+}, is shared between the positron and neutrino, which could be calculated as follow (Eq. 2.5), neglecting the electron binding energy to the nucleus, assuming that the neutrino has essentially zero rest mass and no charge and the positron mass is equal to the electron mass (Attix, 2004). It is important to refer that the recoil kinetic energy given to the daughter is extremely small because of its relatively large mass, so it may be neglected (Turner, 2007; Podgorsak, 2010).

$$ Q_{\beta^+} = M_{N,X} - \left[M_{N,Y} + m_{\beta^+}\right] = M_X - M_Y - 2m_e \qquad \text{Eq. (2.5)} $$

Where M_N is the nuclear mass, *M* the atomic mass and m_e the electron rest mass energy equal to 0.511MeV. According to this equation, in order for β^+ decay to occur, the atomic mass of the parent must exceed the atomic mass of the daughter in at least $2m_e$=1.022MeV.

The radionuclides that emit a positron, such as fluorine-18 (^{18}F) or nitrogen-13 (^{13}N), are truly useful in diagnostic imaging. The positron, after losing its kinetic energy in collisions with the surrounding atoms, comes to rest and combines with its antiparticle, the electron, in an annihilation reaction. In this reaction, the masses of the two particles are converted into energy, which appears in form of two photons travelling in opposite directions (180° between them), each one with 0.511MeV. These two opposite photons are detected by PET scanners, enabling a spatial and functional imaging of the body (Podgorsak, 2010).

However, if the parent-daughter atomic mass difference is less than two times the electron rest mass energy, 1.022MeV, the positron emission cannot take place. Instead, an Electron Capture (EC) can occur. This is a competitive or an alternative to the positron decay for neutron-deficient radionuclides.

In the EC decay, an orbital electron, usually from the K-shell, is captured by a proton in the nucleus, converting the proton into a neutron with the ejection of a neutrino. The net effect of the EC is the same as in the positron emission: the *Z* is decreased by one, *N* is increasing by one and *A* remains unchanged. The general equations of EC can be written as follows:

$$p + e^{-} \rightarrow n + \nu \qquad \text{Eq. (2.6)}$$

$${}^{A}_{Z}X \overset{\text{EC}}{\rightarrow} {}^{A}_{Z-1}Y + \nu + Q_{\text{EC}} \qquad \text{Eq. (2.7)}$$

$$Q_{EC} = M_{N,X} + m_e - M_{N,Y} - B_e = M_X - M_N - B_e \qquad \text{Eq. (2.8)}$$

In this case, the neutrino carries away some of the transaction energy that equals the difference in atomic rest mass between parent and daughter, less the electron binding energy, B_e, of the electron captured. The remaining energy appears in the form of characteristic x-rays and/or Auger electrons emitted by the daughter nuclide. This is due to the fact that an electron of an outer shell will fill in the K or L-shell vacancy caused by the capture electron. Characteristic x-ray energy is equal to the energy difference of the orbitals involved in the process, which can be transferred to another electron knocking it out of its shell (Cherry *et al.*, 2003).

Positron decay and EC decay may be accompanied by gamma emission if the daughter is not in a completely stable level and the EC is always accompanied by characteristic x-rays and/or Auger electrons by the daughter nuclide. Thus, the radionuclides with parent-to-daughter transition energies greater than 1.022MeV may decay by EC or β^+ emission, or both, as it can be seen in figure 2.1., which represents the decay scheme of the ^{18}F into oxygen-18 (^{18}O) (Cherry *et al.*, 2003; Attix, 2004; Podgorsak, 2010).

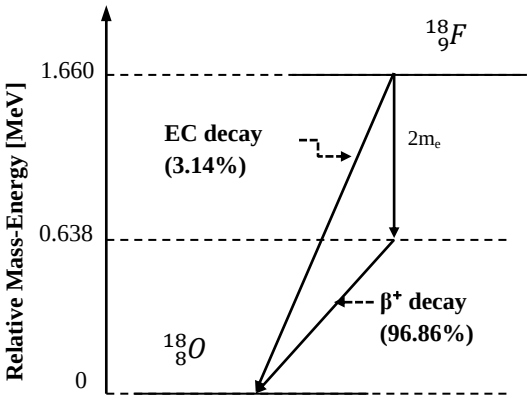

Figure 2.1. Decay scheme for ^{18}F into a stable nuclide ^{18}O, which may decay by both EC or β^+, with E_{max,β^+}=0.638MeV. For the ^{18}F, 3% of the nuclei decay by EC and 97% decay by beta plus emission (Adapted from Cherry *et al.*, 2003; LNHB, 2006)

NEGATIVE BETA DECAY (β^-)

Contrary to the positron emission, negative beta decay occurs when the radionuclide nucleus has an excess of neutrons (high *N/Z* ratio), when compared with the number of protons. In this case, a neutron in the nucleus is transformed into a proton with a simultaneous ejection of a negative beta particle (β^-, identical to electron, with the exception of their origin) and an antineutrino ($\bar{\nu}$). When a β^- particle is emitted, the *N* decreases by one, the *Z* increases by one, so that *A* remains unchanged. Schematically, the previous process and the negative beta emission equation may be written, respectively, as:

$$n \rightarrow p + \beta^- + \bar{\nu} \qquad \text{Eq. (2.9)}$$

$$^{A}_{Z}X \xrightarrow{\beta^-} {}^{A}_{Z+1}Y + \beta^- + \bar{\nu} + Q_{\beta^-} \qquad \text{Eq. (2.10)}$$

The energy released in the negative beta decay, Q_{β^-}, is the difference between the mass energies of the parent and daughter nuclides, considering the electron binding energy neglected and assuming the antineutrino, such as the neutrino, with zero rest mass and no charge (Turner, 2007; Podgorsak, 2010).

$$Q_{\beta^-} = M_{N,X} - \left[M_{N,Y} + m_{\beta^-}\right] = M_X - M_Y \qquad \text{Eq. (2.11)}$$

This energy is shared between the electron and the antineutrino. As explained before, the recoil nucleus (daughter), because of its relatively large mass, receives negligible energy. Therefore, if E_{β^-} and $E_{\bar{\nu}}$ are the initial kinetic energies of the electron and antineutrino is possible to write:

$$Q_{\beta^-} = E_{\beta^-} + E_{\bar{\nu}} \qquad \text{Eq. (2.12)}$$

Decay modes, such as the beta decays (β^-, β^+ and EC), in which the mass number do not change, are called isobaric transactions (Bushberg *et al.*, 2002). A beta minus emission is shown in figure 2.2., representing the carbon-14 (^{14}C) decay into nitrogen-14 (^{14}N).

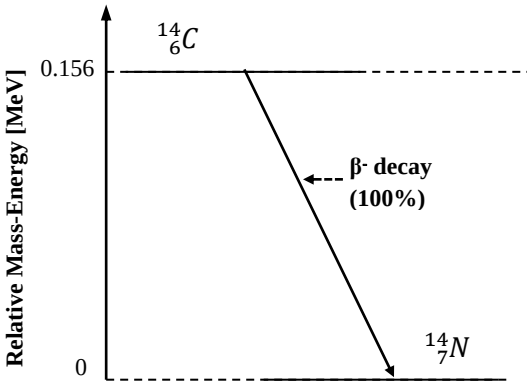

Figure 2.2. Decay scheme diagram for ^{14}C into a stable nuclide ^{14}N, which decay only by β^- emission, with E_{max,β^-}=0.156MeV (Adapted from Cherry *et al.*, 2003; LNHB, 2012)

In opposition to the β^+ emitters, β^- are not useful in diagnostic medical imaging because they travel a short distance inside the tissue and do not produce any gamma photons capable of being detected externally. However, according to Joseph (2006), the pure beta-minus emitters demonstrate good results in clinical therapeutic purposes, being therefore used in radionuclide therapy, as seen in section 2.3.

In contrast with α- and EC decays, where the energies of the decay products are uniquely defined by the production of a monoenergetic spectrum, β^- and β^+ decays emit the most of their particles with energies lower than the maximum of the particle decay energy (T_{max}). These particles exhibit a continuous spectral kinetic energy distribution, resulting in a polyenergetic spectrum ranging from zero to T_{max}, calculated according to the Fermi theory of the beta decay (Podgorsak, 2010). The average energy of the β particles emitted is approximately $1/3T_{max}$. Typical shapes of β^- and β^+ spectra are presented in figure 2.3.

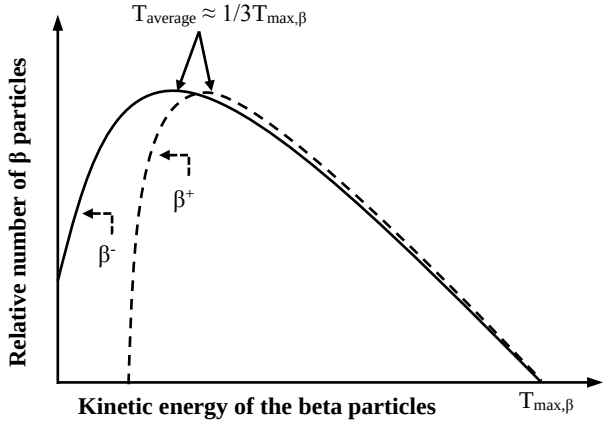

Figure 2.3. Typical spectrum of beta particle energy. Energy distributions of beta particles emitted (Adapted from Podgorsak, 2010)

The differences at low kinetic energies are related to the particle charge. The electrons are attracted by the nucleus while the positrons are repelled, causing an energy shift to lower energies for electrons and to higher energies for positrons (Bushberg *et al.*, 2002; Podgorsak, 2010).

ISOMERIC TRANSITION (IT) AND INTERNAL CONVERSION (IC)

After an isobaric transition, the daughter nuclide could remain with an excess of energy and it will further decay until it achieves a stable level. In order to reach stability, the daughter nucleus may emit a nonparticulate radiation in form of gamma photon, with the Z and N remaining constant. This process, in which energy is given off as a gamma photon, without change of mass and atomic number, is called isomeric transition (IT) (Mettler & Guiberteau, 2006).

The gamma rays are very useful in diagnosis imaging, since the nuclear medicine imaging equipment, as the gamma camera, are tuned to detect photons. The detected energy is determined by the difference between the intermediate and final states of the daughter nucleus and generally is in the range of 100keV to 500keV (Sprawls, 1993). It is noted that the intermediate state could emit more than one gamma ray, with different energies, until it reaches stability.

The isomeric transitions occur quickly after the isobaric ones. However, if the nuclear excited state has a long lifetime, this intermediate state is called metastable, as in the case of the ^{99m}Tc. According to Sprawls (1993), metastable states are important in nuclear medicine due to the fact that in a metastable state the only energy emitted from the nucleus and detected from the external equipment are the gamma rays. This avoids, consequently, the electron emissions in the body, which do not contribute to the medical image formation but only to the radiation dose in the patient.

Figure 2.4. represents the decay scheme of molybdenum-99 (^{99}Mo) which undergoes an isobaric transition to technetium-99 in the metastable state, ^{99m}Tc. The ^{99m}Tc will later undergo an isomeric transition to ^{99}Tc.

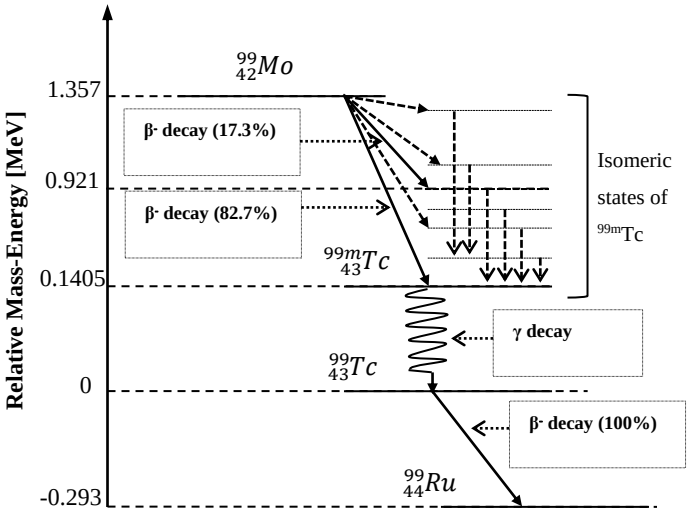

Figure 2.4. Simplified decay scheme of isobaric nuclides: ^{99}Mo/^{99m}Tc/^{99}Ru. The decay starts with a β^- decay of ^{99}Mo into ^{99m}Tc, followed by a gamma ray emission of ^{99m}Tc into ^{99}Tc, and ending with a β^- emission of ^{99}Tc into a stable ^{99}Ru (Adapted from Podgorsak, 2010)

In some cases, the excess of energy emitted by the intermediate nucleus in the form of gamma ray ($h\upsilon$) may be transferred to an orbital electron within the atom. If the energy transferred to this electron is higher than its binding energy (B_e), the electron escapes from the atom with a net kinetic energy of $h\upsilon$-B_e (Attix, 2004).

This process is known as internal conversion (IC) and competes with the IT. However, IC just can occur when the energy transferred to the orbital electron exceeds its biding energy. After the electron being ejected, a vacancy is created. If the vacancy is replaced by an electron from a higher energy level, characteristic x-rays and/or an Auger electron are emitted (Sprawls, 1993).

The ratio between the internal conversion electrons and internal transition is called by internal-conversion coefficient (α). A low conversion ratio is preferable since it allows a greater number of gamma emissions used in medical imaging, avoiding the electrons production (Mettler & Guiberteau, 2006).

2.1.2. Characteristics of Radioactive Decay

According to the Advisory Committee on Human Radiation Experiments (ACHRE), the act of emitting radiation spontaneously by an unstable nuclide is called radioactivity. Radioactivity is "*a physical, not a biological, phenomenon"* from the radioactive nuclides (HSS, 1995). Hence, radioactive nuclei, either natural or artificially, decay by a spontaneous process in which is impossible to predict exactly the moment of its transformation into another stable nuclide.

However, since nuclear medicine works, not with individual nuclei, but with a sample or collection of radioactive material, the radioactive decay could be described in terms of probabilities and average decay rates. The amount of radioactivity present in a sample is measured by its activity (A). The activity of a sample is the rate at which the nuclei, within the sample, undergo transformations. It can be measured by counting how many atoms are spontaneously decaying in each second and it is express in units of curie [Ci], or currently, in the SI unit, the Becquerel [Bq], which is defined as one disintegration per second ($1Ci=3.7x10^{10}Bq$) (Sprawls, 1993; Barnes, 1996).

The activity, independently of the nature of the decay mechanism, is described mathematically as the change (dN) of the total number of radioactive atoms in a sample (N) in a given period of time (dt), or simplified, is equal to the decay constant (λ) times the total number of unstable atoms in a sample in that time. Both methods are represented in equation 2.13.

$$A(t) = -dN/dt = \lambda N(t) \qquad \text{Eq. (2.13)}$$

The minus sign indicates the decline of the radioactive nuclei during time. The decay constant is equal to the fraction of the number of radioactive atoms remaining in a sample, or alternatively, is the probability of any nucleus to undergo a decay per unit time. The decay constant has a characteristic value for each radionuclide and is measured in seconds^{-1}. By integrating equation 2.13., it is possible to define the exponential radioactive decay law (Eq. 2.14), which expresses the exponential decay of every kind of radioactive nucleus over time (Bushberg *et al.*, 2002).

$$N = N_0 e^{-\lambda t} \; or \; A = A_0 e^{-\lambda t} \qquad \text{Eq. (2.14)}$$

This equation allows calculation of the number of unstable nuclei in the sample at any time *t*, knowing the initial amount of radionuclides, N_0, at t=0sec. On the other hand, equation 2.14., permits to identify the remaining activity, *A*, in the sample after *t* time, assuming an initial activity equal to A_0. Figure 2.5., plots equation 2.14 during successive times *T*, called the half-life of the radionuclide in which the activity drops by factors of one-half, as shown.

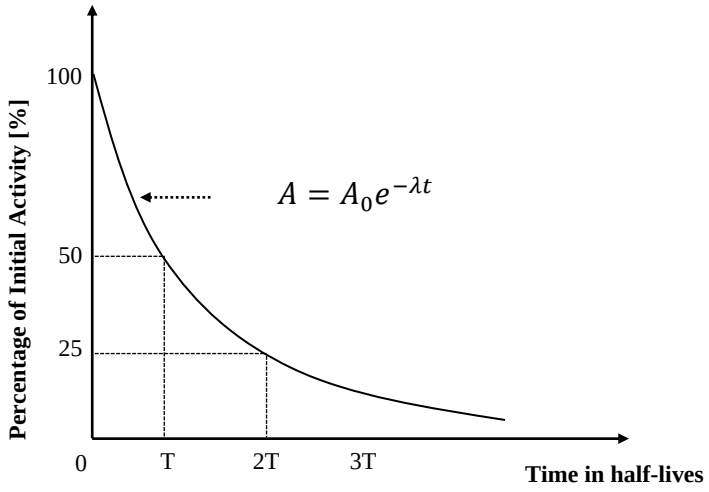

Figure 2.5. Exponential radioactivity decay law, showing the activity *A* of a sample as a function of time *t.* Linear scale is used (Adapted from Bushberg *et al.*, 2002)

The half-life ($T_{1/2}$) is a parameter related to the decay constant. It is defined as the necessary time for the radioactive atoms to decrease to one half, in a given sample, which means that the sample will be reduced to half of its existing activity. So, if in the beginning a sample has N_o radiative atoms, after an half-life, particular for each radionuclide, the remaining number of radioactive atoms (*N*) will be $N_o/2$. The decay constant and the half-life are related as follows:

$$\lambda = ln2/T_{1/2} \qquad \text{Eq. (2.15)}$$

Both the decay constant and the half-life are unique parameters for each radionuclide (Turner, 2007). Thus, it is possible to say that the half-life, together with the nature of the decay process (α, β and γ-decay) can be a signature for the identification of the isotope. The half-lives of the radioactive isotopes range from fractions of a second to billions to years (ISNAP, 2011).

In nuclear medicine, the radioactive material is administered in a living organism. Therefore, the material might be removed from the organism by normal radioactive decay of the radionuclide but also by biological transport. The half-life used to designate the normal radioactive decay, such as nominated above, is generally called physical half-life (T_p). In addition to the physical half-life, two other half-life terms are commonly used: the biological half-life (T_b), which refers to the time that an organism takes to eliminate half of the radioactive material administered by biological ways, and the effective half-life (T_e) which is associated with both physical and biological half-lives (Mettler & Guiberteau, 2006). When the biological transport or elimination occurs, the lifetime of the radioactive material in the body is reduced and it is generally expressed in terms of an effective half-life, by the follow equation:

$$T_e = (T_p x\, T_b)/(T_p + T_b) \qquad \text{Eq. (2.16)}$$

It is important to highlight that when both physical and biological half-life exist, the effective half-life is always shorter than either one or other (Sprawls, 1993).

Choosing a radiopharmaceutical with an effective half-life that agrees with the duration of the study is crucial for dosimetric purposes. If the radionuclide has a long life then the effective half-life can be reduced by choosing a chemical component with a short biological half-life (Podgorsak, 2010).

Subsequently to the radionuclide disintegration into a stable state, the particles and/or photons emitted, with certain energy according to the radionuclide, will interact with the surrounding tissues. Sometimes, photons may eventually dissipate without transferring any energy to the surrounding medium. The transferred energy to the matter is truly important for dosimetric purposes. According to Stabin (2007), it has important implications for radiation biology, radiation shielding, radiation detection, and for every practical application of radiation protection.

In the next section, the interaction mechanisms of the photons and particles with matter will be described. However, since the present work concerns, primarily, with the beta-emitting radionuclides, only the electron interactions will be discussed, as well as the photons interaction types which provide energy loss during the collision with matter, such as the photoelectric effect, Compton scattering and pair production. Photon interactions occur both in tissue and in the gamma camera.

2.1.3. Photons Interactions

Photons (x-, γ-rays or bremsstrahlung) may transfer all of their energy to matter, being totally absorbed, or they may transfer part of their energy when they are scattered or deflected from their original direction. In this last case, the photons no longer carry useful imaging information. Photons, eventually, may also penetrate the matter without interacting, and consequently, without losing any of their energy (Joseph, 2006; Turner, 2007). Most of the time, when the photons energy is low to moderate, photons interact with the whole atom or with the orbital electrons, whereas those with high energy interact with the atomic nuclei (Stabin, 2007).

One should emphasize that photons do not steadily lose energy via coulombic interactions with matter, as do charged particles (MIT NSE, 2005). This is due to the fact that photons are indirectly ionizing radiation, electromagnetic radiation with zero mass and electrically neutral. For that reason, photons travel a considerable distance before undergoing an interaction and when they do interact, the energy is transferred to the matter into two single steps (MIT OCW NSE, 2007a). The initial step involves the kinetic energy transfer to the medium, with subsequently ejection of electrons from the atoms involved in the interaction. The second phase comprises the energy transfer from these high-speed electrons (such as the beta particles) to the matter, by producing ionization and excitation of the atoms along their paths, causing biological effects (Khan, 2003).

The consequences of those facts will be analysed in section 2.3. The types of photon interactions with matter will be described below, including pair production, an uncommon interaction in gamma camera imaging, but possible to occur since in the current work the beta particles energies, and hence the bremsstrahlung photons energies, may exceed 1.022MeV.

PHOTOELECTRIC EFFECT

In the photoelectric process, a photon with energy $h\nu$ experiences an interaction with an atom of the absorbing medium. The photon energy is completely absorbed by an orbital electron. The orbital electron is ejected from its shell with kinetic energy $T=h\nu-B_e$, where B_e is the binding energy of the ejected electron, and it is called of photoelectron. Thus, the incident photon completely disappears and the photoelectron carries off the resultant energy by producing ionizations and excitations, along a path until its energy is dissipated.

The photoelectron creates a vacancy in the orbital shell which is filled in by an electron from the previous shell with a lower biding energy. In turn, it creates another vacancy filled in by an electron from an even lower binding energy shell. This process keeps creating an electron cascade from outer to inner shells until the atom remains in a stable state. These electronic transitions are followed by simultaneous emission of characteristic x-rays (more frequent in

high *Z*-materials), with energy equal to the difference of the binding energies, or Auger electrons (more frequent in low *Z*-materials). Usually, the majority of photoelectric events involves interactions with the innermost orbital shell, the K-shell. The energy of the incident photon must be greater or equal than the biding energy of the K-shell, in order for the photoelectric effect occurs (Cherry *et al.*, 2003; Khan, 2003; Attix, 2004; MIT NSE, 2005; Heard, 2007; Stabin, 2007; Tu rner, 2007). Figure 2.6., represents a photoelectric event with characteristic x-ray emission.

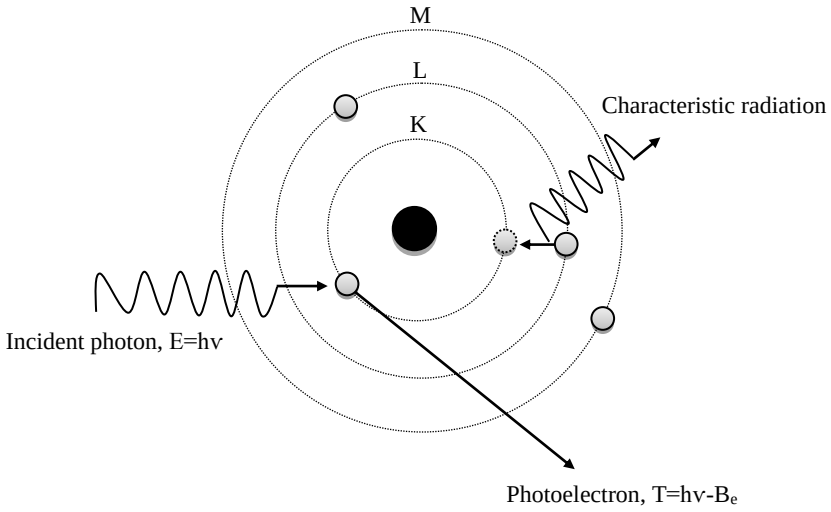

Figure 2.6. Representation of the photoelectric effect with characteristic x-ray emission. Note that, although not shown on this diagram, Auger electrons can be emitted instead of the characteristic x-ray (Adapted from Alpen, 1990)

According to Attix (2004), Stabin (2007) and Turner (2007), the probability of photoelectric effect occurrence depends strongly on the photon energy, *E*, as well as, on the atomic number *Z* of the absorbing medium. The probability of producing a photoelectron per atom or the atomic cross section, symbolized by ${}_a\tau$, varies accordingly Z^4/E^3. This relationship is used for energies equal or below 0.1MeV, where the photoelectric effect becomes more important. Consequently, with base of the relation above, the photoelectric effect has a higher probability of occurring in high-*Z* materials and low-energy photons.

The angular distribution of the photoelectron also depends on the photon energy. The photoelectron is emitted at 90° when low-energy photons interact and in a more forward direction when high-energy photons interact with the atoms (Khan, 2003).

COMPTON SCATTERING

The Compton scattering, also known as inelastic or incoherent scattering, is the most dominant interaction mechanism in the biological tissues, as well as, the predominant interaction mechanism for photons with energies typically in a range from 100keV to 10MeV (MIT OCW NSE, 2007a).

In this process, an incident photon with energy $h\nu$, interacts with an orbital electron, which is assumed to be unbound, stationary, with total energy m_0c^2 and usually in an outer atomic shell (Bushberg *et al.*, 2002; Attix, 2004; Podgorsak, 2010). The incident photon, referred to as scattered photon, is deflected from its original path, losing some energy to the electron. The electron is ejected from the atom with kinetic energy T and referred to as Compton or recoil electron (Khan, 2003; Attix, 2004; Turner, 2007; Podgorsak, 2010). Just like in the photoelectric effect, this recoil electron loses its kinetic energy by producing ionizations and excitations along a path (MIT OCW NSE, 2007a). The incident photon is deflected with an angle θ, designated as photon scattering angle and the recoil electron is ejected with an angle φ, designated as electron scattering angle. A typical Compton scattering interaction is shown, schematically, in figure 2.7.

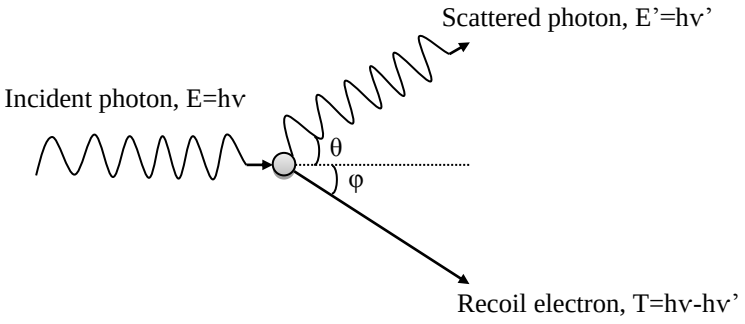

Figure 2.7. Schematic representation of the Compton Scatteringm where $h\nu$ is the incident photon energy, $h\nu'$ the scattered photon energy, θ photon scattering angle and φ electron scattering angle (Adapted from Alpen, 1990)

According to Khan (2003) and Anderson (2007), the Compton process can be analysed according to quantum-mechanics (double nature of radiation), *i.e.*, considering the interaction between two particles, photon and electron. The expressions that relate the energy transferred and the scattering angle for the resultant particles can be derived by applying the laws of conservation of energy and momentum, as shown below in equations 2.17., 2.18. and 2.19. (Templeman, 2000; Attix, 2004). Since the energy and momentum are conserved in this process, the energy of the incident photon, $h\nu$, is equal to the sum of the energy of the scattered

photon, *hν'*, and the kinetic energy of the recoil electron, *T* (Bushberg *et al.*, 2002; MIT OCW NSE, 2007a; NDT Resource Center, 2007).

Scattered photon energy: $$h\nu' = \frac{h\nu}{1 + \alpha(1 - cos\,\theta)}$$ Eq. (2.17)

Recoil electron energy: $$T = h\nu - h\nu'$$ Eq. (2.18)

Electron scattering angle: $$\cot\varphi = (1 + \alpha)\tan(\theta/2)$$ Eq. (2.19)

Where $\alpha = h\nu/m_0c^2$ and m_0c^2 is the electron rest mass, 0.511MeV.

Scattering angles between 0° and 180° are possible. Therefore, the energy transferred to the recoil electron may vary from zero to a value near to the maximum photon energy. This energy shift depends on the angle of scattering and not on the nature of the scattering medium (NDT Resource Center, 2007).

The incident photon can be deflected from its original direction, with ranges from 0° (forward scattering) to 180° (back scattering), whereas the recoil electron may have a scattering angle with ranges from 0° to 90° (Podgorsak, 2010). When the incident photon interacts directly with the orbital electron, the electron is scattered in a forward direction and the scatter photon travels in a backward direction, resulting in a backscattering collision with φ=0° and θ=180°. In this case, the electron receives maximum energy T_{max}, and the scattered photon is deflected with minimum energy $h\nu'_{min}$. Consistent with Khan (2003), replacing φ=0° and θ=180° in equations 2.17 and 2.18, one can obtain:

Maximum recoil electron energy: $$T_{max} = h\nu\frac{2\alpha}{1 + 2\alpha}$$ Eq. (2.20)

Minimum scattered photon energy: $$h\nu'_{min} = h\nu\frac{1}{1 + 2\alpha}$$ Eq. (2.21)

On the contrary, if the incident photon makes a grazing hit with the orbital electron, this is scattered in the perpendicular direction of the incoming photon, φ=90°, whereas the scattered photon goes in the forward direction, θ=0°. In this situation, the recoil electron does not receive any energy and the scattered photon receive the maximum energy, T=0 and $h\nu'=h\nu$ (Khan, 2003; MIT OCW NSE, 2007a). This last type of interaction is of little significance in terms of biological consequences or shielding, since the recoil electron does not have any energy and therefore do not cause damage to the surrounding tissues (Stabin, 2007).

However, the amount of energy transferred to the recoil electron varies with photon energy. Using the relativistic quantum mechanical Klein-Nishina formulation, which considers the

electron at rest and unbound, and is used for photons energies higher than 100keV, it is possible to determine the relative probability of each energy transfer. Consequently, one may also determine the average fraction of the incident energy given to the electron, which is relevant for dosimetric calculations since it contributes to the dose (Johns & Cunningham, 1983; Attix, 2004; Stabin, 2007). The total Klein-Nishina cross section or the Compton collision cross section per electron gives the probability of a photon interact with a "free electron" of the medium by Compton scatter (Turner, 2007; Podgorsak, 2010). This Compton scattering probability, symbolized by $_e\sigma$, is independent of atomic number Z considering that the electron binding energy is assumed to be zero (Khan, 2003; Attix, 2004; MIT OCW NSE, 2007a).

In general, the probability of Compton scattering to occur, decreases with the increasing photon energy and with the increasing atomic number of the medium. As a result, the Compton scattering is a predominant mode of interaction in low atomic-number media (Stabin, 2007). If a Compton scattering interaction takes place for low-energy photons (10 to 100keV), just a small amount of energy is transferred to the medium and the main part of it is merely scattered. Whereas for high-energy photons, above 10MeV, almost all of the energy is transferred to the recoil electron and a fractional part is scattered (Johns & Cunningham, 1983; Cherry *et al.*, 2003; Khan, 2003; MIT OCW NSE, 2007a). As the energy of the incident photon increases, both scattered photon and recoil electron are dispersed more toward the forward direction (Bushberg *et al.*, 2002). According to Heard (2007), the energy distribution of the recoil electrons forms a continuum spectrum from zero up to T_{max}, which is also known as the Compton edge.

PAIR PRODUCTION

When a photon, with energy greater than twice of the electron rest mass energy ($2m_oc^2$), interacts strongly with the electromagnetic field of an atomic nucleus, a pair-production interaction may occur. In this interaction, the photon is completely absorbed and its energy is converted into matter, together with the production of a pair of particles, an electron and a positron. Both particles tend to be emitted in a forward direction relatively to the incident photon. The remaining energy (hv-1.022) is shared between the particles as kinetic energy. The inverse process, namely the conversion of mass into energy, takes place when the positron, at rest, quickly annihilates with another electron of the medium, producing two photons, each one with 0.511MeV, emitted in opposite direction by conservation of momentum, as seen in figure 2.8. (Sprawls, 1993; Khan, 2003; Joseph, 2006). The probability of a pair production event to occur, increases with the increasing of the atomic number approximately as Z^2, as well as with the photon energy, above the threshold 1.022MeV (Turner, 2007).

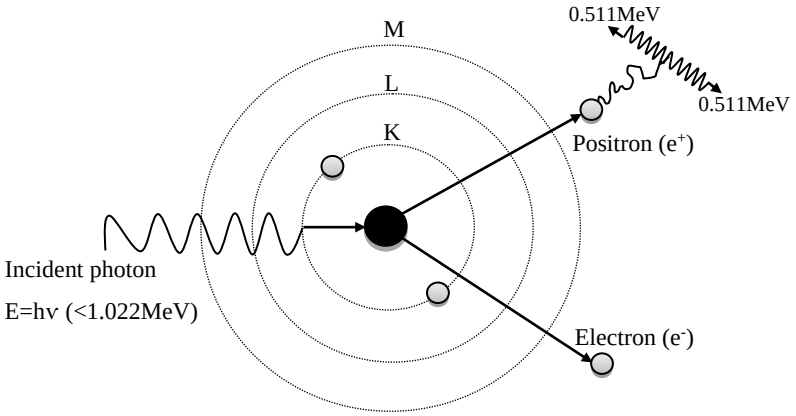

Figure 2.8. Representation of the pair production interaction with annihilation photons (Adapted from Alpen, 1990)

PHOTON ATTENUATION

The relative importance of the photoelectric effect, Compton scattering and pair production, depends both on the incident photon energy, $h\nu$, as on the atomic number, Z, of the absorbing medium, as seen in figure 2.9. The curves delimit the regions in which each interaction predominates and where two kinds of interactions are equally probable. As previously stated, the photoelectric effect is dominant at lower energies and the pair production at higher energies. Compton Scattering takes over at medium energies but for low-Z media, such as soft tissue or water, the region of this interaction is very broad (dashed line), being this the main interaction in imaging diagnosis and therapy in nuclear medicine (Advanced Laboratory of Physics, 2001; Attix, 2004).

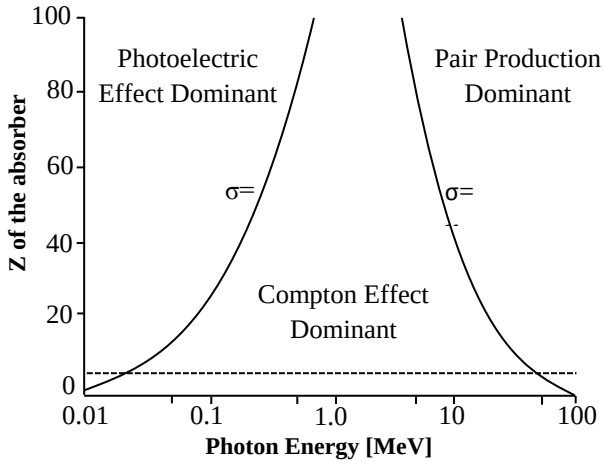

Figure 2.9. Relative importance of Photoelectric effect, Compton scattering and Pair production over a wide range of energy, $h\nu$, of the incident photons and atomic numbers, Z, of the attenuating material (Adapted from Evans, 1955)

The incident photon interacts with the absorber medium by only one of the three (or more, not mentioned in this work) processes referred before. Each type of interaction has a probability to occur, proportional to the cross section of that process. Therefore, according to Johns and Cunningham (1983), the probability of an interaction is proportional to the sum of the individual cross sections of each type of process. This probability is represented by the macroscopic attenuation coefficient or total linear attenuation coefficient (μ), written as the sum of the individual linear attenuation coefficients for each type of interaction (Bushberg *et al.*, 2002; Attix, 2004; Turner, 2007; Podgorsak, 2010)

$$\mu = \tau + \sigma + \kappa \qquad \text{Eq. (2.22)}$$

Where τ, σ, and κ denote, respectively, the linear attenuation coefficients for the photoelectric effect, Compton scattering and pair production.

It is the total linear attenuation coefficient that governs the distance penetrated by the incident photon in the matter (Turner, 2007). The term *attenuation* refers to the removal of photons from a beam, caused by the absorption and scattering of the primary photons (Bushberg *et al.*, 2002). A collimated and monoenergetic beam, with initial intensity I_0, is attenuated exponentially when it passes throughout a slab of material, as a function of the linear attenuation coefficient and depth of material, x, such that the intensity is reduced to I, according to the following exponential relationship:

$$I = I_0 e^{-\mu x} \qquad \text{Eq. (2.23)}$$

The linear attenuation coefficient varies according to the energy of the incident photon, hv, and to the atomic number, Z, of the absorber medium or its density. A photon beam is more attenuated with the decreasing of the energy photon, with the increasing of the atomic number as well as with the increasing thickness of the absorber (MIT NSE, 2005; Bushberg *et al.*, 2002; Stabin, 2007).

It is noted that, contrary to the charged particles, when I falls off exponentially, no specific range [cm] to photons may be described (MIT NSE, 2005). However, the distance travelled before an interaction may be predictable as the inverse to the attenuation coefficient (Sprawls, 1993; Knoll, 2000, MIT NSE, 2005).

2.1.4. Electron Interactions and Bremsstrahlung Photons Production

In this section only the electron interactions will be referred, since the present dissertation comprises the study of the radionuclide therapy with pure beta-minus emitters, *i.e.*, electrons emitters. Contrary to the photons, electrons and positrons (described as light charged particles) are responsible for the dose in the patient.

In case of electrons, produced either by decay of pure beta emitter's radionuclides or produced by photons interactions, they release all their kinetic energy in the surrounding medium. For this reason, in radiation dosimetry the main concern regards to the energy absorbed per unit mass of the absorbing medium (Podgorsak, 2010). It is the parameter *stopping power*, the one used to describe the average rate of energy loss per unit of path length, *x*, by a charged particle of type *Y* with kinetic energy *T*, when it travels throughout a medium of atomic number *Z*. The stopping power is represented by the following equation (Attix, 2004).

$$S = (dT/dx)_{Y,T,Z} \qquad \text{Eq. (2.24)}$$

The stopping power, *S*, may be also represented by taking into account the density, ρ, of the material penetrated by the charged particle. In this case the stopping power is divided by the density of the absorbing medium, resulting in a quantity called *mass stopping power*, which is represented by S/ρ [MeV.cm^2/g] (Attix, 2004; SNMMI, 2012).

An electron may interact with one or more orbital electrons or with the nucleus of practically every atom it encounters, as it penetrates into matter. These interactions are mediated by the Coulomb force between the electric field of the traveling particle and the electric field of the orbital electrons or atomic nuclei of the material (Khan, 2003). When an electron interacts with another orbital electron, a collisional loss occurs. Whereas, when an electron interacts with a nucleus of the absorber the result is a radiation loss. Those two mechanisms of energy transfer by the electron to the medium are shown in figure 2.10. (Podgorsak, 2010).

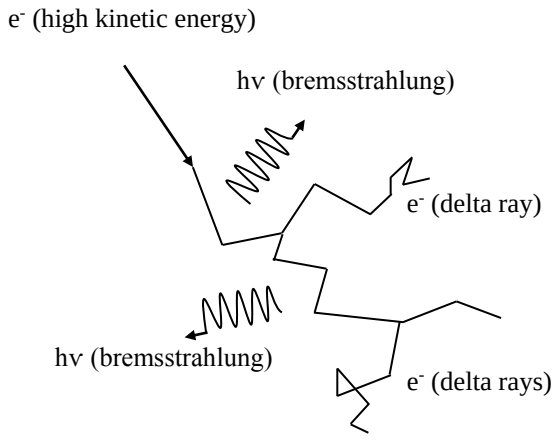

Figure 2.10. Electrons depositing energy through collisional and radiative losses when interact with the surrounding matter (Adapted from MIT OCW NSE, 2007b)

As a result, the *total mass stopping power* ($(S/\rho)_{tot}$) corresponds to the sum of two components: the *mass collision stopping power* ($(S/\rho)_{col}$), resulting from electron–orbital electron interactions (atomic excitations and ionizations), and the *mass radiative stopping power* ($(S/\rho)_{rad}$), resulting from electron–nucleus interactions (bremsstrahlung production) (Turner, 2007; Podgorsak, 2010; SNMMI, 2012).

$$\left(\frac{S}{\rho}\right)_{tot} = \left(\frac{S}{\rho}\right)_{col} + \left(\frac{S}{\rho}\right)_{rad} \qquad \text{Eq. (2.25)}$$

COLLISIONAL LOSSES

The collision stopping power theory is based on quantum mechanical and relativistic concepts. It is further subdivided into two components: the soft collision and the hard collision.

A soft collision interaction occurs when the electron passes from a considerable distance from an atom. The influence of the electron Coulomb force field affects the atom as a whole and may cause atomic polarization (distorting), excitation (when an orbital electron absorbs energy and moves into a higher energy state), or even ionization (by ejecting a valence shell electron, which is less common).

In the soft collisions, only a small fraction of energy (a few eV) is transferred to the bound electron. However, the number of these interactions is large and therefore half of the energy transferred to the medium occurs through the soft collisions (Attix, 2004; Podgorsak, 2010). On the other hand, a hard collision occurs when the electron interacts directly with a single orbital electron, which is ejected from the atom as a delta (δ) ray or as a secondary electron with significant amount of energy. It should be noted that characteristic x-rays and/or Auger electrons may be emitted as consequence of the fill in the vacancy by another electron from a higher energy shell. Although hard collisions are just a few compared to soft collisions, the fraction of energy transfer by these two processes are generally comparable. Since δ rays are energetic enough, they are able to undergo their own Coulomb interactions. These interactions occur along a considerable distance away from the primary particle track, forming, thus, secondary particles tracks (Attix, 2004; Stabin, 2007; Podgorsak, 2010).

The energy transferred to the medium through ionizations and excitations by the primary electron or δ-rays is responsible for the absorbed dose on the patient. This fact implies that the calculus of the energy absorbed per unit mass (mass stopping power), necessary to dosimetric purposes, encompasses the collision losses of the primary electron along with the additional interactions caused by the δ-rays (Sprawls, 1993; Martin & Sutton, 2002; Khan, 2003; Stabin, 2007; Turner, 2007; Podgorsak, 2010).

In this way, according to Evans (1955) and Kase and Nelson (1978) (quoted in Attix, 2004) the total mass collision stopping power for electrons (soft collision stopping power plus hard collision stopping power), derived from the Bethe's soft collision formula with a hard-collision relation based on the Møller cross section for electrons, is given by:

$$\left(\frac{S}{\rho}\right)_{col} = \left(\frac{S}{\rho}\right)_{soft} + \left(\frac{S}{\rho}\right)_{hard} \qquad \text{Eq. (2.26)}$$

$$\left(\frac{S}{\rho}\right)_{col} = 2\pi r_e^2 \frac{Z}{A} N_A \frac{m_e c^2}{\beta^2}\left[ln\frac{T}{I} + ln\left(1+\frac{\tau}{2}\right) + F^-(\tau) - \delta\right] \qquad \text{Eq. (2.27)}$$

$$F^-(\tau) = (1-\beta^2)[1+\tau^2/8-(2\tau+1)ln2] \qquad \text{Eq. (2.28)}$$

Where Z and A are, respectively, the atomic and mass numbers of the material, $\tau = T/m_0c^2$ is the kinetic energy T normalized to the rest mass of the electron, r_e is the classical electron radius equals to 2.818×10^{-13}cm, $\beta = v/c$ is the electron velocity normalized to the speed of light, I refers the mean ionization/excitation potential of an atom of the absorbing medium and δ is the density-effect correction or polarization correction, introduced by Ugo Fano (1960) (Attix, 2004; Podgorsak, 2010).

Equation 2.27, shows that collisional losses are dependent of the velocity of the particle, *i.e.*, the collisional lose increases as the electron's velocity decreases. Also, the factor *Z/A*, makes the mass collisional stopping power to be dependent of the number of electrons per unit mass of the absorber. Therefore, if Z increases, the number of electrons per gram declines, and consequently, the stopping power decreases (Heard, 2007; Podgorsak, 2010).

Stopping powers calculated from the Bethe equation are available from a National Institute of Standards and Technology (NIST) database and ICRU Report 37 for electron energies from 10keV to above (Berger *et al*, 2005; Heard, 2007).

RADIATIVE LOSSES (BREMSSTRAHLUNG PRODUCTION)

When the electron's Coulomb force field interacts with the external nuclear field, elastic or inelastic scattering may occur, with a change in the electron's direction. In almost 97-98% of the interactions, the electrons are deflected elastically by the nucleus, losing only an insignificant amount of kinetic energy to satisfy the conservation of momentum. In this case, there is no transfer of energy to the medium but just a defection of the electron, reason why the electrons follow very tortuous paths (Attix, 2004).

According to Attix (2004) only 2-3% of the scattering interactions are inelastic. In this case, the electron, at high speed, passes close enough to the static external field nucleus and undergoes a change in acceleration. According to the classical theory, when the electron suffers a deflection

from its path with a change in its velocity, it emits electromagnetic radiation, called *bremsstrahlung*, from the German word for "braking radiation", whose amplitude is proportional to the deceleration (Evans, 1955; Attix, 2004). The larger the change in acceleration is, the more energetic the bremsstrahlung photon becomes (MIT OCW NSE, 2007b; Stabin, 2007). Therefore, the electron may radiates any amount of energy from zero up to its total kinetic energy, T_{max}, obtaining, thus, a continuum spectrum of energies (similarity with figure 2.3. relative to the spectrum of beta particle) (Evans, 1955). The classical description of bremsstrahlung production is shown in figure 2.11. (Bushberg *et al.*, 2002).

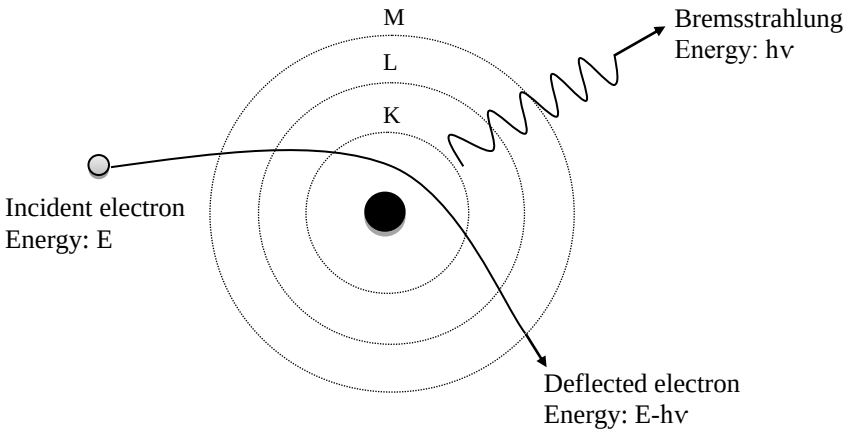

Figure 2.11. Electron–nucleus interaction with bremsstrahlung production (classical description) (Adapted from MIT OCW NSE, 2007b)

The probability of occurrence of bremsstrahlung production is given by Koch & Motz (1959) by complex formulas established for the electron kinetic energy and the medium. Their paper (Koch & Motz, 1959) is based on the quantum mechanical description of bremsstrahlung production, which differs from the classical theory. In quantum-mechanical theory, developed by Bethe and Heitler (Becker-Szendyl *et al.*, 1993; Podgorsak, 2010), the electron - represented by a plane wave, interacts with the nucleus filed and is scattered from it accompanied with a very small but finite probability of photon emission. In contrast with the classical description which predicted the emission of bremsstrahlung in every collision in which the electron is deflected (Evans, 1955).

However, in both theories the cross section for emission of bremsstrahlung, σ_{rad}, has the same form. Generically, this probability per atom is proportional to Z^2, and it also depends on the inverse square of the mass of the particle, for a given particle velocity. For this reason, bremsstrahlung production by heavy charged particles is negligible or insignificant when compared to electrons, due to the differences in their masses.

Likewise, the bremsstrahlung production increases with the kinetic energy and the atomic number *Z*. Thus, high-*Z* materials provide a considerably greater bremsstrahlung production than low-*Z* materials, such as tissue (MIT OCW NSE, 2007b). If the electron has a high kinetic energy, the bremsstrahlung is mostly emitted in the forward direction relatively to the incident electron trajectory, whereas low-energy electrons lead, preferentially, to bremsstrahlung emission in a right-angle (between 60° and 90°) to the electron direction (Bushberg *et al.*, 2002; Turner, 2007).

At very high energies (>10MeV), the dominance of radiative over collisional energy losses gives rise to electron-photon cascade showers. Therefore, electrons with high energy may produce high energy bremsstrahlung photons, which in turn, produce photoelectric effect, Compton scattering and pair production, creating thus additional bremsstrahlung photons and others electrons, and so on.

Analogous to the calculus of the rate of energy transfer to the medium by the mass collision stopping power, also the rate of energy transfer to the medium by bremsstrahlung is calculated by the mass radiation stopping power, which is given by the following equation:

$$\left(\frac{S}{\rho}\right)_{rad} = \alpha r_e^2 Z^2 \frac{N_A}{A} T_i B_{rad} \qquad \text{Eq. (2.29)}$$

Where α stands for the fine structure constant, approximately equal to 1/137 ("coupling constant", which measure the strength of the electromagnetic force that governs how electrically charged particles and photons interact), r_e corresponds to the classical electron radius, *Z* is the atomic number of the absorber, T_i matches with the initial kinetic energy of the electron plus its rest mass, and B_{rad} is a slowly varying function of *Z* and *T* (kinetic energy of electron), with values given by table 2.1. (Attix, 2004; Podgorsak, 2010). Seltzer and Berger (1986) have provided extensive tables of mass radiative stopping power for a wide range of absorbing materials (see Seltzer and Berger, 1986).

Table 2.1. Parameter B_{rad} for some initial kinetic energies of the electrons (Attix, 2004; Podgorsak, 2010)

Initial Kinetic Energy of the electron	**Non-relativistic ($<<m_0c^2$)**	**1MeV**	**10MeV**	**100MeV**
B_{rad}	≈5.3	≈6	≈12	≈15

RADIATION OR BREMSSTRAHLUNG YIELD

It is possible to calculates the radiation or bremsstrahlung yield, represented by $Y(T_0)$ and given by the equation 2.30. $Y(T_0)$ is the fraction of initial electron kinetic energy (T_0) converted into bremsstrahlung photons, as the electron slows down to rest (Attix, 2004; USYD Department of Physics, 2012).

$$Y(T_0) = \frac{1}{T_0}\int_0^{T_0} \frac{(S/\rho)_{rad}}{(S/\rho)_{tot}}\, dT \qquad \text{Eq. (2.30)}$$

For heavy charged particles, one considered that $Y(T_0) \approx 0$. Since the bremsstrahlung production increases with increasing of kinetic energy and atomic number *Z*, the radiation yield also increases with increasing of the kinetic energy and *Z* (Podgorsak, 2010).

According to Martin and Sutton (2002), Stabin (2007) and Casto (2008) a generalised approximation formula to calculate the fraction of electron energy converted to bremsstrahlung, *f*, may be given by the follow equation.

$$f = 3.5x10^{-4}.Z.T_{max} \qquad \text{Eq. (2.31)}$$

Where *Z* is the atomic number of the absorber medium and T_{max} stands for the maximum beta energy, in MeV. However, according to Turner (2007) a problem may be encountered with this formula for high values of energies and Z, where the fraction can exceed 1.0, which is not possible. Therefore, equation 2.32 given by Turner avoids this possibility.

$$f = (6x10^{-4}Z.T_{max})/(1 + 6x10^{-4}Z.T_{max}) \qquad \text{Eq. (2.32)}$$

Additionally, Martin and Sutton (2002) estimated the average energy, E_{av} (Eq. 2.33) of bremsstrahlung produced by beta particles with a maximum kinetic energy T_{max}, in keV, when they interact with a material of atomic number *Z*.

$$E_{av} = 1.4x10^{-7}Z.{T_{max}}^2 \qquad \text{Eq. (2.33)}$$

An estimate of bremsstrahlung yield and the average energy of bremsstrahlung produced may give an indication of the potential bremsstrahlung hazard of a specific beta-particle source.

The bremsstrahlung photons are the only energy detected by the gamma camera in radionuclide therapy able to produce an image. However, as it will be seen afterwards, there are some difficulties in producing a good image. The bremsstrahlung radiation is also used in the radiology diagnostic imaging, but only 1% of bremsstrahlung x-rays are produced and used whilst the others 99% are dissipated (Bushberg *et al.*, 2002).

PATH LENGTH AND RANGE

After an interaction, charged particles transfer only minute fractions of the incident particle's kinetic energy to the absorbing medium. Therefore, it is convenient to think in the light charged particles losing its kinetic energy gradually and continuously, along the medium, in a process often referred to as the continuous slowing down approximation (CSDA) (Strydom *et al.*, 2005).

According to Bushberg *et al.* (2002) the *path length* of a particle is defined as the real distance travelled by the particle, composed by successive ionizations and excitations until it comes to rest. In contrast, the *range, R,* of a particle is defined as the actual depth of penetration of the particle in matter, which depends of the particle's kinetic energy, mass, charge, and on the composition of the absorbing medium (density). The range of charged particles increases with the energy of the particle and decreases in denser absorbers (Saha, 2013).

A quantity introduced by Berger and Seltzer is the range in the continuous slowing down approximation - CSDA range (R_{CSDA}), which represents the mean path length along the particle's trajectory (Attix, 2004; Strydom *et al.*, 2005).

Heavy charged particles do not experience radiation losses.They transfer only small amounts of energy in each collisional interaction and mainly suffer small angular deflections. Therefore, heavy charged particles have an essentially linear path, whereas the electrons have a very tortuous path, since they are scattered with very large scattering angles in the elastic collisions and radiative losses. Consequently, for light charged particles, R_{CSDA} exceeds the average range, $\bar{R}$, in an absorbing medium, whereas the straight ionization track of a heavy charged particle results in the R_{CSDA} and average range being nearly equal, as shown in figure 2.12. (Evans, 1955; Attix, 2004; Podgorsak, 2010). The range is an important parameter for dosimetric purposes because it indicates the electron depth dose distribution.

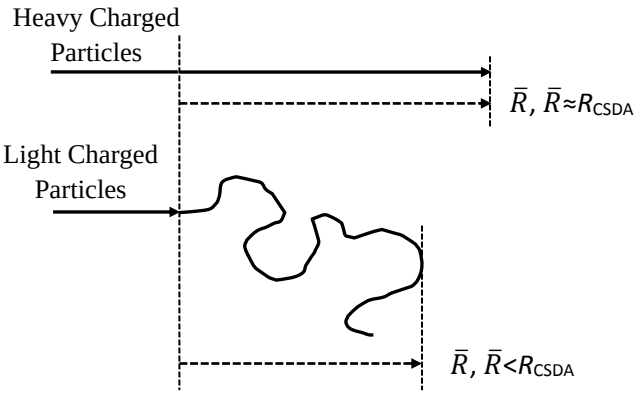

Figure 2.12. Representation of heavy and light charged particle tracks. Heavy charged particles produce rectilinear tracks, resulting in the mean path length, $R_{CSDA,}$ and mean range, $\bar{R}$, being essentially equal, whereas, the light charged particles produce a R_{CSDA} being greater than its $\bar{R}$ (Adapted from Podgorsak, 2010)

2.2. Gamma Camera Imaging

Nuclear medical imaging is based on detecting the radiation emitted by the radiopharmaceutical decay after its administration inside the body. The drugs used in diagnostic imaging are labelled with gamma or positrons emitting radionuclides. Consequently, nuclear medicine imaging is divided into two lines: **a)** single-photon or gamma-emission imaging, where the emitted radiation is x- or γ-rays, detected by the conventional scintillation or gamma camera (2D) or by the SPECT (3D), **b)** or positron-emission imaging, where two gamma rays photons are detected by the PET, following the annihilation of the emitted positrons (Singh & Waluch, 2000).

The present investigation of bremsstrahlung imaging deals, unavoidably, with imaging acquisition by the gamma camera or SPECT, which works with the same principles of a gamma camera. Therefore, the basic principles and characteristics of the scintillation imaging are described in this section. The explanation in this section is carried out based on the more common nuclear medicine procedure, diagnostic imaging with monoenergetic gamma emitting radionuclides, such as ^{99m}Tc. For this reason, a small clarification about the characteristics and types of radionuclides used in diagnostic nuclear medicine imaging is also undertaken. The characteristics of the radionuclides used in therapeutic procedures and the features of the therapeutic nuclear medicine imaging are addressed in the section 2.3.

2.2.1. Radionuclides used in Diagnostic: Characteristics and Applications

To visualize a specific organ or disease states in the body, a radiopharmaceutical is administered (by injection, swallowing, or inhalation) to the patient. A radiopharmaceutical is formed by attaching one or more radionuclides with a specific chemical compound with structural or chemical properties according to the physiological system to analyse. To determine, *in vivo,* the distribution and physiological behaviour of the radiopharmaceutical, a gamma camera detects the photons (x- or γ-rays) emitted from the radionuclide decay (Farstad, 2012). Through the measure of the radiopharmaceutical uptake by the gamma camera, it is possible create an image from the body or certain organ. The image has functional information at a molecular and cellular level that contributes to the determination of health status (Baert & Sartorm, 2006; National Research Council, 2007).

The radionuclides used in nuclear medicine are produced in linear accelerators, cyclotrons or nuclear reactors. Each radionuclide has unique properties that make it suitable for certain diagnostic or therapeutic purpose (Cherry *et al.*, 2003; National Research Council, 2007).

When talking in diagnostic nuclear medicine some characteristics of the radionuclides are necessary take into account. The first of these is that the radionuclide should ideally be a pure γ-

ray emitter, decaying by EC capture or IT, with a define energy within the range of 50-250keV. The energy must be high enough to be detected outside the patient and to match the optimum scanning range of a gamma camera. The physical half-life, T_p, should be greater than the time required to prepare material for injection (minutes to hours). The effective half-life, T_e, should be short enough to minimise the radiation dose to the patients and long enough than the examination time. Ideally, it should be approximately 1.5 times the duration of the diagnostic procedure.

The choice of the pharmaceutical, which is attached to the radionuclide, is also very important. The choice must be done according to the place to study to maximise the efficacy of the diagnosis and minimise the radiation dose to patient. The radionuclide should have few particulate emissions (alpha or beta) and a high abundance of clinically useful photons, with the purpose of creating a low dose rate to both patient and personnel. It should be also non-toxic to the patient, readily available, easily produced and inexpensive, easy to prepare and with appropriate quality control (Sadek, 2003; Mettler & Guiberteau, 2006; National Research Council, 2007; Karesh & Lipps, 2010; Ryder, 2012). Some of the mostly radionuclides used in diagnostic nuclear medicine are shown in table 2.2. These are applied to diagnose some diseases, such as cancer, neurological disorders (*e.g.*, Alzheimer's and Parkinson's diseases) and cardiovascular disease in their initial stages, permitting earlier initiation of treatment, as well as reduced morbidity and mortality (National Research Council, 2007).

Table 2.2. Physical characteristics of the radionuclides used in diagnostic nuclear medicine (Bushberg *et al.*, 2002; Ziessman *et al.*, 2006)

RADIONUCLIDE	PHYSICAL HALF-LIFE (T_P)	MODE OF DECAY	PARTICLE ENERGY AND ABUNDANCE [keV]	IMAGING TECHNIQUE
Fluorine-18 (^{18}F)	110 min	β^+ (97%) EC (3%)	2 γ-rays: 511 (annihilation radiation)	PET
Gallium-67 (^{67}Ga)	78.3 hrs	EC (100%)	γ-ray: 93 (37%), 185 (20%), 300 (17%), 395 (5%)	SPECT
Iodine-123 (^{123}I)	13 hrs	EC (100%)	γ-ray: 159 (83%)	SPECT
Indium-111 (^{111}In)	2.8 days	EC (100%)	γ-ray: 171 (90%), 245 (94%)	SPECT
Nitrogen-13 (^{13}N)	10 min	β^+ (100%)	2 γ-rays: 511 (annihilation radiation)	PET
Technetium-99m (^{99m}Tc)	6.02 hrs	IT (100%)	γ-ray: 140 (88%)	SPECT

Nearly 95% of the radiopharmaceuticals are used for diagnostic purposes, while the rest is used for therapy. According to Heard (2007), gamma cameras are designed primarily for diagnostic

nuclear medicine imaging. Since the ^{99m}Tc is the main radionuclide used in nuclear medicine, the equipment was tuned for energies around this radionuclide. Therefore, the components systems and modes of operation of the gamma camera are personalised to detect monoenergetic gamma radiation within an ideal energy around 50-250keV, mainly to 140keV (Baert & Sartorm, 2006; Heard, 2007; Farstad, 2012).

2.2.2. System Components to Detect the Radiation

The gamma camera or scintillation camera, invented by Hal Anger in 1958, is an image device used in nuclear medicine. The equipment allows obtaining a planar or two-dimensional project image of the three-dimensionally distributed radiopharmaceutical. The gamma camera converts photons, emitted isotropically by the radionuclide decay in the patient, into light pulses which are in turn converted into electric signals. The information derived from those signals indicates the original photon's energy and its position of interaction in the scintillator crystal. The basic components of a gamma camera system used in this process are: the collimator, the scintillation crystal, a light guide, an array of photomultipliers tubes (PMT), electronic circuits, such as positioning circuit, and a pulse-height analyser (PHA), as show in figure 2.13. (Singh & Waluch, 2000; Heard, 2007).

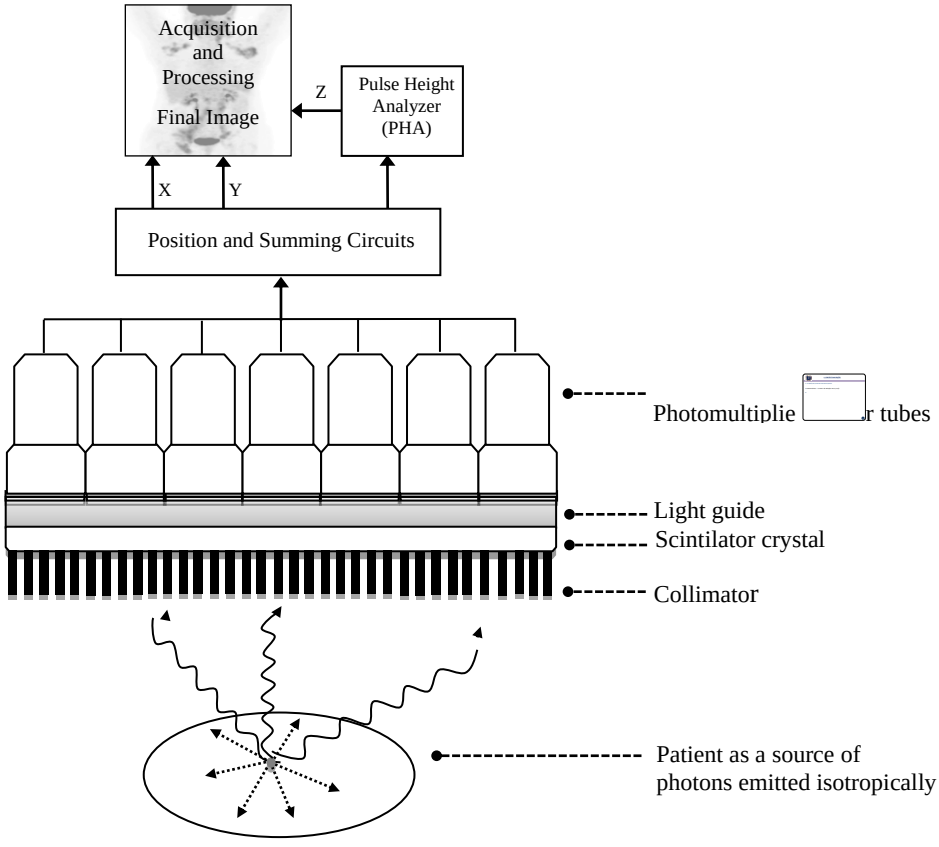

Figure 2.13. Basic components of a gamma camera (Adapted from Singh & Waluch, 2000)

COLLIMATOR

The collimator is the first component of the gamma camera after the photons leave the patient. It is usually made of lead or a similar high atomic number substance, such as tungsten. In the collimator a large array of holes (circular, triangular, square or more frequently hexagonal shaped) are close to each other with a narrow lead walls thickness, called septa, separate them. The collimator characteristics influence the field of view (FOV) and hence the performance characteristics of the gamma camera, such as the spatial resolution and sensitivity.

The collimator is truly essential. A scintillation camera without a collimator does not generate meaningful images. The photons are emitted isotropically after the radionuclide decay and some of them escape the patient without interaction, some are scattered within the patient before escaping, and some are absorbed within the patient. The only photons desired to create an image with valid information are the ones that do not interact within the body and are emitted parallel to the axis of the collimator FOV. Therefore, the function of the collimator is to restrict the direction of the incident photons reaching the scintillation crystal. The scattered photons that escape the patient with a certain angle do not carry the true information. However, they may, eventually, be emitted in a perpendicular direction of the collimator FOV and reach the crystal. When photons are emitted at oblique angles, the collimator septa stop or absorb the most photons, allowing that only the perpendicular photons reach the scintillation crystal (Bushberg *et al*., 2002; Ziessman *et al*., 2006).

Most of the emitted photons are absorbed by the collimators and only a minute fraction has appropriated trajectories. According to Ziessman *et al.* (2006), less than 1% of emitted photons are used to generate the desired image, being the others 99% "wasted". Even though, 35% or more events recorded by the gamma camera come from Compton-scattered photons which escape perpendicularly to the collimator face or can pass through the septa, degrading the spatial resolution of the image. Thus, the collimator is the "rate limiting" step in the imaging chain of gamma camera technology, influencing the performance characteristics of the imaging system.

There are two basic types of collimators: the *pinhole* and *multihole* (Attix, 2004; Mettler & Guiberteau, 2006).

A *pinhole collimator* has a conic form (20-25cm of height and 3-5mm of aperture) with only one hole at the end. This type of collimator was created to small organs, such as thyroid and bones of the hand and feet, because this collimator offers the advantage of image magnification, providing a high image resolution. However, beyond the focal point, the image orientation is reversed. The image is magnified when the distance from source to pinhole aperture is smaller than the collimator cone length to the aperture. The magnification decreases when the distance source-aperture increases. The major disadvantage of the pinhole collimator is the poor

sensitivity, which means that only a small percentage of the photons can pass through this collimator. Also, certain distortion is possible in the image because of the magnification produced (Bushberg *et al.*, 2002; Cherry *et al.*, 2003; Ziessman *et al.*, 2006).

On the other hand, a *multihole collimator* is set up by an array of multiple holes, which may be aligned in a diverging, converging or parallel manner.

A *converging-hole collimator* has holes converging to a unique point in front of the collimator, usually at 40-50cm away. This convergence forms a magnified image in the crystal, and therefore, it is mostly used in paediatric nuclear medicine. The magnification increases as the object is moved away from the collimator. However, since magnification depends on distance there is also some distortion in the image. The sensitivity increases as the source (patient) is moved away from the collimator face up to the focal point. In contrast, the resolution decreases with increasing the distance. Converging collimators are usually used in cameras having large detectors to allow a full utilization of the area, for imaging small areas (Cherry *et al.*, 2003; Mettler & Guiberteau, 2006).

Contrary to converging collimator, *diverging-hole collimator* has holes and septa diverging from the crystal face, usually from a point 40-50cm behind the collimator. It produces a minified image in which the amount of minification increases as the object is moved away from the camera. This collimator allows a decreasing in the image size on the crystal, whilst the imaged area increases. Such as the others collimators referred above there is a small image distortion. The sensitivity and resolution decrease when the source is moved away from the collimator. A diverging collimator is usually used on cameras with smaller detectors, in order to large organs of a patient, such as liver or lungs, be imaged on a single view (Bushberg *et al.*, 2002; Cherry *et al.*, 2003).

The *parallel-hole collimator* is the most commonly used collimator in nuclear medicine. This collimator contains thousands of parallel holes, usually in a hexagonal form. There is no magnification when the parallel-hole collimator is used. Thus, the image created has the same size as the source distribution onto the scintillation crystal (Cherry *et al.*, 2003). The characteristics of the parallel-hole collimators, such as septal thickness, septal length and size of the collimator hole, are chosen according to the energy of the radionuclide being imaged, to prevent photons with high energy cross the holes and reach the crystal septal. Figure 2.14 shows the four types of gamma camera collimators referred before.

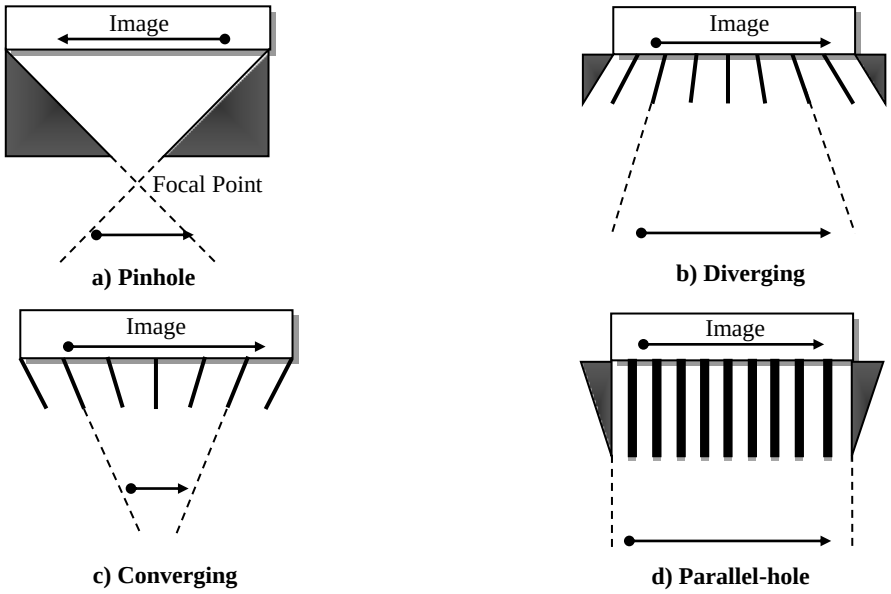

Figure 2.14. Types of the gamma camera collimators: a) pinhole collimator, b) diverging-hole collimator, c) converging-hole collimator and d) parallel-hole collimator (Adapted from Mettler & Guiberteau, 2006)

As the parallel-hole collimators provide a wide range of specifications, diverging and converging collimators are seldom used today. However, a hybrid of the parallel-hole and converging collimator, called a *fan-beam collimator,* is used in SPECT to take advantage of the favourable imaging characteristics of the parallel-hole and converging collimators (Bushberg *et al.*, 2002).

SCINTILLATION CRYSTAL

After the photons have passed through the collimator they reach the detector. The detector is a scintillation crystal made of sodium iodine activated with thallium, NaI(Tl). The role of the crystal is to convert the incident photons into visible light. Scintillators materials have the ability to emit visible or ultraviolet light when an excited electron in the scintillator returns to its ground state, after a photon-crystal interaction (Prekeges, 2009). The amount of light produced is proportional in intensity to the energy of the incident photon (Mettler & Guiberteau, 2006). Therefore, the desired event is the complete photoelectric absorption of a primary photon, where the energy is completely absorbed. However, the probability of that happen decreases as energy increases, since the Compton scattering becomes more likely (Singh & Waluch, 2000; Ziessman *et al.*, 2006).

The sodium iodine crystal has a conversion efficiency of 13%, being considered a highly efficient detector. This means that 13% of the deposited energy is converted into light. Since a light photon has an energy of 3eV, approximately one light photon is emitted for every 23eV

absorbed by the crystal. NaI(Tl) is considered the ideal scintillator for the detection of the 140keV γ-rays emitted by ^{99m}Tc decay. According to Peterson and Furenlid (2011), the attenuation coefficient at 140keV (2.64cm^{-1}) is sufficient to reach a good detection efficiency.

Unfortunately, the scintillation crystal is fragile and hygroscopic, *i.e.*, it absorbs moisture from the atmosphere. Therefore, the crystal is surrounded by a highly reflective material to maximise light output and hermetically encapsulated with aluminium housing with an optical glass window on the back surface of the casing. The glass allows the light reaches the PMTs. It works as a light distribution device to spread the scintillation light optimally over more PMTs to improve the accuracy of position-decoding calculation (Kim & Yang, 2001; Cherry *et al.*, 2003, Mettler & Guiberteau, 2006).

Crystals may be manufactured with a circular or rectangular geometry and with a variable thickness. Usually, a modern gamma camera has a rectangular crystal with 6 to 12.5mm of thickness and 25x50cm of diameter, with sizes up to 40x60cm. Currently, the gamma cameras to general purpose have a crystal thickness of 9.5mm. The choice of the crystal thickness is a trade-off between its detection efficiency and its intrinsic spatial resolution (Cherry *et al.*, 2003), as such will be seen in the next section 2.2.3. (Mettler & Guiberteau, 2006, Peterson & Furenlid, 2011).

It is important to refer that gamma camera achieves count rates on the order of 10^5 per second since the scintillation light rise time is very quickly and the decay time is short. A schematic cross section of a typical NaI(Tl) crystal is shown in the figure 2.15.

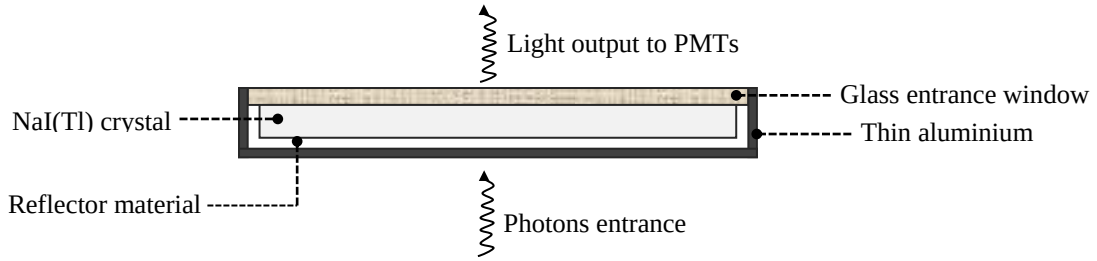

Figure 2.15. Schematic cross-section of a NaI(Tl) crystal used in a typical gamma camera (Adapted from Cherry *et al.*, 2003)

PHOTOMULTIPLIERS TUBES (PMTS)

After the conversion of the photons into visible light, the light produced falls on the PMTs. Only about 30% of the light from each event reach the PMTs. This electronic device has two main functions: it converts the visible light into electrical signals, and it amplifies those signals by more than a million times, in order that the electrical signal from each event is large enough to be received and processed by conventional electronic circuits (Kim & Yang, 2001).

An array of PMTs is coupled optically behind the NaI(Tl) crystal surface, usually arranged in a circular pattern or in a hexagonal pattern to maximise the area of the crystal that is covered. A modern gamma camera employs 30 to 100 PMTs, each one approximately 5cm in size. The PMTs may be placed directly to the crystal or connected to the crystal by light guides (usually quartz). The light guide minimise reflection losses by channelling scintillation light away from the gaps between the PM tubes and improves the uniformity of light collection as a function of position. The light guide may be eliminated in the cases where a hexagonal array is used, assuming there is sufficient spreading of the light in the glass entrance window for an accurate positioning (Cherry *et al.*, 2003; Peterson & Furenlid, 2011).

As shown in figure 2.16., a PMT consists of a glass tube in vacuum (shielded against magnetic fields) containing a photocathode, 10 to 12 dynodes, and an anode.

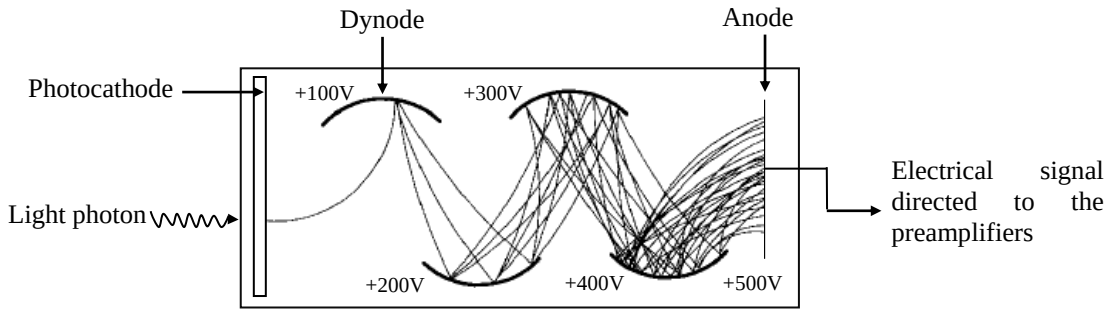

Figure 2.16. Schematic diagram of a typical photomultiplier tube (Adapted from Bushberg *et al.*, 2002)

The photocathode emits electrons when it is struck by visible light. According to Bushberg *et al.* (2002), approximately one electron is emitted from the photocathode for every five light photons incident upon it. The electrons are released into the vacuum space of the PMT, directed to the first dynode. The dynode multiplies the number of the electron, emitting three to six electrons, according to the potential difference of the dynodes. Those accelerated electrons are, in turn, accelerated to the next dynode with kinetic energy equal to the potential difference between the dynodes. This process continues down the chain of dynodes, with the number of electrons being multiplied in each dynode. Usually, a typical PMT has dynodes with 100V of voltage, where in each one are released 5 electrons. If a PMT has 10 dynodes the total amplification is 5^{10}. Finally, the anode collects all the electrons produced and emits an output voltage signal. The electric signal amplitude is directly proportional to the amount of light that reach the photocathode or to the energy deposited on the crystal.

The amount of light reaching each PM tube is inversely proportional to the lateral distance between the photon interaction site and the centre of that PM tube. Consequently, the signal output of the PMTs decreases in amplitude with increasing distance from the photon interaction

point, *i.e.*, the PMT nearest to the scintillation crystal receives the most scintillation light, whereas the PMT further away receives less light (Bushberg *et al.*, 2002; Prekeges, 2009; Peterson & Furenlid, 2011). The amplification can be adjusted by changing the voltage applied to the PMT. A change of 1% in the high voltage results in a 10% change in the pulse size. Therefore, the high voltage supply must be steady and well regulated (Bushberg *et al.*, 2002). Although measurable, there is a preamplifier attached directly to the PMT to amplify the signal output created, to facilitate the passage of the signal to the remaining electronic circuits.

ELECTRONICS CIRCUITS: POSITION AND SUMMING ENERGY

The localisation of photon interaction on the crystal and hence in the final image depends on the distribution of signal amplitudes in the PMTs. According to Peterson and Furenlid (2011), Anger's original process for decoding the photon interaction position on the crystal involved calculate the centroid of the position-weighted PMT signal outputs, a process often referred to as Anger Logic or Anger Arithmetic. In older style analog gamma camera the pulses from each preamplifier were sent to two different electronic circuits, the positioning and summing circuit. The summing circuit added all the signals from each preamplifier to form a pulse known as the Z pulse, which is proportional in amplitude to the total energy deposited in the crystal, in each event (Saha, 2013). This electrical pulse was analysed by a pulse-height analyser (PHA) to verify if Z was within a specific energy range chosen by the operator. If the pulse corresponds to a lower or higher energy outside the chosen range it was discriminated against and rejected, and the positioning was not accounted for that event (Ziessman *et al.*, 2006). On the other hand, the positioning circuit received the output signals from each preamplifier and by determining the centroid of these signals the X and Y coordinates of the location of photon interaction in the crystal were found (Bushberg *et al.*, 2002).

In those cameras, all the PMTs were connected through resistors to four outputs leads representing four directional signals, X^+, X^-, Y^+ and Y^-. The output signal from each PMT were weighted by the appropriate resistance value, the PMT closest to the event collected the greatest number of light photons with lesser contributions from the far away tubes. The four directions were then combined, to form each of the X^+, X^-, Y^+ and Y^- individually, as differences normalized by sums to give direct position values (Peterson & Furenlid, 2011), *i.e.*, the X-position was given by the difference in the X^+ and X^- signals and normalized by the total X signal, with the same calculus for the Y-position. The analog X- and Y-position pulses and the Z pulse in accordance with the energy range chosen by the user, were then sent to a cathode ray tube (CRT). The CRT produced a momentary dot of light in the X and Y position. A photographic camera aimed at the CRT recorded the flashes of light forming an image on film, dot by dot (Kim & Yang, 2001; Cherry *et al*, 2003; Saha, 2013).

Today, the scintillation cameras might be either hybrid or totally digital. In a hybrid camera, the X, Y, and Z pulses from the position and summing circuits are acquired in analog form, as did the earlier fully analog scintillation cameras, and then digitalized by analog-to-digital converters (ADCs) to digital signals. In turn, digital cameras calculate the position signals and the total energy deposited, Z, through a completely digital circuit. The resistors have become microprocessors and each PMT has its own ADC being each signal individually digitalized. The X, Y, and Z signals are corrected by digital correction circuits and the energy discrimination is applied, also in the digital domain. Nowadays, the Anger arithmetic is carried out in software, allowing the application of various weighting schemes to framing-up the digital image. According to Peterson and Furenlid (2011) the equation 2.33 shows a fairly general form for this type of processing with weighting factors of the amount of light regarding the interaction position. The approximation position $\hat{x}$ and $\hat{y}$, are computed by combining only the PMTs at known locations, x_i and y_i which have signals, S_i, that exceed a threshold S_{min}. The functions w return just the raw signals Si.

$$\hat{x} = \frac{\sum_{S_i \geq S_{min}} x_i w_i(x_i, S_i)}{\sum_{S_i \geq S_{min}} w_i(x_i, S_i)} \qquad and \qquad \hat{y} = \frac{\sum_{S_i \geq S_{min}} y_i w_i(y_i, S_i)}{\sum_{S_i \geq S_{min}} w_i(y_i, S_i)} \qquad Eq.(2.34)$$

This form allows diminishing the noise from the PMTs by excluding some negligible pulse amplitudes and also by detecting of multiple events simultaneously, since only some PMTs surrounding by the interaction are used, letting the others far away available to detect other event (Cherry *et al.*, 2003). At the end, if the sum of the signals *Si* (Z signal) is within the energy acceptance range, the pixel in the computer matrix corresponding to the estimated position of the event is incremented, creating thus the final image in the computer (Bushberg *et al.*, 2002). Currently, the electronics, such as preamplifiers, PHA, and ADCs are connected directly to the PMTs to minimise the signal distortions.

PULSE-HEIGHT ANALYSER (PHA)

As stated previously, the summing circuit gives the amplitude pulse, Z, which is proportional to the amount of energy deposited in the crystal in each event. Since a photon may interact in different ways with the crystal, all or just part of its energy could be deposited on it, and consequently, the Z pulse could have different values corresponding to a variety of possible interaction scenarios. In this way, a PHA is necessary to do a selective counting of only those pulses within certain amplitude range of interest. It is useful to discriminate against background radiation or scattered radiation with energy outside the desired energy range. The PHA only counts the Z pulses that falling within a selected amplitude intervals or energy channels defined by the operator, which is usually chosen according to the radionuclide being imaged (Mettler &

Guiberteau, 2006, Prekeges, 2009). If this is done for only one amplitude interval at a time the device used is a single-channel analyser (SCA), whereas a multi-channel analyser (MCA) is used to analyse simultaneously many different intervals, capable to show all radiation events on an energy or pulse-height spectrum (Simmons, 1996; Cherry *et al.*, 2003).

A typical energy spectrum includes several peaks. Given the example of the pulse height spectrum of ^{99m}Tc, shown in figure 2.17., it is possible to see: a) the *photopeak*, which represents the total energy of the γ-ray (140.5keV) absorbed in the crystal, by photoelectric effect; b) the *iodine escape peak*, resulting from the characteristic K-shell x-rays of iodine (28 to 33keV) which escape from the crystal after the photon has undergone photoelectric effect, with a consequent measured energy of the γ-ray of only 112keV; c) the *backscatter peak*, which may result when primary γ-rays undergo a 180° scattering and then enter into the detector, being totally absorbed. The 180° scattering may occur inside the patient, when the photon strikes the tissue behind the source and go back into the detector, or if the photon passes through the crystal without interact and strike the PMTs back, returning into the crystal; d) the *lead x-ray peak*, which is caused by the detection of the lead characteristics x-rays (75 to 90keV) when the photon interacts by photoelectric effect with the shielding or collimator, and e) the *Compton edge*, given by the effect of Compton scattering in the detector with a peak from 0 to 50keV. Also, some scattered photons, created inside the patient by Compton scattering, may travel toward the detector with energy from 90 to 140keV, which causes imaging difficulties, since the Compton scattering overlaps with the photopeak distribution (Bushberg *et al.*, 2002; Mettler & Guiberteau, 2006; Saha, 2013).

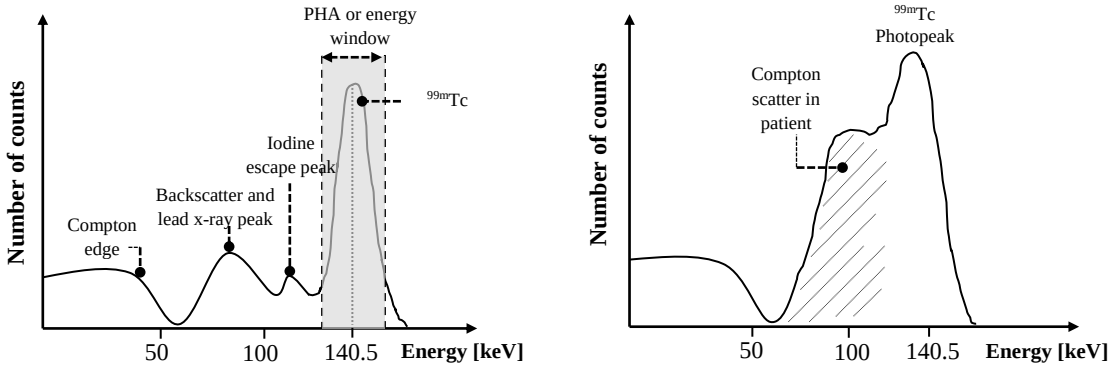

A B

Figure 2.17. Energy spectrum of the ^{99m}Tc, when it is viewed by the gamma camera as a point source (A) and as inside a patient (B). The use of a symmetric window (A) defined by the operator allows some of the Compton scatter to be counted and displayed (Adapted from Mettler & Guiberteau, 2006)

An energy range covering the photopeak, shown as the shaded area (fig. 2.17.), contains the acceptable events that fall within the energy window selected by the operator. The window settings are expressed in percentage with values between 10% to 20% window centred symmetrically on the photopeak (Prekeges, 2009). A 20% energy window set symmetrically over the ^{99m}Tc photopeak is equivalent to 140±10%keV or a window spanning 126–154keV (IAEA, 2003). It should be noted that X and Y positioning pulses are just accepted if the Z pulse is within the energy range selected by the PHA, being discarded if they are outside this range.

The PHA output pulse is sent to the count register and then to the computer matrix for inclusion in the final image. In a typical study the data are collected for pre-set counts or a pre-set time, and the image data is storage in computer memory. New computer's software allows the manipulation of image contrast on liquid crystal display (LCD) providing a better view of the images to a more accurate diagnostic (Saha, 2013).

2.2.3. System Performance and Factors Affecting the Image Quality

A gamma camera is not capable of producing "perfect" images of the radionuclide distribution. The images obtained by the gamma camera are affected by several parameters intrinsic to the gamma camera system, which define its performance and hence the quality and detail existing in the final image. Certain inherent limitations arise from the performance characteristics of the detector, electronic circuits and collimator. Some of these performance parameters include spatial and energy system resolution, system efficiency, uniformity, linearity and dead time.

SYSTEM SPATIAL RESOLUTION

The spatial resolution of a gamma camera system is a measure of the ability of the device to faithfully reproduce the image of the object with proper sharpness and detail, in order of clearly representing the variations in the distribution of radioactive objects in close proximity. According to Saha (2013) is usually defined as the "*minimum distance between two points in an image that can be detected by the system"*.

The spatial resolution of a gamma camera is determined by the components of the system. Part of the blurring visualized in the images arises from collimator characteristics and part arises from the crystal detector and positioning electronics. Therefore, the system spatial resolution, *Rs*, comprises two components: the intrinsic resolution, *Ri*, which depends on the crystal characteristics without the collimator, and the extrinsic resolution, *Rc*, due to the collimator design. These components are related by the following equation:

$$R_s = \sqrt{(R_i)^2 + (R_c)^2} \qquad \text{Eq. (2.35)}$$

The smaller the value of R_s, the better the spatial resolution achieved by the system, and hence the better the resolution of the image (Saha, 2013).

The system spatial resolution of the gamma cameras is expressed quantitatively by determining the full width at half maximum (FWHM) of a line spread function (LSF). The LSF is a cross-sectional profile of the image of a line source and is obtained by imaging a line source radioactive on the collimator (extrinsic) or on the crystal face (intrinsic). If the system had a perfect spatial resolution the LSF would be a single peak. However, a broadened peak, as a bell shaped curve, is seen because of the imperfect resolution (spatial and energy) of the detector, which follows a normal or Gaussian distribution (Bushberg *et al.*, 2002), as shown in figure 2.18.

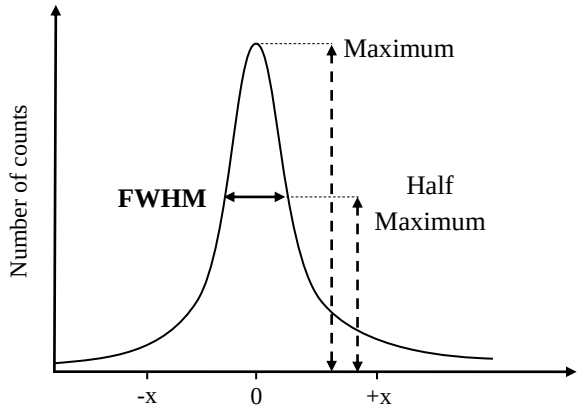

Figure 2.18. Representation of the LSF and the FWHM, which is the distance encompassed by the curve halfway down from its peak (Adapted from Mettler & Guiberteau, 2006)

The FWHM of the LSF gives the spatial resolution of the system and it reflects the number of the counts detected by the crystal at different lateral distances from the source. The FWHM is a measure of the width of the peak at the half height position of the LSF expressed in units of the horizontal axis. A narrow peak shape of the LSF indicates a better spatial resolution and therefore the ability to resolve objects close to each other (Saha, 2013).

The *intrinsic resolution* is the component contributed by the crystal and associated electronics. It refers to the ability of the detector localise and record the exact position of an interaction on the image. The intrinsic resolution arises from two factors: from the multiple scattering events, in which two photons interact with the crystal simultaneously in different places but recorded as a single event and the result is a single count mispositioned in the image, and primarily, from the statistical variations coming from the conversions between energy (photons) and mass

(electrons) during the radiation detection process, which produce the broadening peak, as a bell shaped curve (Prekeges, 2009).

The collection of visible light photons and subsequent production of electrical signals by the PMTs has significant random errors. Therefore, if *N* light photons are recorded on average by a certain PMT, the number recorded from one event to the next varies with a standard deviation given by $\sqrt{N}$. According to Cherry *et al.* (2003), it is possible verify this fluctuation by visualize on the image a blur created around the central peak when a narrow point source is imaged. The position of each event is distributed over a certain area with a certain size, which differs according to the magnitude of the statistical fluctuations.

Intrinsic resolution depends of the energy of the radionuclide imaged, as well as of the detector thickness. Intrinsic resolution improves with higher-energy photons and becomes worse for low-energy photons. This is because lower energy photons produce fewer light photons per scintillation event, and a smaller number of light photons results in higher random errors and vice-versa (Mettler & Guiberteau, 2006). Therefore, the FWHM will be larger for lower-energy photons than for higher-energy photons.

On the other hand, the intrinsic resolution decreases with thicker NaI crystals and becomes better with thinner detectors. A thinner crystal permits less spreading of the scintillation light photons before they reach the PMTs and also reduces the likelihood of detecting multiply Compton-scattered events. However, despite of the thinner crystals increase the spatial resolution, the efficiency of the photons detection decreases, since less photons are absorbed. Consequently, there is a trade-off between resolution and efficiency. Currently, the 9.5mm crystal thickness used on the most detectors is considered with intermediate and appropriate values of resolution and efficiency (Simmons, 1996; Saha, 2013).

Likewise, the intrinsic resolution is improved by increasing the number of PMTs and decreasing their diameter, in order to provide better sampling of the light emitted following each interaction. A narrow PHA window setting also helps to improve the intrinsic resolution, because background and scattered radiation are avoided (Singh & Waluch, 2000; Bushberg *et al.*, 2002; Mettler & Guiberteau, 2006; Ziessman *et al.*, 2006; Saha, 2013). In modern gamma cameras, the intrinsic resolution (collimator off) approaches 2.7 to 4.2 mm FWHM (Bushberg *et al.*, 2002).

In most practical situations, however, the intrinsic spatial resolution has a negligible contribution to the overall system resolution comparison with the resolution of the collimator, *i.e.*, the extrinsic resolution.

The *extrinsic resolution*, also called *collimator or geometric resolution*, contributes the most to the system spatial resolution and arises from the geometry of the holes and hence from the collimator design. An equation for the parallel-hole collimator extrinsic resolution is given by:

$$R_c = \frac{d(t_e+b+c)}{t_e} \qquad \text{Eq. (2.36)}$$

Where *d* is the hole diameter, *b* is the distance between the collimator face and the radioactive source, *c* is the distance between the back face of collimator and the midplane of the detector, t_e is the effective length of collimator holes (given by $t_e=t-2\mu^{-1}$) and *t* is the septal length or thickness of the collimator (Saha, 2013), such as shown in figure 2.19.

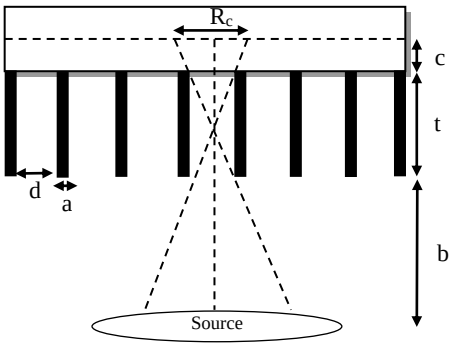

Figure 2.19. Schematic representation of a parallel-hole collimator, with length or collimator thickness *t*, hole diameter *d*, septal thickness a and source-to-collimator distance *b*. The collimator midplane is represented by *c*. R_c is the collimator resolution (Adapted from Saha, 2013)

From the equation 2.36., it is possible to realise that the collimator resolution is improved by increasing the length (*t),* decreasing the diameter (*d)* of the holes and also decreasing the source-to-collimator distance (*b)*. The collimator spatial resolution is degraded (*i.e*., FWHM of the LSF increases) as the source-to-collimator distance increases for all types of collimators. This is one of the most important factors in image acquisition and for that reason the patients should be placed as close as possible of the collimator to provide the best resolution (Bushberg *et al.*, 2002).

Septal thickness is also an important parameter on the collimator design, since the septal penetration by photons degrades the resolution, mainly for high-energy photons which easily penetrate the septa and interact with the detector blurring the image. No thickness of septal material is sufficient to stop all the γ-rays. So according to Cherry *et al.* (2003) and Saha (2013), the rule of thumb is to accept some reasonably small level of septal penetration, approximately 5%. Therefore, low-energy photons are stopped by using a collimator with a thinner septa, whereas high-energy need much thick septa. Also, materials with a large value of μ, high atomic number *Z* and high density ρ are preferred for the collimator septa (Simmons, 1996).

The septal length may be modified. However, there is an inherent compromise between the spatial resolution and efficiency (sensitivity) of the collimators when the septal length is changed. Longer septa result in higher spatial resolution and lower sensitivity, once the

collimator has a smaller acceptance angle resulting in more absorbed photons, whereas shorter septa result in lower spatial resolution and higher sensitivity (Mettler & Guiberteau, 2006). Thus, there is a trade-off between spatial resolution and count rate sensitivity. This compromise is the single most significant limitation on scintillation camera performance (Bushberg et al., 2002). Figure 2.20., shows the different parallel-hole collimators with variations on the septal thickness and length.

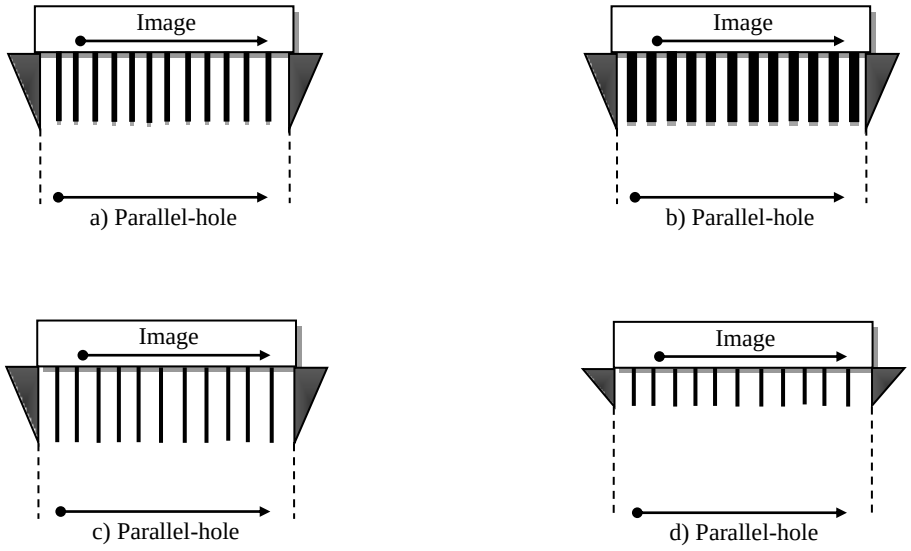

Figure 2.20. Effect of the septal thickness and length in parallel-hole collimators. Different septal thickness and length influence the sensitivity and resolution of the collimator: a) thickness septa used to stop low energy photons, b) thickness septa used to stop high energy photons, c) longer septa attenuate more photons, increasing the resolution and decreasing the sensitivity, and d) smaller septa allow more photons reach the crystal increasing the sensitivity but decreasing the resolution (Adapted from Mettler & Guiberteau, 2006)

Due to this compromise between sensitivity and spatial resolution, most scintillation cameras are provided with a selection of parallel-hole collimators with different septal length and thickness, according to the necessary specifications. These may include: *low-energy*, *general-purpose* (LEGP), *low-energy*, *high-resolution* (LEHR) (with a few tenths of a millimetre septal thickness and used to a maximum of energy of 150keV), *medium energy*, *general-purpose* (MEGP) (with few millimetres septal thickness and used for ^{67}Ga and ^{111}In, up to 300keV), *high-energy*, *general-purpose* (HEGP) (for ^{131}I) and *ultrahigh-energy* (for ^{18}F) collimators, for imaging the 511keV photons of positron emitters (Mettler and Guiberteau, 2006; Ziessman *et al.*, 2006). Some properties and values of the parameters used in those collimators are given in the table 2.3.

Table 2.3. Features and properties of different types of parallel-hole collimators, calculated at 10cm of collimator face (Saha, 2013)

COLLIMATOR TYPE	HOLE DIAMETER [mm]	HOLE LENGTH [mm]	SEPTAL THICKNESS [mm]	COLLIMATOR RESOLUTION [mm]	SENSITIVITY [cpm/μCi]	OPTIMUM ENERGY [keV]
LEGP	1.43	23.6	0.2	9.1	360	≈140
LEHR	1.11	23.6	0.3	7.5	230	≈140
MEGP	3.02	40.6	1.1-1.4	12.1	288	≈280
HEGP	4.32	62.8	1.3-3.0	13.8	176	≈360
Ultrahigh energy	3.4	75.0	3.0-4.0	10.4	60	≈511

SYSTEM SENSITIVITY

Another parameter that influences the gamma camera performance is the sensitivity or efficiency, which has been enunciated so far. The efficiency refers to the detected count rate per unit of activity present in a source and it is usually related with the images contrast (difference in the grey scale of the image). It is normally expressed in counts per second per MBq [cps/ MBq]. Such as the resolution, also the sensitivity arises from two components: the extrinsic sensitivity, associated with the collimator efficiency, and intrinsic sensitivity, associated with the crystal efficiency (Heller & Zanzonico, 2011).

The sensitivity of the gamma camera is mostly affected by the collimator efficiency. The *extrinsic sensitivity*, also known as *collimator efficiency* or *geometrical efficiency* (E_c), is defined as the number of photons passing through the collimator holes per unit activity present in a source. For parallel-hole collimators, the geometrical efficiency is given by the follow equation (Saha, 2013).

$$E_c = k^2 \frac{d^4}{t_e^2 (d+a)^2} \qquad \text{Eq. (2.37)}$$

Where d is the hole diameter, t_e the effective length of the collimator hole, a the septal thickness and k is a function of the shape and arrangement of holes in the collimator (≈0.24 for round holes, ≈0.26 for hexagonal holes, ≈0.28 for square holes) (Cherry *et al.*, 2003). Geometrical efficiency is affected by changes in the septal thickness, septal length and hole diameter. The efficiency increases with the diameter of the collimator holes (d) and decreases with increasing collimator length (t) and septal thickness (a), which is quite opposite to the spatial resolution. Therefore, as the collimator resolution of a system increases, its sensitivity decreases and vive-

versa. Note that, the collimator efficiency is not affected by the source-to-detector distance in contrast to the extrinsic resolution (Bushberg *et al.*, 2002).

On the other hand, the *intrinsic sensitivity* (collimator off), which is the fraction of photons reaching the detector, is determined by the thickness of the crystal and the energy of the incident photons. Intrinsic efficiency becomes better for thicker crystal and higher-energy photons. However, when intrinsic efficiency increases and consequently the image contrast, the intrinsic spatial resolution decreases. Once again, there is a trade-off between intrinsic efficiency (which improves with thicker crystals and lower-energy photons) and intrinsic spatial resolution (which improves with thinner crystals and higher-energy photons).

The contrast in nuclear images (planar images, SPECT, and PET), which are maps of the spatial distribution of the radiopharmaceutical in the patient, depends on the tissue's ability to concentrate the radioactive material. The contrast is improved with increasing administered activity. Nevertheless, according to Heard (2007), in diagnostic imaging the image quality is limited by dose limitations and patient tolerance, and therefore it is important to optimize sensitivity in order to reduce the dose and the image noise. Currently, the gamma camera is designed to provide acceptable intrinsic efficiency while maintaining high intrinsic spatial resolution in the energy range of 50-250keV (Bushberg *et al*., 2002; Heller & Zanzonico, 2011; Saha, 2013).

ENERGY RESOLUTION

The energy resolution is an extremely important performance parameter of the gamma camera. It is a measure of a gamma camera ability to distinguish between interactions depositing different energies in the crystal. In broad terms, the purpose of the energy resolution is to discriminate the primary radiation from the scattered radiation with lower energy. PHA is the only option available to discriminate primary photons from scattered ones. If the energy resolution of the gamma camera is gradually improved, consequently the energy window width has to be decreased accordingly (Saha, 2013).

The energy resolution is generally calculated by the FWHM and expressed as a percentage of the photopeak energy of the bell-shaped curve. The energy resolution is given by the following equation (Bushberg *et al.*, 2002).

$$Energy\ Resolution\ (\%) = \frac{FWHM}{Pulse\ heigh\ at\ center\ of\ photopeak} x100\% \quad \text{Eq. (2.38)}$$

A small value of energy resolution indicates better gamma camera ability in to reject scattered photons, and consequently a better system spatial resolution is reached. The inadequate energy

measurement by the gamma camera, results from the statistical uncertainties in the detection process. This fact causes random amplitude pulses around the mean pulse height, giving a peak broadening with a Gaussian shape. For a Gaussian distribution the position of the mean (peak centre) and the FWHM are related to the standard deviation (σ) by (Bushberg *et al.*, 2002):

$$FWHM = 2.36\sigma \qquad \text{Eq. (2.39)}$$

A broadened Gaussian shape with a wider FWHM implies poorer energy resolution resulting in a worse image quality. Currently, the energy resolution is typically of the order of 10% for ^{99m}Tc (Heller & Zanzonico, 2011), varying according to the incident photon energy.

UNIFORMITY AND SPATIAL LINEARITY

Uniformity is a performance characteristic of a scintillation camera which measure the camera's response to a uniform irradiation (flood field uniformity) of the detector surface, that is, when it is flooded with a spatially uniform flux of incident photons. Flood field uniformity may be quantified intrinsically, when the uniformity is exhibited by the detector itself (intrinsic uniformity) or extrinsically using the collimator (extrinsic uniformity). The ideal response is a perfectly uniform image throughout the FOV, that is, a point source counted at different places in the FOV should give the same count rate by the detector at all locations (IAEA, 2009a).

However, the detector response is not consistent over the entire FOV. This nonuniformity in detector response may arise from several factors, such as failure or damage of the PMTs, poor coupling between the PMTs and light guide, spatial non-linearities, defects in the crystal, incorrect setting of the position or width of the PHA window. Acceptable field nonuniformity is on the order of 2% to 5%. Much of this can be corrected by the computer system, through uniformity correction software (Bushberg *et al.*, 2002; Mettler & Guiberteau, 2006; IAEA, 2009a; Saha, 2013). For example figure 2.21., shows three images (30 million counts in each image for ^{99m}Tc) with different intrinsic uniformity as the window width (PHA) decreases. Uniformity can be slightly degraded as the energy window width decreases (IAEA, 2003).

20% symmetric energy window. 15% symmetric energy window 10% symmetric energy window

Figure 2.21. Comparison of the intrinsic uniformity in three images as the window width is decreased (Adapted from IAEA, 2003)

On the other hand, *spatial distortion* or *linearity*, is a performance characteristic of a scintillation camera which measure the camera's ability to represent the shapes of the objects accurately. Spatial nonlinearity is caused by the non-random mispositioning of events, *i.e.*, systematic errors in the positioning of X- and Y-coordinates over the FOV and it can be estimated by inspecting the image of a linear object. If severe spatial displacements occur, the uniformity will be poor in the same areas.

It is notable that the spatial distortion and flood field uniformity are closely related and the factors that affect the linearity are the same as those listed for flood field uniformity. Currently, modern cameras have digital circuits that use tables of correction factors to correct X- and Y-position signals for spatial nonlinearity (Bushberg *et al.*, 2002; Saha, 2013).

Figure 2.22 shows an intrinsic image of the National Electrical Manufactures Association (NEMA) slit phantom pattern of a point source of ^{99m}Tc, which shows a distinct nonlinearity of the lines and hence a loss of spatial resolution (IAEA, 2003).

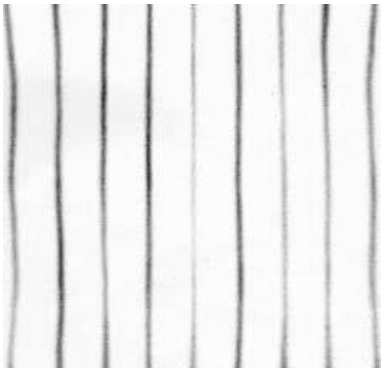

Figure 2.22. Nonlinearity of the NEMA slit phantom pattern (Adapted from IAEA, 2003)

According to Heard (2007), a combination of PMTs tuning and correction maps are used to ensure linear and uniform images, improving, thus, the spatial resolution and consequently the quality of the image.

COUNT RATE AND DEAD TIME

Any scintillation system takes a certain time to process an event and remain inoperable to receive a second event during this period of time, which is called *dead time*. If a second interaction occurs in this time the event is not counted, occurring a losing on the system sensitivity. On the other hand, the gamma camera may detect two or more events simultaneously, if they occur too close together in time. As a consequence, the photons are counted as one with the signal equal to the sum of the amplitudes of each one of them. This is referred to as *pulse pileup*. If the final signal is within the PHA window the two photons appears

as a photon of interest with consequent losing in the spatial resolution. Contrary, if the signal falls outside the PHA window the sensitivity of the system is diminished. Dead time loss at high count rates is a serious problem for any counting system, mainly in the scintillation cameras due to pulse pileup. Currently, there are several methods implemented in gamma camera systems to determine or correct the dead time (Mettler & Guiberteau, 2006; Saha, 2013).

The next table encompasses all the performance characteristics explained so far and indicates some typical values of intrinsic performance parameters of a gamma camera with 9.5mm thickness detector (Bushberg *et al.*, 2002).

Table 2.4. Typical intrinsic gamma camera performance characteristics (Bushberg *et al.*, 2002)

Intrinsic Spatial Resolution (FWHM of LSF for 140keV)	2.7mm to 4.2mm
Energy Resolution (FWHM of photopeak for 140keV)	9.2% to 11%
Uniformity	2% to 5%
Absolute Spatial Linearity	Less than 1.5mm
Observed maximal count rate (measured without scattered)	170000 to 500000 counts/sec

2.2.4. Modes of Image Acquisition

There are numerous parameters that must be decided before starting the image acquisition on a gamma camera, which will affect the exam and consequently the data collected, such as the scan duration, the sampling frequency (pixel size and number of views), the energy window, the collimator characteristics and the type of image and data acquisition (Heard, 2007). Currently, the data acquisition, and the procedures after it, such as, data processing, image display and manipulation, data storage and system control, are carried out by digital computers and may be acquired and stored in one of two ways: (a) *frame mode* and (b) *list mode*.

FRAME MODE ACQUISITION

Frame mode is the most common practice in nuclear medicine. In this type of acquisition the incoming data are placed in a spatial matrix used to generate an image. The matrix size, formed of pixels, is chosen according to the area of the detector and all the pixels are set to zero. This means that each spatial position X and Y corresponds to a pixel position in the matrix. Therefore, a digital X and Y coordinate is stored in the corresponding pixel position of the matrix and one count is added to the counts in that pixel, and so on until the image is formed. In

frame mode acquisition the data are acquired for either a pre-set time interval or until the total number of counts reaches a stipulated number (Cherry *et al.*, 2003; Saha, 2013).

The size and the depth (8 or 16bits/pixel) of the matrix and the number of frames per study must be specify. Typical image matrix sizes are 64x64 and 128x128, although others may be possible. It is the matrix size which specifies the spatial resolution of a digital image, and hence the pixel size. The pixel size is calculated by dividing the FOV by the number of pixels across the matrix. Therefore, if the FOV has 40cm and the data is acquired over a 128x128 matrix size, the pixel size of the image is 3.1cm. However, the greater the matrix size, the greater the acquisition time and memory used in computer. Thus, there is a trade-off between the spatial and temporal resolution (Mettler & Guiberteau, 2006; IAEA, 2009a).

The frame mode acquisition is widely used in static, dynamic, and tomographic (SPECT) studies. In a *static study*, a conventional 2D (planar) static image of an unchanging distribution of radioactivity is acquired in a single view of the region of interest (ROI). The static planar mode or planar scintigraphy is useful for whole-body studies, which may be obtained by scanning the gamma camera across the entire length of the patient (Bushberg *et al.*, 2002).

Alternatively, *dynamic studies* are used to study dynamic physiological processes, such as the transport of a radiopharmaceutical through the heart or the extraction and excretion of it by the kidneys. In dynamic studies, a series of static images (frames) are acquired and each frame is collected over a certain period of time (frame rate) selected by the operator. The frames are obtained one after the other until the desired number of frames is reached (Kantzas *et al.*, 2000; Bushberg *et al.*, 2002; Saha, 2013). Both static and dynamic studies acquire projections which represent a two-dimensional image of a three-dimensional distribution of the radiopharmaceutical and they can be either recorded directly onto film or stored in a computer (Kantzas *et al.*, 2000; Mettler & Guiberteau, 2006).

Although planar imaging is sufficient for many clinical applications, this technique suffers from artefacts and errors due to superposition of underlying and overlying objects which interfere with the region of interest (ROI) (Singh & Waluch, 2000; Ziessman *et al.*, 2006). The technique of computer tomography (CT), which have been developed for both single-photon and positron tomography, offers some advantages over planar images, because it allows an accurate portrayal of the distribution of the radioactivity in the patient, improving consequently, the diagnostic accuracy (Fahey & Harkness, 1996; Groch & Erwin, 2000; Ziessman *et al.*, 2006).

The principle of tomographic imaging in nuclear medicine is based on the detection of photons emitted isotropically from inside the patient and detected at different angles around the patient, providing a series of static images at distinct depths (slices) of the organ in study (Kantzas *et al.*, 2000). Therefore, contrary to the planar images, the SPECT allows an *in vivo* quantitative

acquisition of the distribution of the radiopharmaceutical in truly three dimensions, through reconstruction of the projections views according to the principles of the tomographic imaging (Saha, 2013).

The most common SPECT system is characterized by a typical rotating gamma camera with one to three NaI(Tl) detector heads (multihead) mounted on a gantry, an online computer for acquisition and processing of data, and a display system (Singh & Waluch, 2000; Saha, 2013). A typical dual-head SPECT system is shown in figure 2.23.

Figure 2.23. A dual-head SPECT camera, GE NM630 model (From GE Healthcare, 2011)

The detector head rotates around and parallel to the long axis of rotation (AOR). The gantry may rotate with an orbit of 180 or 360 degrees, acquiring the data in several projections simultaneously, over multiple angular views with small angle increments, 3 to 10 degrees. In typical applications about 32 stops per 180° of rotation and 64 stops per 360° of rotation are obtained, in order to acquire sufficient counts per pixel. At each angular position the data are collected in the form of pulses from the PMTs and then stored in a 64×64 or 128×128 matrix in the computer (Saha, 2013). Reconstruction mathematical algorithms, such as filtered backprojection technique or an interactive reconstruction algorithm, are then used to assimilate all the two-dimensional projection images and reconstruct them into three-dimensional images (Fahey & Harkness, 1996; Groch & Erwin, 2000; Kantzas *et al.*, 2000).

In SPECT, as well as in planar scintigraphies, the patient must be placed the closest as possible to the detector head, in order to improve the spatial resolution. Since the circular orbits deviate some centimetres from the surface body when they pass in noncircular body parts (chest or abdomen), decreasing the system resolution, body contouring orbits must be used instead of the

circular ones, in order to keep the radius of rotation as small as possible (Tsui, 1996; Mettler & Guiberteau, 2006; Ziessman *et al.*, 2006).

According to Mettler and Guiberteau (2006), the rotational SPECT has highlighted the need to improve every aspect of gamma camera system performance. Performance characteristics of the SPECT are the intrinsic spatial resolution, FWHM of 3 mm, linearity distortion of 1 mm or less, uncorrected field uniformity within 3% to 5%, and corrected field uniformity within 1%. All current rotational SPECT systems have correction circuits such as uniformity correction, energy correction and attenuation correction. The SPECT systems use the Chang method in the attenuation correction which assumes a uniform attenuation throughout the patient (Ziessman *et al.*, 2006). Currently, the existence of hybrids instrumentations, such as SPECT-CT, solves many of problems associated with the attenuation correction, affording a better anatomic localization of radiopharmaceutical distribution (Ziessman *et al.*, 2006).

LIST MODE ACQUISITION

Contrary to the frame mode acquisition, in list mode acquisition the digital data, representing the coordinates of each photon interaction in the crystal, are simply stored as lists. Consequently, all data are put in the memory as a time sequence list of events. If a physiologic monitor is being used, as in gated cardiac study, trigger marks are also included in the list (Bushberg *et al.*, 2002).

This type of data acquisition is really flexible regarding to the images formation. List mode allows combining, dividing, sorting or eliminating some X and Y positions to form images in a variety of ways to suit a specific need, at a later time. However, it has the disadvantage of a low acquisition rate and a large memory requirement, since it generates large amounts of data (IAEA, 2009a; Saha, 2013).

A schematic representation of data acquisition in the frame mode and the list mode is represented in figure 2.24.

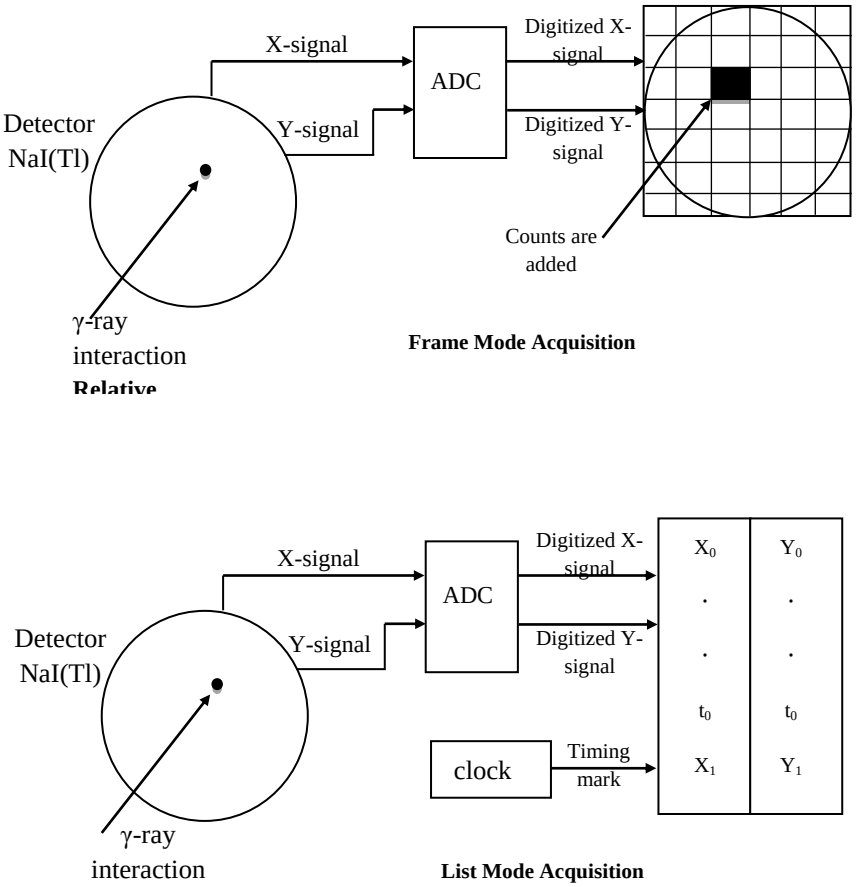

Figure 2.24. Data acquisition in frame mode and list mode (Adapted from Saha, 2013)

2.3. Targeted Radionuclide Therapy and Imaging Radionuclide Therapy

The present dissertation relies in understanding the behaviour of the bremsstrahlung photons created within the body when the patient is subject to radionuclide therapy. The information acquired may be used to improve the bremsstrahlung imaging, in order to allow a patient-specific dosimetry in the future. To achieve this purpose is useful recognise the physics underlying the radionuclide therapy. Therefore, the follow section explains the principles of radionuclide therapy, the radiopharmaceuticals used in this therapeutic and the dosimetry required in this type of procedures.

The focus of this section is mainly based on a pure beta emitter, the ^{90}Y. This radionuclide has a high amount of applications in the radionuclide therapy. Since the ^{90}Y do not emit any γ-ray, its detection relies on the bremsstrahlung imaging. The challenges to detect the bremsstrahlung photons are explained on section 2.3.4., the ^{90}Y applications are described in section 2.3.2. and the internal dosimetry associated with pure beta emitters in section 2.3.3.

2.3.1. Principles of Radionuclide Therapy

According to Stanciu (2012), the concept of *targeted radionuclide therapy* (TRT), also designated as unsealed source therapy, has developed from the diagnostic radionuclide imaging and appeared for the first time in 1898, when Paul Erlich used an antibody as vector of a radionuclide. The antibody recognised antigens associated to the tumour.

Nowadays, the TRT is a promising modality in cancer treatment. It has developed due to advances in the understanding of tumour biology, molecular biology and radionuclides, allowing for the creation of new therapeutic radiopharmaceuticals (IAEA, 2010).

TRT has the aim of targeting and destroying both malignant and non-malignant cancer cells, as well as, treating specific diseases such as rheumatoid arthritis (IAEA, 2009b). TRT uses an unsealed source of ionising radiation, combined with a biological vector of known biodistribution, such as monoclonal antibodies, antibody fragments, small peptides, liposomes or microspheres. The radiopharmaceutical delivery in the TRT takes advantage of the biokinetics of the patient, once the biological compound can selectively target particular cancer cells and bind to them (Stanciu, 2012), in contrast with the delivery principle used in traditional radiotherapy. Consequently, the efficacy of the TRT relies on the delivery of the radiopharmaceutical to the intended tumour site. When the radiopharmaceutical is effectively delivered, it is retained on those tissues and decays for a certain period of time, emitting a prolonged radiation dose to those tumoral cells and destroying them. Since the

radiopharmaceutical is retained on the tumour site, this therapeutic approach protects the surrounding normal tissue (Manjunatha & Rudraswamy, 2010; Wheat *et al.*, 2011).

Usually, when a monoclonal antibody is used as a vector, the therapy is usually called of *radioimmunotherapy* (RIT). In RIT the tumour-specific antibodies are derived from the patient's own cancer and, hence, the antibody labelled to the radionuclide selectively targets the tumour when injected into the patient. In the same way, radiopharmaceutical binds to the cancer cells, allowing the delivery of a high dose of radiation directly in the tumour (NAS, 2007; SNMMI, 2012). Figure 2.25., shows the RIT process.

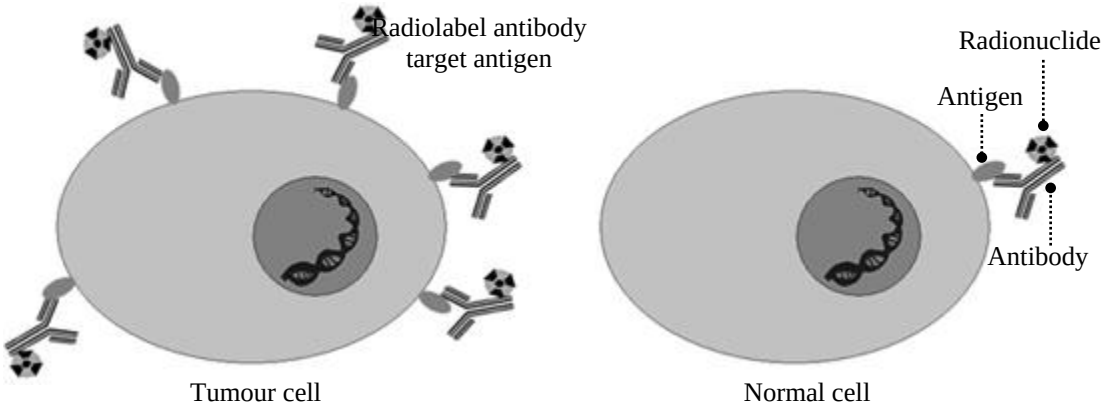

Figure 2.25. Schematic representation of the RIT, through the use of an antibody as biological vector. TRT takes advantage of the differences between cancer cells and normal cells, for example by different protein expressions on the cell surface. Therefore, antibodies labelled with radionuclides are used to target those structures (Adapted from Nestor, 2012)

Although the principle of the radiation therapy (radiotherapy) and radionuclide therapy is the same, there are some significant differences that make TRT a promising method. While external beam radiation and brachytherapy emissions are composed of photons, TRT employs particulate emissions, damaging only the target volume with significantly lower collateral damage of the surrounding tissues; TRT uses antibodies and specific peptides as biological compound, allowing a selective uptake to the specific cancer cells; and the radiopharmaceutical is administered in a systemic fashion, which mean that TRT can deliver therapeutic doses to both a primary tumour and distant (including widespread) metastases concurrently. Therefore, in comparison with others therapeutic approaches, TRT has the advantage of both systemic administration, as in chemotherapy, and the selective irradiation of tissues, like brachytherapy and external beam radiation (Ersahin *et al.*, 2011). According to Flux (2006), is also considered as a relatively benign treatment that does not incur the side-effects seen in more conventional treatments, such as the hair loss and prolonged nausea.

The radiopharmaceutical may be administered by some routes such as oral, intra-tumoural, intra-arterial, intra-portal, intravenous and intra-cavital. According to each therapeutic procedure, the route is chosen to maximising and optimising the dose delivery, to retain the radiopharmaceutical (biodistribution) in the target site (tumour) and to minimising the radiation burden to non-target tissues (Eary, 2007; Wheat *et al*., 2011).

2.3.2. Radionuclides used in Therapy: Characteristics and Applications

Such as in diagnostic imaging, in which the radionuclides have some specific characteristics, also in nuclear medicine therapy the physical characteristics of the radionuclides must be considered. The choice of the therapeutic radionuclide is governed by some ideal properties such as clinical indication, chemical and physical properties (type of emission, mode of decay, energy, abundance and half-life), range in tissue penetration, good stability when attached to a vector, quick excretion through a known simple route, readily available at needed scale, easily produced and cheap (Eary & Brenner, 2007; Rajendran, 2007; Ersahin *et al.*, 2011; Wheat *et al.*, 2011; Stanciu, 2012).

In terms of half-life, the physical and effective half-life of the radionuclide constitute a significant consideration for the therapy planning. The physical half-life should be similar to the drug or biologic agent half-life, so that the resulting effective half-life be an appropriate time for maximum therapeutic effect and minimal to eliminate radiation hazards and toxicity to the health cells (Eary & Brenner, 2007; Wheat *et al.*, 2011). In therapy, the half-life of the radionuclides is higher than those used in diagnostic. It is also important that the radiopharmaceutical reaches a high target-to-background ratio. This means that it is preferred a prolonged retention of the radiopharmaceutical in the target tumour and a rapid elimination of it from normal tissues, by the kidneys and bladder (Wheat *et al.*, 2011).

The type and energy of radiation used in TRT are one of the most important factors when a therapeutic radionuclide is selected. Whereas the radionuclides used in diagnostic imaging emit γ-rays, which may penetrate deeply into the body, the radionuclides used in TRT emit particulate radiation, such as beta particles, alpha particles, and Auger electrons (National Research Council, 2007). Each type of charged particle transfers to the medium energy, which contributes to the dose in the patient. This energy may be calculated by the linear energy transfer (LET), as the following equation.

$$LET = \frac{dE_L}{dl} \qquad \text{Eq. (2.40)}$$

Where dE_L is the average energy locally imparted to the medium by a charged particle passing through a length of medium *dl* (SNMMI, 2012). The value of LET is important to understanding the effects of each charged particle on living cells (Stabin, 2007).

The specifications of the radionuclide chosen to be used in the therapy, and consequently the type of charged particle used, takes into account the characteristics of the lesion to treat.

Alpha particles have a range of 40 to 100μm, for mean energies of around 5 to 8 MeV. These particles might be preferred if high LET, usually greater than 10keV/μm, over a very short distance is preferred (Stanciu, 2012). These values of LET are ideal for inducing fatal double-strand breaks in DNA, since the ionizing events occur in a range of about 2nm, close to the diameter of the DNA double helix. *Beta particles* have the longest range in tissue followed by alpha particles. The range of beta particles is 0.2 to 12mm, for mean energies of around 0.1 to 1MeV. Low energy beta emissions might be suitable for small tumours while higher energy beta emissions are needed for penetration of the tissues up to 1cm. Beta particles have a LET less than about 10keV/μm, which causes less damaging than high-LET radiation. *Auger electrons* have the lowest energy of all charged particles, typically just a few keV, and the shortest range in tissue, in order of a few nanometres (Heard, 2007).

According to Manjunatha and Rudraswamy (2010), beta particles emitters are preferable in nuclear medicine therapy since they have lower tissue penetration (typically less than 1cm), which maximise the self-irradiation in the target region and minimise irradiation in non-target regions. Increasingly, pure beta emitters are being considered and used as therapeutic radionuclides. There are clinical therapeutic values in use the pure beta emitters. From the radiation safety perspective, these radionuclides without γ-rays emissions are desirable since they eliminate any external radiation hazards. In this way, the amount of radiation involved is only confined to the patient. There is no exposure of the staff, public or others through external irradiation and patients may go home immediately (Zanzonico *et al.*, 1999; Joseph, 2006; IAEA, 2009b).

Whilst the particulate property of the radiation decay process determines the therapeutic potential, the photon emission provides the ability to image the biodistribution *in vivo*, indicating the tumour localization and non-target uptake and retention. Therefore, the presence of a photon emission in the radionuclide decay affords the luxury of imaging the biodistribution. However, in the case of the pure beta emitters the only photons produced are the bremsstrahlung. Consequently, the pure beta emitters are subjected to the bremsstrahlung imaging to do the map of the biodistribution *in vivo* of the radiopharmaceutical.

Currently, researchers aim to finding new radionuclides, with simultaneous β- and γ-rays emission, which offer the possibility to both administer treatment and imaging the radiation of

the treatment *in vivo* (Wheat *et al.*, 2011; Stanciu, 2012).). However, the gamma rays will give a dose to the normal tissues.

There are some radionuclides like ^{131}I, Samarium-153 (^{153}Sm) and ^{177}Lu which have both beta emitters, for therapeutic effects, and γ-ray emitter for external imaging of the biodistribution (Stanciu, 2012), making them as ideal radionuclides for TRT. A wide range of radionuclides available for TRT and their characteristics is shown in table 2.5.

Table 2.5. Physical characteristics of the radionuclides available for common use in the therapeutic nuclear medicine (Rajendran, 2007; Wheat *et al.*, 2011)

RADIONUCLIDE	PHYSICAL HALF-LIFE (T_P)	MODE OF DECAY	MAXIMUM PARTICLE ENERGY [MeV]	GAMMA ENERGY USED FOR IMAGING[MeV]	MAXIMUM RANGE IN TISSUE [mm]
Phosphorous-32 (^{32}P)	14.3days	β^-	1.71	-	8.2
Yttrium-90 (^{90}Y)	64.1hrs	β^-	2.28	-	11.3
Iodine-131 (^{131}I)	8.0days	β^-	0.61	0.364	2.3
Lutetium-177 (^{177}Lu)	6.7days	β^-	0.50	0.113 and 0.208	1.8
Strontium-89 (^{89}Sr)	50.5days	β^-	1.49	-	7.0
Rhenium-188 (^{188}Re)	17hrs	β^-	2.12	0.155	10.4
Samarium-153 (^{153}Sm)	1.95days	β^-	0.81	0.103	3.0
Copper-64 (^{64}Cu)	12.9hrs	β^- and β^+	0.57	1.35	-
Bismuth-212 (^{212}Bi)	60.5min	α	7.8	-	0.075
Radium-223 (^{223}Ra)	11.4days	α	27.4	0.154	0.05

According to the International Atomic Energy Agency (2009a, 2009b) some therapeutic applications include the treatment of numerous cancers, bone pain (palliation) and rheumatoid arthritis, bone marrow ablation, and inhibition of coronary restenosis.

TRT is well established for the treatment of hyperthyroidism, mostly Graves and Plummer's disease, and thyroid cancer by administration of the radioactive iodine ^{131}I, because ^{131}I administered as radionuclide NaI takes the advantage of the thyroid gland's activity for iodine. Oral administration of ^{131}I has been used to treat benign conditions of the thyroid gland since the 1940s, making this procedure the oldest and the most commonly practiced TRT. In the case of

thyroid cancer, ^{131}I therapy aims at destroying residual tumour tissue to reduce the recurrence rate, whereas in hyperthyroidism, ^{131}I is used to decrease thyroid bulk (volume) and thus decrease thyroid function without necessarily removing function altogether (Stokkel *et al.*, 2010; Wheat *et al.*, 2011).

TRT is also used in palliation of painful bone metastases through the intravenous administration of ^{89}Sr chloride, ^{153}Sm lexidronam (^{153}Sm EDTMP), and ^{186}Re etidronate (^{186}Re HEDP). Among these agents, ^{186}Re HEDP is approved in Europe while the others are approved in the US. The goal of palliation is to improve the life quality of the patients who have widespread skeletal metastases (Ersahin *et al.*, 2011; Wheat *et al.*, 2011).

^{32}P phosphate was the first therapeutic radioisotope used in leukaemia about 70 years ago. Nowadays, it is used in others conditions such as myeloproliferative disorders (haematological proliferations with a poor survival) by intravenous or oral administration. ^{32}P is usually used in older patients who does not responding to other treatments, in order to induce a long survival with an excellent quality of life (Tennvall & Brans, 2007; Wheat *et al.*, 2011).

Beyond the radionuclides describe before, one of the most important radionuclide used in TRT is the ^{90}Y. ^{90}Y is a high-energy pure β^- particle emitter (table 2.5.) and it is used in numerous treatments in nuclear medicine therapy. It takes the advantages of the beta particle decay, delivering a well located dose to the target cells with minimum radiation safety concerns. For example, ^{90}Y-microspheres have been used in radioembolization. An innovative therapeutic approach used to treat primary liver cancers, which may cause rapidly fatal liver failure in a large majority of the patients. Radiomicrospheres treatment involves the intrahepatic arterial administration of either ^{90}Y bound to resin, ^{90}Y-resin (SIR-Spheres®, Sirtex Medical, Lane Cove, Australia) or embedded in a glass matrix, ^{90}Y-glassmicrospheres (TheraSphere®, MDS Nordion, Kanata, ON, Canada) (Gulec & Siegel, 2007; Ersahin *et al.*, 2011; Francesco *et al.*, 2011). According to Gulec and Siegel (2007) ^{90}Y-microspheres are not registered as unsealed sources, since they are not metabolized. However, the microspheres are delivered in aqueous solution, and therefore the radioactive contamination must be taken into account and microspheres should be handled as an open source, like other radiopharmaceutical.

Beside this type of treatment, the most important application of the ^{90}Y is in RIT. Specific peptides, such as ^{90}Y-labelled octreotide or ^{90}Y-labelled monoclonal antibodies are used in RIT. The European Association of Nuclear Medicine (EANM) approved the ^{90}Y-radiolabelled ibritumomab tiuxetan (Zevalin®; Biogen-Idec Pharmaceuticals, San Diego, CA) in 2004, to be used in B-cell lymphoma treatment and related cancers. The FDA approved Zevalin® in 2002, together with the ^{131}I tositumomab (BEXXAR®, GlaxoSmith- Kline, Philadelphia, PA) (Tennvall *et al.*, 2007; Ito *et al.*, 2009).

Zevalin® and BEXXAR®, commercially approved at present, are two RIT agents that used murine anti-CD20 antibodies. These antibodies target the CD20 antigens expressed in more than 95% of the patients with B-cell malignancies, inducing *in vitro* apoptosis in $CD20^{+}$ B-cell lines. Particles emitted from ^{90}Y and ^{131}I damage target B and neighbouring cells. The treatment is mainly used for patients with non-Hodgkin's lymphoma (NHL), which accounts for 85% of all lymphomas in the lymphatic system (National Research Council, 2007; Tennvall *et al.*, 2007; Minarik *et al.*, 2010; Rhymer *et al*., 2010; Ersahin *et al.*, 2011).

Zevalin® and BEXXAR® are now in general clinical use with impressive response rates and limited and reversible toxicity. The number of European nuclear medicine departments using Zevalin® is continuously increasing, since the therapy is often considered successful (Tennvall *et al.*, 2007).

Others radiopharmaceuticals have the ^{90}Y as radionuclide, such as ^{90}Y-DOTATOC and ^{90}Y lanreotide, which are used in TRT to treat neuroendocrine tumours (NETs), metastatic carcinoid and pancreatic neuroendocrine tumours in patients whose symptoms are not controlled by conventional therapy (Lewington, 2003).

2.3.3. Internal Dosimetry for Radionuclide Therapy

Radiation is an inherent characteristic of all radiopharmaceuticals and the patients always receive an unavoidable radiation dose when subject to diagnostic or therapeutic purpose. In case of therapeutic procedures, the radiation is what produces the therapeutic effect (Farstad, 2012). However, the effectiveness of the TRT is limited by the amount of undesired radiation given to a dose-limiting normal tissue.

Through the internal dosimetry, the concentration and the spatial and temporal distribution of the radiation energy deposited in tissues may be determined (Zanzonico, 2000; DeNardo *et al*, 2002). There are three fundamental quantities that should be considered in dosimetry and in radiation protection: the *absorbed dose, D*, which define the mean energy absorbed per unit mass of tissue or organ and measured in Grays [$Gy=J.kg^{-1}$], the *equivalent dose, H_T*, established when the adsorbed dose is weighted for harmfulness of different radiations (type and energy) which is measured in Sieverts [Sv], and finally the *effective dose* [Sv], which is defined as a summation of the tissue equivalent dosses, each one multiplied by the appropriate tissue weighting factor. This last quantity takes into account the radiation sensitivity of particular tissues (Martin & Sutton, 2002; IAEA, 2005).

The current system of radiation protection that is internationally accepted (International Commission on Radiological Protection, ICRP, and IAEA) provides no dose limits for patients

and comforters or carers. However, dose limits are prescribed for staff and members of the public. The dose limits recommended by the ICRP and the IAEA for members of the general public, staff, patients and carers are set out in table 2.6. (IAEA, 2009b).

Table 2.6. Annual dose limits recommended by ICRP 1990, 2007 and IAEA (IAEA, 2009b).

Application	Employees (18 years and above) dose limit	General public dose limit	Patient, comforter and carer dose limit
Effective Dose	20mSv	1mSv	No dose limit
Equivalent dose to lens of eye	150mSv	15mSv	No dose limit
Equivalent dose to skin	500mSv	50mSv	No dose limit

Absorbed dose calculations are based on modelled biodistribution data and on quantitative imaging procedures. The Medical Internal Radiation Dose Committee (MIRD) of the American Society of Nuclear Medicine has developed a method of estimating organ absorbed dose after the radiopharmaceutical administration. This method is referred to as the MIRD schema and the aim is estimating average doses to critical organs resulting from diagnostic procedures (Flux *et al.*, 2006). In the MIRD schema, the body is considered to consist of source organs, which accumulate radioactivity, and target organs, which are irradiated by activity of the source organs. According to the MIRD schema, the mean absorbed dose to a target organ (r_k) from its exposure to a source organ (r_h), $\overline{D}(r_k \leftarrow r_h)$ is given by the follow equation.

$$\overline{D}(r_k \leftarrow r_h) = \tilde{A}_h S(r_k \leftarrow r_h) \qquad \text{Eq. (2.41)}$$

Where $\tilde{A}_h$ is the source organ cumulated activity, measured in terms of the activity time product [MBq.s] (which represents the number of millions of decays) and the term $S(r_k \leftarrow r_h)$, usually referred to as the S-value or S-factor, represents the mean dose in the target organ per unit cumulated activity in the source organ, which may include the situation of a target organ and a source organ being the same (Martin & Sutton, 2002). The cumulated activity is dependent on biological parameters whereas the S-factor deals with the physical components of the absorbed dose. The MIRD S-factor are published for most source-target pairs and calculated for a range of clinically relevant radionuclides. The S-values takes into account the energy released from each radioactive decay, the relative geometry of the source organ and the organ in which the absorbed dose is calculated (Flux *et al.*, 2006).

Beside the MIRD schema, there are others dosimetry approaches to estimate radiation doses in the patients, such as the use of MIRD methodology with voxel S-values; convolution of the cumulated activity with dose point kernels (DPKs) derived analytically or by Monte Carlo methods; and full Monte Carlo simulation of radiation transport through the patient. These methods generally depend on quantitative gamma camera imaging to determine the time-

varying activity distribution and on target volume determination (see *e.g.* Wilderman & Dewaraja, 2007; Kinase, 2011; Ljungberg & Sjögreen-Gleisner, 2011).

The focus of dosimetry in diagnostic nuclear medicine is the assessment of risk to normal tissues during imaging procedures. In MIRD schema traditional application to diagnostic radiopharmaceuticals, the method assumes that activity and cumulated activity are uniformly distributed within organ size source regions and that radiation energy is uniformly deposited within organ size target regions (Heard, 2007).

However, the dosimetry in radionuclide therapy estimates delivered absorbed doses to tumours and ensures that absorbed dose levels to normal organs are below tolerance levels, avoiding the toxicity to normal tissues (Ljungberg & Sjögreen-Gleisner, 2011). In therapeutic procedures, far higher quantities of radioactivity are administered than in diagnostic procedures. Consequently, it is vital to calculate real absorbed doses.

Adaptations and alternative methods are required to deal with therapeutic applications, since specific patients deviate kinetically and anatomically from the model used (Zanzonico, 2000; Martin & Sutton, 2002; Flux *et al*, 2006).

With the increasing therapeutic applications and the need for greater accuracy and efficacy, various techniques beyond the traditional MIRD schema have been developed. Radiation dosimetry in TRT is now evolving to patient-specific dose estimation, in order to improve the accuracy of dose estimates (Zanzonico, 2000).

Nevertheless, most of the TRT treatments still based on empirical fixed administered activities, or, more rarely, according to the patient's weight, or yet, age- and sex-specific reference data for human anatomy and body composition, according to MIRD schema (Flux *et al.*, 2006). This approach provide errors of internal dosimetry calculations, since two patients may react in a different way for the same amount of radioactivity administered, either in the quantity of radiation that is taken up in a tumour or in a normal organ, or in the time that the radiation remains there (Flux, 2006). As a result, internal and individual patient dosimetry is currently the only possible way to establish an individual minimum effective absorbed dose and a maximum tolerated absorbed dose to the normal organ. The aim is to calculate the tumour response and the normal organ toxicity on the basis of pre-therapy dosimetry and increase the knowledge of clinical radionuclide radiobiology by observation the post-therapy effects (DeNardo *et al*, 2002; Flux *et al*, 2006).

If the tumour dose can be calculated then the treatment dose for a particular patient may be verified, and dose-response relationships for the treatment in general may be developed. Additionally, clinicians can use dose predictions to determine the effectiveness of the trial and whether they can hope for curative or only palliative results (IAEA; 2005).

Ideally, each radionuclide therapy patient should receive dedicated treatment planning and verification. The planning stage includes pre-therapy dosimetry by imaging *in vivo* the time-varying distribution of the radiopharmaceutical. The therapeutic absorbed dose required is determined by measure the organ and tumour volumes and biokinetics. Subsequently, the verification stage requires post-therapy dosimetry to calculate the actual doses delivered through the images obtained at various time-points after administration (Heard, 2007).

Pre-therapy imaging of ^{90}Y biodistribution (Zevalin®) is required by FDA. The nonexistence of γ-rays emission from ^{90}Y-ibritumomab tiuxetan has led to the use of ^{111}In-ibritumomab tiuxetan as a substitute tracer for prediction of the absorbed dose, which it is possible due to its similar chemical properties. However, according to Ito *et al.* (2009) and Minarik *et al.* (2008, 2010), ^{111}In imaging may not completely reflect the distribution of ^{90}Y, since the behaviour of free circulating ^{90}Y and ^{111}In has been shown to be different. Jonsson *et al* (1992) and Lovqvist *et al* (2001), quoted in Ito *et al.* (2009) claim that free ^{111}In accumulates in the liver, spleen and bone marrow, whereas uptake of free ^{90}Y occurs at bone surfaces.

Once there is no solid evidence that currently available dose calculations can predict the therapeutic efficacy or toxicity of ^{90}Y treatment, European countries (with exception of Switzerland) do not require pre-therapeutic imaging with ^{111}In-ibritumomab tiuxetan, in accordance with the guidelines of the EANM (Ito, *et al.*, 2009). However, because ^{90}Y is a high-energy pure beta emitter with bremsstrahlung photons production, a quantitative bremsstrahlung imaging of ^{90}Y biodistribution is necessary for confirming its uptake and estimating the absorbed doses. There are, however, several problems associated with the use of ^{90}Y bremsstrahlung imaging for quantitative purposes (Minarik *et al.*, 2008, 2010).

In clinical practice, internal treatment planning has not yet been implemented and simplistic dosimetry assessment procedures are frequently reported which cannot accurately predict or evaluate the absorbed doses delivered. The necessary measurements to trace a patient-specific dosimetry planning are not always made for a diversity reasons, including the challenges of therapeutic imaging or simply a lack of resource or expertise (Walrand *et al.*, 2011). Therefore, technicalities and knowledge have to be augmented and stimulated in order to achieve a more satisfactory correlation between absorbed dose estimates and treatment response or correlation with organ toxicity. Many practical issues remain before patient-specific dosimetry in radionuclide therapy becomes standard procedure.

2.3.4. Why is Bremsstrahlung Imaging Difficult?

The image quality of bremsstrahlung photons is compromised due to several reasons. Such as explained in section 2.2.3., gamma cameras are designed primarily for diagnostic nuclear medicine imaging. The equipment is tuned to detect monoenergetic gamma radiation, particularly radionuclides emitters of γ-rays with energies between 50 to 250keV.

In the case of bremsstrahlung imaging, for high-energies radionuclides, such as ^{32}P and ^{90}Y, a set of gamma camera performance characteristics cause problems in the image quality. The performance characteristics of gamma cameras provide a difficult precision on the radiopharmaceutical distribution imaging.

One of the main problems in the bremsstrahlung image acquisition is the choice of the energy window. For conventional gamma emitters, the energy window is centred on the photopeak energy, accepting the majority of primary photons and rejecting the scattered photons. However, in bremsstrahlung imaging there is no photopeak, since bremsstrahlung radiation produces a continuous spectrum from the highest beta particle energy down to zero (see section 2.1.4.). Therefore, there has been great inconsistency on the choice of the energy window due to the continuous and broad energy distribution of the bremsstrahlung photons, becoming inefficient the simplest method of the scatter correction. The challenge in bremsstrahlung imaging is to choose an appropriate width and position in the spectrum, and hence in the energy window, in order to maximise the proportion of primary photons and minimise the scatter ones (Gulec & Siegel, 2007; Rong *et al.*, 2012).

Another challenge to take into account is the collimator. In diagnostic imaging, the collimator is chosen according to the trade-off between the spatial resolution and the sensitivity. According to Heard (2007), in bremsstrahlung imaging this choice is more complicated. First, the spatial resolution is already poorer due to the septal penetration and because the fact that electrons may travel several mm from the source before photons are produced. Even for medium- and high-energy collimators, the septal penetration may happen since the high-energy of the bremsstrahlung photons. This fact, consequently, produces lead characteristic x-rays which may blur the images. On the other hand, bremsstrahlung sensitivity is small. As mentioned before (section 2.1.4.), only 2 to 3% (or even less) of the electron interactions produce bremsstrahlung photons (Attix, 2004), which difficult the collimator choice (Minarik *et al.*, 2008, 2009, 2010).

Performance characteristics, such as uniformity, linearity and attenuation correction, are energy-dependent. In diagnostic nuclear medicine, those features are tailored to standard monoenergetic imaging with values around to the photopeak energy. However, for a wide energy spectrum created by bremsstrahlung photons, the correction's maps and the attenuation coefficients are

not established causing errors in the acquisition signals and in the accuracy of the image produced (Ito *et al.*, 2009; Minarik *et al.*, 2010; Rong *et al.*, 2012).

Thus, the gamma camera systems are tailored for diagnostic nuclear medicine and consequently windowing and scatter correction techniques for the pure beta emitters are complicated by the lack of the photopeak in the bremsstrahlung spectrum (partly due to septal penetration and down scatter into the imaging window).

Today, with the revolution in medical equipment, hybrids SPECT-CT systems have implemented advanced software for acquisition and reconstruction. Therefore, according to Fabbri *et al.* (2009), the quantitative analysis of SPECT-CT ^{90}Y bremsstrahlung images and the appearance of the three-dimensional dose distributions are feasible, allowing to address the dosimetric verification to patients during the course of the therapy. These systems provide better information of the density distribution (by CT) and biokinetics of pure beta-emitter radiopharmaceuticals (by SPECT), improving images quality during the therapeutic procedures. Figure 2.26. shows the benefits when imaging ^{90}Y glass microspheres administered in hepatic radioembolization, with following quantitative bremsstrahlung imaging acquired with SPECT-CT.

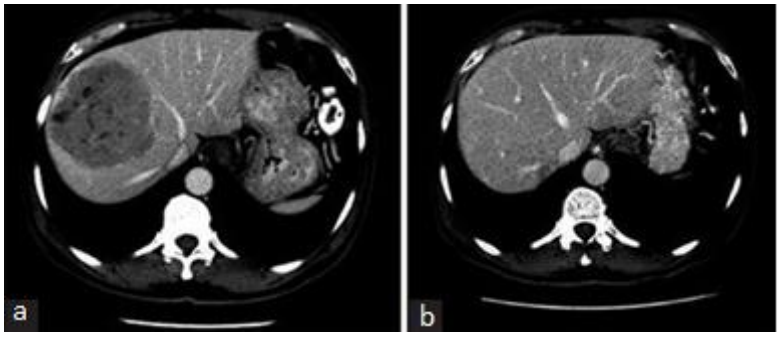

Figure 2.26. Application of hepatic radioembolization with ^{90}Y glass microspheres. **(a, b)** illustrate the benefit of hepatic radioembolization with ^{90}Y glass microspheres in a cystic hepatocellular carcinoma. **(a)** Image after the first dose of ^{90}Y, and **(b)** after two doses of ^{90}Y (Adapted from Khan *et al.*, 2011)

CHAPTER 3.

DISSERTATION METHODOLOGY

3. DISSERTATION METHODOLOGY

3.1. Methods and Materials

With the increasing therapeutic use of relatively high-energy pure beta emitters (<1MeV), such as ^{32}P or ^{90}Y, particularly in materials with high atomic number (such as bone), the production *in vivo* of bremsstrahlung photons is sufficient for external detection and imaging.

According to Zanzonico *et al.* (1999) and Gulec and Siegel (2007), the bremsstrahlung component of the beta emitters has been traditionally ignored in internal and external dosimetry calculations. This fact may be due to a lack of available methods for including this component in the calculations or to the belief that the contribution of this component is negligible compared to that of other emissions. However, with the ample use of those radionuclides in therapy, evaluation of the bremsstrahlung contribution to dosimetry calculations should be considered.

Thus, the present study aims at investigating the properties of the emitted bremsstrahlung photons. One attempts to understand the characteristics of the bremsstrahlung photons, such as efficiency, direction or radiative yield, when those photons are formed inside different biological mediums and taking into account different features of the beta particles source, such as emission direction or energy of the particles.

To achieve this purpose it was used the Monte Carlo simulation. Amongst the available systems that use Monte Carlo simulation, the one chosen in this investigation was the EGSnrc (V4 2.3.2), due to its advantages relatively to the electrons transport, in comparison with the others methods. EGSnrc is a Monte Carlo simulation package for coupled electron-photon transport, widely used in medical physics applications. It is a free software where the source code along with a user manual is available in official Ionizing Radiation Standards (IRS) web page from the National Research Council (NRC) of Canada (IRS/NRC, 2011). The computational language to create the EGSnrc code is written in an extended Fortran language known as Mortran3, which in turn is translated by a processor into a Fortran program.

Other of the main aims of this study was to obtain the strong knowledge of EGSnrc system in order to be able to modify and produce a wide range of different simulations in different physical conditions.

EGSnrc software, supporting documents and the computational codes developed constitute the main material used in this investigation.

To reach the aim proposed two main Mortran codes were computed in EGSnrc, in order to study the bremsstrahlung photons. First, a *scintillation detector model* was developed to detect and count the interactions with the crystal from a point source of photons, and second, a *source*

model was created to mimic a point source of beta particles inside the patient with the purpose of produce bremsstrahlung photons *in vivo*. These two codes were modified along the study according to the measurements to test in this investigation. The results and method used in each simulation are explained in chapter 4.

Consequently, the Monte Carlo simulations were split into two broad areas. The first part and the initial simulations were executed with the scintillation detector model using a point source of photons. This model was initially used to validate the code developed, since the photons behaviour may be easily understood and there is more literature and data available (see section 4.1.). With this model, a full understanding of the EGSnrc system was undertaken, as well as the accuracy of the obtained results by comparison with the theoretical data.

After assessed the first computational code, some simulations were developed with the source model. Realistic events with a beta particles source were simulated in different homogeneous media and with different beta energies. The bremsstrahlung photons produced from those simulations were recorded and studied (see section 4.2.).

It would have been interesting to continue to the next step of the bremsstrahlung investigation, *i.e.*, imaging the bremsstrahlung photons in a gamma camera. For that purpose an EGSnrc *gamma camera model* would have to be properly developed and the information obtained in this study would have to be read it on that model. The aim would have been change the performance characteristics of the gamma camera, such as collimator characteristics, energy windowing or crystal size and its material, in order to improve the quantitative analysis of bremsstrahlung images. However, due to lack of time this part of the study was not possible concretize, since a faithful and realistic gamma camera model written in Mortran3 is very time consuming. Nevertheless, the preliminary information acquired is useful, not only to understand the behaviour of bremsstrahlung photons, but also for to be used in future investigations.

In addition with the bremsstrahlung measurements undertaken for this study, some list mode acquisitions were made in the INM, using a ^{99m}Tc cylindrical source. This part of the investigation was performed on a NM/CT 670, a hybrid SPECT-CT dual head camera by GE Healthcare (GE Healthcare, 2010), and the data were stored in the *GE Xeleris* nuclear medicine workstation, which is the software used to display, process, film, archive, and communicate nuclear medicine images. The purpose of these measurements was the verification and validation of a specific list mode decoding program developed by the University College London Institute for Cancer Research (ICR), in confidentiality agreement with the GE healthcare. The final data obtained by the decoding program were binned in sequential and small energies bins, forming an energy spectrum according to the PHA window chosen. The spectrum was compared with the theoretical values to validate and prove the accuracy of the

decoding program (method explanation in section 4.3.). As list mode would be used in patient studies, the decoding program had to be verified.

The decoding program read the raw data from the SPECT-CT and the output is the X and Y pixel positions and the respective energies of each single photon interaction, which are represented in a table format. To visualise the final image, a Matlab code was computed and developed and tested in order to "frame up" the list mode data, forming a frame image.

All the simulations were undertaken with a computer HP Pavilion dv6-1120ep, 32-bit Operating System Architecture and 2GHz Pentium (R) Dual-Core CPU T4200 processor with 4GB RAM.

The next sections explain how the EGSnrc models were created, and consequently, the principles of Monte Carlo Simulation.

3.1.1. Principles of Monte Carlo Simulation

The Monte Carlo simulation is used in various fields of science, such as radiation protection, diagnostic radiology, radiotherapy and nuclear medicine, with applications in both diagnostic and therapeutic purposes. This method allows simulate and understand complex phenomena and physical systems, through simulated processes by statistical methods employing random numbers. It is a useful and effective method, because in complex systems, at a microscopic level, the interaction processes are random and the analytical method become extremely difficult. This contrasting to the physical simple systems (e.g. homogeneous medium and monoenergetic particle) where it is possible to predict the outcomes from the interactions of radiation with matter through analytical calculations, for example by using the appropriate attenuation coefficient (Zaidi, 2004; Heard, 2007).

In the concrete case of radiation transport, this is simulated by the creation of photons or electrons from a defined source region. The particles are tracked as they travel through the system, with sampling of the *probability distribution functions* (PDFs) for their interactions, to evaluate their trajectories and energy deposition at different points in the system (Zaidi, 2004). The key of the Monte Carlo method is, thus, the use of PDFs and *random number generators* (RNGs).

The user defines some details relative to the conditions of the particle transport (energy, geometry, medium). The PDFs express the range of possible outcomes for each particle at each step, which are stored within the Monte Carlo program as material- and energy-dependent cross-sections. In each step of each particle's simulated progress is determined at random, as well as its changing attributes (Brown, 2009).

Once the PDFs are known, the Monte Carlo simulation can proceed by random sampling from the PDFs to generate random numbers uniformly distributed on the interval 0 to 1, which map to unique values of the *cumulative PDFs*, based on experimental data, theoretical models, or both. By simulating a large number of photons or electrons transported through the medium (source events, called "histories", "showers" or "cases"), the information can be obtained about average values of the result of the system. As the simulation converges on this result, the macroscopic and final result of the system is revealed.

In many practical applications, one may predict the statistical error (the "variance") in this average result, and hence, an estimated number of Monte Carlo trials that are needed to achieve a given error (Heard, 2007; Rogers & Bielajew, 2012).

The accuracy of the method is dependent on the number of histories. A larger number of histories improves the accuracy of the simulation, which means that the statistical uncertainty decreases. However, increasing the number of cases involves a large computational time and large data storage capacity.

The Monte Carlo technique is useful to answer questions which cannot be addressed by analytical investigation (Brown, 2009). Examples of studies that used the Monte Carlo method in the area of nuclear medicine, both to investigate electron transport, as well as, the bremsstrahlung production, may be read in Lauterbach *et al.* (1999), Natter *et al.* (2003), Calderaro (2004), Cengiz and Almaz (2004), Salvat *et al.* (2006) and Peeples and Gardner (2012).

Several Monte Carlo codes systems to model coupled electron–photon transport are freely available in the public domain. The code systems vary in aspects such as, the type of the particle, the physics theories and cross-sections and the sampling techniques for using them, their ease of use and the speed with which simulations run. According to Rogers (2006), the most commonly Monte Carlo systems used in nuclear medicine are the EGSnrc, PENELOPE, MCNP and GEANT4.

The code system used in this investigation was the EGSnrc. Rogers (2006) claims that EGSnrc remains the most widely used general purpose Monte Carlo radiation transport package in medical physics.

3.1.2. How EGSnrc works?

The EGSnrc system is a package for the Monte Carlo simulation of coupled electron-photon transport, which uses an arbitrary medium and geometry defined by the user. Its current energy range of applicability, for electrons, is a few tens of keV up to a few hundred GeV, whereas for photons is 1keV to several hundred GeV (IRS/NRC, 2011).

In EGSnrc the electrons and photons "born" in accordance to the user input. The particles travel certain distances to the site of a collision, which are determined by the PDF depending on the total interaction cross section, and are absorbed or scatter to the next point of collision. The procedure is continued until all the particles are absorbed or leave a specific geometry defined by the user. EGSnrc takes into account all the physical processes that happen in radiation interactions with matter (section 2.1.3. and 2.1.4.).

Because of the complex nature of electron transport in the process of slowing down, in which hundreds of thousands of interactions may occur with the surrounding medium, the EGSnrc employs the *condensed history* (CH) technique, develop by Berger (1963). For electrons, a simulation event-by-event is not possible due to limitations in computing power. Therefore, the CH method "condenses" large numbers of interactions into a single step. According to Kawrakow *et al.*, (2011) this technique is possible due the fact of single electron collisions with the atoms cause small changes in the particle's energy and direction of flight. The final and single step takes into account the cumulative effect of the individual interactions by sampling the change of the particle's energy, direction of motion, and position from appropriate multiple scattering distributions.

The EGSnrc is an extended and improved version of the EGS4 package originally developed at Stanford Linear Accelerator Centre (SLAC). It incorporates significant improvements. The new physics models included a new CH scheme for the simulation of electron transport - Class II, an option to apply more accurate bremsstrahlung cross-sections (IRS/NRC, 2011).

The computational language used in EGSnrc is Mortran3, an extended Fortran language with a powerful macro facility. The Mortran language is implemented as a set of macros which are used by the macro processor to translate the language into Fortran. To create any EGS program code the user must write a "user code". The user code comprises the MAIN routine and three user-written subroutines HOWFAR, HOWNEAR and AUSGAB. The EGS code itself consists of two user-callable subroutines, HATCH and SHOWER, which in turn call the others three subroutines developed by the user. This relationship is illustrated in Figure 3.1.

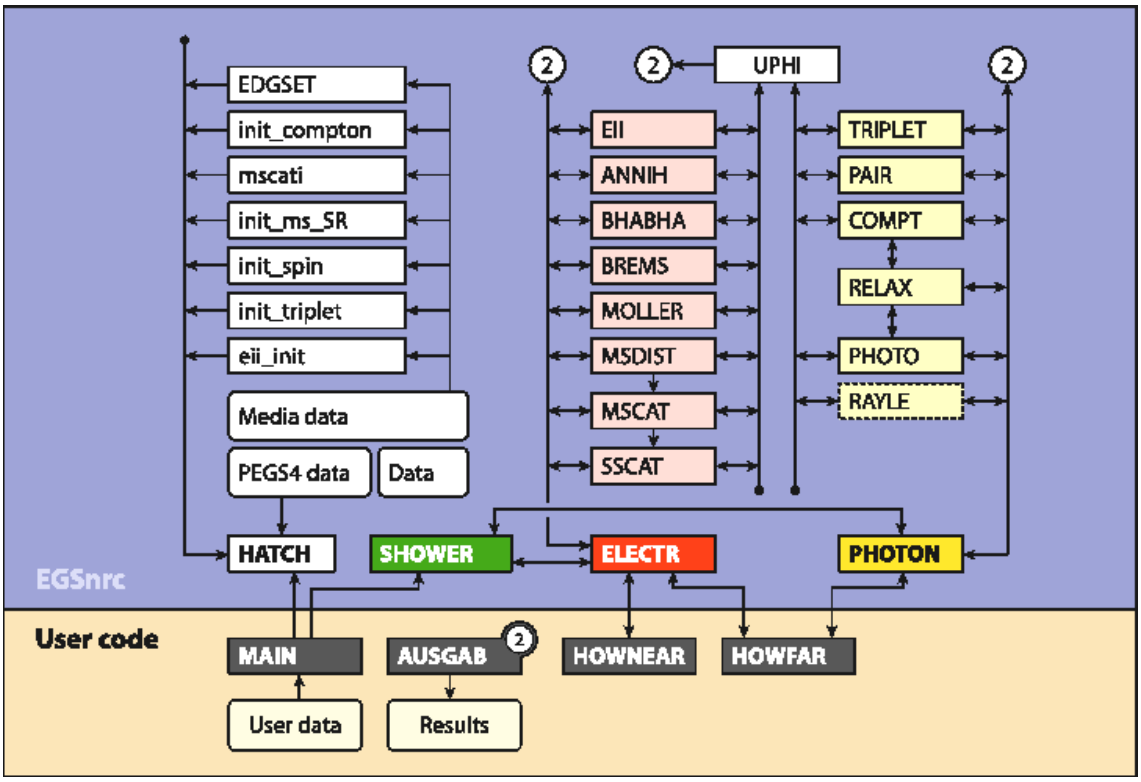

Figure 3.1. Structure of the EGSnrc code system (Kawrakow *et al.*, 2011)

In the blue rectangle are represented the subroutines of the EGS code itself. These are used to establish the cross-sections for the media and particles in the simulation. The subroutines inside the bottom rectangle are those by which the user interacts with the EGS code system. The user communicates with EGS by means of various COMMON blocks, which are sets of parameters that define the variables to use in the program (Kawrakow *et al.*, 2011, see appendix 1).

In the MAIN routine, the user executes any initialisation needed for the HOWFAR and HOWNEAR subroutines, as well as defines initial parameters by using the COMMON variables or creating new ones in Macros definitions. For example, in the COMMON block called "MEDIA" the variables MEDIA and NMED are used to define the array of media names and the number of media used in the system, respectively. In MAIN routine the user may specify such things as the initial particle characteristics (type of particle, position, energy, trajectory), the number of histories, the desired electrons and photons cut-off energies (MeV) defined as ECUT and PCUT, respectively, or the materials in which interactions will take place.

The user creates the composition of the medium in a package called PEGS4, which is a data pre-processor for the EGS system. The medium may be an element, compound, or mixture. Also, two or more media may be selected in the same PEGS4 file. The energy thresholds at

which EGS will be desired to transport electrons and photons are defined in PEGS4. Together with the medium composition and energy thresholds, the interaction cross-sections for each material are calculated and consequently the PDFs to be used in subsequent Monte Carlo simulation will be formed. In PEGS4, the short form AP and UP define, respectively, the PEGS lower and upper photon cut-off energy and AE and UE define, respectively, the PEGS lower and upper electron cut-off energy. When the particles reach any of those values, or the ECUT or PCUT defined in MAIN, their histories are complete and any remaining energy is deposited and absorbed locally.

After finishing of the user code, the HATCH subroutine is called by MAIN and initialises the simulation by reading the material interaction cross-sections from the specific PEGS4 data file previously created. When this initialisation is complete, the MAIN routine may then call the SHOWER. Each call to SHOWER results in the generation of one history or event, initialising the interaction cascade. For the initial particle and for any subsequent particles sets in motion, the EGS subroutines (ELECTR, PHOTON, BREMS, COMPT, ANNIH, etc.) determine the characteristics of the interaction, whether interaction takes place, what kind, and how energy will be shared between resultant particles and the medium.

The user-written HOWFAR are HOWNEAR are subroutines that define the geometry of the physical condition to test. Those subroutines determine the location of the particles in the system at each step and determine whether the particles may or may not continue to the next interaction without encountering a boundary. The other user-written subroutine, AUSGAB, is responsible by the results output. In AUSGAB the user selects and defines which data will be stored in a text file. This selection is undertaken through the parameters available in the AUSGAB (IARG) which the user has the ability to switch on or off, in order to know, respectively, when a certain event are about to occur or after it has occurred (Kawrakow *et al.*, 2011, see appendix 2). When all histories are complete, the information collected in MAIN and AUSGAB is summarised and stored according to the user's instructions.

Concisely, the user communicates with EGS by means of subroutines (HATCH - to establish media data; SHOWER - to initiate the cascade; HOWFAR & HOWNEAR - to specify the geometry and AUSGAB - to store and output the results), COMMON blocks by changing values of variables and finally by Macros definitions to call all the pre-defined variables or create new ones.

3.1.3. The Models' Code in Words

The codes developed in this study were based on the tutor1.mortran, a tutorial program provided in the EGS manual (Kawrakow *et al.*, 2011). In broad terms, the EGS program may be divided into 9 steps, *i.e.*, EGS has a sequence of operations needed be followed for the correct operation of the program. The step 0 is the file initialisation and the statement *call egs_init* must be written to this purpose (should be the first executable statement and thus is usually after step 1 and possibly in step 2); in step 1 the user overrides the EGS Macros; the step 2 is the pre-HATCH call initialisation. This step consists of setting the EGS COMMON variables that are used by HATCH. The subroutine HATCH is called in step 3. The step 4 is responsible for the initialisation of the user-written subroutines HOWFAR and HOWNEAR, whilst the step 5 is used to initialise the user-written subroutine AUSGAB. In step 6 the user defines all the parameters of the incident particle, such as type of particle, kinetic energy, particle position, and number of histories or events. In step 7 the SHOWER is called. This EGS subroutine is called as often as desired, according with the number of histories considered necessary. In step 8 the output of results are defined as well as the display format. Finally, the step 9 properly closes files and places them back on the user-code's directory through the use of a last executable statement *call egs_finish*.

All those steps are declared in the MAIN routine and written with base on the COMMON variables existent on EGS. However, in order to create a properly EGS code the user must specify the physical system, *i.e.*, the geometry of the process. Consequently, it is necessary define all the regions along which the particle may travel in the subroutines HOWFAR and HOWNEAR. The geometry system could have one or more media.

HOWFAR determines the exact distance at which the particle can intersect a boundary. This subroutine can answer if the particle may or may not travel a certain distance, defined randomly by the EGS in the variable USTEP, without crossing a boundary. If USTEP is smaller than the distance to the next boundary then the particle may travel USTEP. Otherwise, the program defines USTEP equal to the distance to the boundary and identifies a new region to the particle equal to the far side of the boundary.

The most trivial geometry that may be written in HOWFAR is the case of a homogeneous infinite medium, in which one can define two infinite parallel planes delimiting three regions of any material, as shown in figure 3.2. A plane is defined by the coordinates of one point on the plane and its direction vector. The triangles point in the direction of the unit normal vector that is generally initialized in MAIN routine, in step 4. Independently of the geometry, the unit vector of any individual plane must be defined.

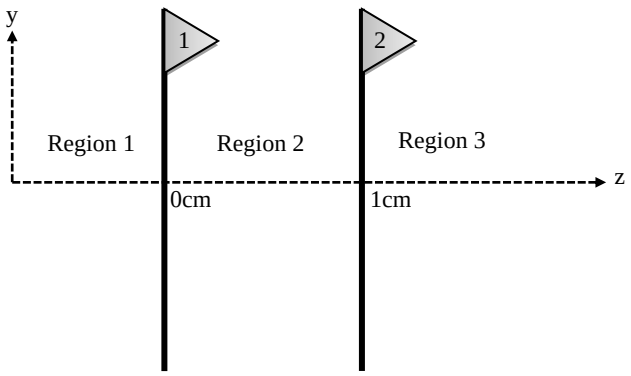

Figure 3.2. Simple geometry to the HOWFAR subroutine: two parallel planes separating three regions along z. This is a three region geometry example for HOWFAR. The x axis is into to the paper (Adapted from Kawrakow *et al.*, 2011)

For inhomogeneous media and complex geometries with arbitrary surfaces, the subroutine HOWFAR becomes more difficult to define. However, a number of geometry subprograms and their macro-equivalents are distributed within the EGS system in order to make it easier to write the HOWFAR. For example, the subroutine that defines the geometry in figure 3.2. is the *PLANE1* (determines if particle trajectory strikes a planes surface). Other examples of geometry subroutines are: *CYLNDR* (determines if the particle trajectory strikes a cylindrical surface), *CONE* (determines if the particle trajectory strikes a conical surface), *SPHERE* (determines if the particle trajectory strikes a spherical surface), *PLAN2P* (Determines the intersection point for two parallel planes), *PLAN2X* (determines the intersection point for two crossing planes), *CYL2* (determines the intersection point for two concentric cylinders), *CON2* (determines the intersection point for two concentric cones), *SPH2* (determines the intersection point for two concentric spheres). Information to explain those geometries and others is available in documents as Nelson and Jenkins (1988) and Bielajew (1995).

The subroutine HOWNEAR defines the minimum distance (direction independently) to any surface from the location of the particle position. HOWNEAR is used to speed up the simulation by comparing the value returned with a user supplied constant TPERP. If the distance to the boundary is greater than TPERP the 'condensed' electron transport, where many individual interactions are grouped into one, is used. This is much faster than using single stepping where every individual interaction is simulated separately (single stepping). Only when the distance to the boundary is less than TPERP is single stepping used.

When the user defines TPERP with a high value, the simulation condenses all the interactions in that distance. However, if TPERP is set to zero all the interactions are considered and the program takes long time to run.

The subroutines HOWFAR and HOWNEAR will be different according to the physical geometry necessary to each simulation. Both subroutines may be modified depending on the specific study. For example, in one simulation a sphere may be used as geometry and for another test a cube may be preferable.

The subroutine HOWFAR defined in each EGS models (scintillation detector model and source model), as well as some variables necessary to undertake the simulations, are described below.

SCINTILLATION DETECTOR MODEL

The scintillation detector model was the first model to be constructed and developed in EGSnrc. The model is similar with a detector head of the gamma camera. Such as the gamma camera function, also this model was developed to detect and count all the photon interactions that occur with the crystal. It was developed to understand and simulate all the interactions mechanisms that take place inside the crystal.

The code of the scintillation detector model is presented in appendix 3. The sequence of operations needed for the correct operation of EGS, *i.e.*, the 9 steps described above and the subroutines are properly identifiable in the code.

In terms of geometry (HOWFAR), the detector may be thought of as a rectangular prism, created as a series of slabs (infinite slabs that when intersected produce a rectangular prism). This detector is constituted by two materials, NaI and Glass, which is placed in front of the crystal. Those two media were created in the same PEGS4 file. The thallium activator was not modelled since it constitutes only about 10^{-3} fraction of the crystal. Though existent in the real gamma camera, also the collimator and the aluminium shield involved in the detector were not computed since it would require much time and because this model was developed to validate the accuracy of the results produced by EGSnrc. The general model is shown in figure 3.3..

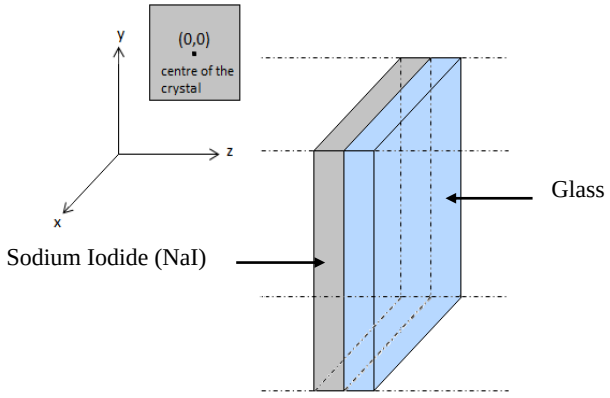

Figure 3.3. Scintillation detector model created in EGSnrc. A slab of NaI and Glass close together

Six different infinite planes were defined to create a rectangular prism, plus one to separate the NaI of the Glass, the two media used in this model. The planes were defined in step 4: initialization of HOWFAR. When the infinite planes are intersected, they generate the rectangular prism, as well as, eight different and separate regions: two finite regions inside the prism, NaI and Glass, and six infinite regions outside the prism. The particle is transported along to the regions and the regions are identifiable when the particle interacts. Figure 3.4. shows the planes to create the detector geometry and figure 3.5. the regions produced. The regions 7 and 8 match to the regions inside the rectangular prism, made of NaI and Glass, respectively, and the others 1 to 6 regions, were defined as vacuum placed around the detector, which served as an air gap.

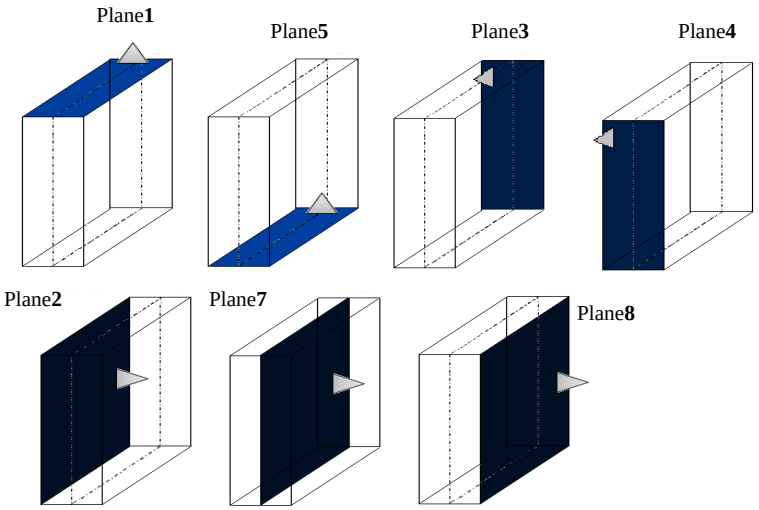

Figure 3.4. Planes necessary to define the detector geometry. The planes 1 to 6 separate the vacuum regions and the plane 7 separate the crystal from the glass

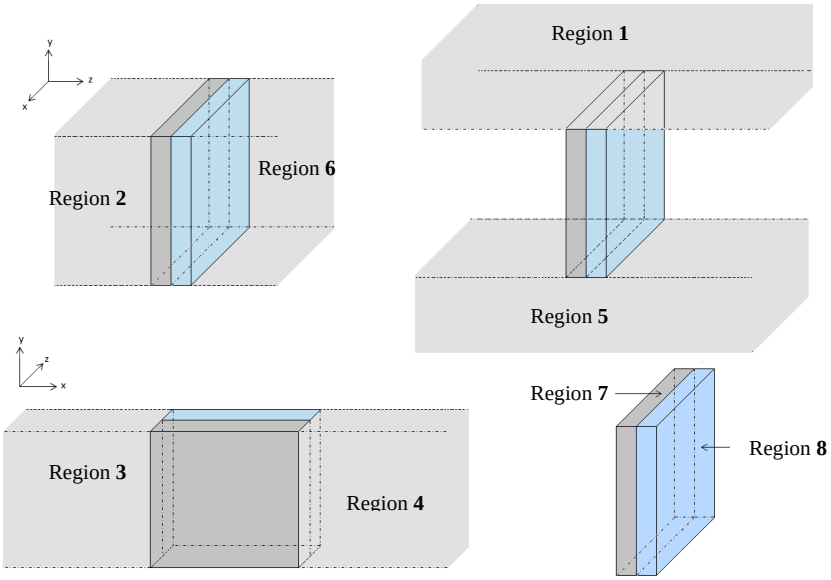

Figure 3.5. Regions produced by the creation of the planes. The regions 1 to 6 are vacuum, the region 7 is the crystal made of NaI and the region 8 is the glass

Due to the existence of the macro-equivalents in EGS, the creation of the detector geometry in the subroutine HOWFAR is easily feasible. In this model the Macro used was the PLAN2P. This Macro defines a pair of parallel planes. Since to create a rectangular prism is necessary three pairs of parallel planes, one pair normal to the *x*-*y* plane, other to the *x*-*z* plane and the last to the *z*-*y* plane, it was necessary to write the Macro PLAN2P three times.

When the HOWFAR is called, it works exactly how was explain before, but now taking into account more planes. This subroutine considers the direction of the particle, which plane is closest and what region is after that plane, in case the particle cross the boundary.

Some components of this model were modified along with the simulations, such as, the dimensions of the camera, the thickness of the NaI and Glass, the region where the photon point source was placed and the direction of the particle, which could travel along the z-axis or in an isotropic direction (see code lines for isotropic emission, explain in step 7). The photon interactions were counted inside the crystal (region 7), being discarded outside of it. But once again, the region of interest could be modified according to the simulation.

For all regions and for all simulations tested using this model the cut-off energies were defined as follows: ECUT=3.511MeV (0.511MeV rest mass + 3MeV) and the PCUT=0.01MeV. EGSnrc requires the addition of the rest mass energy of the electrons to the kinetic energy. Since this model was used to simulate photons and calculate the energy absorbed in the crystal, the chosen value to the ECUT was high (3MeV) in order to stop all the electrons with kinetic energy immediately below this value, avoiding unnecessary transport calculations and CPU time-consuming. In contrast, the photons were followed until they deposit almost all of their energy. Therefore, 0.01MeV for the PCUT was chosen.

When the NaI and Glass data file was created in PEGS4, also the energy thresholds at which EGS will be desired to transport electrons and photons were defined. Those were chosen according to the ICRU report 37, *i.e.*, AE=0.521MeV (0.511+0.01MeV), AP=0.01 MeV, UE=55 MeV and UP=55 MeV. The subroutine HATCH read both values ECUT/AE and PCUT/AP and chooses the maximum between both of them. EGSnrc stops tracking the particles inside the crystal when they fell off below those energy thresholds.

SOURCE MODEL

The source model was used to simulate bremsstrahlung photons inside the patient. The geometry (HOWFAR) of this model tries to mimic a pure beta particles point source placed inside a biological material. The code created is presented in appendix 4.

To achieve this purpose a sphere was created by the geometric subroutine SPHERE. In this subroutine only one boundary and two regions were defined. The boundary corresponds to the total surface of the sphere which separates the region inside from the region outside the sphere. The region outside the sphere was set up as vacuum and the material inside the sphere was changing according to the simulation. Four different biological materials were used: inflated lung, soft tissue, cortical bone and adipose tissue. All those materials were created in PEGS4, providing a data file for each material with the interactions cross-sections and the energy thresholds.

The general model is shown in figure 3.6. One may thinks in this model as a spherical phantom, used to do the simulations.

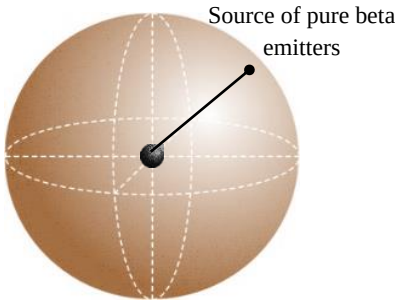

Figure 3.6. Source model created in EGSnrc. Radionuclide emitting beta particles in the middle of a sphere, made of biological material

A point source of electrons was positioned in the middle of the sphere and the particles emitted isotropically. The radius of the sphere was varying according to the simulations, as well as the kinetic energy of the electrons. Such as in the scintillation detector model, also in this one the energy thresholds defined in PEGS4 were chosen according to the ICRU report 37, *i.e.*, AE=0.521MeV (0.511+0.01MeV), AP=0.01 MeV, UE=55 MeV and UP=55 MeV.

However, the cut-off energies, ECUT and PCUT, were defined differently. Since the interest in this model is the production of the bremsstrahlung photons inside the sphere, the photons that cross the surface sphere are discarded. For that reason, cut-off energies were manipulated in order to stop the bremsstrahlung photons immediately over the surface area of the sphere. Consequently, in the region inside the sphere ECUT=0.521MeV (0.511+0.01MeV) and PCUT=0.01MeV, and outside the sphere the ECUT=0.521MeV (0.511+0.01MeV) and PCUT=5MeV. Inside the sphere the electrons are followed until their kinetic energy reached 10keV, as well as, the photons. This value ensures the simulation of all bremsstrahlung photons of high enough energy (usually 50keV for a gamma camera imaging). For the region outside the sphere the photons were terminated as soon as they were created by setting the PCUT=5MeV, higher than the maximum electron energy used in the simulation. This ensures that the photons are stopped when they cross the surface of the sphere. Below the PCUT the photons are discarded, depositing locally all of their energy, which may be counted if the user requires it.

3.2. Simulations

3.2.1. Photons Simulations

In order to validate the computed codes and verify the accuracy of the EGSnrc outcomes, the followed measurements were realised with a point source of photons:

- Verification of the inverse square law;
- Analysis the effect of the crystal thickness, by testing the detector count efficiency and linear attenuation coefficient;
- Analysis the effect of the glass in front of the crystal by testing the backscattered photons.

3.2.2. Bremsstrahlung Simulations

To achieve the aim proposed to this investigation the following simulations were tested, in order to understand the properties of the bremsstrahlung photons:

- Analysis of the bremsstrahlung production efficiency by varying the sphere thickness and the beta particles energy;
- Analysis of the bremsstrahlung yield by varying the biological material;
- Comparison of the bremsstrahlung spectrum shapes produced in different materials;
- Analysis of the angular distribution of the bremsstrahlung produced;
- Analysis of the spatial distribution of the bremsstrahlung photons from the point source;
- Analysis of the bremsstrahlung spectra produced by ^{90}Y and ^{32}P.

3.2.3. List mode Acquisitions

In order to validate the list mode decoding program, planar acquisitions (2D) were undertaken with a cylindrical source of ^{99m}Tc. Different energy windows were chosen according to the measurements. The measurements carried out are listed below.

- List mode acquisitions using ^{99m}Tc point source, positioned in different places of the gamma camera, acquired in two energy windows (140.5±10% and 450±10%);
- List mode acquisition of the full energy spectrum (256±100%).

CHAPTER 4.

RESULTS AND DISCUSSION

4. RESULTS AND DISCUSSION

Chapter 4 describes all the results and respective discussions relative to the measurements undertaken in this study. The method used in each simulation is properly explained for each one.

4.1. Photons Simulations

A substantial part of the work involved in producing a Monte Carlo simulation consists in its validation. In Monte Carlo simulation is important for the user to check whether the results given by the program are within the expectations. Therefore, it is advisable to do a validation of the code and see if the outcomes are according to the physics theory.

Since the photons behaviour and their interactions are easier to understand, photons were used in this part of the study to validate the first code computed, *i.e.*, the scintillator detector model. This part of the work also aimed to gain a working knowledge of the EGSnrc system, in order to be easier to change the code to any physical condition.

All the simulations undertaken in this part of the study were performed with a point source of photons, using the scintillator detector model with the geometry and components described in section 3.1.3.

The photons simulations and the corresponding method and discussion are explained below. The data recorded in each simulation were processed with Excel (Microsoft Corp., Redmond, USA).

4.1.1. Verification of the Inverse Square Law

The first simulation consisted in verifying whether the inverse square law is obeyed for photons. The inverse square law is used to understand the influence of the distance on the intensity of the radiation beam. When an isotropic radioactive source is placed at a certain distance from the detector, *r*, only a fraction of radiation (number of photons detected divided by the total number of photons emitted) is detected. At a distance *r*, the radiation emitted passes through the surface of an imaginary sphere having a surface area $4\pi r^2$. Therefore, the fraction of radiation detected by the crystal *per unit of area* is given by $A/4\pi r^2$, where A is the detector surface area, $4\pi r^2$ the total spherical area reached by the photons and *r* the source-detector distance (Cherry *et al.*, 2003, Saha, 2013). If one considers an isotropic point radiation source at the center of the sphere, the surface area over which the radiation is distributed increases as the square of the

distance from the source ($A \propto r^2$). Consequently, the inverse square law states that the radiation detected by the detector *per unit area* decreases with the inverse square of distance between the source and the detector (photons detected$\propto 1/r^2$), since the radiation is spread out over larger areas when *r* increases (Bushberg *et al.*, 2002). If the distance is doubled, the radiation is spread out over four times as much area, so the dose is only one fourth as much. The inverse square law is an important fact to takes into account at a dosimetric level.

To undertake the simulation a point source of monoenergetic photons, with 140keV of kinetic energy, was placed behind the crystal. 10^6 photons (histories) were emitted uniformly with equal intensity in all directions (isotropically). The Mortran code lines written to define the photons isotropy are clear in the EGSnrs code (appendix 3).

To achieve this purpose the number of photons that reach the crystal was stored by varying the source-detector distance and the size of the crystal. The sizes of the crystal chosen to be simulated were: 1, 5, 10, 20 and 40cm^2. For each detector surface area, the photon point source was moved away from the detector. The source-detector distances tested, for each surface area, were as following: 1, 3, 5, 10, 20, 30, 50, 75 and 100cm. In all simulations, both crystal and glass had 1cm of thickness.

Figure 4.1. gives the output data obtained from the simulation, *i.e.*, number of photons detected by the crystal *vs.* the source-detector distance. Considering figure 4.1., it is possible to confirm an exponentially relationship between the amount of photons that reaches the crystal and the source-detector distance. Each line in the figure represents one of the five different crystal sizes.

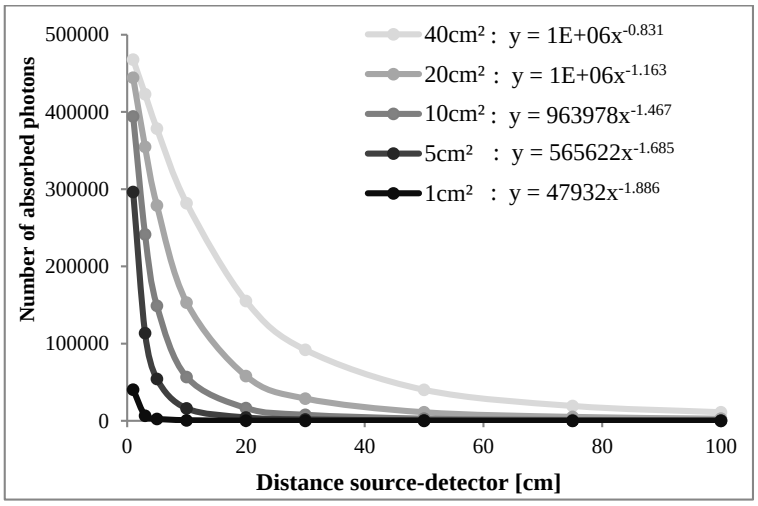

Figure 4.1. Analysis of the Inverse Square Law. Number of photons detected *vs* distance from the crystal to the source [cm]. Different crystal sizes [cm^2] tested. Simulation using 10^6 photons, emitted isotropically

When the source-detector distance increases the number of absorbed photons decreases exponentially. The error bars are not visible in the figure, since they are smaller compared with the thickness of the line, less than 1%.

Analysing the trend line equations (potential function in form a/x^b, where x is the source-detector distance), one notices that only the detectors with small sizes are in agreement with the inverse square law. This is because the inverse square law is only valid when the source to detector distance is large in comparison to detector size. A general rule of thumb states that the distance to a radiation source should be greater than five times the crystal size. For that reason, the smaller crystal size, $1cm^2$, was chosen to do a detailed analysis using distances higher than five times the crystal size. Those values were compared with the theoretical ones, given by the formula above ($A/4\pi r^2$) (Cherry *et al*., 2003). Table 4.1. gives the simulated and the theoretical values, in fraction, of the photons detected by the crystal.

Table 4.1. Simulated and analytical values of the fraction of photons reaching the detector by varying the source-detector distance. Simulation for $1cm^2$ crystal size and 1million photons emitted isotropically with 140keV kinetic energy (Theoretical Data from Cherry *et al*., 2003)

		PHOTONS DETECTED (by 10^6 emitted)	SIMULATED VALUES AND ERROR (±2σ)	ANALYTICAL VALUES	PERCENT ERROR [%]
DISTANCE SOURCE-DETECTOR [cm]	**5**	2582	0.0025820 ± 0.0001016	0.0031831	18.88
	10	677	0.0006770 ± 0.0000520	0.0007958	14.93
	20	187	0.0001870 ± 0.0000273	0.0001989	6.00
	30	74	0.0000740 ± 0.0000172	0.0000884	16.31
	50	26	0.0000260 ± 0.0000102	0.0000318	18.32
	75	11	0.0000110 ± 0.0000066	0.0000141	22.25
	100	10	0.0000100 ± 0.0000063	0.0000080	25.66

The simulated values give the fraction of photons detected by the crystal taking into account 10^6 photons emitted. For this reason, the uncertainty of the simulated values is also represented as a fraction of the total particles emitted, within two standard deviations (±2σ). Percent errors between the simulated and analytical values as a fraction of the analytical values (multiplied by 100) were calculated to determine how close or accurate to the analytical values, the simulated values really are. To an easier interpretation and verification of the inverse square law, the latest five values of the source-detector distances were plotted in figure 4.2. together with the theoretical values.

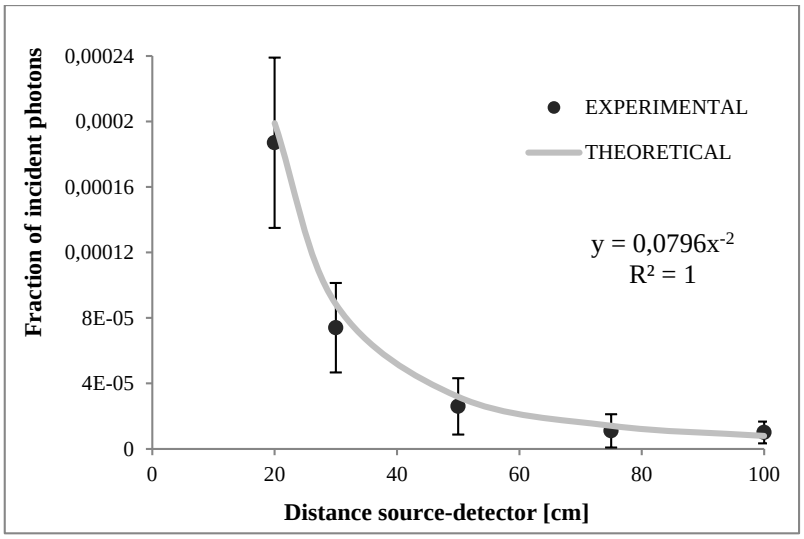

Figure 4.2. Comparison between simulated and theoretical of the fraction of photons reaching the crystal in order to verify the Inverse Square Law (Theoretical Data from Cherry *et al*., 2003)

The simulated values demonstrate a close match with the theoretical values, with the trend line equation following the inverse square law. Also, the coefficient of determination (R^2) is equal to 1, indicating the goodness of the fit in the regression analysis.

The values are consistent with the expected with approximately 95.45% confidence, within $\pm 2\sigma$. Therefore, there is a 95.45% chance that the confidence interval covers the true value. Since the theoretical values are inside the confidence interval for each simulated value is it possible to confirm that the isotropic photon beam propagating through the air or vacuum (in this model the vacuum is used) is governed by the inverse square law, proving thus the accuracy of the user-written EGSnrc code.

Table 4.2. gives the CPU times for each simulation undertaken in this section. The time does not include the store of parameters in the computer memory, such as energy absorbed or interaction position (X, Y, Z) in the detector.

Table 4.2. CPU times [seconds] spent in the simulations to test the inverse square law. Longest CPU times were obtained for small distances and shortest CPU times were acquired in major distances. Values obtained for 10^6 photons emitted isotropically with 140keV

	SOURCE-DETECTOR DISTANCE [cm]								
CRYSTAL SIZE [cm^2]	**1**	**3**	**5**	**10**	**20**	**30**	**50**	**75**	**100**
1	1.7	1.6	1.5	1.5	1.5	1.5	1.5	1.6	1.5
5	2.6	2.0	1.8	1.6	1.5	1.6	1.5	1.6	1.6
10	3.0	2.4	2.1	1.8	1.7	1.6	1.6	1.6	1.6
20	3.2	2.9	2.6	2.1	1.8	1.7	1.6	1.6	1.6
40	3.2	3.1	2.9	2.6	2.1	1.9	1.7	1.7	1.6

4.1.2. Analysis the Effect of the Crystal Thickness

Other simulation undertaken consisted in the analysis of the detector counting efficiency, by varying the crystal thickness and the energy of the photon beam. For this purpose, 10^6 photons were emitted along the z-axis, incident perpendicularly to the crystal (the director cosines were defined in scintillator detector model as U=0; V=0 and W=1), simulating a narrow beam. All the simulations were performed at 10cm away from the crystal (source-detector distance) and for a crystal size of $40cm^2$ (surface area). A range of photon energies were run individually for several crystal thicknesses. The energies chosen were: 50, 100, 250, 500, 1000, 1500, 2000, 2250 and 2500keV. The crystal thicknesses chosen were: 2, 5, 7.5, 10, 15, 25, 30 and 50mm.

In order to evaluate the intrinsic efficiency of the detector, the number of absorbed photons by the detector was stored, for every crystal thickness mentioned above and varying the kinetic energy of the photon beam. The simulated data were compared with the theoretical ones.

From the theory, the detector counting efficiency relates the amount of radiation emitted by a radioactive source to the amount of that radiation measured in the detector. It is calculated as a ratio between the detected photons by the total radiation emitted from the source. To facilitate a comparison between simulated and theoretical values the percentage of absorbed photons were calculated.

The narrow beam used in this simulation is a difficult condition to test in real life. For this reason, it was also possible modelled the true narrow beam attenuation. Since the absorbed photons are calculated by the simulation and the total emitted photons is known (10^6 photons emitted), it is possible to identify the transmitted photons, and hence the attenuation coefficients considered for the energies used in the simulation. Consequently, besides the analysis of the detector counting efficiency, also the attenuation coefficients were calculated and compared with the theoretical attenuation coefficients.

Figure 4.3. shows the detector intrinsic efficiency *vs*. photon energies (keV), for different thicknesses of the crystal. Each line in figure represents one crystal thickness.

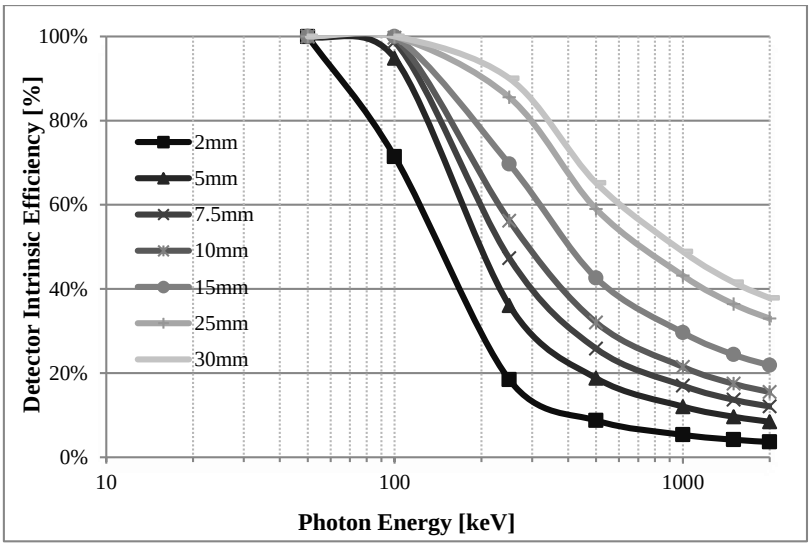

Figure 4.3. Intrinsic Efficiency of the NaI crystal. Simulation obtained for several crystal thicknesses [mm] by varying the energy of the incident photons [keV]. 10^6 photons emitted, normally incident on the crystal

The error bars are not visible in the figure (smallest than 1% for all the measurements). To an easier analysis and comparison with the theoretical values, the x-axis of the figure is represented in logarithm scale. Each line represents the percent absorption of a narrow beam of photons normally incident on the detector in accordance to its thickness. As expected, it is possible verify that the gamma camera is nearly 100% efficient for energies up to about 100keV, for all crystal thicknesses. After this energy, however, the detector shows a rather marked decrease in efficiency with increasing energy, which depends of the crystal thickness.

Analysing the figure 4.3., it is possible to infer that as the energy increases the intrinsic efficiency decreases, due to the decreasing in the attenuation coefficient when the energy increases which implies less attenuation of photons. Likewise, one verifies that the intrinsic efficiency increases with increasing crystal thickness, since the volume of the crystal rises allowing more interactions and absorbed photons inside the crystal. Consequently, the detector efficiency tends to zero for high-energy photons and thinner detectors. Those conditions are applied to all solid scintillation detectors.

Figure 4.4. gives the theoretical data of the detector efficiency for a NaI(Tl) crystal, collected from the Saint-Globain Crystals (SGC, 2008). Several crystal thicknesses are represented.

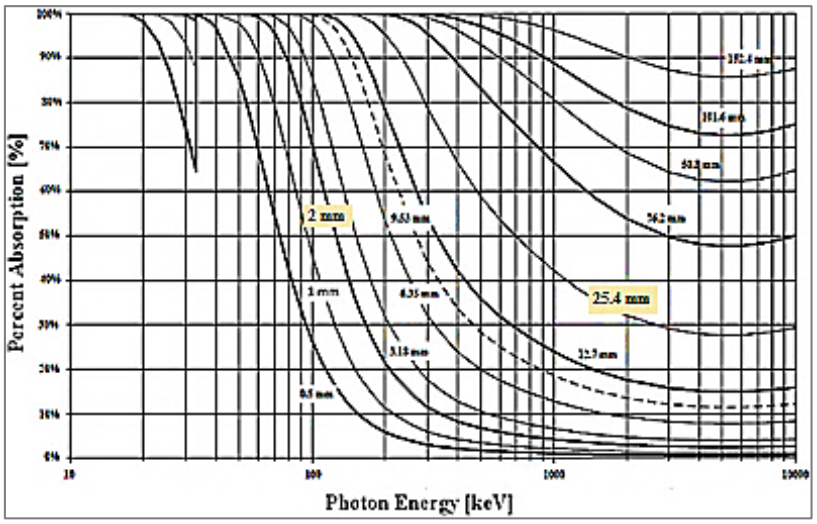

Figure 4.4. Absorption Efficiency of NaI(Tl) crystal. Theoretical data collected from SGC (2008). The calculation of these data was based on the exponential function given in equation 2.23, for certain values of thickness

Comparing the simulated data with the theoretical values by a qualitative analysis procedure, it is possible to realise that the curves are very similar. For example, comparing the curves of 2mm and 25mm thickness in both figures 4.3. and 4.4., one verifies that the curves follow the same shape with identical values, which demonstrate, once again, the truthfulness of the code. For photons with 100keV of energy, 2mm thickness attenuates almost 75% of the photons, whilst for higher thicknesses all the photons are attenuated. Low-energy photons, 100keV or less, are predominantly absorbed by photoelectric events in the detector. Above that energy, Compton scattering becomes more appreciable and above 2MeV the pair production become more relevant.

From the figures illustrated above, one confirms that the probability of the photon interactions depends of the energy of the photons, the crystal thickness and the material traversed. This probability, known as linear attenuation coefficient, μ, was calculated based on the simulated values obtained above. From equation 2.23., the natural log of fractional reduction of the intensity beam was taken to determine the linear attenuation coefficient for the energies simulated, *i.e.:*

$$-Ln\left(\frac{I}{I_O}\right) = \mu x \qquad \text{Eq. (4.1)}$$

Consequently, by plotting the *Ln(I/Io)* against the crystal thickness, *x*, the linear attenuation coefficient, μ, can be calculated as the gradient of the slope, given from figure 4.5.

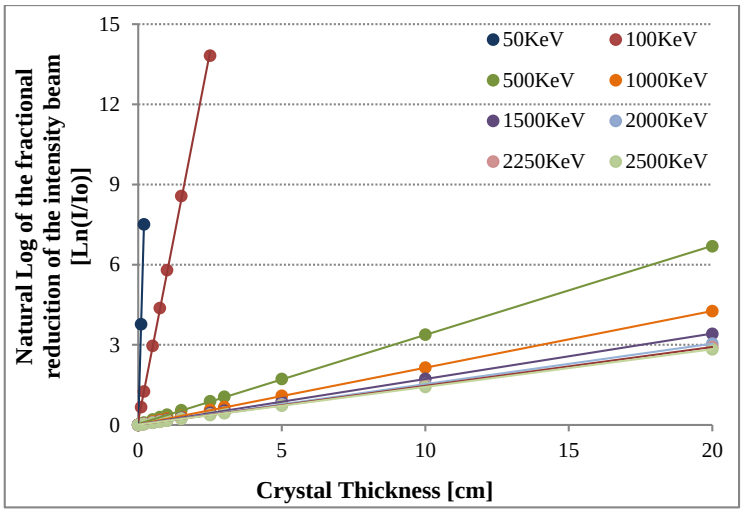

Figure 4.5. Natural Log of the fractional reduction of the intensity beam. Simulation obtained to find the linear attenuation coefficient

By linear regression analysis and additional regression statistics in Excel, it is possible to find the slope of the regression line, μ, and the standard error of the slope. The values of μ and the standard error ($\pm 1\sigma$) of the slope are shown in table 4.3., in addition with the analytical values of the μ given by XCOM from NIST (Berger et al., 1998).

Table 4.3. Simulated and analytical values of the linear attenuation coefficient (Theoretical Data from XCOM: Berger *et al*., 1998 in NIST)

ENERGY [keV]	TREND LINE	SIMULATED [cm^{-1}] AND ERROR ($\pm 1\sigma$)	ANALYTICAL [cm^{-1}]	PERCENT ERROR [%]
50	y = 37.528x + 0.0052	37.528 ± 0.0901	38.4302	2.35
100	y = 5.5235x + 0.1571	5.5235 ± 0.05343	6.1202	9.75
500	y = 0.3331x + 0.0402	0.3331 ± 0.00102	0.3484	4.38
1000	y = 0.2122x + 0.0229	0.2122 ± 0.00062	0.2156	1.59
1500	y = 0.1701x + 0.0177	0.1701 ± 0.00053	0.1723	1.30
2000	y = 0.1517x + 0.0132	0.1517 ± 0.00038	0.1522	0.32
2250	y = 0.1454x + 0.0127	0.1454 ± 0.00037	0.1479	1.67
2500	y = 0.1411x + 0.0117	0.1411 ± 0.00034	0.1436	1.72

In all trend lines the coefficient of determination (R^2) was equal to 0.999, presenting a very good linear relationship between the thickness and natural log of the fractional reduction of the intensity beam. Percent errors (difference between theoretical and simulated values as a fraction of the theoretical value, multiplied by 100) show a good accuracy between simulated and theoretical values. The percent errors are larger at low photon energies than at high energies. This smooth discrepancy might result from the slight difference between the material used in the simulation (just NaI) and the real material used in equipment (NaI(Tl)), being the difference much more marked at low photon energies. Theoretical and simulated attenuation coefficients are shown in figure 4.5. for an easier comparison.

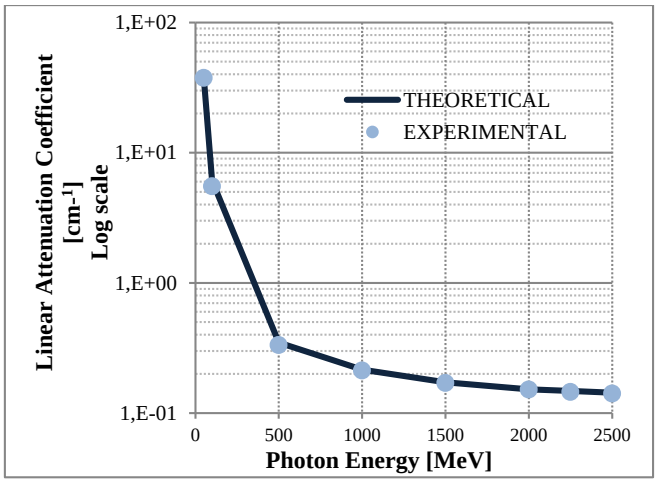

Figure 4.6. Simulated and analytical values of the linear attenuation coefficients. (Theoretical Data from XCOM: Berger *et al*., 1998 in NIST)

The y-axis of the figure 4.6. is represented in a logarithm scale to an easier analysis and comparison with the theoretical data. The error bars, uncertainty of the simulated values, are represented by ±1σ. However, they are not visible because they are smaller (<1%) in comparison with the size of the dots. Since one might expect that roughly 2/3 (68.2%) of one's simulations will fall within this range, one may infer that the simulated values are consistent with the expected values. Consequently, the linear attenuation coefficients for primary photons, obtained from the simulation, agree well with the published data providing an additional validation of the EGS code model.

It is important to refer that in radionuclide therapy, the number of incident and transmitted photons is activity-dependent. However, the product μx is an important parameter relating to the anatomy of the patient along a given ray photon. Therefore, patients with larger anatomy attenuate more photons in comparison with a thin anatomy.

Table 4.4. gives the CPU times for each simulation undertaken in this section. The time includes the store, in the computer memory, of the energy absorbed and interaction positions (X, Y, Z), for each photon event.

Table 4.4. CPU times [seconds] spent in the simulations to test the effect of the crystal thickness. Values obtained for 10^6 photons emitted perpendicularly to the crystal

	CRYSTAL THICKNESS [mm]							
ENERGY [keV]	2	5	7.5	10	15	25	30	50
50	51.4	54.6	53.5	52.3	52.5	52.5	52.4	53.9
100	49.6	56.9	57.0	55.5	57.4	57.0	57.3	56.1
250	32.3	39.7	46.0	49.0	58.3	65.5	69.5	75.1
500	26.3	31.2	35.7	39.2	47.0	62.1	66.8	83.8
1000	22.0	25.8	28.9	32.1	38.1	49.2	55.4	76.5
1500	20.5	23.1	26.8	29.0	34.4	44.5	50.0	68.1
2000	19.5	21.5	23.7	27.1	31.1	41.5	46.1	64.7
2250	19.2	21.3	23.5	25.8	31.2	40.3	45.3	64.7
2500	18.6	20.9	23.2	25.8	30.5	40.0	45.5	64.7

4.1.3. Analysis the Effect of the Glass behind the Crystal

The analysis of backscattering photons was also tested. In this simulation the point source of photons was placed on the surface of the glass and 10^6 photons were emitted. Photons were emitted both in a straight direction, along the z-axis and entering perpendicularly into the glass (U=0; V=0 and W=1) and also isotropically, in order to see the spectrum differences.

Since the amount of energy transferred to the scattered photon varies with photon energy, three different photons energies were tested, being these: 100, 200 and 500keV. Also, for every photon energy, different glass thicknesses were simulated. The glass thicknesses tested were: 1, 5, 10, 20 and 50mm. The crystal was unchanged, with measures of 1cm thickness and 40cm2 size. The aim was to detect the backscattering photons by varying the thickness of the glass and the energy of the photons emitted.

The subroutine HOWFAR was defined to discard all the photons outside the crystal and count only the ones that interact with the crystal. Therefore, since the point source is placed at the beginning of the surface glass, in front of the crystal, it is to expect that, according to the Klein-Nishina formulation, only the photons scattered with angles higher than 90º are detected and added to the count.

In a first analysis, the effect of the glass thickness was investigated in order to analyse the backscattered photons, by varying the energy of the photons and the thickness of the glass.

The first figure on the left corresponds to the photons emitted along the z-axis perpendicularly to the glass whereas the figure on the right is related with the photons emitted isotropically.

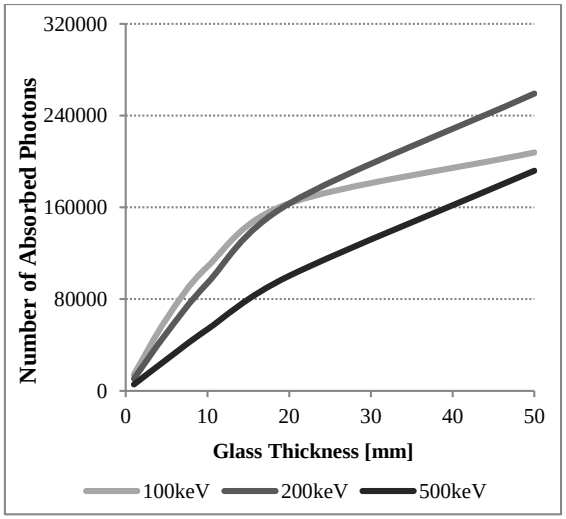

Figure 4.7. Effect of the glass thickness to analyse the photons' backscatter. Photons emitted along the z-axis, perpendicularly to the crystal

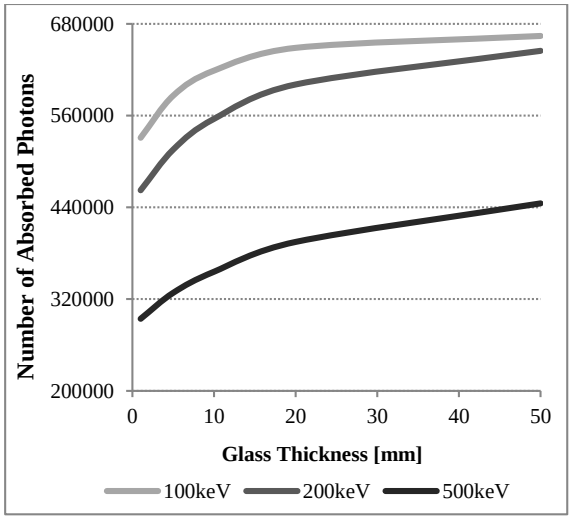

Figure 4.8. Effect of the glass to analyse the photons' backscatter. Photons are emitted isotropically

As expected, when the photons are emitted perpendicularly to the glass and the glass thickness is small, an insignificant amount of backscattered photons are detected by the crystal. As the thickness increases, the photons encounter a higher volume in their path. Consequently, increase the number of interactions and the likelihood of the photons being backscattered. Thus, when the glass thickness increases, more photons are backscattered and hence more photons are detected and counted by the crystal.

In figure 4.7. the idea is the same with the slight difference that the photons are emitted isotropically. In this case the monoenergetic photons are emitted equally in all directions. Therefore, the number of photons detected by the crystal is much higher in comparison with the photons emitted normally to the glass even when the glass thickness is insignificant. In broad terms, all the photons emitted in the semicircle inside the crystal are counted, as well as the photons emitted through the glass and scattered by it, in an angle higher than 90º.

It is possible to note in both figures that low energies cause more backscattering photons and high energies less backscattering photons. This is due to the fact of low energies are easily attenuate and have a highest likelihood of interact, contrary to the high-energy photons that might pass through the material without interact, having for that a high value of attenuation coefficient.

The following figure shows the number of absorbed photons by the crystal vs. their energy deposited, plotted for 1, 10 and 50mm of glass thickness. All the graphics on the left are related with the photons emitted along the z-axis, normally to the glass and the graphics on the right side correspond to the photons emitted isotropically. The first line of the graphics represent simulation for photons with 100keV, followed 200keV and the last line represent photons with 500keV.

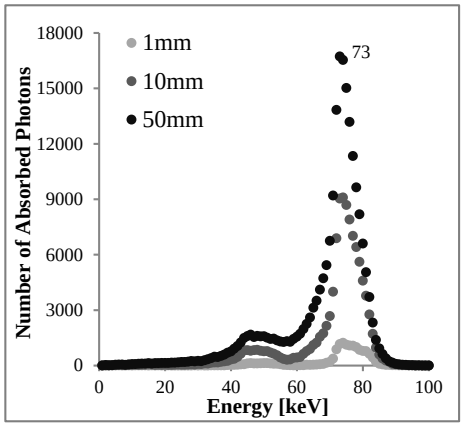

A

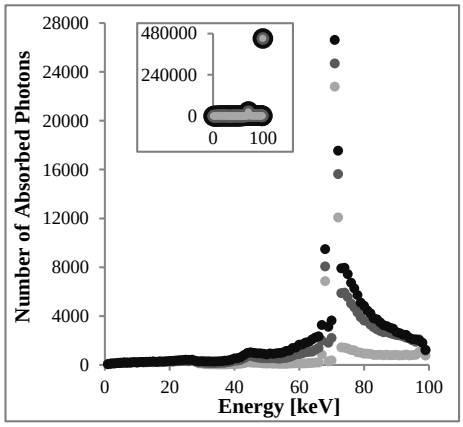

A1

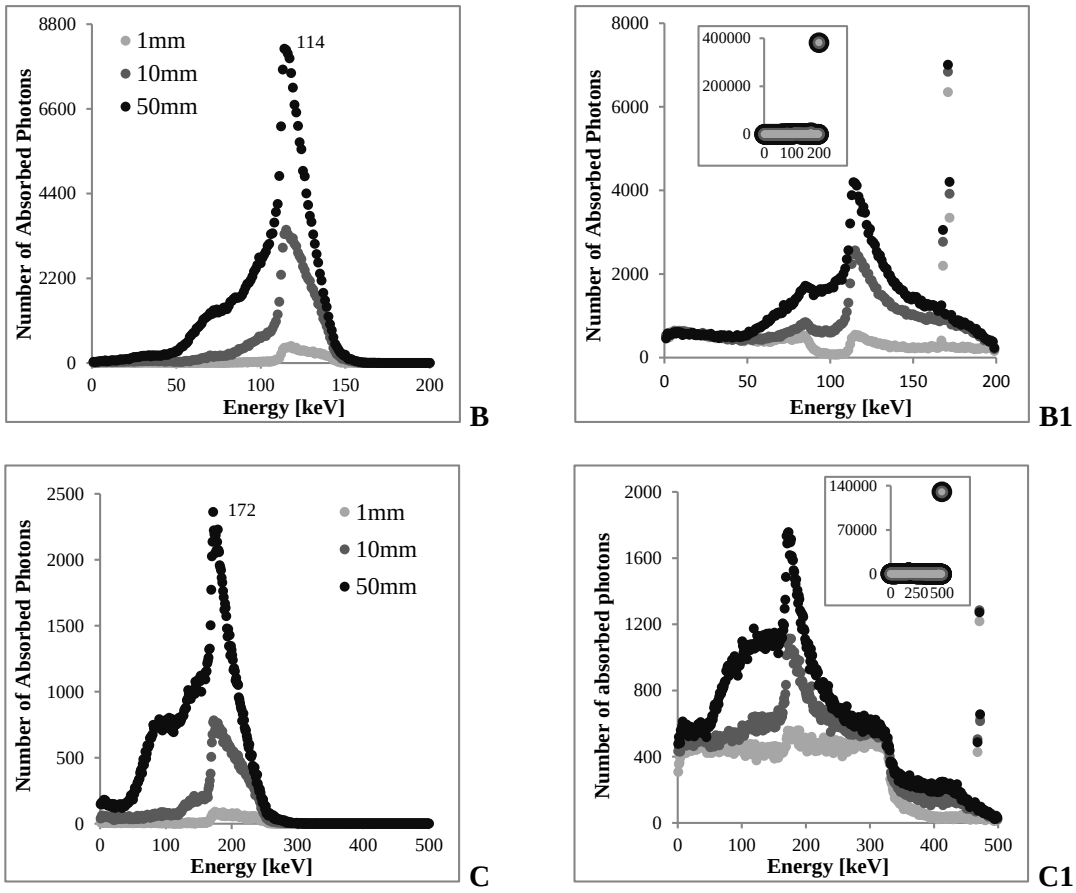

Figure 4.9. Analysis of backscattering photons. Spectrum A and A1 acquired for 100keV photons energies; spectrum B and B1 acquired for 200keV photons energies and spectrum C and C1 acquired for 500keV photons energies. Spectra A, B and C developed for photons emitted perpendicularly to the glass, forming the backscatter peak, and A1, B1 and C1 created for photons emitted isotropically

From the theory, as explained in section 2.1.3., backscatter peak is caused by the detection of photons that have been scattered toward the crystal after undergoing a 180º scattering outside the detector. Usually, the majority of scatter events occur from the photons which have undergone Compton interaction. In this case the electron receives the maximum energy and the scattered photon the minimum. The energy of the backscatter peak is the energy of the scattered photon after a 180º scattering. This energy varies according to the energy of the photons emitted, *i.e.*, high-energy photons, high-energy backscatter peak. For that reason three different energies were simulated. The backscattering energy can be calculated applying the Klein-Nishina formula, given in equation 2.17., defining the angle θ equal to 180°. From this equation, theoretical values of the energy of the backscatter peak are given in following table, together with the values of the backscatter peak energy obtained in the simulations.

Table 4.5. Analytical and simulated values of the energy of the scatter photons, for a point source of photons with 100, 200 and 500keV of energy. Klein-Nishina formula applied with θ=180°

ENERGY [KEV]	ANALYTICAL VALUES [keV]	SIMULATED VALUES [keV] AND ERROR (±1σ)	PERCENT ERROR [%]
100	71.87	73 ± 8.54	1.57
200	112.18	114 ± 10.68	1.62
500	169.09	172 ± 13.12	1.72

Analysing, in broad terms, the theoretical and the simulated values, one verifies that there is a close correspondence between those values, with percent errors in all of them less than 2%.

Such as verified in figures 4.6 and 4.7 and for the same reasons explained, in all graphics presented above it is possible verify that the greater glass thickness causes more absorption of photons, contrary to the small glass thickness. According to the figure, it is also notable that as the energy increases (comparison between lines) the backscatter peak is shifting the right. The centre of peak undergoes a translocation to the right, which mean that the energy of the backscatter peak increases as the photon energy increases, which is in accordance with the theory. Also, when the energy increases the number of photons absorbed decreases, for the same reason explain above. For example, for 50mm of glass thickness, a point source of photons emitted in straight direction with 100keV generates twice and seven times more scatter photons in comparison with a point source of photons with 200keV and 500keV, respectively.

The figure shows, for all the materials, a broad backscatter peak because backscattered photons may enter the crystal from angles other than 180º.

In the spectra A, B and C, which were modelled with photons emitted perpendicularly to the glass, two peaks are visible: the backscatter peak and a peak that appears on the left side of the backscatter peak. This corresponds to the iodine escape peak, resultant from the photoelectric event between the scatter photons and the iodine atoms. The iodine escape peak occurs at an energy approximately equal to the photon energy subtracted ≈30keV, corresponding to the biding K-shell energy of the iodine. From the analysis of the figure, one confirms that the energy of the iodine peak, in each figure, is in accordance with the theory.

In isotropic emissions, represented by the spectra A1, B1 and C1 there are four different peaks. Since in an isotropic emission the photons emitted inside the semicircle of the crystal are counted, a photopeak is created. The photopeak (represented by a dot on the small figure in the corner) results from the total absorption of the major photons from the radionuclide. The other three peaks corresponds to the backscatter peak, and a two iodine escape peaks, one caused by

the interaction between the scatter photons and iodine and other between the primary photons emitted from the source and iodine.

All the events represented in the figure are in agreement to the expected and therefore with the theory, which proves once more the truth and veracity of the code.

Table 4.6. and 4.7. gives the CPU times for each simulation undertaken in this section. The time includes the score of the parameters, energy absorbed, interaction position (X, Y, Z), and direction cosines (U,V,W) for each photon interaction, in the computer memory.

Table 4.6. CPU times [seconds] spent in the simulations to test the effect of the glass thickness. Values obtained for 10^6 photons emitted along the z-axis, perpendicularly to the glass

	GLASS THICKNESS [mm]				
ENERGY [keV]	**1**	**5**	**10**	**20**	**50**
100	23.4	34.4	50.1	78.2	134.4
200	21.9	31.6	44.9	71.5	150.2
500	20.7	28.1	37.6	60.1	134.9

Table 4.7. CPU times [seconds] spent in the simulations to test the effect of the glass thickness. Values obtained for 10^6 photons emitted isotropically

	GLASS THICKNESS [mm]				
ENERGY [keV]	**1**	**5**	**10**	**20**	**50**
100	65.8	79.9	92.1	110.0	128.2
200	62.2	79.5	90.9	112.3	145.3
500	52.8	62.9	78.9	99.1	145.2

4.2. Bremsstrahlung Simulations

The conditions simulated before were according to the theoretical and published data, proving the accuracy of the code. After this confirmation of the veracity of the code, different simulations in different types of physical conditions were undertaken to test the bremsstrahlung comportment.

The source model was the EGSnrc code used for all the simulations tested in this section, with the geometry and components described in section 3.1.3. The parameters of the sphere defined in this model were changed according to the physical conditions to test. A point source of pure beta emitters, placed in the middle of the sphere, also change its kinetic energy according to the simulation. It is important to refer, once again, that in EGSnrc it is necessary add the rest mass energy of the electrons into the energy parameter. Therefore, if 100keV of kinetic energy must be chosen, 611keV have to be defined in the energy parameter.

In order to understand in what way the bremsstrahlung photons are produced in different media, using different energies of the beta particles, four different biological materials were chosen to do the simulations. These are cortical bone, inflated lung, soft tissue and adipose tissue. All the media were previously defined in PEGS4.

It is also important to refer that, in order to know with accuracy the effective atomic number of each material used in the simulations some calculations were made.

According to Murty (1965) a heterogeneous material, compose by different elements in varying proportions can be defined as a "fictitious element" having an effective atomic number (Z_{eff}). Mayneord, quoted by Khan (2003), developed the following expression to calculate the $Z_{eff,}$ which was used in the study.

$$Z_{eff} = \sqrt[2.94]{\sum a_i . {Z_i}^{2.94}} \qquad \text{(Eq. 4.1)}$$

Where a_i is the relative electron fraction of the element i and Z_i the atomic number of each element i that compose the material. The fractional contribution of each element to the total number of electrons, a_i, is given by:

$$a_i = \frac{N_A . P_i . Z_i}{n_o . A_i} \qquad \text{(Eq. 4.2)}$$

Where N_A is the Avogadro's number, P_i is the percentage weight of element i, A_i the atomic weight and n_o is the total number of electrons/g of the material, which is given by:

$$n_o = N_A . \sum \frac{P_i . Z_i}{. A_i} \qquad \text{(Eq. 3)}$$

Substituting n_o in Eq. 4.2, the effective atomic number of any material might be achieved (Khan, 2003). Z_{eff} was founded in this investigation with base in the values given by PEGS4 data files for each compound. After the creation of the PEGS4 file for individual material, it provides all the elements that compose the medium, the respect fraction weight, and the atomic weight. The effective atomic number calculated for each biological material is given in table 4.8.

Table 4.8. Effective atomic number of some biological compounds

COMPOUND	EFFECTIVE ATOMIC NUMBER (Z_{eff})
Cortical Bone	12.970
Lung Tissue	7.489
Soft Tissue	7.223
Adipose Tissue	6.231

Bremsstrahlung simulations and the corresponding method and discussion are explained below. The data recorded by the simulation were processed Excel (Microsoft Corp., Redmond, USA).

4.2.1. Analysis of the Bremsstrahlung Production Efficiency

The first simulation to assess bremsstrahlung photons consisted in to test its efficiency of production in different sphere thicknesses. The aim was to see what is the maximum sphere thickness required from which the number of bremsstrahlung photons become constant.

This simulation was undertaken for different beta particles kinetic energies, namely for 0.5, 1, 1.5, 2.23 and 3MeV. The point source of beta particles was placed in the middles of the sphere, and various sphere radii were simulated. These radii ranged from 0.01 to 10mm, according to the medium. 10^6 beta particles were emitted isotropically.

From the theory the efficiency of bremsstrahlung production is related with the penetration of the beta particles in the media, which in turn depends of the beta particles energy and the atomic number of the material penetrated. It is to expect that, as the energy and the atomic number of the media increase, the bremsstrahlung production efficiency also increases.

The figure below shows the results obtained from the simulation. The outcome is the bremsstrahlung production efficiency by varying the sphere thickness and the beta particles kinetic energy, in the four different materials.

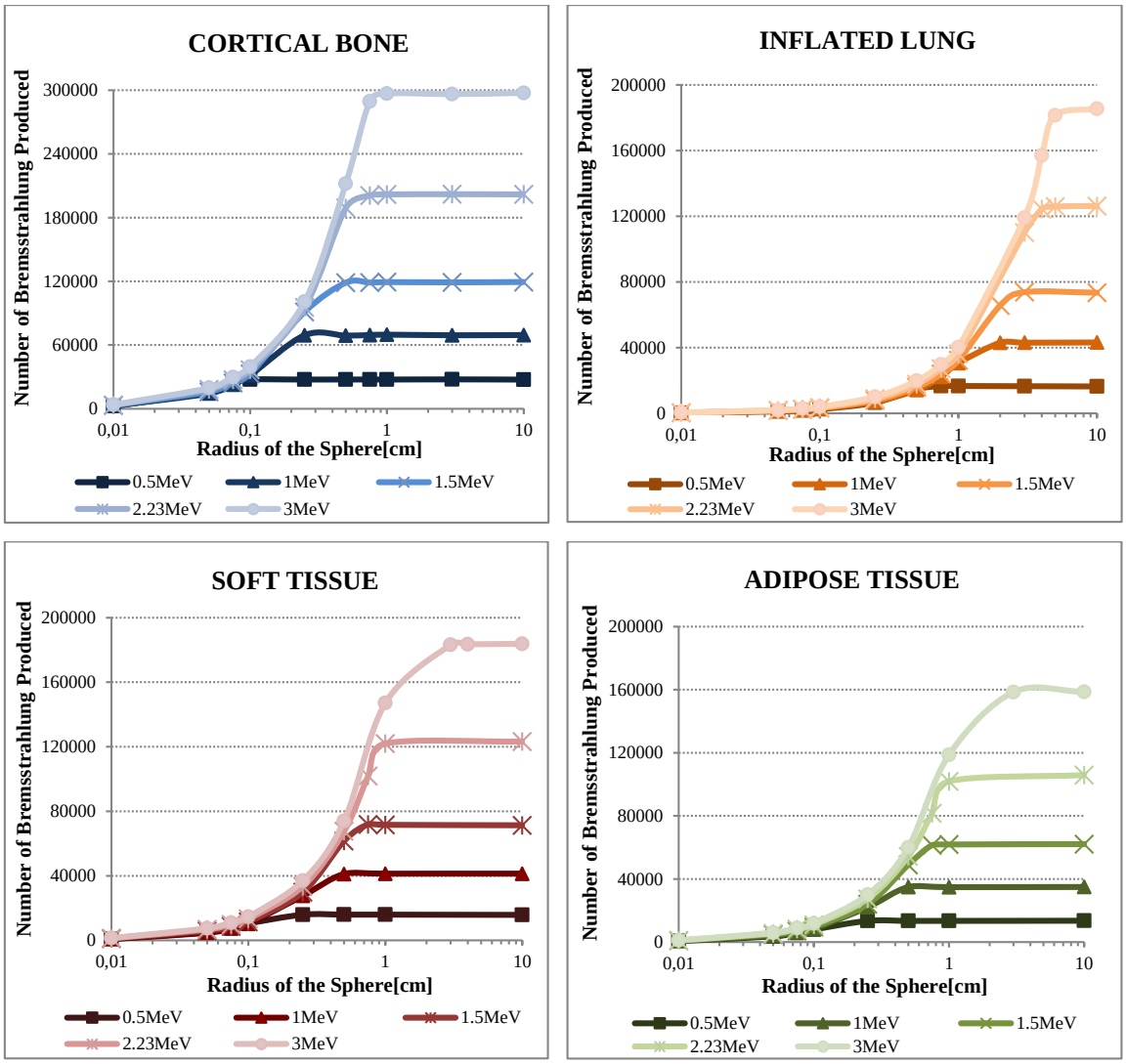

Figure 4.10. Bremsstrahlung production efficiency by varying the radius of the sphere and the beta particles energy, in the four different materials. 10^6 beta particles emitted from a point source in the middle of the sphere

From the analysis of the figure, one notices that some characteristics are common for all the biological materials. It is possible to verify that the number of the bremsstrahlung produced increases with increasing of the kinetic energy of the beta particles and also with increasing of the radius of the sphere, which is in accordance with the physics theory.

In all the materials, when the sphere thickness is insignificant almost no bremsstrahlung photons are produced. As the radius of the sphere increases, the efficiency of the photons production also increases, creating a steep line. However, from a certain radius this number becomes constant, and the line becomes flat. One confirms that the radius of the sphere, from which this flat line starts to appear, is slightly higher for high-energy beta particles. Those mechanisms are related with the range of the electrons, since they continue to produce photons until come to

rest. The electrons range is in turn related with electrons kinetic energy. Thus, in comparison with low-energy beta particles, high-energy beta particles create a greater range, consequently there is a greater bremsstrahlung efficiency and therefore it is necessary a greater radius of the sphere until the efficiency becomes constant.

Beyond the increase of the bremsstrahlung photons with the electrons kinetic energy, they also increase with the effective atomic number, Z_{eff}, of the absorber. Comparing the materials between each other, such as it was expected, the cortical bone is the material that produces more bremsstrahlung photons, due to its high value of Z_{eff} (12.97). On the other hand, adipose tissue has the smallest value of Z_{eff} (6.231) and consequently the lowest number of bremsstrahlung produced. Soft tissue and the lung have almost the same efficiency of bremsstrahlung production since both have Z_{eff} very similar (7.223 and 7.489, respectively). For example, considering the electron kinetic energy equal to 1.5MeV, the cortical bone produced 38% more bremsstrahlung photons than the lung, and 39% and 48% more bremsstrahlung photons than the soft tissue and adipose tissue, respectively. However, the lung requires the higher sphere thickness to achieve a constant production efficiency, in comparison with all the others materials. This is because inflated or expanded lung is considered in these measurements and therefore, the electrons may travel a large distance until losing all their energy.

Values in the table 4.9. show, for all the biological materials, the maximum number of the bremsstrahlung produced for a certain sphere thickness, taking into account the different initial beta particles kinetic energy.

Table 4.9. Maximum radius of the sphere, from which the number of bremsstrahlung produced inside it become constant. Bremsstrahlung photons produced when 10^6 beta particles are emitted isotropically, for different beta particle kinetic energy and in four different biological materials

		KINETIC ENERGY OF THE BETA PARTICLES [keV]					
		250	**500**	**1000**	**1500**	**2230**	**3000**
CORTICAL BONE	Sphere Radius [cm]	**0.05**	**0.1**	**0.25**	**0.5**	**0.75**	**1**
	Num. of Brem. Produced and Error (±1σ)	10849±104	27539±166	69202±263	118665±345	200740±448	296790±545
INFLATED LUNG	Sphere Radius [cm]	**0.25**	**0.75**	**2**	**3**	**4**	**5**
	Num. of Brem. Produced and Error (±1σ)	6476±81	16573±129	42939±207	73771±272	124330±353	181445±426
SOFT TISSUE	Sphere Radius [cm]	**0.075**	**0.25**	**0.5**	**0.75**	**1**	**3**
	Num. of Brem. Produced and Error (±1σ)	6321±80	15969±126	41104±203	71883±268	121926±349	183218±428
ADIPOSE TISSUE	Sphere Radius [cm]	**0.075**	**0.25**	**0.5**	**0.75**	**1**	**3**
	Num. of Brem. Produced and Error (±1σ)	5190±72	13465±116	34922±187	61372±248	101878±319	158483±398

The uncertainties of the counts are given within ±1σ. Therefore, there is a 68.2% chance that the confidence interval covers the true value.

Figure 4.9. and the table 4.8., show that the maximum value of the sphere radius, for which the efficiency of the bremsstrahlung production stagnates, is dependent of the material composition and the initial kinetic energy of the beta particles.

From table 4.8., one verifies that, for each material, when the initial kinetic energy increases, the radius of the sphere also increases, as well as the efficiency of bremsstrahlung production. This fact is due to the greater penetration of the electrons inside the sphere. On the other hand, denser materials produce a shorter electrons range. Therefore, for the same initial kinetic energy, denser materials have the shorter radius of the sphere and the highest number of bremsstrahlung produced. At a dosimetric level, it is vital to know the maximum electrons range, since it is along this path that occurs the dose absorption in the tissues. As explained in section 2.1.4., figure 4.9. confirms that the efficiency of photons production increases with the atomic number of the material and with the initial kinetic energy of the electrons.

Table 4.10. gives the CPU times. The values presented in the table correspond only to the simulations whose values are presented in the table above, table 4.8., *i.e.*, the values in which the bremsstrahlung production is maximum. The time includes the score of the parameters – produced and escaped bremsstrahlung spectra (number of bremsstrahlung photons produced/escaped *vs.* respective energies), in the computer memory.

Table 4.10. CPU times [seconds] obtained for the maximum radius of the sphere from which the number of bremsstrahlung produced become constant

		KINETIC ENERGY OF THE BETA PARTICLES [keV]					
		250	**500**	**1000**	**1500**	**2230**	**3000**
CORTICAL BONE	Sphere Radius [cm]	**0.05**	**0.1**	**0.25**	**0.5**	**0.75**	**1**
	CPU time [sec]	134.0	203.1	328.0	448.2	629.5	782.6
INFLATED LUNG	Sphere Radius [cm]	**0.25**	**0.75**	**2**	**3**	**4**	**5**
	CPU time [sec]	90.5	139.1	223.3	302.8	421.5	510.5
SOFT TISSUE	Sphere Radius [cm]	**0.075**	**0.25**	**0.5**	**0.75**	**1**	**3**
	CPU time [sec]	90.8	137.8	217.4	178.6	309.9	410.4
ADIPOSE TISSUE	Sphere Radius [cm]	**0.075**	**0.25**	**0.5**	**0.75**	**1**	**3**
	CPU time [sec]	66.7	97.1	160.7	222.8	282.2	405.6

4.2.2. Analysis of the Bremsstrahlung Yield (%)

The radiation or bremsstrahlung yield (Y) was also investigated. In order to know the fraction of kinetic energy of primary electrons converted into bremsstrahlung photons, 10^6 beta particles were emitted isotropically inside a sphere with 1cm of radius. For all the biological materials considered in these study and such as the previously simulations, different initial kinetic energy were tested, namely, 250, 500, 1000, 1500, 2230 and 300keV.

To identify the bremsstrahlung yield the number of bremsstrahlung produced and the respective energy were scored. Then, the total of energy produced by bremsstrahlung was calculated, for each energy tested and for individually materials. Such as explained in section 2.1.4., the bremsstrahlung yield is defined as the fraction of kinetic energy of primary electrons converted into bremsstrahlung photons, through the slowing down process of the particle in the absorber

Therefore, to calculate it, the total bremsstrahlung energy was then divided by the total of kinetic energy emitted from the source (the kinetic energy tested multiply by the 10^6 particles emitted). Instead the fraction, the analysis of the percent of bremsstrahlung produced was preferable. Figure 4.11. illustrates the result of this simulation for the different materials, i.e., the percentage of the total energy emitted from the source converted into bremsstrahlung.

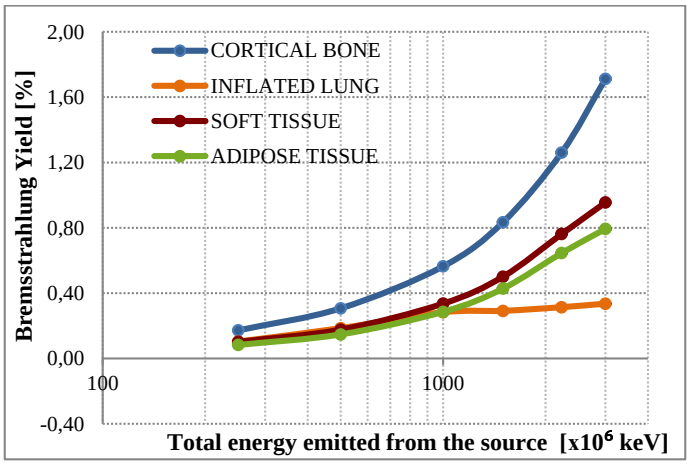

Figure 4.11. Bremsstrahlung yield, in percentage. Values obtained for four biological materials, when 10^6 beta particles are emitted isotropically inside a sphere of 1cm of radius

The graph presents a logarithm scale, in the x-axis, to an easier analysis. The uncertainty of the bremsstrahlung yield and hence, the error bars, are represented as percentage (%), with $\pm 1\sigma$. However, the values are smallest than 1% and the error bars are not visible.

From the analysis of the figure and for all the biological materials, it possible to verify that, as it was expected in accordance with the theory, the radiation yield increases with the electron kinetic energy. At very high energies, the dominance of radiative over collisional energy losses gives rise to electron-photon cascade showers. This means that high-energy beta particles emit high-energy photons, which in turn in turn, produce Compton electrons and electron-positron pairs. Those, in turn produce additional bremsstrahlung photons, and so forth. The

bremsstrahlung yield also increases with the atomic number, *Z* of the material, since cortical presents the highest value of *Z*, followed by soft tissue and adipose tissue. The bremsstrahlung yield in the inflated lung is small in comparison with the other materials because in these simulations the sphere radius used is 1cm. By the analysis of the table 4.8., one verifies that, from 1MeV, the number of bremsstrahlung produced in inflated lung might only increase if the sphere radius also increases. For that reason the value of bremsstrahlung yield almost stagnates from 1MeV onwards.

Since for light charged particles the radiation yield is determined from stopping power data, a comparison between the theoretical and the simulated values are possible. Throughout the ESTAR program (Berger *et al*., 2011), available in NIST, the radiation yield was calculated for the diverse materials and energies investigated. Figure 4.11. shows the comparison between simulated and analytical data.

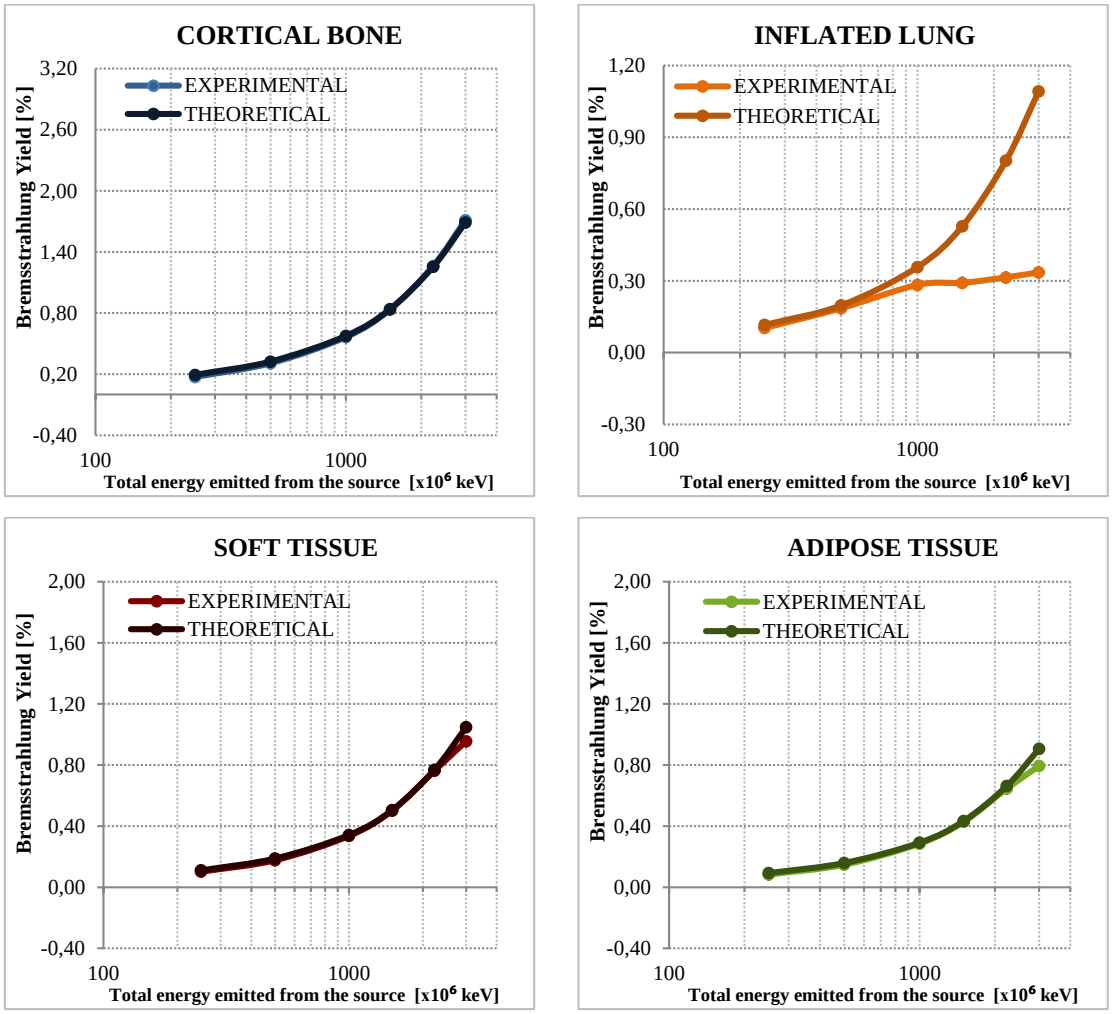

Figure 4.12. Analytical and simulated values of bremsstrahlung yield, in percentage. Values presented for different biological material. 10^6 beta particles emitted from a sphere with 1cm radius (Theoretical Data from ESTAR database: Berger *et al*., 2011in NIST)

Once again the errors are given as percentage uncertainty (%) with ±1σ. The values simulated agreed well with the analytical values. However, there are slight differences at high-energies because a fixed sphere radius of 1cm is used. At high-energies, the range of the electrons is higher and consequently the radius of sphere should be higher in order to permits the increase of bremsstrahlung photons production. Using 1cm radius this production is restricted to that thickness. Furthermore, the inflated lung presents differences between the values. Beyond the fact explained previously, also this may be due to the values given by the ESTAR do not take into account the inflated lung but the radiation yield in lung tissue.

Table 4.11. gives the simulated and analytical values, as well as the percentage uncertainty and the percent error.

Table 4.11. Simulated and analytica values of the bremsstrahlung radiation yield (Theoretical Data from ESTAR database: Berger *et al*., 2011in NIST)

		TOTAL KINETIC ENERGY EMITTED FROM THE SOURCE [x10^6 keV]					
		250	**500**	**1000**	**1500**	**2230**	**3000**
CORTICAL BONE	ANALYTICAL VALUES [%]	0.1931	0.3236	0.5755	0.8382	1.2550	1.6890
	SIMULATED VALUES±ERROR [%]	0.1725±0.0022	0.3073±0.0028	0.5641±0.0036	0.8346±0.0043	1.2606±0.0053	1.7126±0.0062
	PERCENT ERROR [%]	10.6844	5.0476	1.9764	0.4344	0.4485	1.3985
INFLATED LUNG	ANALYTICAL VALUES [%]	0.1159	0.1973	0.3576	0.5279	0.8026	1.0920
	SIMULATED VALUES±ERROR [%]	0.1031±0.0017	0.1853±0.0022	0.2829±0.0027	0.2915±0.0029	0.3140±0.0031	0.3355±0.0032
	PERCENT ERROR [%]	11.0109	6.0746	20.8900	44.7801	60.8789	69.2768
SOFT TISSUE	ANALYTICAL VALUES [%]	0.1102	0.1880	0.3416	0.5051	0.7690	1.0470
	SIMULATED VALUES±ERROR [%]	0.1019±0.0017	0.1769±0.0021	0.3360±0.0028	0.5014±0.0034	0.7622±0.0042	0.9554±0.0048
	PERCENT ERROR [%]	7.5296	5.9002	1.6314	0.7402	0.8783	8.7500
ADIPOSE TISSUE	ANALYTICAL VALUES [%]	0.0924	0.1588	0.2915	0.4334	0.6630	0.9055
	SIMULATED VALUES±ERROR [%]	0.0830±0.0015	0.1476±0.0019	0.2856±0.0026	0.4282±0.0046	0.6456±0.0038	0.7935±0.0044
	PERCENT ERROR [%]	10.2345	7.0723	2.0187	1.1935	2.6287	12.3656

In most of the measurements the percent error is less than 10% which show a good accuracy between theoretical and simulated values. The simulated values are consistent with the published data, with approximately 68.2% confidence, within ±1σ. This provides an additional validation of the Monte Carlo model and of the method for calculating Y.

Analysing the table, one confirms that, except the cortical bone at high-energies, the percentage of the total energy emitted from a monoenergetic point source converted into bremsstrahlung is less than 1%, when 10^6 beta particles are emitted. In practical cases, for example patients with hepatic tumours, who may be treated with ^{90}Y resin or glass microspheres, receive more than 3GBq of activity. These represent ≈10^{15} radiative atoms, which mean that less than 3% of the

total energy emitted inside the patient will be converted into bremsstrahlung, and consequently will be the only radiation available to be imaged. These values demonstrated the small efficiency of bremsstrahlung photons production, which difficult the pure beta emitters.

Table 4.12. gives the CPU times for each simulation undertaken in this section. The time includes the score of the parameters – produced and escaped bremsstrahlung spectra (number of bremsstrahlung photons produced/escaped *vs.* respective energies) and the photons escaped position (X, Y, Z), in the computer memory.

Table 4.12. CPU times [seconds] spent in the simulations to analyse the bremsstrahlung yield. Values obtained for 10^6 beta particles emitted isotropically inside a sphere with 1cm radius

		TOTAL KINETIC ENERGY EMITTED FROM THE SOURCE [x10^6 keV]					
		250	**500**	**1000**	**1500**	**2230**	**3000**
CORTICAL BONE	CPU time [sec]	94.5	141.7	229.0	314.7	448.4	575.1
INFLATED LUNG	CPU time [sec]	63.6	97.1	92.0	71.7	66.9	68.5
SOFT TISSUE	CPU time [sec]	64.3	96.8	159.4	222.1	310.1	279.6
ADIPOSE TISSUE	CPU time [sec]	63.8	97.9	159.9	221.8	284.6	249.8

4.2.3. Analysis of the Bremsstrahlung Spectrum Shapes

Other simulation undertaken consisted in to analyse the shapes of the bremsstrahlung spectrum produced in each material. For this purpose 10^6 beta particles were emitted isotropically, inside a sphere with 1cm of radius. The beta particles were emitted with 500keV of kinetic energy. The spectrum of bremsstrahlung was studied for all the materials. Therefore, the number of bremsstrahlung produced inside the sphere *vs*. its respective energy of production was scored.

To compare the spectra shapes between the four different biological materials, normalization of each spectrum were required. The y-axis data – number of bremsstrahlung, was normalized as a function of the total of bremsstrahlung photons produced. Normalizing the data is useful to scale heterogeneous sets of data, so that might be compared relevantly. This process, followed for eliminating redundant data, establishes a meaningful relationship among the spectrum in order to maintain integrity of data.

Figure 4.12. shows the bremsstrahlung spectra obtained in the simulation, for cortical bone, inflated lung, soft tissue and adipose tissue, when 10^6 monoenergetic beta particles are emitted

isotropically with 500keV of energy. The entire spectrum is normalized as a function of the total number of bremsstrahlung produced.

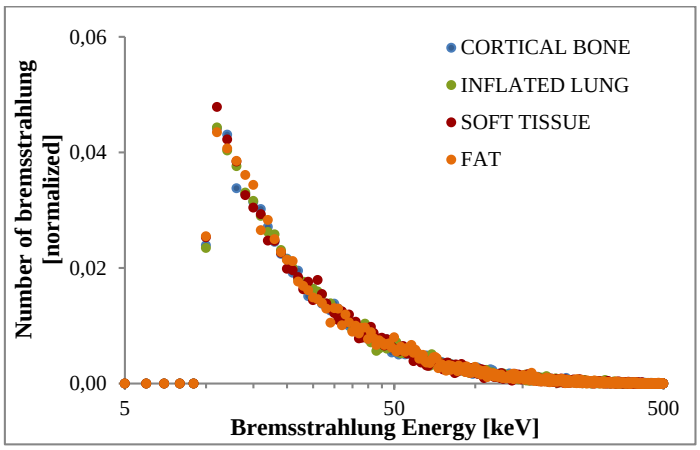

Figure 4.13. Normalized spectra of bremsstrahlung produced, in the four different biological materials. 10^6 beta particles emitted with 500keV kinetic energy, in the middle of a sphere of 1cm diameter

The x-axis is presented in a logarithmic scale to show an exponential decrease in the underlying quantity for the given base.

By simply looking at the normalized spectra it is observable that shapes of the bremsstrahlung spectra are identically analogous between all the materials. One deduces that the composition of the material has reasonably little effect on the shape of the bremsstrahlung spectra. Therefore, after the normalization, it is visible that the number of bremsstrahlung produced with certain energy varies in the same way in all the materials. This means that if anyone wants to use the bremsstrahlung spectrum data might do it for any one of these biological material by normalizing the data.

It is also evident a steep fall off in the curves when the energy is 10keV. This is because the PCUT and AP, the cut-off energies, defined in the EGSnrc code are equal to 10keV. Therefore, the photons that have energies below the specified transport threshold energies are stopped and their histories terminate in the region. This fact proves, once again, the veracity of the code.

In order to understand how the bremsstrahlung spectrum looks like without normalization, for each biological material, individual spectra were constructed. The data used were the same to generate the figure 4.13..

The figure below illustrate the bremsstrahlung spectrum for every individually material. Two spectra are presented in each image, the bremsstrahlung produced spectra, which comprise the bremsstrahlung photons created inside the sphere, and the bremsstrahlung escaped spectra. The escaped spectrum has considered the photons that cross the sphere surface boundary and are stopped and counted by order of the user.

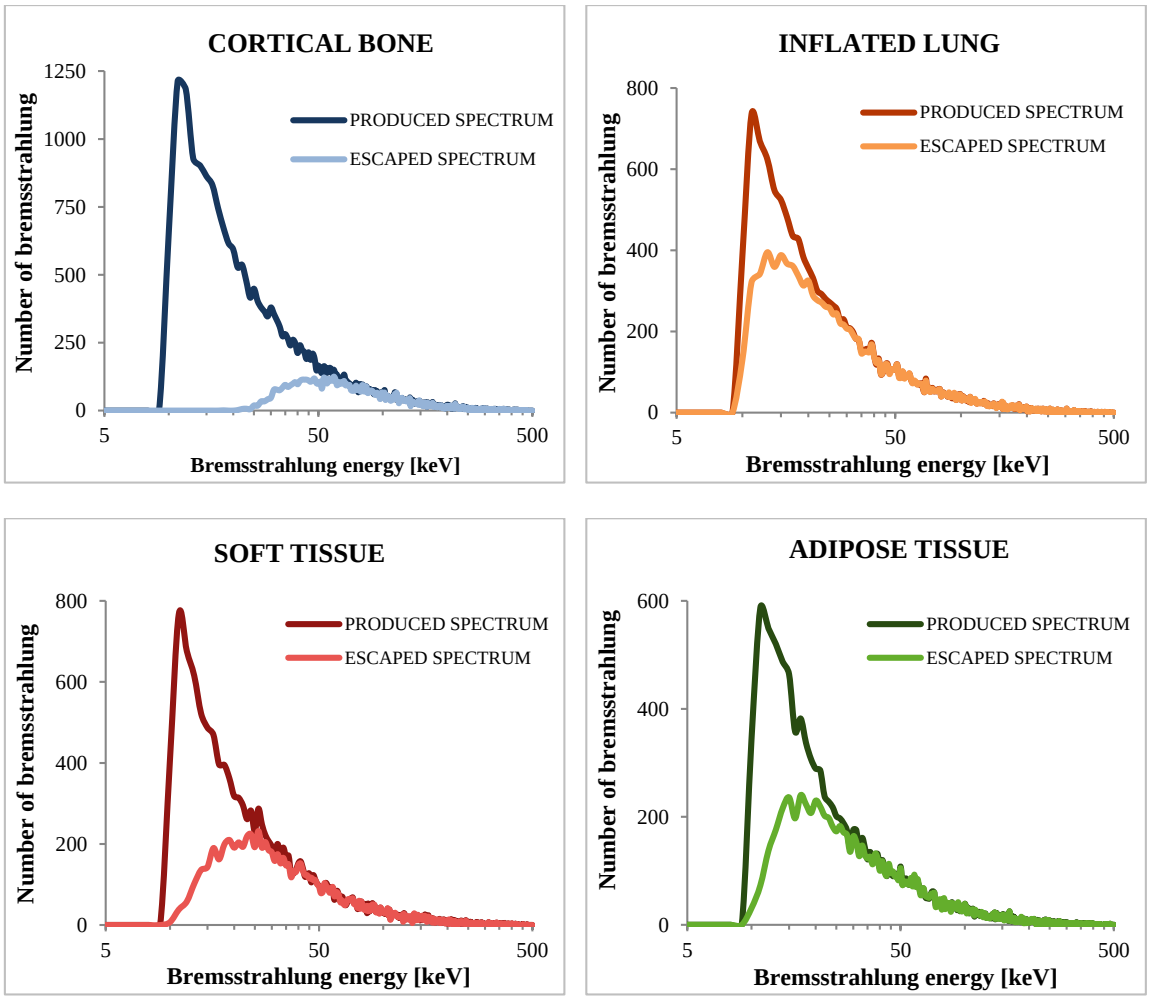

Figure 4.14. Bremsstrahlung spectra produced and escaped in the four different materials. Bremsstrahlung spectra produced by a monoenergetic point source of 10^6 beta particles emitted with 500keV kinetic energy inside a sphere with 1cm of radius and bremsstrahlung spectra escaped from the sphere, in the four different materials

It is noticeable that more than a half of the photons produced are absorbed or attenuated inside a sphere with of 1cm radius. In the case of the cortical bone, only 10% of the produced bremsstrahlung photons are detected outside the surface sphere being the other 80% attenuated inside the material. On the other hand, inflated lung absorb 50% of the photons produced, followed by the adipose tissue, which absorb 60% of the photons and finally the soft tissue, which absorb almost 75% of the photons produced. This fact is in accordance with the values of the linear attenuation coefficients, for the energies of the bremsstrahlung produced which ranged from 10 to 100keV. Analysing the figure 4.15., the cortical bone presents the highest μ, and therefore almost the photons are attenuated by the material, followed by the soft tissue, adipose tissue and finally the inflated lung which attenuated just 50% of the photons.

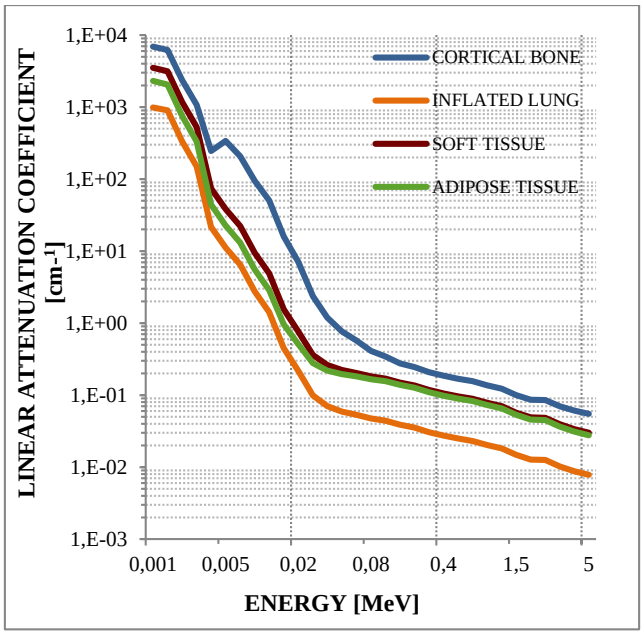

Figure 4.15. Linear attenuation coefficients [cm^{-1}] for cortical bone, inflated lung, soft tissue and adipose tissue (Theoretical Data from XCOM: Berger *et al*., 1998 in NIST)

By the analysis of the spectra in figure 4.14, it is perceptible that only a small fraction of the bremsstrahlung photons produced inside the patient are able of reaching the gamma camera. Also, the energies of the majority bremsstrahlung photons produced ranged from 10 to 100keV, which means that there is a higher likelihood of the photons being absorbed by the septa collimator if they do not reach the crystal perpendicularly. However, photons from the higher energy range have an increased probability of transversing the collimator septum (producing lead characteristic x-rays) and detector crystal, resulting in a significant image degradation.

To perform patient-specific dosimetry, one needs to apply quantitative methods to correct for scatter, photon attenuation and the degradation in spatial resolution due to the design of the collimator. With a better knowledge of how different components contribute to the image, such as scattered photons, un-scattered photons, which have penetrated the septa, back-scattered photons etc., one will be able to optimize acquisition parameters such as the choice of an energy window and a collimator.

Table 4.13. gives the CPU times for each simulation undertaken in this section. The time includes the score of the parameters – produced and escaped bremsstrahlung spectra (number of bremsstrahlung photons produced/escaped *vs.* respective energies) and the photons escaped position (X, Y, Z), in the computer memory.

Table 4.13. CPU times [seconds] spent in the simulations to analyse the spectra shapes. Values obtained for 10^6 beta particles emitted with 500keV, isotropically, inside a sphere with 1cm radius

	CORTICAL BONE	INFLATED LUNG	SOFT TISSUE	ADIPOSE TISSUE
CPU time [sec]	148.2	100.7	100.0	99.0

4.2.4. Analysis of the Angular Distribution of the Bremsstrahlung Produced

The distribution of angles (degrees) between incident electrons and emitted bremsstrahlung photons as a function of electron kinetic energy was investigated. In order to analyse the angular distribution 10^6 beta particles were emitted isotropically, also inside a sphere with 1cm of radius. The beta particle energies chosen to do the simulation were: 250, 500, 2230 and 3000keV.

Figure 4.16., shows the results from the simulation number of bremsstrahlung produced *vs.* angle of emission, for the different biological materials.

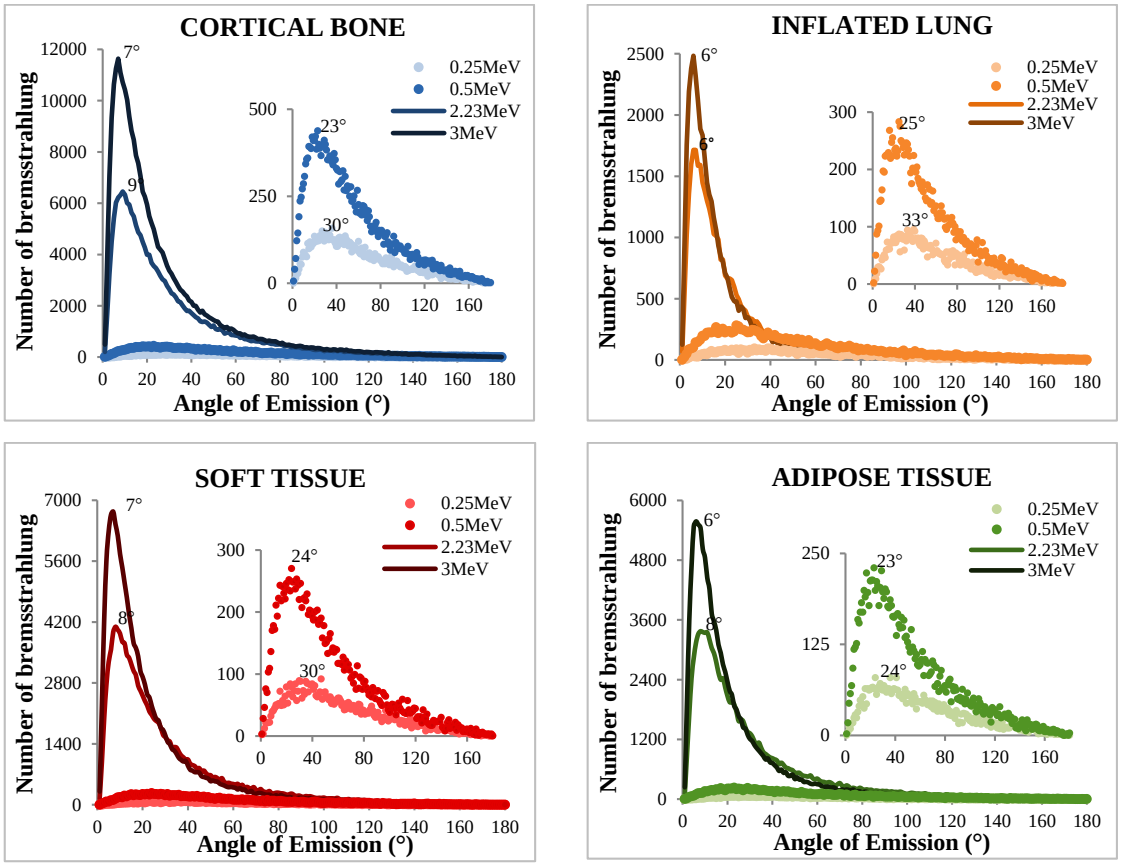

Figure 4.16. Angular distribution between incident electrons and emitted bremsstrahlung photons as a function of electron kinetic energy [MeV]. Values obtained from 10^6 beta particles emitted isotropically, inside a sphere with 1cm radius

It can be seen by the figure that, in all the materials, the tendency for backward scattering decreases with increasing electron kinetic energy. The lower the electron kinetic energy becomes, the more backward the bremsstrahlung photons are emitted, in comparison with the electron direction. Contrary, when the electron kinetic energy increases, bremsstrahlung photons are mainly emitted in a forward direction, *i.e.*, the bremsstrahlung photons and the electrons which originate them, follow roughly the same direction. Thus, comparing between the four biological materials, one verifies that there are small differences in the photon emission angle,

which mean that the effective atomic number is slightly important in the angular bremsstrahlung distribution.

Table 4.14. gives the CPU times. The time includes the score of the parameters – produced and escaped bremsstrahlung spectra (number of bremsstrahlung photons produced/escaped *vs.* respective energies) and the angle distribution spectra, in the computer memory.

Table 4.14. CPU times [seconds] spent in the simulations to analyse the angular bremsstrahlung distribution. Values obtained for 10^6 beta particles emitted isotropically, inside a sphere with 1cm radius

		ELECTRON KINETIC ENERGY [keV]			
		250	**500**	**2230**	**3000**
CORTICAL BONE	CPU time [sec]	79.4	115.6	368.2	484.4
INFLATED LUNG	CPU time [sec]	54.2	82.0	55.6	54.8
SOFT TISSUE	CPU time [sec]	54.0	134.7	249.0	232.5
ADIPOSE TISSUE	CPU time [sec]	53.4	81.8	230.5	204.1

4.2.5. Analysis of the Spatial Distribution of the Bremsstrahlung Produced

The spatial distribution of bremsstrahlung photons produced in the vicinity of the beta particles point source, as a fraction of the electron kinetic energy was investigated. To study the spatial distribution of the bremsstrahlung produced, 10^6 beta particles were emitted in a forward direction (U=0; V=0; W=1) inside a sphere, to the four biological materials studied so far. In order to assess the spatial distribution with more accuracy, the radius of the sphere was chosen with the purpose of ensure a constant efficiency in the bremsstrahlung production, *i.e.*, maximise the bremsstrahlung production. As previously explained the bremsstrahlung efficiency varies with the media and the beta particles kinetic energy. Therefore, by the analysis of the table 4.8., the highest and maximum radius sphere for each material was chosen. For the cortical bone 1cm radius was used, for the inflated lung 5cm radius and for the soft tissue and adipose tissue 3cm radius was tested in the simulations. For every single material, the beta particles kinetic energy chosen to undertaken the simulations was 500keV and 1500keV.

The distribution of all photons in terms of the radial distance between the point source and the bremsstrahlung production according to the beta particles kinetic energy is shown in the figure 4.16. The figure 4.17 illustrates the histogram of the total number of bremsstrahlung photons produced between certain distances from the point source, with a distance binned of 0.05cm chosen for the cortical bone, soft tissue and adipose tissue, and 0.2cm for the inflated lung, since this material require a great radius sphere in comparison with the other materials. Figure 4.18., represents the histogram of the total bremsstrahlung energy (in MeV) produced within those

distances. To create this histogram the energies of all bremsstrahlung photons produced within a certain distance (bin) were identified and summed.

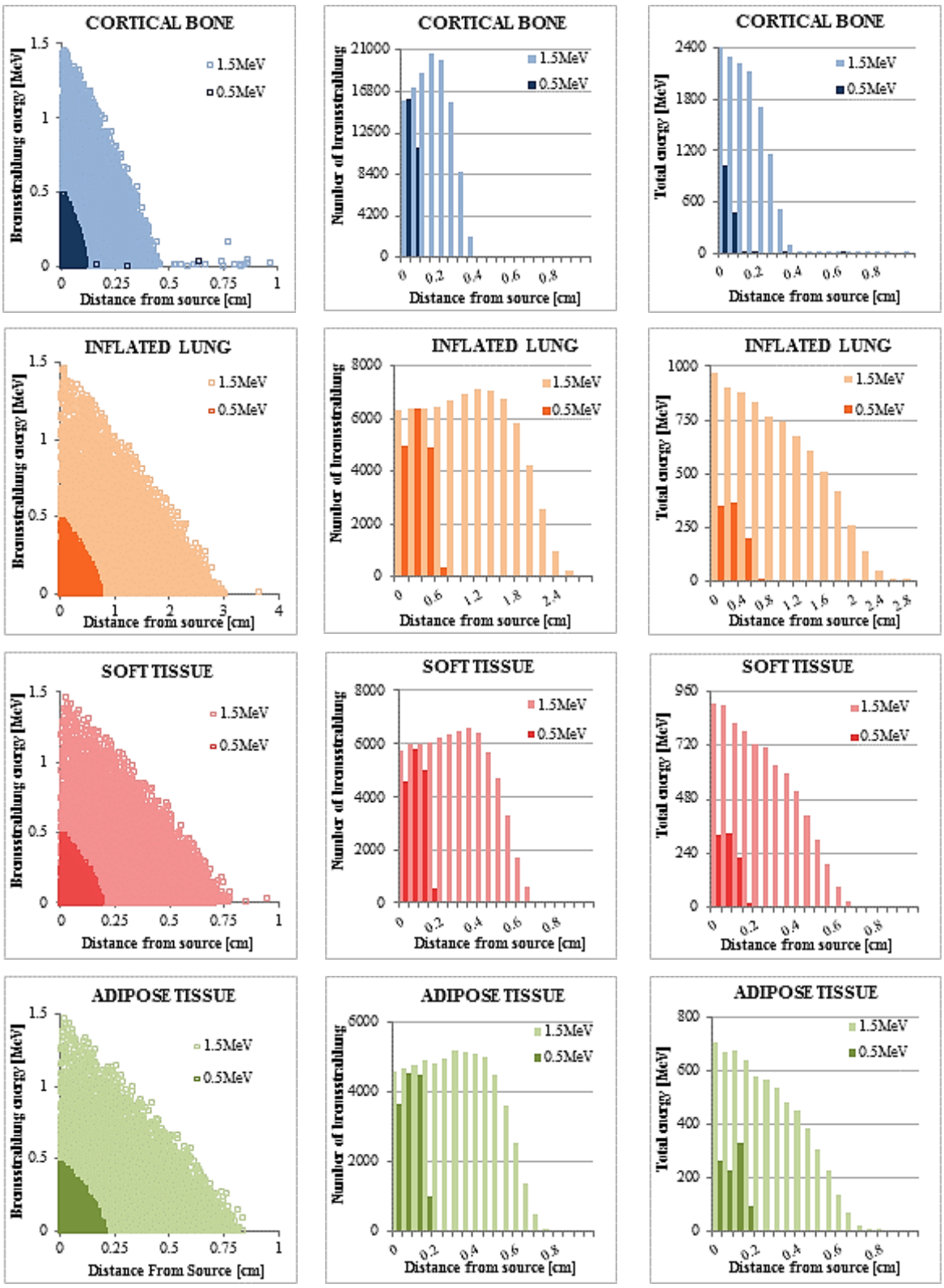

Figure 4.17. Spatial distribution of bremsstrahlung photons as a fraction of the electron energy

Figure 4.18. Frequency of the number of bremsstrahlung produced within distance ranges

Figure 4.19. Total energy of the bremsstrahlung produced within distance ranges

By the analysis of the figure 4.17., in all the materials, it is possible verify that the bremsstrahlung photons with the highest energies are produced near to the point source. As the electrons move along the material and move away from the point source, they lose their energy and consequently, the energy of the bremsstrahlung photons produced decreases.

Analysing the figure 4.18. and 4.19., one verifies that in the cortical bone, of all bremsstrahlung photons produced when the beta particles are emitted with 0.5MeV, about 99.99% of those, are produced within 2mm, which corresponds to 1.5GeV of energy produced. When the beta particles are emitted with 1.5MeV, of all bremsstrahlung photons produced, approximately 86% are created inside a sphere with 5mm, corresponding to 7GeV of energy.

In the case of the inflated lung, when beta particles are emitted with 0.5MeV, all the bremsstrahlung photons produced are radially distributed within 1cm, which correspond to 0.9GeV of kinetic energy. On the other hand, beta particles emitted with 1.5MeV, create 81.22% of all bremsstrahlung photons within 2cm, resulting in 6.8GeV of photons energy.

For the soft tissue and the adipose tissue, all the bremsstrahlung photons are created within 2mm, when the beta particles are emitted with 0.5MeV. The total kinetic energy of the bremsstrahlung photons is 0.9GeV, for both the biological materials. In contrast, when the electrons are emitted with 1.5MeV, approximately 86% of all bremsstrahlung photons are radially distributed within 5mm of soft tissue, corresponding to 7GeV of kinetic energy. For the adipose tissue, roughly 80% of photons are produced within 5mm, corresponding to 5.7GeV of kinetic energy.

It is possible to confirm that, the higher the beta particles energy, the wider the spatial distribution of the bremsstrahlung photons produced. Therefore, bremsstrahlung photons are produced further away from the point source with the increase of the electrons kinetic energy.

Table 4.15. gives the CPU times. The time includes the score of the parameters – produced and escaped bremsstrahlung spectra (number of bremsstrahlung photons produced/escaped *vs.* respective energies) and the spatial distribution spectra, in the computer memory.

Table 4.15. CPU times [seconds] spent in the simulations to analyse the spatial bremsstrahlung distribution. Values obtained for 10^6 beta particles emitted in forward direction, along the z-axis

		ELECTRON KINETIC ENERGY [keV]	
		500	**1500**
CORTICAL BONE	CPU time [sec]	189.6	435.0
INFLATED LUNG	CPU time [sec]	131.3	290.4
SOFT TISSUE	CPU time [sec]	75.8	171.7
ADIPOSE TISSUE	CPU time [sec]	75.6	170.5

4.2.6. Analysis of the ^{90}Y and ^{32}P Bremsstrahlung Spectra.

To finalise the set of Monte Carlo simulations, the bremsstrahlung production of the two most commonly used pure beta emitters in radionuclide therapy was characterised. The pure beta emitters tested were ^{90}Y and ^{32}P.

The bremsstrahlung production with the point sources of ^{90}Y and ^{32}P was characterised in terms of the number of bremsstrahlung photons produced relatively to the energy spectrum of those bremsstrahlung photons. Also the radiation yield was calculated for each radionuclide.

As referred in section 2.1.1., beta particles exhibit a continuous spectral kinetic energy distribution, resulting in a polyenergetic spectrum, ranging from zero to E_{max}. So far, all the simulations have considered monoenergetic beta point sources. However, the polyenergetic energy spectra for the beta sources, ^{90}Y and ^{32}P, was considered to undertaken the simulation of the bremsstrahlung spectra. To evaluate the bremsstrahlung production of the pure beta emitters, ^{90}Y and ^{32}P point sources were simulated in a sphere of cortical bone, inflated lung, soft tissue and adipose tissue, at a depth of 1cm in a 2cm diameter sphere. Polyenergetic beta particles were emitted isotropically. 10 million histories were tested (10^7 beta particles emitted) for each radionuclide and in each biological material.

Before the polyenergetic spectra being used to characterize the bremsstrahlung photons production, verification was first made in order to ensure a correct used of the energy spectra in the EGSnrc code. The confirmation was done by comparing the values of the energy spectra of the beta sources generated by the EGSnrc code with the theoretical data given by RADAR (2012).

Theoretical data of the ^{90}Y and ^{32}P just provide 20 energy points, distributed in wide bins of 114.2keV and 85.5keV, respectively. The points, at the mid-value of each bin, give the probability of the beta particles emission with certain energy. Theoretical points were used in Excel to find the energy spectra equations of the ^{90}Y and ^{32}P, with the intention of be used in EGSnrc code.

In the case of the ^{90}Y, the best fit was found with a fifth degree polynomial equation, whereas to ^{32}P the best fit was found with a fourth degree polynomial equation. The equations of ^{90}Y and ^{32}P were placed in EGSnrc code, such as represented below, respectively, and verified against the theoretical points.

```
"-------------------------------------------------------------"
"STEP 6   DETERMINATION-OF-INICIDENT-PARTICLE-PARAMETERS     "
"-------------------------------------------------------------"
"90Yttrium equation - polyenergetic spectra"
SPECTNUMYT(1)=0;
DO I=1,223
     [SPECTENYT(I)=I*0.01;
     SPECTNUMYT(I)=0.01458*(SPECTENYT(I))*(SPECTENYT(I))*
(SPECTENYT(I))*(SPECTENYT(I))*(SPECTENYT(I));
     SPECTNUMYT(I)=SPECTNUMYT(I)-0.07973*(SPECTENYT(I))*
(SPECTENYT(I))*(SPECTENYT(I))*(SPECTENYT(I));
     SPECTNUMYT(I)=SPECTNUMYT(I)+0.16173*(SPECTENYT(I))*
(SPECTENYT(I))*(SPECTENYT(I));
     SPECTNUMYT(I)=SPECTNUMYT(I)-0.19089*(SPECTENYT(I))*
(SPECTENYT(I));
     SPECTNUMYT(I)=SPECTNUMYT(I)+0.12946*(SPECTENYT(I));
     SPECTNUMYT(I)=SPECTNUMYT(I)+0.03522; ]


"32Phosphorous equation - polyenergetic spectra"
SPECTNUMPH(1)=0;
DO I=1,167
     [SPECTENPH(I)=I*0.01;
     SPECTNUMPH(I)=0.05063*(SPECTENPH(I))*(SPECTENPH(I))*
(SPECTENPH(I))*(SPECTENPH(I));
     SPECTNUMPH(I)=SPECTNUMPH(I)-0.10889*(SPECTENPH(I))*
(SPECTENPH(I))*(SPECTENPH(I));
     SPECTNUMPH(I)=SPECTNUMPH(I)-0.06523*(SPECTENPH(I))*
(SPECTENPH(I));
     SPECTNUMPH(I)=SPECTNUMPH(I)+0.16286*(SPECTENPH(I));
     SPECTNUMPH(I)=SPECTNUMPH(I)+0.02385; ]
```

In both equations, the values were represented with five decimal numbers to reduce the uncertainty. In the case of ^{90}Y spectrum, the variable `SPECTENYT` (x-axis variable) denotes the input beta particles energy in intervals of 10keV. This variable was substituted into the resultant equation to obtain the output spectrum - the number of beta particles emitted with particular energy, which is given by the variable `SPECTNUMYT` (y-axis variable). For the ^{32}P those variables are represented, respectively, by `SPECTENPH` and `SPECTNUMPH`.

In order to compare the theoretical spectra with the simulated spectra, the theoretical energy bins width of the ^{90}Y (114.2keV) and ^{32}P (85.5keV) were scaled to 10keV, such as in the equations used in EGSnrc code. The emission spectra of the beta sources were simulated to the cortical bone, inflated lung, soft tissue and adipose tissue. The average of the number of beta particles emitted with certain energy obtained in all the materials was calculated, as a fraction of the total beta particles emitted (10^7 events), with the intention of to achieve the probability. The simulated and the analytical results of the energy spectra for the beta point sources, ^{90}Y and ^{32}P, are shown in figure 4.20.

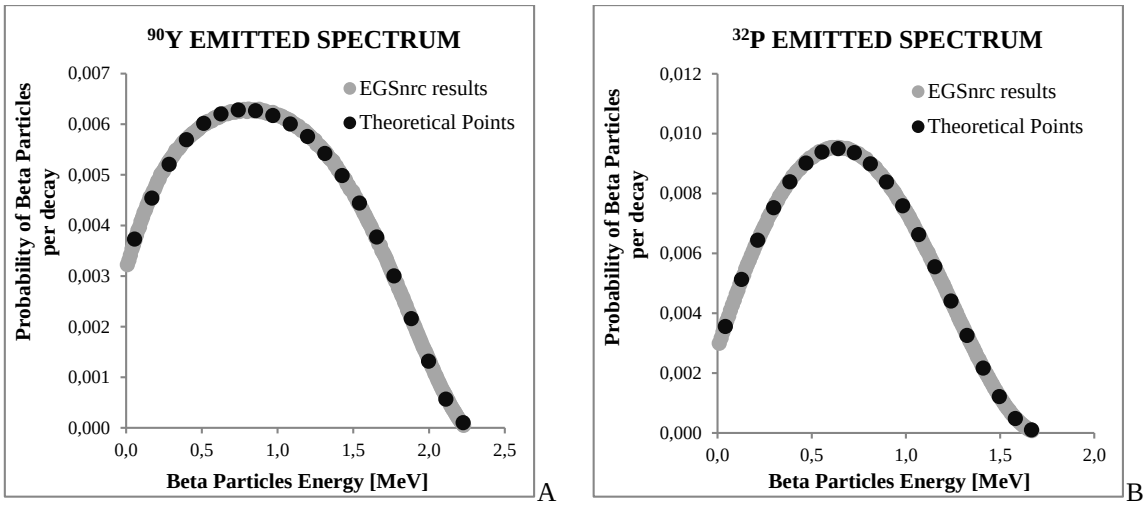

Figure 4.20. Comparison between theoretical and simulated energy emitted spectra for A) ^{90}Y point source and B) ^{32}P point source (Theoretical data from RADAR, The Decay Data, 2012)

By the comparison between the theoretical data and the simulated values, both for ^{90}Y and ^{32}P, it is possible to confirm that the simulated values fit the theoretical points accurately. Therefore, simulation with polyenergetic spectra of ^{90}Y and ^{32}P point sources could be used and carried out, in order to characterise the bremsstrahlung photons spectra of those pure beta emitters in different homogeneous and biological materials. The small errors in figure 4.20., might be associated with the polynomial degree chosen to define the equation. The higher the polynomial degree, the higher the probability of associated errors in the obtained values. Polyenergetic spectra of the beta sources were then used in EGSnrc to generate the emission of the beta particles with random energy, between 0 and 2.23MeV for ^{90}Y and 1.67MeV for ^{32}P.

The data presented in figure 4.21 were summed to create the cumulative probability density functions shown in figure 4.20.

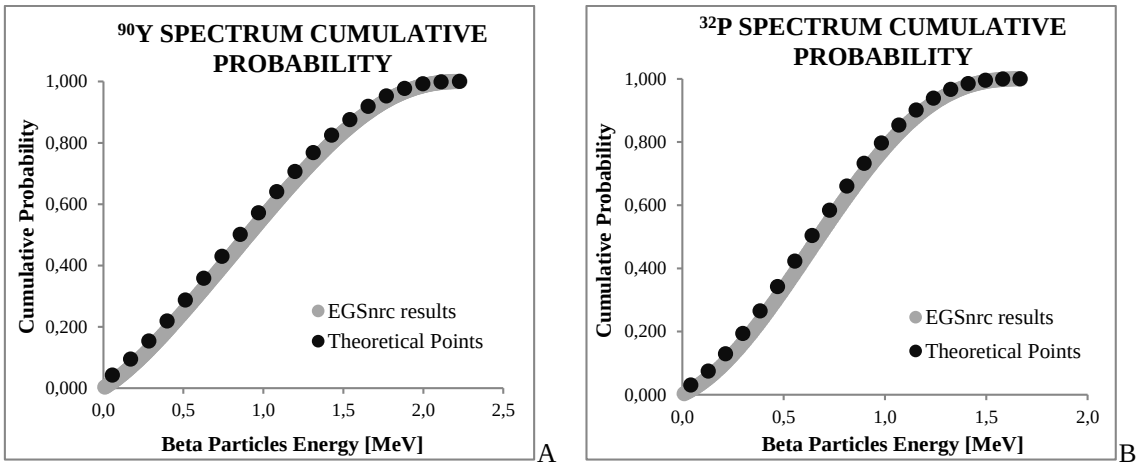

Figure 4.21. Comparison between theoretical and simulated cumulative probabilities for A) ^{90}Y point source and B) ^{32}P point source (Theoretical data from RADAR, The Decay Data, 2012)

After the validation, the bremsstrahlung photons production was simulated and characterised in a simulation of 10^7 histories, using the polyenergetic ^{90}Y and ^{32}P spectra. As previously referred, the pure beta emitters were tested individually in a sphere of cortical bone, inflated lung, soft tissue and adipose tissue, at a depth of 1cm in a 2cm diameter sphere.

Bremsstrahlung produced spectra and bremsstrahlung escaped spectra were scored. The simulated spectra - number of bremsstrahlung photons *vs.* their energy, for both radionuclides, are shown in figure below.

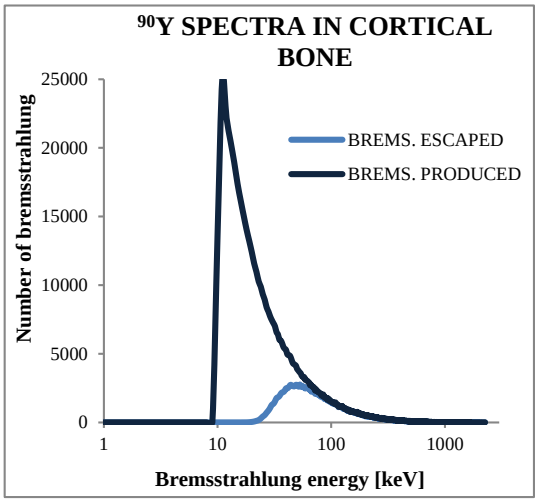

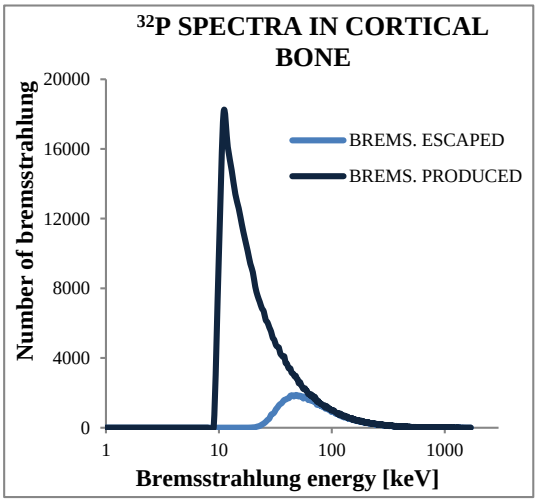

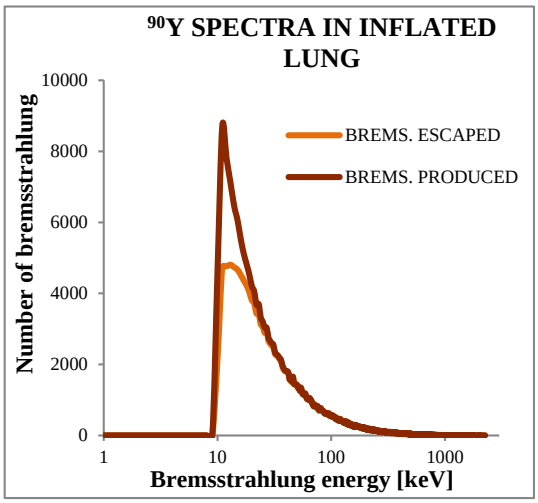

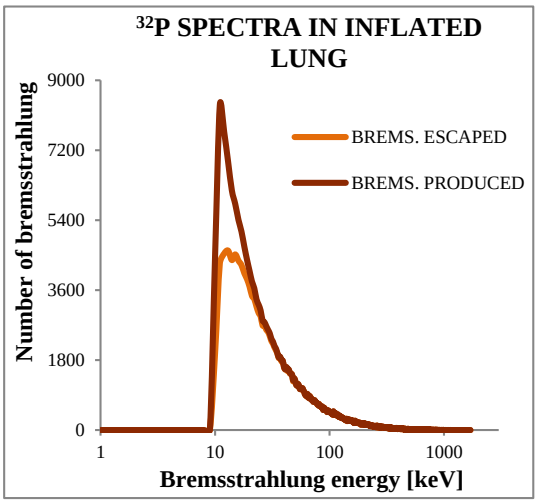

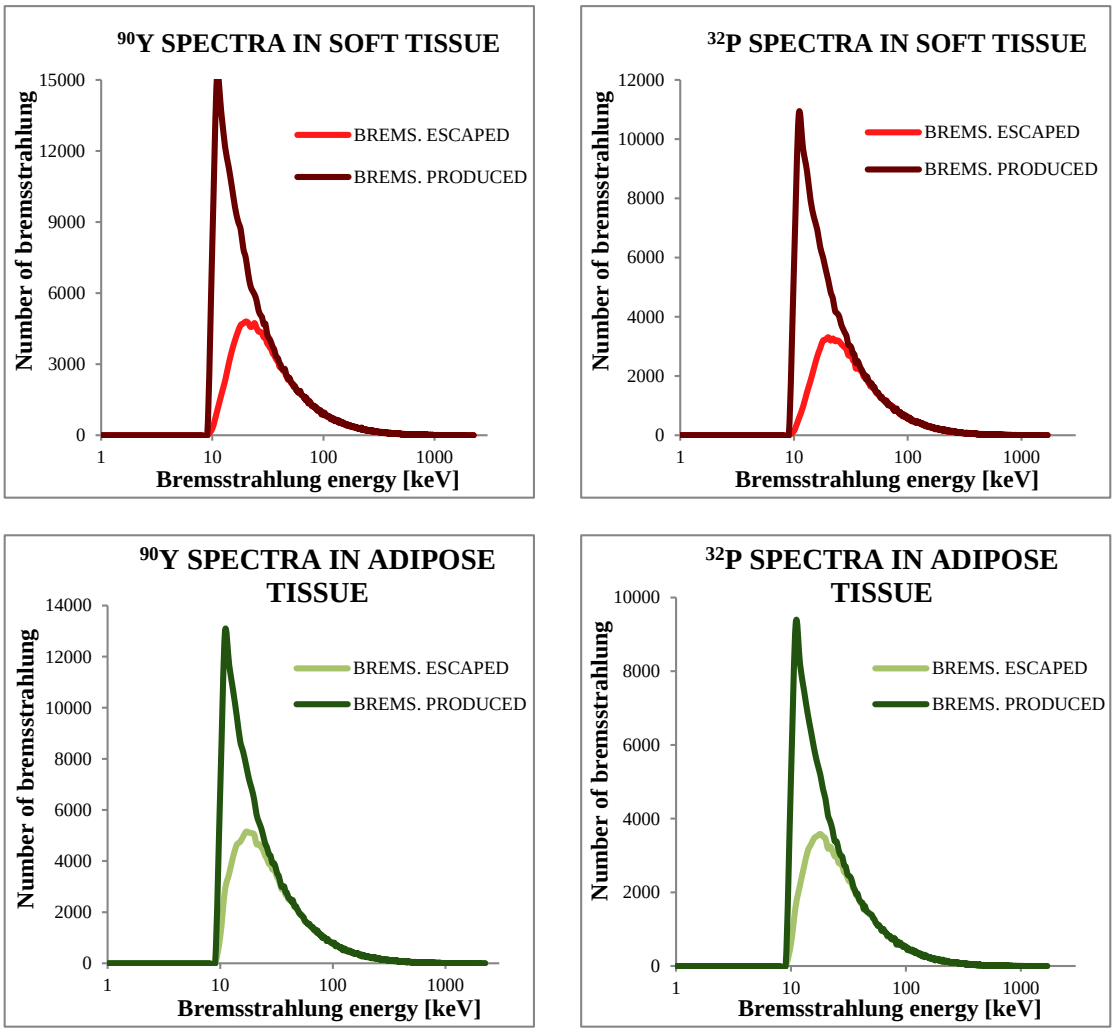

Figure 4.22. Bremsstrahlung photons spectra created from polyenergetic point sources of ^{90}Y and ^{32}P, for different biological materials. 10^7 beta particles emitted isotropically

By the analysis of all the spectra in the figure 4.22., for both radionuclides ^{90}Y and ^{32}P, it is possible to perceive that the shapes of the spectra are very similar, with slight differences in the escaped spectra. By the comparison between ^{90}Y and ^{32}P spectra, it is possible observe that when the ^{90}Y is the source more bremsstrahlung photons are produced, and consequently more emitted photons. This fact is caused by the fact of the ^{90}Y has a wide energy spectrum in comparison with the ^{32}P – ^{90}Y has a maximum energy of 2.23MeV whereas ^{32}P has a maximum energy of 1.67MeV. It is also evident a steep falloff in the curves when the energy is 10keV. As explained previously this is because the PCUT and AP chosen in the EGSnrc code, which is defined as 10keV. All photons with energy below this threshold are stopped and their histories terminate in the region.

Investigating, individually, each physical medium and taking into account that 10^7 pure beta particles are emitted, one verifies that in the cortical bone when the ^{90}Y is the source, about

6.8% of all the beta particles interactions produce bremsstrahlung photons. Of those photons, about 47.1% escape from the geometric sphere in study, which means that of all beta interactions only 3.2% of bremsstrahlung photons produced are able to escape and being detected outside 1cm radius sphere. The others 52.9% of all bremsstrahlung photons produced are absorbed inside the sphere. On the other hand, when the ^{32}P is the point source, 4.5% of all pure beta particles emitted are able to produce bremsstrahlung photons. Of those photons, 43.3% may escape from the sphere and 56.7% are totally absorbed. In comparison with the others biological materials, one verifies that in the cortical bone the escaped spectra, in both sources, are more shifted to the right. This fact is caused by the high linear attenuation coefficient of the material (see table 4.14). Therefore, the low-energy bremsstrahlung photons are absorbed easily by the medium whereas only the high-energy photons may escape from the sphere.

Examining the inflated lung, one confirms that when the ^{90}Y is the point source, only 2.4% of all interactions are able to produce bremsstrahlung photons. 91.7% of those photons escape from 1cm radius sphere, able to be detected outside this thickness. The others 8.3% are completely absorbed. Alternatively, for the ^{32}P, about 2.14% of all interactions produce bremsstrahlung photons. 88.8% of those photons escape from the sphere and 11.2% are absorbed. Since the inflated lung has the lower linear attenuation coefficient, in comparison with the other materials, it is perceptible this small value of absorbed photons.

In case of the soft tissue, when the ^{90}Y is the particles source, about 4.1% off all beta interactions produce bremsstrahlung photons. Of all those photons produced, 76.1% may escape from the sphere, which means that of all bremsstrahlung photons produced only 3.12% are able to escape from 1cm radius sphere. The remaining 23.9% photons are absorbed. For the ^{32}P, about 2.7% of all beta interactions may produce bremsstrahlung photons. Of those, 73.3% has a range superior of 1cm radius and therefore they escape from the sphere in study. The others 26.7% are absorbed.

In the adipose tissue, when the ^{90}Y is the point source, about 3.47% of all interactions are able to produce bremsstrahlung photons. Of all those photons, 83.6% may escape from the sphere in study. This means that only 2.9% of all bremsstrahlung produced are able to be detected outside of 1cm radius sphere. The remaining 16.4% are totally absorbed inside the adipose tissue. For the ^{32}P, only 2.3% of all beta interactions may originate bremsstrahlung photons. Of all those photons, 78.3% may be detected outside the sphere, being the others 21.7% absorbed inside the adipose tissue.

The next table illustrates clearly the differences between the bremsstrahlung produced, absorbed and escaped from the sphere with 1cm radius. The values are shown in percentage and the

values of the absorbed and escaped photons are associated with the total bremsstrahlung photons produced.

Table 4.16. Percentage of the bremsstrahlung photons produced, absorbed and escaped, for ^{90}Y and ^{32}P sources. Percentage of the bremsstrahlung photons produced when 10^7 beta particles are emitted and percentage of those photons absorbed inside the material and escaped from 1cm radius sphere

	^{90}Y SOURCE			**^{32}P SOURCE**		
	Brems. produced	Brems. escaped	Brems. absorbed	Brems. produced	Brems. escaped	Brems. absorbed
CORTICAL BONE	6.8%	47.1%	52.9%	4.5%	43.3%	56.7%
INFLATED LUNG	2.4%	91.7%	8.3%	2.14%	88.8%	11.2%
SOFT TISSUE	4.1%	76.1%	23.9%	2.7%	73.3%	26.7%
ADIPOSE TISSUE	3.47%	83.6%	16.4%	2.3%	78.3%	21.7%

In comparison with all the materials, the cortical bone is the medium that produces and absorbs more bremsstrahlung photons, respectively, due to its high atomic number *Z* and its high linear attenuation coefficient.

Contrary, the inflated lung is the material that produces and absorbs the less percentage of bremsstrahlung photons, respectively, due to its low density material and its low linear attenuation coefficient. Also, the low percentage of the bremsstrahlung photons produced is due the small radius sphere that is taking into account in this simulation. By the analysis of the table 4.9., and the figure 4.18., inflated lung required a higher radius sphere to produce more number of photons. The spatial distribution of the bremsstrahlung photons (figure 4.8.) shows that, for electrons with energies higher than 500keV, the highest amount of the bremsstrahlung photons are produced in the inflated lung after 1cm of distance from the point source.

Soft tissue and adipose tissue show analogous values since the atomic number and the linear attenuation coefficients are similar.

Table 4.17., shows the bremsstrahlung yield, in percentage, produced in the four biological materials when 10^7 beta particles are emitted from ^{90}Y and ^{32}P point sources.

Table 4.17. Radiative yield [%] produced by 10^7 beta particles emitted from ^{90}Y and ^{32}P point sources. Percentage values of the total energy emitted from the sources converted into bremsstrahlung

	SIMULATED RADIATION YIELD AND ERROR [%]	
	^{90}Y	^{32}P
CORTICAL BONE	0.689 ± 3%	0.505 ± 3.6%
INFLATED LUNG	0.269 ± 2.8%	0.25 ± 2.6%
SOFT TISSUE	0.417 ± 3.3%	0.298 ± 2.8%
ADIPOSE TISSUE	0.354 ± 3%	0.255 ± 2.6%

The total energy emitted from the point sources were divided by the total energy of the bremsstrahlung produced, and the error was calculated throughout the propagation of errors within ±1σ, both transformed to percentage. Analysing the table, one confirms, such as before, that the cortical bone is the material with the highest radiation yield and the inflated lung with the lowest value of radiation yield. However, the radiation yield is less than 1% in all the materials, which show the low efficiency of the bremsstrahlung photons production.

From the figure 4.22. and the table 4.17., it is perceptible some of the problems found in the bremsstrahlung imaging. First, in all the materials and for both the radionuclides, it is visible that the spectrum set up by the bremsstrahlung photons that escape from the area in study is a continuous spectrum, ranged from 10keV (because the PCUT chosen to do the simulations) to the maximum kinetic energy of the pure beta particles which originate them. This is, indeed, a problem in the bremsstrahlung imaging since there is no a clear photopeak. Therefore, the choice of the energy window becomes a difficult step to imaging the bremsstrahlung photons.

Another difficult regards to the choice of the collimator. By the figure 4.22., it is seen that the majority of the photons produced have energies less than 100keV. If a low-energy collimator is used, the high-energy photons may pass through the septa, producing lead characteristic x-rays and consequently the quality of the image is degraded. With this type of collimator there is a high sensitivity but low spatial resolution. On the other hand, if a high-energy collimator is used, the high-energy photons may be stopped but also the majority of the photons produced, reducing the sensitivity. By the analysis of the table 4.16., it is visible that the sensitivity is already small (less than 1%), therefore, if this collimator is used, the sensitivity may be further diminished, becoming insignificant to produce an image with quality.

Thus, all the bremsstrahlung spectra, showed the three main characteristics that confirm the challenge in imaging the bremsstrahlung photons: they are continuous (without a photopeak),

they include high-energy photons (difficult to be stopped by the collimator) and they are of low efficiency (quantity, less than 1%).

Table 4.18. gives the CPU times spent in these simulations. The time includes the score of the parameters – produced and escaped bremsstrahlung spectra (number of bremsstrahlung photons produced/escaped *vs.* respective energies) and the emission beta particles spectra, in the computer memory.

Table 4.18. CPU times [seconds] spent in the simulations to analyse the bremsstrahlung spectra created by polyenergetic pure beta emitters, ^{90}Y and ^{32}P. Values obtained for 10^7 beta particles emitted isotropically, inside a sphere with 1cm radius

		^{90}Y	^{32}P
CORTICAL BONE	CPU time [sec]	3049.7	2357.1
INFLATED LUNG	CPU time [sec]	635.0	1196.2
SOFT TISSUE	CPU time [sec]	1783.7	1636.0
ADIPOSE TISSUE	CPU time [sec]	1208.1	1555.8

With the knowledge of the characteristics of the bremsstrahlung photons produced by the ^{90}Y and ^{32}P sources, such as the photons energy, spectrum shape, the material or the radiation yield, it would be essential expand the study and use these information to find the better performance parameters of the gamma camera in order to maximise the quality of the bremsstrahlung image.

There are relevant issues regarding to the formation of the bremsstrahlung image which require particular attention. If the bremsstrahlung imaging is improved, a patient-specific dosimetry can be done and consequently a reduction in the patient dose might be achieved.

4.3. List-mode Acquisitions

Beyond the bremsstrahlung simulations, it was done a set of measurements in the NM/CT 670, a hybrid SPECT-CT dual head camera (GE Healthcare), available in the INM. The purpose was to test a developed program to decoding the list mode data obtained from each acquisition, as well as, to assess the accuracy and performance of the gamma camera in to detect the energy of the photons.

As explained previously, the data acquired during the gamma camera scan may be stored in frame mode or list mode. The frame mode is the most commonly used. Currently, the NM/CT 670 SPECT-CT performs through the standard frame mode acquisition and, consequently, the images are visualised with based of this mode. However, the NM/CT 670 SPECT-CT, also allows, the storage of the list-mode data in the *GE Xeleris* workstation system. In the *GE Xeleris* software, the user define the parameters and specifications of the acquisition, such as the type of acquisition, time of acquisition, radionuclide used, patient details, collimator type and desired energy window(s).

It was important validate and test the list mode decoding program, since the list mode acquisition allows much more flexibility the in post-processing data than is possible with frame mode. The list mode acquisitions the energy and positional information are stored individuality for each photon interaction and therefore this type of acquisition offers a widely variation of choices to re-binned repeatedly the data into various energies windows, matrix sizes and time periods. As a result, it may permit improvements in the choice of the set of the performance characteristics to imaging the bremsstrahlung photons.

In each measurement undertaken to achieve the purpose, the list mode data was stored in the *GE Xeleris* workstation. Then, the data were exported to a specific directory and decoding by the specific program. Table 4.19. shows a simplified sample of raw data after the use of the decoding program.

Table 4.19. List mode acquisition data after the use of the decoding program

ENERGY	X POSITION	Y POSITION
143.91	292.70	306.67
140.44	297.00	297.05
133.13	301.71	280.00
129.28	294.00	298.40

Each line of the table represents a single event. The first column represents the total energy deposited in the NaI(Tl) crystal of the gamma camera and the second and third columns characterize, respectively, the x and y positions of each interaction. In order to validate the list

mode decoding program, 60seconds planar (2D) acquisitions were done by using a cylindrical source of ^{99m}Tc, with 10MBq of activity. The source was completely shielded with lead, with only one side of the cylindrical able to allow the photons emission. Different energy windows and collimators (LEGP or MEGP) were chosen according to the measurements. The data were treated and binned in order to form the resultant spectrum.

To visualize a final image obtained from the processed data and, consequently, from the acquisition, a Matlab code was developed. The Matlab code creates an image in a binary format. The code created is presented in appendix 5.

4.3.1. List mode acquisitions with two energy windows selected (140.5±10% and 450±10%). Source placed in different positions

The first set of measurements consisted in planar acquisitions with the LEGP collimator and two energy windows defined in the *GE Xeleris* software, 140.5keV±10% and 450keV±10%. Three planar acquisitions were undertaken with these features. The two heads of the gamma camera were positioned front to front (180° between them), in a vertical position. Only one head were used as detector and this was defined in the workstation (head 1 or head 2).

In the first acquisition the ^{99m}Tc source was placed in the centre of the patient table. The inferior head, below the table, functioned as the detector. Therefore, the open space of the lead shielding was pointed down and the photons were emitted through the patient table. In the second acquisition, the source was placed in the corner of the inferior collimator and the photon interactions were detected on the crystal beyond that collimator. In the last acquisition, the source was placed in the centre of the collimator of the inferior head, with the open space of the lead shielding pointed up to the superior head which functioned as the detector. Five slabs of perspex, with 1cm each, were placed in the patient table, right above the cylindrical source, in order to test the scattering and therefore see the blur in the resultant image. The setting-up of these acquisitions is represented in the figure 4.23.

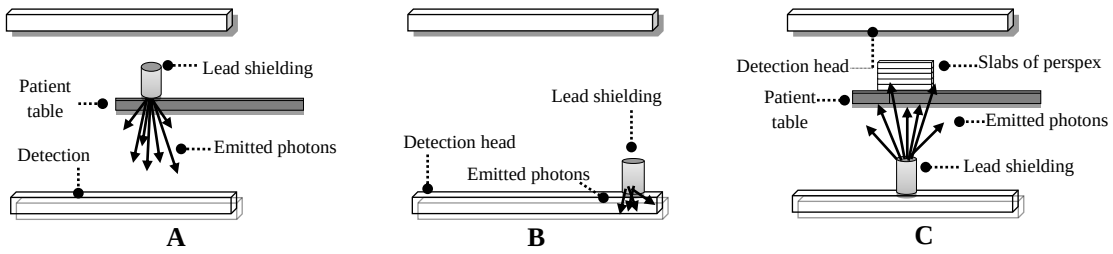

Figure 4.23. Schematic representation of the setting-up used to undertake the list mode acquisitions with two energy windows (140.5keV±10% and 450keV±10%). Cylindrical source was placed in the A) centre of the patient table, B) corner of the collimator and C) centre of the patient table with 5slabs of perspex

After the acquisitions, the list mode data were decoded one at a time by the specific program. The column of the energy of the raw processed data was used to plot a histogram of the total number of photons detected by the gamma camera *vs.* their energy. Therefore, three histograms were plotted with an energy binned of 2keV, starting in 36keV up to 176keV, since outside this energy range only an insignificant percentage of photons were detected. To plot the histograms, a program developed by Professor Rui Assis (2012) was used to an easy data processing. The figure 4.24 illustrates the histograms, *i.e.*, the ^{99m}Tc spectrum of the three acquisitions.

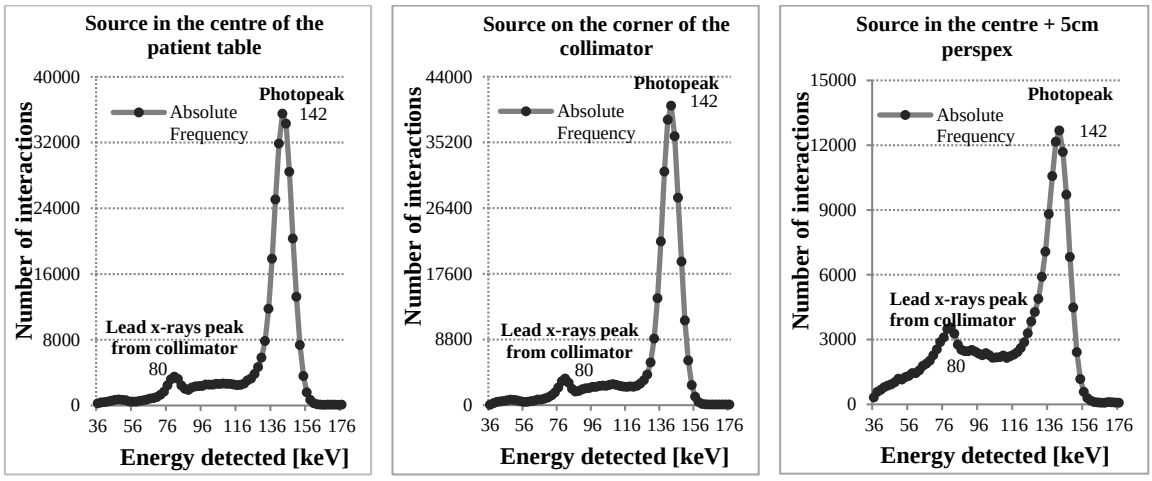

Figure 4.24. ^{99m}Tc spectra acquired in a 60sec planar acquisitions, using a MEGP collimator and two energy windows 140.5±10% and 450±10%. A) cylindrical source placed in the centre of the patient table, B) cylindrical source placed in the corner of the collimator and C) cylindrical source placed in the centre of the patient table with 5slabs of perspex

Two photopeaks are clearly visible in all the spectra. The photopeaks are broader due to various statistical variations in the process of forming the pulses, such as referred in section 2.2.3. The first photopeak easily identifiable regards to the characteristic x-ray peak of the collimator or shield lead. This peak is caused by the absorption of the lead K-shell characteristics x-rays by the gamma camera, when the photons interact with the collimator or shield. The lead x-ray peak appears, approximately, at 80keV. The second peak is caused by the total absorption in the crystal of the γ-rays emitted from ^{99m}Tc. In the spectra this peak appears at 142keV. It is visible that the spectrum B has the highest number of photons interactions, whereas the spectrum C admits the lowest number, followed by the spectrum A. From the acquisition A, 247883 counts were detected by the gamma camera in 60seconds. In the acquisition B, 266000 counts were detected and from the acquisition C, 102271 counts were identified by the detector.

The different values of the detector counts are explained by the setting-up used in each acquisition. Such as represented in figure 4.23., in the acquisition B the source is upon the collimator, which provides a highest absorption of photons. On the other hand, the interaction of

the photons with the slabs of perspex causes many scattered photons. Therefore, fewer amounts of photons are absorbed and the highest left portion of the spectrum appears due to the scattered and backscattered γ-rays.

For the same reason, it is expected that the images of the acquisitions A and B will appear with better spatial resolution than image obtained from acquisition C, which should appear more blurred. Applying the developed Matlab code to create a binary image from the decoding list mode data, one obtains the following figure.

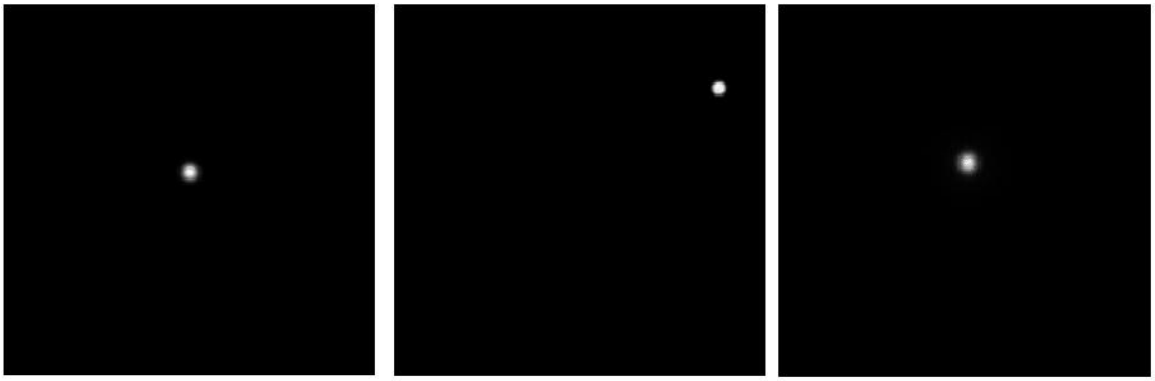

A **B** **C**

Figure 4.25. Binary images obtained from the Matlab code. Images acquired from the processed list mode data and obtained from the three different setting-up. A) cylindrical source placed in the centre of the patient table, B) cylindrical source placed in the corner of the collimator and C) cylindrical source placed in the centre of the patient table with 5slabs of perspex

The images were obtained with a matrix size of 256x256, a binary image with 16bits (2bytes), an energy window of 20% (±10%), a photopeak on the 140.5keV, which imply an energy range starting in 126.5keV up to 154.5keV. The value of the FOV was defined as 56.5cm (values of the GE NM/CT 670) which imply a pixel size approximately of 2.2mm, by the formula: pixel size=FOV/matrix size. All the formulas required to create the images are in the Matlab code, in appendix 5.

After the decoding of the list mode data by the specific program and the spectra construction, one verified that all the spectra represented in figure 4.24. were continuously distributed, whereas only the values inside of the energy window defined by the user (140.5±10% and 450±10%) should appear in the spectra. Once there was no photon interaction with an energy absorption highest than 176keV, only one photopeak was supposed to appear in the spectra (140.5±10%). Therefore, the decoding list mode files were analysed. In the files, one notices that there were some incident photons with different energies but the same X and Y positions. One realised that the duplicated values were related with the photons that reached the crystal with energies outside the energy window defined by the operator. Consequently, the position of

those photons was equal to the last position of the incident photon with energy between the acceptable values. These duplicated position values do not affect the image but only the spectra. Thus, after the mistake discovered the program to decoding the list mode data obtained from the planar acquisitions was modified and the duplicated values were eliminated.

The first acquisition - cylindrical source placed in the centre of the patient bed (acquisition A), was repeated in order to recognise the spectrum which takes into account the energy window selected by the user. Figure 4.26., shows the correct ^{99m}Tc spectrum where the photons are absorbed with energy inside the energy window selected. Such as the spectra above, also this spectrum was plotted with an energy binned of 2keV, starting in 36keV up to 176keV. Figure 4.27., illustrates the duplicated position values which correspond to the absorbed photons with energy outside the energy window.

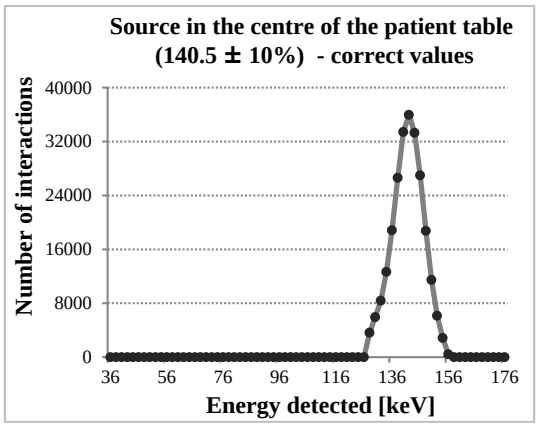

Figure 4.26. ^{99m}Tc spectrum by incident photons with energies inside the energy window selected

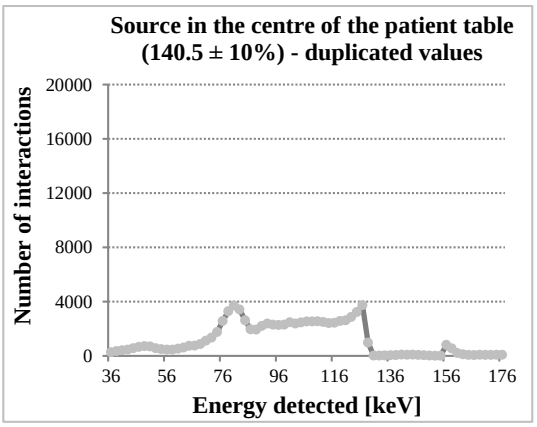

Figure 4.27. ^{99m}Tc spectrum by incident photons with energies outside the energy window selected

One verifies that if both spectra were overlapping, the resultant spectrum would represent the spectrum A in the figure 4.24. Thus, the decoding program was tested and validated. To test once more the correct decoding program other measurement was undertaken.

4.3.2. List mode acquisition with one energy window (256±100%) defining the full energy spectrum

The last measurement undertaken to validate the correct program to decoding the list mode data had the same setting-up as the image A of the figure 4.23., *i.e.*, the ^{99m}Tc source was placed in the centre of the patient table and the inferior head served as detector. In this planar acquisition the LEGP collimator was used. Only one energy window was selected in the *GE Xeleris* software, 256keV±100%, which means that a full energy range was defined, from 0keV up to

512keV. After the acquisition, the list mode data were decoded by the specific program and once again, the column of the energy of the raw processed data was used to plot a histogram of the total number of photons detected by the gamma camera *vs.* their energy, also with an energy binned of 2keV. Despite the fact of the full energy window has been select the maximum energy binned in the spectrum was 176keV, because only an insignificant percentage of photons were detected with highest values. By reducing the energy range in the spectrum the photopeaks are more easily visible.

Since a full energy window was selected, it is expected visualise a continuous spectrum after the decoding of the list mode files. Figure 4.28., shows the ^{99m}Tc spectrum, plotted up to 176keV of energy, instead of 512keV as it was expected since the full energy window was selected. Figure 4.29., illustrates the binary image after applying the developed Matlab code.

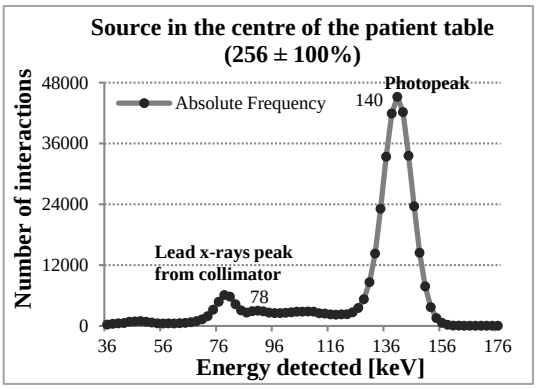

Figure 4.28. ^{99m}Tc spectra acquired in a 60sec planar acquisitions, using a LEGP collimator and one energy window, 256±100%. The cylindrical source was placed in the centre of the patient table

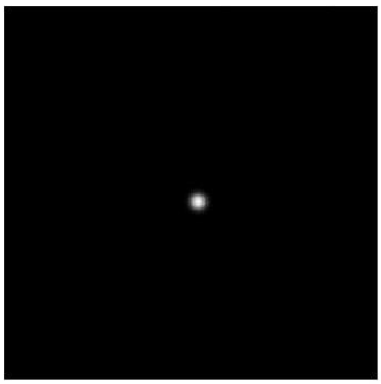

Figure 4.29. Binary image obtained from the Matlab code by using the processed list mode data. The cylindrical source was placed in the centre of the patient table

The binary image were obtained with a matrix size of 256x256, with 16bits (2bytes), an energy window of 200% (±100%), a photopeak on the 256keV, which imply a full energy range starting in 0keV up to 512keV. The value of the FOV was defined as 56.5cm (values of the GE NM/CT 670) which imply a pixel size approximately of 2.2mm, by the formula: pixel size=FOV/matrix size.

Analysing the figure 4.28., as it was expected the ^{99m}Tc spectrum is continuously distributed, proving once again the veracity of the decoding program.

In all these measurements, the histograms were plotted with 2keV of energy bin. This value may change according to the specifications of the investigator, as well as, the energy window selected. This could be an asset to be used in further investigations of bremsstrahlung imaging.

CHAPTER 5.

CONCLUSION

5. CONCLUSION

TRT has becoming increasingly important because of the number of treatments that it now offers to both malignant and non-malignant conditions. Relatively high-energy pure beta particle emitters, such as ^{90}Y, are the most used radionuclides in therapeutic nuclear medicine, with the consequent production *in vivo* of bremsstrahlung photons. As a result, it is crucial to perform new dosimetric calculations in order to measure the absorbed dose when TRT is performed, namely in radioimmunotherapy, since higher quantities of activity are administered.

At a dosimetric level, the bremsstrahlung photons have an important role. Despite the fact that hese photons increase the absorbed dose in the patient, they are the only radiation able to be detected externally when the high-energy pure beta particles are administered. Thus, bremsstrahlung imaging may allow a dedicate treatment planning (pre-therapy), in order to achieve an optimal activity administered to minimise the absorbed dose by the organs, and also the verification of the dose delivered (post-therapy). Nevertheless, there are great challenges in bremsstrahlung imaging. Therefore, in many cases, the actual doses delivered are not verified and are simply based on pre-therapy dosimetry. On the other hand, in some circumstances, the administered activity is determined by minimum toxicity levels established in clinical trials. Accordingly, there are great benefits in to know the features of the bremsstrahlung photons in order to facilitate their detection externally.

The present dissertation reports the development of a study of the characteristics of bremsstrahlung photons obtained through Monte Carlo simulations. The project aim was to investigate the characteristics and the behaviour of bremsstrahlung photons, produced by the emission of fast electrons in different biological homogeneous media. To reach this purpose the EGSnrc software (V4 2.3.2), a package of Monte Carlo simulation, was used. With this study, it was also intended to obtain a strong knowledge of EGSnrc system in order to be able to modify and produce a wide range of different simulations. Mortran codes were developed to simulate photon and electron transport.

A source of photons was initially used to attain a complete knowledge of the EGSnrc system and to allow an easy interpretation of the results, since photons are easily understandable. Basic simulations with photons were firstly undertaken to test the proper working of the developed codes by comparing the results with the theory. The conditions simulated were in accordance with the theoretical and published data and therefore the codes were validated and their accuracy proved. Afterward, monoenergetic electron sources were simulated in four different biological media, namely, cortical bone, inflated lung, soft tissue and adipose tissue, with the

intention to study the bremsstrahlung photons. The pure beta emitters ^{90}Y and ^{32}P were also simulated by using their polyenergetic spectra.

Results showed that the bremsstrahlung efficiency increases with the electron's kinetic energy and also with the effective atomic number of the material. Cortical bone showed to be 38% more efficient than the lung, 39% more efficient than the soft tissue and 48% more efficient than the adipose tissue, when the electrons were emitted with 1.5MeV of kinetic energy. The production efficiency also became constant, for a particular electron kinetic energy, which implies a maximum electron range where the bremsstrahlung photons might be produced. For electrons with 1.5MeV kinetic energy, it was found that the maximum distance from which the bremsstrahlung efficiency has become constant depends of the material. In the cortical bone this distance is equal to 0.5cm, in the inflated lung it is 3cm and in the soft tissue and adipose tissue the value is equal to 0.75cm. After these maximum distances, the 1.5MeV electrons cannot produce any bremsstrahlung photons and therefore the efficiency remains independently of the material thickness.

Also, results revealed that the bremsstrahlung yield (%) was less than 1% when 10^6 beta particles were emitted with energies up to 3MeV, in inflated lung, soft tissue and adipose tissue. In the cortical bone, bremsstrahlung yield was less than 1% for electrons with kinetic energy up to 1.5MeV, and 1.7% for electrons with 3MeV kinetic energy.

When 10^6 electrons were emitted with 500keV in the four biological materials studied, the bremsstrahlung spectra obtained were normalized and the results showed that the composition of the material has reasonably little effect on the shape of the bremsstrahlung spectra. This means that the data of the bremsstrahlung photons obtained in one of these materials, may be used in any other study with other of these materials, if the data are normalized.

The simulation of the angular distribution of the bremsstrahlung emission revealed, in all the materials, that the tendency for backward emission decreases with increasing electron kinetic energy, in comparison with the electron direction. When the electron kinetic energy increases, bremsstrahlung photons are mainly emitted in a forward direction. It was concluded the effective atomic number of the material is slightly important in the angular bremsstrahlung distribution. On the other hand, the simulation of the spatial distribution of the bremsstrahlung showed that the bremsstrahlung photons are produced further away from the point source with the increase of the electrons kinetic energy. Therefore, the higher the beta particles energy, the wider the spatial distribution of the bremsstrahlung photons produced.

^{90}Y and ^{32}P polyenergetic spectra were simulated, revelling that ^{90}Y produce more bremsstrahlung photons than ^{32}P, due to its wide energy spectrum. In the case of the ^{90}Y which is one of the most used radionuclides in TRT, for 10^7 beta particles emitted isotropically, the

results of the simulation showed that the number of the bremsstrahlung photons produced, absorbed and escaped from 1cm radius sphere, varied according to the material used in the simulation. The cortical bone was the material in which the electron interactions produced the highest number of bremsstrahlung photons, followed by the soft tissue, adipose tissue and inflated lung. On the other hand, inflated lung has revealed as the material in which more bremsstrahlung photons escape from 1cm radius sphere, followed by the adipose tissue, soft tissue and cortical bone. Thus, it was concluded that, cortical bone is the material which absorbs more photons inside 1cm radius sphere, followed by the soft tissue, adipose tissue and finally inflated lung.

All the bremsstrahlung spectra showed three main characteristics: they are continuous (without a photopeak), they include high-energy photons (difficult to be stopped by the collimator) and they are of low intensity. These features confirm the challenges of imaging the pure beta emitters, explained in detail in section 2.3.4.

With the knowledge and understanding of the bremsstrahlung photons production, one expects contribute with useful and significant information to future investigations. There are relevant issues regarding to the formation of the bremsstrahlung image which require particular attention. If the bremsstrahlung imaging is improved, a patient-specific dosimetry can be done and consequently a reduction in the patient dose might be achieved. It would be essential expand the study and use the acquired information to find the better performance parameters of the gamma camera in order to maximise the quality of the bremsstrahlung image.

Due to the fact that this is an emerging area and in great development needs, further studies are required in order to establish and confirm the benefits of the practice, namely in the dosimetry field, to understand the real uptake of radionuclides in the patients treated by radionuclide therapy.

5.1. Future work

It would be convenient to extend the study in order to relate and adapt the bremsstrahlung characteristics to the gamma camera performances. Should be undertaken an investigation to improve quantitative bremsstrahlung image.

Modifications in gamma camera instrumentation, on the imaging protocol or in computational algorithms and reconstruction, according to the bremsstrahlung features may improve imaging in TRT. Recent investigations shows (see Minarik *et al*., 2010) that adequate compensations for attenuation, scatter, and collimator response make ^{90}Y bremsstrahlung imaging feasible, with a relatively good image quality and useful quantitative accuracy.

For dosimetric purposes, the information available may be of great importance for absorbed-dose planning of high-dose radioimmunotherapy and for future improved dosimetry protocols, such as for present ^{90}Y-based radionuclide therapies. New advances and developments in the patient-planning procedures should also be considered, as well as new protocols and measurements at a dosimetric level to regulate the exposure dose of the staff (mainly inside the gamma camera room) and general public, due to bremsstrahlung photons.

Individualised image-based treatment promises dramatic benefits. A specific treatment plan for every TRT patient is an important procedure, both for the safety of the patient, as well as the protection of the staff and visitors, in order to measure the real absorbed dose.

In the future, improvements in the bremsstrahlung imaging and, consequently, in the patient-specific dosimetry planning are necessary and indispensable.

REFERENCES

REFERENCES

ABBAS N., HEYERDAHL H., BRULAND O.S., BORREBÆK J., NESLAND J. & DAHLE J. (2011). Experimental α-particle radioimmunotherapy of breast cancer using ^{227}Th-labeled p-benzyl-DOTA-trastuzumab. *EJNMMI Research* 1:18

ADVANCED LABORATORY OF PHYSICS. (2001). *Interactions of Gammas*. University of Wisconsin, Madison, Wisconsin, USA. Available: http://www.hep.wisc.edu/~prepost/407/gamma/gamma.pdf. [Accessed: 2 Sep 2012]

ALPEN E.L. (1990). *Radiation Biophysics*. 2nd ed. Academic Press. San Diego, CA, USA

ANDERSON L. (2007). *Compton Scattering*. Physics-Astronomy Department, University of Washington, Seattle, USA. Available: http://www.astro.washington.edu/users/lmanders/compton.pdf. [Accessed: 2 Sep 2012].

ATTIX F.H. (2004). *Introduction to Radiological Physics and Radiation Dosimetry*. 2nd ed. WILEY-VCH Verlag GmbH & Co. KGaA. Weinheim, Germany

BAERT A.L. & SARTOR K. (2006). Diagnostic Nuclear Medicine. 2nd ed. Christiaan Schiepers. Los Angeles, USA

BARNES W.E. (1996). Basic Physics of Nuclear Medicine. In Henkin R.E., Boles M.A., Dillehay G.L., Halama J.R., Karesh S.M., Wagner R.H. & Zimmer A.M. (Eds.). *Nuclear Medicine: The Scientific Basis of Nuclear Medicine*. Vol. 2, 1st ed. Mosby. St Louis, Missouri, USA. pp. 43-63

BECKER-SZENDYL R., ANTHONY P., BOSTED P., *et al.,* (1993). Quantum-Mechanical Suppression of Bremsstrahlung. Presentation at the 21st Annual SLAC Summer Institute on ParticJe Physics;Stanford, CA, and the 23rd International Symposium on Ultra-High-Energy Multiparticle Phenomena, Aspen, CO

BERGER M.J., COURSEY J.S., ZUCKER M.A. & CHANG J. (2005). *ESTAR, PSTAR, and ASTAR: Computer Programs for Calculating Stopping-Power and Range Tables for Electrons, Protons, and Helium Ions* (version 1.2.3). National Institute of Standards and Technology, Gaithersburg, MD. Available: http://physics.nist.gov/PhysRefData/Star/Text/method.html. [Accessed: 10 Nov. 2012]

BERGER M.J., COURSEY J.S., ZUCKER M.A. & CHANG J. (2011). Stopping-Power and Range Tables for Electrons, Protons, and Helium Ions. NIST, Standard Reference Database, ESTAR Database. Available: http://www.nist.gov/pml/data/xcom/index.cfm. [Accessed: 22 September 2012]

BIELAJEW A.F. (1995) HOWFAR and HOWNEAR: Geometry Modeling for Monte Carlo Particle Transport. PIRS-0341. IRS, INMS, NRC. Ottawa, Canada

BNMS: British Nuclear Medicine Society. (2010). *What is Nuclear Medicine*. Available: http://www.bnms.org.uk/nuclear-medicine-for-patients/. [Accessed: 22 July 2012]

BRITTON K.E. (1995). Nuclear Medicine, State Of The Art and Science. *Radiography* 1: 13 - 27

BROWN F.B. (2009). *Fundamentals of Monte Carlo Particle Transport*. Los Alamos National Laboratory. California, USA

BUSHBERG J.T., SEIBERT J.A., LEIDHOLDT E.M. & BOONE J.M. (2002). *The Essential Physics of Medical Imaging*. 2nd ed. Lippincott Williams & Wilkins. Philadelphia, USA

CALDERARO E. (2004). Evaluation using m.c.n.p. code of the bremsstrahlung energy spectrum produced by interactions between structural materials and accelerated electrons. *Radiation Physics and Chemistry* 71: 277–279

CASTO J. (2008). *Radiation Safety Technical Guide*. UCSB Environmental Health & Safety. Available: http://www.ehs.ucsb.edu/units/rad/radrsc/radsaftypdfs/technicalguide.pdf. [Accessed: 3 Sep 2012]

CENGIZ A. & ALMAZ E. (2004). Internal bremsstrahlung spectra of β^- particle emitters using the Monte Carlo method. *Radiation Physics and Chemistry* 70: 661–668

CHERRY S.R., SORENSON J.A. & PHELPS, M.E. (2003). *Physics in Nuclear Medicine*. 3rd ed. Saunders/Elsevier. Philadelphia, USA

DENARDO G.L., SIANTAR C.L.H. & DENARDO S.J. (2002). Radiation Dosimetry for Radionuclide Therapy in a Nonmyeloablative Strategy. *Cancer Biotherapy & Radiopharmaceuticals 17:107-118*

EARY J.F. (2007). Principles of Therapy with Unsealed Sources. In Eary J.F. & Brenner W. (Eds.). *Nuclear Medicine Therapy*. Informa Healthcare. NY, USA

EARY J.F. & BRENNER W. (2007). *Nuclear Medicine Therapy*. Informa Healthcare. NY, SA

ERSAHIN D., DODDAMANE I. & CHENG D. (2011). Targeted Radionuclide Therapy. *Cancers 3*, 3838-3855

EVANS R.D. (1955). *The Atomic Nucleus*. 1st ed. McGRAW-Hill Publishing Company LTD

FABBRI C., SARTI G., CREMONESI M., *et al.* (2009). Quantitative Analysis of ^{90}Y Bremsstrahlung SPECT-CT Images for Application to 3D Patient-Specific Dosimetry. *Cancer Biotherapy & Radiopharmaceuticals* 24: 145-155

FAHEY F.H. & HARKNESS B.A. (1996). SPECT Imaging with Rotating Gamma Camera Systems. In Henkin R.E., Boles M.A., Dillehay G.L., Halama J.R., Karesh S.M., Wagner R.H. & Zimmer A.M. (Eds.). *Nuclear Medicine: The Scientific Basis of Nuclear Medicine*. Vol. 2, 1st ed. Mosby. St Louis, Missouri, USA. pp. 232-246

FARSTAD B. (2012). Radiopharmacy Technology. In Lantheus Medical Imaging et al. (Eds.). *The Radiopharmacy: A Technologist's Guide*. European Association of nuclear Medicine. Vienna, Austria. pp. 6-7. Available: http://www.eanm.org/publications/tech_guidelines/docs/tech_radiopharmacy.pdf. [Accessed: 5 Sep 2012]

FLUX G. (2006). Dosimetry for Targeted Radionuclide Therapy. Physics and Radiotherapy ICR Annual Research Report. United Kingdom. Available: http://www.icr.ac.uk/about_us/annual_research_report/5872.pdf. [Accessed: 24 July 2012]

FLUX G., BARDIES M., MONSIEURS M., *et al.* (2006). The Impact of PET and SPECT on Dosimetry for Targeted Radionuclide Therapy. *Z. Med. Phys* 16: 47–59

FRANCESCO G., BODEI L., CHIESA C., *et al.* (2011). EANM procedure guideline for the treatment of liver cancer and liver metastases with intra-arterial radioactive compounds. *Eur J Nucl Med Mol Imaging* 1-14

GE Healthcare. (2011). *GE Discovery NM630*, GE 630Brochure. Available: http://www3.gehealthcare.co.uk/~/media/Downloads/us/Product/Product-Categories/Nuclear-Medicine/General-Purpose-Scanners/Discovery-NM630/GEHealthcare-Brochure_Discovery-NM-630.pdf?Parent=%7B3A683558-8CF2-4C0D-ACD6-0A1C0CAADB15%7D. [Accessed: 20 Sep 2012]

GE Healthcare. (2010). GE *Discovery NM/CT 670*. Available: http://www.supplychain.nhs.uk/capital/medical-imaging/product-categories/gamma-cameras/~/media/Files/Capital/GE_SPECT%20CT_Discovery%20NM%20670.ashx. [Accessed: 24 Oct 2012].

GRAHAM M.M. & METTER D.F. (2007). Evolution of Nuclear Medicine Training: Past, Present, and Future. *J Nucl Med* 48:257–268

GROCH M. & ERWIN W.D. (2000). SPECT in the Year 2000: Basic Principles. *J.Nuc.Med.Tech* 28(4): 233-244

GULEC S.A. & SIEGEL J.A. (2007). Posttherapy Radiation Safety Considerations in Radiomicrosphere Treatment with ^{90}Y-Microspheres. *J Nucl Med* 48:2080–2086

HEARD S. (2007). *Bremsstrahlung Imaging for Radionuclide Therapy*. Dissertation for Doctor of Philosophy. Institute of Cancer Research, UCL, London

HELLER S. & ZANZONICO P. (2011). Nuclear Probes and Intraoperative Gamma Cameras. *Semin Nucl Med* 41:166-181

HSS: Health, Safety and Security. Advisory Committee on Human Radiation Experiments. (1995). ACHRE Final Report - What Is Radioactivity? Available: http://www.hss.energy.gov/healthsafety/ohre/roadmap/achre/intro_9_2.html. [Accessed: 4 October 2012]

IAEA. (2003). *IAEA Quality Control Atlas for Scintillation Camera Systems*. Vienna, Austria

IAEA. (2005). Applying Radiation Safety Standards in Nuclear Medicine. IAEA Safety Related Publications. IAEA safety standards

IAEA. (2009a). *Quality Assurance for SPECT Systems*. IAEA Human Health Series No. 6. Vienna, Austria

IAEA. (2009b). *Release of Patients after Radionuclide Therapy*. Safety Reports Series No.63. Vienna, Austria

IAEA. (2010). The Development of Therapeutic Radiopharmaceuticals Based on ^{188}Re and ^{90}Y for Radionuclide Therapy. Report on the 2nd Research Coordination Meeting. Vienna, Austria

IRS/NRC. (2011). EGSnrc. Available: http://irs.inms.nrc.ca/software/egsnrc/egsnrc.html. [Accessed: 24 Oct 2012].

ISNAP: Institute for Structure and Nuclear Astrophysics. (2011). The Laws of Radioactive Decay. Available: http://isnap.nd.edu/Lectures/phys10262_2011/Chapter%20I-3%20Radioactive%20decay.pdf. [Accessed: 10 October 2012]

ITO S., KUROSAWA H., KASAHARA H., *et al.***,** (2009). ^{90}Y bremsstrahlung emission computed tomography using gamma cameras. *Ann Nucl Med* 23:257–267

JOHNS H.E. & CUNNINGHAM J.R. (1983). The Physics of Radiology. 4th ed. Charles C Thomas. Springfield, Illinois, USA

JOSEPH N. (2006). *Physical Principles of Ionizing Radiations*. CE Essentials LLC, Online Radiography Continuing Education for Radiologic X ray Technologist. Available: http://www.ceessentials.net/index.php [Accessed: 2 Sep 2012]

KANTZAS A., HAMILTON K., ZARABI T., BHARGAVA A., *et al.,* (2000). Application of gamma camera imaging and SPECT systems in chemical processes. *Chemical Engineering Journal* 77 (2000) 19–25

KARESH S.M. & LIPPS M. (2010). Properties of a Diagnostic Radiopharmaceutical. Tutorial from Consultants in Nuclear Medicine (CNMT), Chicago, USA. Available: http://www.nucmedtutorials.com/dwradiopharm/rad2.html. [Accessed: 5 Sep 2012]

KAWRAKOW I., MAINEGRA-HING E., ROGERS D.W.O., TESSIER F. & WALTERS B.R.B. (2011). The EGSnrc Code System: Monte Carlo Simulation of Electron and Photon Transport. National Research Council of Canada Report PIRS-701, Canada

KHAN F.M. (2003). The Physics of Radiation Therapy. 3rd ed. Lippincott Williams & Wilkins. Philadelphia, USA

KHAN A.N., AL-JAHDALI H., ABDULLAH K. *et al.*, (2011). Pulmonary vascular complications of chronic liver disease: Pathophysiology, imaging, and treatment. *Ann Thorac Med* 6:57-65

KIM E.E. & YANG D.J. (2001). *Targeted Molecular Imaging in Oncology*. 1st ed. Springer-Verlag. NY, USA

KINASE S., MOHAMMADI A. & TAKAHASHI M. (2011). Application of Monte Carlo Simulation and Voxel Models to Internal Dosimetry. *Japan Atomic Energy Agency*, Japan

KNOLL G.F. (2000). *Radiation Detection and Measurement*. 3rd ed. John Wiley & Sons. Hoboken. New Jersey, USA

KOCH H.W. & MOTZ J.W. (1959). Bremsstrahlung Cross-Section Formulas and Related Data. *Rev. Mod. Phys*. 31: 920–955

KRATOCHWIL C., GIESEL F. MORGENSTERN A., *et al.* (2011). Regional ^{213}Bi-DOTATOC peptide receptor alpha-therapy in patients with neuroendocrine liver metastases refractory to beta-radiation. *J Nucl Med*. 52 (S1):29

LAUTERBACH M.H., LEHMANN J. & ROSENOW U.F. (1999). Energy deposition of electrons in low-, medium- and high-Z material: Comparison of the Monte Carlo transport code EGS4 with experiment. *Nuclear Instruments and Methods in Physics Research* 152: 212-220

LEWINGTON V.J. (2003). Target Radionuclide Therapy for Neuroendocrine tumours. *Endocrine-Related Cancer* 10:497-501

LJUNGBERG M. & SJÖGREEN -GLEISNER K. (2011). The accuracy of absorbed dose estimates in tumours determined by Quantitative SPECT: A Monte Carlo study. *Acta Oncologica,* 50: 981–989

LNHB: Laboratoire National Henri Becquerel. (2006). Table de Radionucléides – 18F. Available: http://www.nucleide.org/DDEP_WG/Nuclides/F-18_tables.pdf. [Accessed: 2 October 2012]

LNHB: Laboratoire National Henri Becquerel. (2012). Table de Radionucléides – 14C. Available: http://www.nucleide.org/DDEP_WG/Nuclides/C-14_tables.pdf. [Accessed: 2 October 2012]

MANJUNATHA H.C. & RUDRASWAMY B. (2010). Bremsstrahlung exposure of tissues from beta-therapeutic nuclides. *Nuclear Instruments and Methods in Physics Research* A 621: 581–589

MARTIN C.J. & SUTTON D.G. (2002). Practical Radiation Protection in Health Care. Oxford University Press, NY, USA

MARTIN J.E. (2006). *Physics for radiation Protection*. 2nd ed. WILEY-VCH Verlag GmbH & Co. KGaA. Weinheim, Germany

METTLER F.A. & GUIBERTEAU M.J. (2006). *Essentials of Nuclear Medicine Imaging*. 5th ed. Saunders/Elsevier. Philadelphia, USA. pp. 1-43

MINARIK D., GLEISNER K.S. & LJUNGBERG M. (2008). Evaluation of quantitative 90Y SPECT based on experimental phantom studies. *Phys. Med. Biol*. 53:5689–5703

MINARIK D., LJUNGBERG M., SEGARS P. & SJÖGREEN-GLEISNER K. (2009). Evaluation of quantitative planar ^{90}Y bremsstrahlung whole-body imaging. *Phys Med Biol* 54 5873–5883

MINARIK D., SJÖGREEN-GLEISNER K., LINDEN O., WINGÅRDH K., TENNVALL J., STRAND S. & LJUNGBERG M. (2010). ^{90}Y Bremsstrahlung Imaging for Absorbed-Dose Assessment in High-Dose Radioimmunotherapy. *J Nucl Med* 51(12):1974-1978

MIT NSE. (2005). Interactions of Photons with Matter. Massachusetts, Cambridge, USA. Available: http://mightylib.mit.edu/Course%20Materials/22.01/Fall%202001/photons%20part%201.pdf. [Accessed: 3 Sep 2012]

MIT OCW NSE. (2007a). Interactions of Photons with Matter. MIT OpenCourseWarE Massachusetts, Cambridge, USA. Available: http://ocw.mit.edu/courses/nuclear-

engineering/22-01-introduction-to-ionizing-radiation-fall-2006/lecture-notes/energy_dep_photo.pdf. [Accessed: 3 Sep 2012]

MIT OCW NSE. (2007b). Energy deposition by light charged particles. MIT OpenCourseWarE Massachusetts, Cambridge, USA. Available: http://ocw.mit.edu/courses/nuclear-engineering/22-01-introduction-to-ionizing-radiation-fall-2006/lecture-notes/energy_dep_elect.pdf. [Accessed: 10 Sep 2012]

MURTY R.C. (1965). Effective Atomic Numbers of Heterogeneous Materials. *Nature* 207: 398-399

NAS: National Academy of Sciences. (2007). *Glossary and Acronyms*. Available: http://www.ncbi.nlm.nih.gov/books/NBK11480/. [Accessed: 22 June 2012]

NATIONAL RESEARCH COUNCIL. Committee on State of the Science of Nuclear Medicine. (2007). *Advancing Nuclear Medicine through Innovation*. National Academies Press. Washington (DC), USA

NATTER F.A., GRABMAYR P., HEHL T., OWENS R.O. & WUNDERLICH S. (2003). Monte Carlo simulation and analytical calculation of coherent bremsstrahlung and its polarization. *Nuclear Instruments and Methods in Physics Research* 211: 465–486

NELSON W.R. & JENKINS T.M. (1988).Writing SUBROUTINE HOWFAR for EGS4. Stanford Linear Accelerator Center. Stanford, California, USA

NESTOR M. (2012). Targeted Radionuclide Therapy of Head and Neck Cancer. Biomedical Radiation Sciences, Medical Faculty, Uppsala University. Uppsala, Sweden. Available: http://www.bms.uu.se/node121. [Accessed: 22 Oct 2012]

NDT RESOURCE CENTER. (2007). *Compton Scattering*. Iowa State University, Iowa, USA

NEWS MEDICAL. (2012a). History of Nuclear Medicine. Available: http://www.news-medical.net/health/History-of-Nuclear-Medicine.aspx. [Accessed: 22 July 2012]

PEEPLES J.P. & GARDNER R.P. (2012). Monte Carlo simulation of the nonlinear full peak energy responses for gamma ray scintillation detectors. *Applied Radiation and Isotopes* 70:1058–1062

PETERSON T.E. & FURENLID L.R. (2011). SPECT detectors: the Anger Camera and beyond. *Phys. Med. Biol.* 56: R145–R182

PODGORSA E.B. (2010). *Biological and Medical Physics, Biomedical Engineering.*2nd ed. Berlin, Heidelberg: Springer

PREKEGES J. (2009). *Nuclear Medicine Instrumentation*, 1st ed. Jones & Bartlett Publishers. London, UK

RADAR, The RAdiation Dose Assessment Resource (2012). The Decay Data. Available: http://www.doseinfo-radar.com/RADARDecay.html. [Accessed: 24 October 2012]

RAJENDRAN J.G. (2007). Therapeutic Radioisotopes. In Eary J.F. & Brenner W. (Eds.). *Nuclear Medicine Therapy*. Informa Healthcare. NY, USA

RHYMER S.M., PARKER J.A. & PALMER M.R. (2010). Detection of 90Y Extravasation by Bremsstrahlung Imaging for Patients Undergoing 90Y-Ibritumomab Tiuxetan Therapy. *J Nucl Med Technol* 38:195–198

ROGERS D.W.O. (2006). Fifty years of Monte Carlo simulations for medical physics. *Phys. Med. Biol*. 51: R287–R301

ROGERS D.W.O. & BIELAJEW A.F. (2012). *Monte Carlo Techniques of Electron and Photon Transport for Radiation Dosimetry*. Division of Physics, National Research Council of Canada. Ottawa, Ontario, Canada

RONG X., DU Y., LJUNGBERG M., RAULT E., VANDENBERGHE S. & FREY E.C. (2012). Development and evaluation of an improved quantitative ^{90}Y bremsstrahlung SPECT method. *Med Phys* 39(5):2346-58

RUI ASSIS (2012) Estatística aplica - Análise frequência.XLS. Rui Assis Homepage. Available: http://www.rassis.com/ [Accessed: 15 Dec. 2012]

RYDER H. (2012). Radiopharmacy. In Lantheus Medical Imaging *et al*. (Eds.). *The Radiopharmacy: A Technologist's Guide*. European Association of nuclear Medicine. Vienna, Austria. pp. 22-25. Available: http://www.eanm.org/publications/tech_guidelines/docs/tech_radiopharmacy.pdf. [Accessed: 5 Sep 2012]

SADEK S. (2003). *Radiopharmaceuticals*. New York Medical College. St. Vincent's Hospital, Manhattan, USA

SAHA G.B. (2013). Physics and Radiobiology of Nuclear Medicine. 4th ed. Springer Science. NY, USA

SALVAT F., FERNANDEZ-VAREA J.M., SEMPAU J. & LLOVET X. (2006). Monte Carlo simulation of bremsstrahlung emission by electrons. *Radiation Physics and Chemistry* 75: 1201–1219

SELTZER S.M. & BERGER M.J. (1986). Bremsstrahlung Energy Spectra from Electrons with Kinetic Energy 1KeV-10GeV Incident on Screened Nuclei and Orbital Electrons of Neutral Atoms with Z = 1-100*. *Atomic Data and Nuclear Data tables* 35: 345-418

SGC: Saint-Global Crystals. (2008). *Efficiency Calculations for Selected Scintillators*. Saint-Gobain Ceramics & Plastics, Inc. Ohio, USA

SIMMONS G. (1996). Gamma Camera Imaging Systems. In Henkin R.E., Boles M.A., Dillehay G.L., Halama J.R., Karesh S.M., Wagner R.H. & Zimmer A.M. (Eds.). *Nuclear Medicine: The Scientific Basis of Nuclear Medicine*. Vol. 2, 1st ed., St Louis: Mosby. pp. 85-94

SINGH M. & WALUCH V. (2000). Physics and instrumentation for imaging in-vivo drug distribution. *Advanced Drug Delivery Reviews* 41: 7–20

SNMMI: Society of Nuclear Medicine and Molecular Imaging. (2004). *What is Nuclear Medicine*. Available: http://interactive.snm.org/docs/whatisnucmed.pdf. [Accessed: 22 July 2012]

SNMMI: **Society of Nuclear Medicine and Molecular Imaging**. (2012). *Glossary and Terminology*. Available: http://www.molecularimagingcenter.org/index.cfm?PageID=7834#metabolism. [Accessed: 22 June 2012]

SPRAWLS P. (1993). *The Physical Principles of Medical Imaging*. 2nd ed. Aspen Publication. NY, USA

STABIN M.G. (2007). *Radiation Protection and Dosimetry: An Introduction to Health Physics*. 1st ed. Springer. NY, USA

STANCIU A.E. (2012). Radionuclides in Targeted Therapy of Cancer. *Rev. Roum. Chim. 57*: 5-13

STOKKEL M.P.M., JUNAK D.H., LASSMANN M., *et al.*, (2010). EANM procedure guidelines for therapy of benign thyroid disease. *Eur J Nucl Med Mol Imaging* 37:2218–2228

STRYDOM W., PARKER W. & OLIVARES M. (2005). *Electron Beams: Physical and Clinical Aspects*. International Atomic Energy Agency (IAEA). Department of Medical Physics. Available: http://www-naweb.iaea.org/nahu/DMRP/documents/Chapter8.pdf. [Accessed: 3 Sep 2012]

TEMPLEMAN C.L. (2000). *The Compton Effect*. Physics Department, The College of Wooster. Wooster, Ohio

TENNVALL J. & BRANS B. (2007). EANM procedure guideline for ^{32}P phosphate treatment of myeloproliferative diseases. *Eur J Nucl Med Mol Imaging* 34:1324–1327

TENNVALL J., FISCHER M., DELALOYE A.B., *et al.*, (2007). EANM procedure guideline of radio-immunotherapy for B-cell lymphoma with ^{90}Y-radiolabeled ibritumomab tiuxetan (Zevalin®). *J Nucl Med* 48: 1871-1879

TSUI B.M.W. (1996). Quantitative SPECT. In Henkin R.E., Boles M.A., Dillehay G.L., Halama J.R., Karesh S.M., Wagner R.H. & Zimmer A.M. (Eds.). *Nuclear Medicine: The Scientific Basis of Nuclear Medicine*. Vol. 2, 1st ed. Mosby. St Louis, Missouri, USA. pp. 260-275

TURNER J.E. (2007). *Atoms, Radiation, and Radiation Protection*. WILEY-VCH Verlag GmbH & Co. KGaA. Weinheim, Germany

UCLH NHS FOUNDATION TRUST & UCL. (2011). The Institute of Nuclear Medicine 50 years. Springer Press. Heidelberg, Germany

USYD Department of Physics. (2012). *Interactions of Charged Particles with Matter*. University of Sydney, Physics School. Available: http://www.physics.usyd.edu.au/~kuncic/lectures/RP5_slides.pdf. [Accessed: 3 Sep 2012]

WALRAND S., FLUX G.D., KONIJNENBERG M.W., *et al.*, (2011). Dosimetry of yttrium-labelled radiopharmaceuticals for internal therapy: ^{86}Y or ^{90}Y imaging? *Eur J Nucl Med Mol Imaging* 38:S57–S68

WHEAT J.M., CURRIE G.M., Davidson R. & KIAT H. (2011). Radionuclide Therapy. *The Radiographer* 58: 53-59

WILDERMAN S.J. & DEWARAJA Y.K. (2007). Method for Fast CT/SPECT-Based 3D Monte Carlo Absorbed Dose Computations in Internal Emitter Therapy. *IEEE Trans Nucl Sci*. 54(1): 146–151

ZAIDI H. (2004). *Monte Carlo Techniques in Diagnostic and Therapeutic Nuclear Medicine*. IAEA-CN-96-65

ZANZONICO P.B., BINKERT B.L. & GOLDSMITH S.J. (1999). Bremsstrahlung Radiation Exposure from Pure β-Ray Emitters. *J Nucl Med* 40: 1024-1028

ZANZONICO P.B. (2000).Internal Radionuclide Radiation Dosimetry: A Review of Basic Concepts and Recent Developments. *J NucI Med* 41:297-308

ZIESSMAN H.A., O'MALLEY J.P. & THRALL J.H. (2006). *Nuclear Medicine: The Requisites.* 3rd ed. Mosby Elsevier. Philadelphia, USA

APPENDICES

APPENDICES

APPENDIX 1. The COMMON Blocks (Kawrakow *et al*., 2011, pp. 110-119)

Listed here are some of the COMMON blocks relevant to the user. To declare any of the COMMON blocks the COMIN macro need to be written. For example, COMIN/STACK,BOUNDS/; will automatically expand to the correct COMMON/STACK/; and COMMON/BOUNDS/; forms.

COMMON BLOCK	VARIABLE	DESCRIPTION
BOUNDS	**ECUT**	Array of regions' charged particle cutoff energies(total) in MeV
	PCUT	Array of regions' photon cutoff energies in MeV
	VACDST	Distance to transport in vacuum (default=1)
EPCONT	**EDEP**	Energy deposited in MeV (Double Precision)
	TSTEP	Distance to next interaction (cm)
	TUSTEP	Total (curved) step length requested before check with geometry
	USTEP	straight step length calculated from TUSTEP
	TVSTEP	Actual total (curved) step length to be transported
	VSTEP	actual straight step length after truncation by geometry
	IDISC	User discard request flag (to be set in HOWFAR). IDISC>0 means user requests immediate discard, IDISC<0 means user requests discard after completion of transport, and IDISC=0 (default) means no user discard requested. IDISC=99 or −99 means generate annihilation photons when positron is discarded
	IROLD	Index of previous region
	IRNEW	Index of new region
	RHOF	Value of density correction (default=1) (i.e. ratio of real density to that of dataset
	EOLD	Charged particle (total) energy at beginning of step in MeV
	ENEW	Charged particle (total) energy at end of step in MeV
	IAUSFL	Array(29) of flags for turning on various calls to AUSGAB.
	EKE	Electron kinetic energy in MeV
	ELKE	Natural logarithm of EKE (this is not available for a step in vacuum)
	GLE	Natural logarithm of photon energy
	E_RANGE	For electron IARG=0 steps, this is the range of the electron in the current units (see section 3.11.1)
	x[y][z]_final	position at end of step
	u[v][w]_final	direction at end of step (only used for electrons)

ET-Control (Electron Transport Control)	**SMAXIR**	Array($MXREG) defining upper limit on step size in each region (in whatever units defined by DUNIT). (default=1).
	ESTEPE	Global energy loss constraint.(default=0.25).
	XIMAX	Max. first GS moment per step (roughly half the average MS angle squared.(default 0.5).
	SKINDEPTH_FOR_BCA	Distance from a boundary (in elastic MFP) at which to switch to one of the boundary crossing algorithms (BCAs).(default 3). If set 0 by the user initially and BCA_ALGORITHM = 1, then the code assigns a value consistent with BLCMIN in PRESTA-I, otherwise it is 3.0
	TRANSPORT_ALGORITHM	integer flag telling which transport algorithm to use 0*)* PRESTA-II; 1*)* PRESTA-I.(default 0)
	BCA_ALGORITHM	Integer flag telling which BCA to use. 0*)* use exact(single scattering) algorithm within SKINDEPTH FOR BCA of a boundary 1*)* use multiple scattering but with no lateral deflections within SKINDEPTH FOR BCA of a boundary. Default is 0
	SPIN_EFFECTS	Logical variable, .true.*)* use single & multiple scattering theories which include relativistic spin effects; .false.*)* use single and multiple scattering theories based on Rutherford scattering. (default .true.)
MEDIA	**MEDIA**	Array(24,$MXMED) of media names
	NMED	Number of media being used (default=1)
	IRAYLM	Array ($MXMED) of flags for turning on (=1) coherent (Rayleigh) scattering in various media. Set in HATCH based on values of IRAYLR.
	RLC	Array ($MXMED) containing radiation lengths of the media in cm.
	RLDU	Array($MXMED) containing radiation lengths of the media in distance units established by DUNIT.
	RHO	Array($MXMED) containing density of the media in g/cm**3.
	MGE	Array($MXMED) number of photon mapped energy intervals for a given medium
	MEKE	Array($MXMED) nuber of electron mapped energy intervals for a given medium.
	Comp_xsections	character*16 variable holding the name of the file containing user-supplied Compton cross section data. Full name of the file is

		$HEN HOUSE/data/comp xsections compton.data. Only used if IBCMP=2 (bound Compton, no doppler effect).
MISC	**MED**	Array($MXREG) containing medium index for each region.
	DUNIT	The distance unit to be used. DUNIT=1 (default) establishes all distances in cm; whereas, DUNIT=2.54 establishes all distances in inches.
STACK (data about the particles currently in the shower. All of the following variables are arrays($MXSTACK) except NP, NPold and LATCHI)	**E**	Total energy in MeV (Double Precision).
	X,Y,Z.	Position of particle in units established by DUNIT
	U,V,W	Direction cosines of particle (not necessarily normalized if table lookups used for sines
	DNEAR	A lower bound of distance from (X,Y,Z) to nearest surface of current region.
	WT	Statistical weight of current particle (default=1.0). To be used in conjunction with variance reduction techniques as determined by user.
	IQ	Integer charge of particle (+1,0,-1).
	IR	Index of particle's current region.
	NP	The stack pointer (i.e., the particle currently being pointed to). Also, the number of particles on the stack.
	NPold	Value of NP prior to an interaction (to test how many particles created
	LATCH	An integer variable for use to track histories.
	LATCHI	Initial value of LATCH(1) when shower called.
UPHIOT	**THETA**	Collision scattering angle (polar).
	SINTHE	Sine of THETA.
	COSTHE	Cosine of THETA.
	SINPHI	Sine of PHI (the azimuthal scattering angle of the collision).
	COSPHI	Cosine of PHI.
	PI	Pi.
	TWOPI	two Pi.
	PI5D2	2.5 × Pi.

APPENDIX 2. Specifications for AUSGAB (Kawrakow *et al.*, 2011)

The subroutine AUSGAB is called by EGS with the statement: *CALL AUSGAB(IARG);*

The argument IARG indicates the situation under which AUSGAB is being called. IARG can take on 29 values starting from zero (*i.e.,* IARG=0 through IARG=28), although only the first five are called by default in EGSnrc. The remaining 24 IARG values must be "switched-on" by means of the array IAUSFL, which is set by the value 1, in step 5: initialisation for AUSGAB.

Table 2.1. Values of IARG which are on by default and for which energy is deposited

IARG	Situation
0	Particle is going to be transported by distance TVSTEP
1	Particle is going to be discarded because its energy is below the cutoff ECUT (for charged particles) or PCUT (for photons)—but its energy is larger than the corresponding PEGS cutoff AE or AP, respectively.
2	Particle is going to be discarded because its energy is below both ECUT and AE (or PCUT and AP).
3	Particle is going to be discarded because the user requested it (in HOWFAR usually or by range rejection).
4	The difference between the energy of the incident particle and all of the final products is being deposited locally. This energy is due to sub-threshold relaxation events.

Table 2.2. Values of IARG which are off by default

IARG	IAUSFL	Situation
5	**6**	Particle has been transported by distance TVSTEP.
6	**7**	A bremsstrahlung interaction is to occur and a call to BREMS is about to be made in ELECTR.
7	**8**	Returned to ELECTR after a call to BREMS was made.
8	**9**	A Moller interaction is to occur and a call to MOLLER is about to be made in ELECTR.
9	**10**	Returned to ELECTR after a call to MOLLER was made.
10	**11**	A Bhabha interaction is to occur and a call to BHABHA is about to be made in ELECTR.
11	**12**	Returned to ELECTR after a call to BHABHA was made
12	**13**	An in-flight annihilation of the positron is to occur and a call to ANNIH is about to be made in ELECTR.

13	**14**	Returned to ELECTR after a call to ANNIH was made.
14	**15**	A positron has annihilated at rest.
15	**16**	A pair production interaction is to occur and a call to PAIR is about to be made in PHOTON.
16	**17**	Returned to PHOTON after a call to PAIR was made.
17	**18**	A Compton interaction is to occur and a call to COMPT is about to be made in PHOTON.
18	**19**	Returned to PHOTON after a call to COMPT was made.
19	**20**	A photoelectric interaction is to occur and a call to PHOTO is about to be made in PHOTON.
20	**21**	Returned to PHOTON after a call to PHOTO was made
21	**22**	Subroutine UPHI was just entered. Not entered in all cases now since the sampling is done more efficiently directly in some subroutines.
22	**23**	Subroutine UPHI was just exited
23	**24**	A coherent (Rayleigh) interaction is about to occur.
24	**25**	A coherent (Rayleigh) interaction has just occurred.
25	**26**	A fluorescent photon has just been created in RELAX.
26	**27**	A Coster-Kronig electron has just been created in RELAX.
27	**28**	An Auger electron has just been created in RELAX.
28	**29**	A positron is about to annihilate at rest.

APPENDIX 3. Scintillation Detector Model. EGSnrc code.

It is necessary take into account that the variables are changed according to the simulation.

```
%L
%E
!INDENT M4; "indent each mortran nesting level by 4"
!INDENT F2; "indent each fortran nesting level by 2"

$IMPLICIT-NONE;
$INTEGER I,J,K,L,NCASES,IQIN,IRIN,NHISTORIES;
$REAL XIN,YIN,ZIN,EIN,WTIN,UIN,VIN,WIN,TOTAL;


"-------------------------------------------------------------"
"STEP 1:  USER-OVERRIDE-OF-EGSnrc-MACROS                      "
"-------------------------------------------------------------"
"MACROS"

REPLACE{$CALL-HOWNEAR(#);}WITH{;CALL
HOWNEAR({P1},X(NP),Y(NP),Z(NP),IRL);}
"subroutine Hownear"

REPLACE {;COMIN/DATAOUT/;}WITH{;COMMON/DATAOUT/OUTDATA(1001,12),
ISAVE,ICOUNT,PHOTOELE,COMPTON,PAIRPROD;
$REAL OUTDATA;
$INTEGER ISAVE,ICOUNT,PHOTOELE,COMPTON,PAIRPROD;}
"common block to store the data in array with
"1000levels & 11parameters in the disk

REPLACE{;COMIN/SCORE/;}WITH{;COMMON/SCORE/ABSORBED,PHI,ITOTAL,HI
STNUM,
SPECT(3500),IABSORBED,TOTALSPECT;
$INTEGER SPECT,IABSORBED,TOTALSPECT,HISTNUM;
REAL*8 ABSORBED,PHI,ITOTAL;}
"define a common to pass information about geometry to the
subroutine Howfar"

REPLACE{$MXMED}WITH{2}      "2 medium in the problem"
REPLACE{$MXREG}WITH{10}      "only 8 geometric regions"
REPLACE{$MXSTACK}WITH{15}   "15 particles on stack at once"

"REGIONS-CRYSTAL/GLASS"
REPLACE {;COMIN/PLADTA/;} WITH {;COMMON/PLADTA/
PCOORD(3,$MXPLNS),PNORM(3,$MXPLNS);$REAL PCOORD,PNORM;}
REPLACE{$MXPLNS}WITH{10}   "max 10 planes"

REPLACE{$XTALPOSITION}WITH{5}  "thickness: position of the
crystal back"
REPLACE{$GLASSPOSITION}WITH{1+$XTALPOSITION}  "position of the
glass back"
REPLACE{$CRYSTALRG}WITH{7}  "region of the crystal"

"PARTICLE PARAMETERS"
```

```
REPLACE{$ZIN}WITH{-10}  "position of the particle: 10cm away"
REPLACE{$ENERGYPART}WITH{2.5} "energy of the particle 100keV
[MeV]"
REPLACE{$CHARGEPART}WITH{0} "Charge of the particle"
REPLACE{$MAXENERGY}WITH{3500}  "max energy of the spectra"

REPLACE{$ELOWER}WITH{3.511}   "ECUT energy"
REPLACE{$PLOWER}WITH{0.01}   "PCUT energy"
"electron histories terminates at 0.651MeV (0.140+0.511MeV)"
"photon histories terminates at 0.01MeV=10keV"

"Num. of levels to generate random numbers"
REPLACE{$luxury_level}WITH{2}
REPLACE{$iseed}WITH{314159265}

;COMIN/BOUNDS,MEDIA,MISC,THRESH,SCORE,EPCONT,STACK,
RANDOM,UPHIOT,DATAOUT,PLADTA/;
"The above expands into a series of COMMON statements;"
"call all the common blocks used with properly parameters"


"-------------------------------------------------------------"
"STEP 2 PRE-HATCH-CALL-INITIALIZATION                        "
"-------------------------------------------------------------"
CHARACTER*4 MEDARR(24);
DATA  MEDARR /$S'NaI_GLASS',15*' '/;

CHARACTER*4 MEDARR1(24);
DATA  MEDARR1 /$S'Glass',19*' '/;
"two mediums used; each name store in an array;"
"$ is a Mortran Macro to expand strings"

call egs_init; "---step0---"


NMED=2; "number of media used"

DO I=1,24[MEDIA(I,1)=MEDARR(I);]
DO I=1,24[MEDIA(I,2)=MEDARR1(I);]
"this is to avoid a DATA STATEMENT for a variable in COMMON"

DO I=1,6 [MED(I)=0;] "define the regions: region0=vacuum"
MED($CRYSTALRG)=1; "first region=NaI"
MED(8)=2; "second region=Glass"

%E
DO I=1,$MXREG [ECUT(I)=$ELOWER;PCUT(I)=$PLOWER;]
"define the energies to terminate histories of the particles"


"-------------------------------------------------------------"
"STEP 3   HATCH-CALL                                         "
"-------------------------------------------------------------"

;OUTPUT;('\f Start Test1'//'CALL HATCH to get cross-section
data'/);
```

```
CALL HATCH;   "pick up cross section data for NaI"
              "data file must be assigned to unit 12"

;OUTPUT AE(1)-0.511, AP(1);
(/'knock-on electrons can be created and any electron followed
down to:'
,F8.3,'MeV kinetic energy'
/'brem photons can be created and any photon followed down
to:',F8.3,'MeV');
"Compton events can create electrons and photons below these
cutoffs"


"-------------------------------------------------------------"
"STEP 4  INITIALIZATION-FOR-HOWFAR and HOWNEAR                "
"-------------------------------------------------------------"
"define thickness of the material"
"NaI is 1 cm thick; Glass is 1 cm thick"

"first pair of planes"
PCOORD(1,2)=0.0;
PCOORD(2,2)=0.0;
PCOORD(3,2)=0.0;
PNORM(1,2)=0.0;
PNORM(2,2)=0.0;
PNORM(3,2)=1.0; "normal vector in z direction"

PCOORD(1,7)=0.0;
PCOORD(2,7)=0.0;
PCOORD(3,7)=$XTALPOSITION; "NaI with 1cm"
PNORM(1,7)=0.0;
PNORM(2,7)=0.0;
PNORM(3,7)=1.0; "normal vector in z direction"

"second pair of planes"
PCOORD(1,1)=0.0;
PCOORD(2,1)=20;
PCOORD(3,1)=0.0;
PNORM(1,1)=0.0;
PNORM(2,1)=1.0; "normal vector in y direction"
PNORM(3,1)=0.0;

PCOORD(1,5)=0.0;
PCOORD(2,5)=-20;
PCOORD(3,5)=0.0;
PNORM(1,5)=0.0;
PNORM(2,5)=1.0; "normal vector in y direction"
PNORM(3,5)=0.0;

"third pair of planes"
PCOORD(1,3)=-20;
PCOORD(2,3)=0.0;
PCOORD(3,3)=0.0;
PNORM(1,3)=1.0; "normal vector in x direction"
PNORM(2,3)=0.0;
```

```
PNORM(3,3)=0.0;

PCOORD(1,4)=20;
PCOORD(2,4)=0.0; "normal vector in x direction"
PCOORD(3,4)=0.0;
PNORM(1,4)=1.0;
PNORM(2,4)=0.0;
PNORM(3,4)=0.0;

PCOORD(1,6)=0.0;
PCOORD(2,6)=0.0;
PCOORD(3,6)=$GLASSPOSITION; "Glass with 1cm"
PNORM(1,6)=0.0;
PNORM(2,6)=0.0;
PNORM(3,6)=1.0; "normal vector in Z direction"

PCOORD(1,8)=0.0;
PCOORD(2,8)=0.0;
PCOORD(3,8)=$ZIN-1; "collimator back"
PNORM(1,8)=0.0;
PNORM(2,8)=0.0;
PNORM(3,8)=1.0; "normal vector in Z direction"


"------------------------------------------------------------"
"STEP 5  INITIALIZATION-FOR-AUSGAB                          "
"------------------------------------------------------------"

$INITIALIZE RNG USING $luxury_level AND $iseed;
"Random number generator, with 2 luxury levels;
"luxury levels are from 0 to 4 and a period of greater than
10^165

IAUSFL(7)=1; "a bremsstrahlung interaction is to occur"
"and a call to BREMS is about to be made in ELECTR"
IAUSFL(8)=1; "returned to ELECTR after a call to BREMS was made"

IAUSFL(9)=1; "a Moller interaction is to occur and a call"
"to MOLLER is about to be made in ELECTR"
IAUSFL(10)=1; "returned to ELECTR after a call to MOLLER was
made"

IAUSFL(16)=1; "a pair production interaction is to occur and"
"a call to PAIR is about to be made in PHOTON"
IAUSFL(17)=1; "returned to PHOTON after a call to PAIR was made"

IAUSFL(18)=1; "a Compton interaction is to occur and a call"
"to COMPT is about to be made in PHOTON"
IAUSFL(19)=1; "returned to PHOTON after a call to COMPT was
made.

IAUSFL(20)=1; "a photoelectric interaction is to occur and"
"a call to PHOTO is about to be made in PHOTON"
IAUSFL(21)=1; "returned to PHOTON after a call to PHOTO was
made"
```

```
IAUSFL(24)=1; "a coherent (Rayleigh) interaction is about to
occur"
IAUSFL(25)=1; "a coherent (Rayleigh) interaction has just
occurred"

IAUSFL(26)=1; "a fluorescent photon has jsut been created in
RELAX"
IAUSFL(27)=1; "a  Coster-Kronig electron has just been created
in RELAX"
IAUSFL(28)=1; "an Auger electron has just been created in RELAX"


"------------------------------------------------------------"
"STEP 6   DETERMINATION-OF-INICIDENT-PARTICLE-PARAMETERS     "
"------------------------------------------------------------"

IQIN=$CHARGEPART; "charge of the incident particle - photon"
EIN=$ENERGYPART; "energy of the incident particle"
/YIN,XIN/=0; "incident particle at origin: particle position"
ZIN=$ZIN; "be sure that we start inside the region 7"

"UIN=0.8660254038;" "cos(30)"
"VIN=0;"
"WIN=0.5;" "cos(60)"

UIN=0;VIN=0;WIN=1; "particle moving along Z axis;"
"comment in isotropic emission"

IRIN=2; "start in region 7-inside crystal"
WTIN=1; "weight = 1 since no variance reduction used"
NCASES=100; "number of the loops for the histories"
NHISTORIES=10000;
"number of the histories inside each loop-more n°quickly"


"------------------------------------------------------------"
"STEP 7   SHOWER-CALL                                        "
"------------------------------------------------------------"
"Fortran language; to write something in text files;
"we need to place * in 5 position to change the line
%NL
%F
      OPEN(UNIT=7, FILE='ENERGY_X_Y.txt',
     *STATUS='UNKNOWN')
C     star continuation line before

      OPEN(UNIT=12, FILE='SPECTRA.txt',
     *STATUS='UNKNOWN')

%M

HISTNUM=0;
ITOTAL=0;
ISAVE=1; "array to store interest parameters-position 1"
PAIRPROD=0;
COMPTON=0;
```

```
PHOTOELE=0;

DO K=1,$MAXENERGY  [SPECT(K)=0.0;]
"array to count the number of photons with some specific energy"

"initiate the shower NCASES with NHISTORIES each time"
DO I=1,NCASES [ "OUTPUT I;(//'START LOOP BLOCK',I5,':');"
  DO J=1,NHISTORIES [ "OUTPUT J;(/'EMISSION',I6);"

ABSORBED=0.0; "Energy absorbed by the crystal in each history;
"place to zero each time shower is called

"Determining ISOTROPIC EMISSION"
"$RANDOMSET COSTHE;"
"COSTHE=2.*COSTHE-1;"
"SINTHE=SQRT(1.0-COSTHE**2);"
"$RANDOMSET PHI;" "Direction cosines with randomly angles"
"PHI=TWOPI*PHI;"
"UIN=SINTHE*COS(PHI);"
"VIN=SINTHE*SIN(PHI);"
"WIN=(COSTHE);" "towards"

";OUTPUT;(T2,'CH',T7,'RG',T11,'DEP.EN',T19,'TOT.DEP.EN',T31,"
"'ENERGY',T41,'XPOS',T50,'YPOS',T59,'ZPOS',T67,"
"'UPOS',T75,'VPOS',T83,'WPOS',T91,'ANGLE',T99,'IARG');"

HISTNUM=HISTNUM+1;

CALL SHOWER(IQIN,EIN,XIN,YIN,ZIN,UIN,VIN,WIN,IRIN,WTIN);

    ABSORBED=ABSORBED*1000; "pass energy to keV"
    IABSORBED=INT(ABSORBED+0.5); "pass energy to integer"
    SPECT(IABSORBED)=SPECT(IABSORBED)+1; "write an array to
store the number of photons with some specific energy"
   ]
]


"------------------------------------------------------------"
"STEP 8   OUTPUT-OF-RESULTS                                  "
"------------------------------------------------------------"

"counting number of photons absorbed according its energy"
"DO I=1,$MAXENERGY [ OUTPUT I,SPECT(I);(/,I4,T5,'KeV',"
"T10,'NUM.ABSORBED PHOTONS:',I10);]"

"total number of histories"
OUTPUT NCASES*NHISTORIES;(/'NUMBER OF EMISSIONS:',I10);

"total absorbed photons"
DO I=1,$MAXENERGY  [ TOTALSPECT=TOTALSPECT+SPECT(I);]
OUTPUT TOTALSPECT;(/'TOTAL ABSORBED PHOTONS:',I10);

;OUTPUT ITOTAL;(/'NUM.INTERACTIONS:',F20.0);

;OUTPUT PHOTOELE;(/,'NUM.PHOTOELECTRIC INTERACTIONS:',I20);
```

```
;OUTPUT COMPTON;(/,'NUM.COMPTON INTERACTIONS:',I20);
;OUTPUT PAIRPROD;(/,'NUM.PAIR PRODUCTION INTERACTIONS:',I20);

"newline format"
%NL
%F
      DO 90 L=1,ISAVE-1
      WRITE(7,91)OUTDATA(L,1),OUTDATA(L,2),OUTDATA
     *(L,3),OUTDATA(L,4),OUTDATA(L,5),OUTDATA(L,6),
     *OUTDATA(L,7),OUTDATA(L,8),OUTDATA(L,9)
90    CONTINUE
91    FORMAT(9F18.3)
      CLOSE(7)

      DO 70 L=1,3500
      WRITE(12,71)L,SPECT(L)
70    CONTINUE
71    FORMAT(2I14)
      CLOSE(12)

%M
"-------------------------------------------------------------"
"STEP 9   finish run                                         "
"-------------------------------------------------------------"
call egs_finish;
STOP;
END; "end of the Main Program routine"
%M


"************************************************************"
"                   SUBROUTINE AUSGAB                        "
"************************************************************"
%E
SUBROUTINE AUSGAB(IARG);
$IMPLICIT-NONE;
$INTEGER IARG,IRL;
$REAL ANGLE,EKINE;

COMIN/STACK,EPCONT,SCORE,UPHIOT,DATAOUT/;

"IF(IARG=6) [OUTPUT IARG;(/'BREMS OCCUR',I3);]"
"IF(IARG=7) [OUTPUT IARG;(/'EL AFTER BREMS OCCUR',I3);]"
"IF(IARG=8) [OUTPUT IARG;('MOLLER INT',I3);]"
"IF(IARG=9) [OUTPUT IARG;(/'EL AFTER MOLLER INT',I3);]"
"IF(IARG=15) [OUTPUT IARG;(/'PAIR PROD INT',I3);]"
"IF(IARG=16) [OUTPUT IARG;(/'PHOTON AFTER PAIR PROD',I3);]"
"IF(IARG=17) [OUTPUT IARG;(/'COMPTON INT',I3);]"
"IF(IARG=18) [OUTPUT IARG;(/'PHOTON AFTER COMPTON INT',I3);]"
"IF(IARG=19) [OUTPUT IARG;(/'PHOTOEL INT',I3);]"
"IF(IARG=20) [OUTPUT IARG;(/'PHOTON AFTER PHOTOEL INT',I3);]"
"IF(IARG=23) [OUTPUT IARG;(/'COHERENT INT',I3);]"
"IF(IARG=24) [OUTPUT IARG;(/'AFTER COHERENT INT',I3);]"
"IF(IARG=25) [OUTPUT IARG;(/'CHARACTERISTIC X-RAY',I3);]"
"IF(IARG=26) [OUTPUT IARG;(/'COSTER-KRONIG ELEC',I3);]"
"IF(IARG=27) [OUTPUT IARG;(/'AUGER ELEC',I3);]"
```

```
IF(IARG=16) [PAIRPROD=PAIRPROD+1;] "count pair prod. events"
IF(IARG=18) [COMPTON=COMPTON+1;] "count Compton events"
IF(IARG=20) [PHOTOELE=PHOTOELE+1;] "count photoelec events"

IF(IARG>0 & IARG<=4)[

     IRL=IR(NP);
          IF(IR(NP)=$CRYSTALRG) [ABSORBED=ABSORBED+EDEP;]
     "absorbed energy in the crystal in each history"

     "IF(Z(NP)>2.5)[OUTPUT
Z(NP),ABSORBED;('Z',F8.3,'ABSORBED',F8.3); ]"

"OUTPUT IQ(NP),IR(NP),EDEP,ABSORBED,EKINE,X(NP),Y(NP),Z(NP),"
"U(NP),V(NP),W(NP),ANGLE,IARG;(I3,T5,I3,T11,F6.3,T20,"
"F6.3,T30,F6.3,T39,F7.3,T48,"
"F7.3,T57,F7.3,T65,F7.3,T73,F7.3,T81,F7.3,T90,F7.3,T98,I3);"

OUTDATA(ISAVE,1)=HISTNUM;
OUTDATA(ISAVE,2)=EDEP;
OUTDATA(ISAVE,3)=ABSORBED;
OUTDATA(ISAVE,4)=X(NP);
OUTDATA(ISAVE,5)=Y(NP);
OUTDATA(ISAVE,6)=Z(NP);
"OUTDATA(ISAVE,7)=U(NP);"
"OUTDATA(ISAVE,8)=V(NP);"
"OUTDATA(ISAVE,9)=W(NP);"
"OUTDATA(ISAVE,10)=IQ(NP);"
"OUTDATA(ISAVE,11)=IARG;"

ISAVE=ISAVE+1;
ITOTAL=ITOTAL+1;

"newline format"
%NL
%F
      IF ((ISAVE.EQ.1001)) THEN
      DO 80 ICOUNT=1,1000
      WRITE(7,81) OUTDATA(ICOUNT,1),OUTDATA
     *(ICOUNT,2),OUTDATA(ICOUNT,3),OUTDATA(ICOUNT,4),
     *OUTDATA(ICOUNT,5),OUTDATA(ICOUNT,6),
     *OUTDATA(ICOUNT,7),OUTDATA(ICOUNT,8),OUTDATA(ICOUNT,9)
80    CONTINUE
81    FORMAT(9F18.3)
       ISAVE=1
       END IF

%M
] "close the first IF of the Ausgab"

%M
RETURN;
END; "end of ausgab"
```

```
"************************************************************"
"                     SUBROUTINE HOWFAR                      "
"************************************************************"

%E
SUBROUTINE HOWFAR;
$IMPLICIT-NONE;
$REAL TVAL,UDOTA,UDOTAP;
$INTEGER IHIT;
COMIN/EPCONT,PLADTA,STACK/;
"the arrays PCOORD and PNORM are contained in COMMON/PLADTA"

"Track particles within region 7 and 8"
IF (IR(NP).EQ.$CRYSTALRG)[
$PLAN2P(7,8,1,2,2,-1);
$PLAN2P(1,1,1,5,5,-1);
$PLAN2P(3,3,-1,4,4,1);]

ELSEIF (IR(NP).EQ.8)[
$PLAN2P(6,6,1,7,7,-1);
$PLAN2P(1,1,1,5,5,-1);
$PLAN2P(3,3,-1,4,4,1);]

ELSEIF(IR(NP).EQ.2)[
$PLAN2P(2,7,1,8,9,-1); "define the collimator back"
$PLAN2P(1,1,1,5,5,-1);
$PLAN2P(3,3,-1,4,4,1);]

ELSE [IDISC=1;]
"Discard particles outside region 7 and 8"

RETURN;
END; "end of HOWFAR"

"************************************************************"
"                     SUBROUTINE HOWNEAR                     "
"************************************************************"

%E
SUBROUTINE HOWNEAR(tperp, x, y, z, irl);
$IMPLICIT-NONE;
$REAL tperp, x, y, z;
$INTEGER irl;

tperp = 0.1; "tperp is the closest distance to any boundary;"
"tperp=zero avoid that EGS condense some histories after the
boundary"

RETURN;

END;"end of subroutine HOWNEAR"

"======================end of tutor.mortran================="
```

APPENDIX 4. Source Model. EGSnrc code.

It is necessary take into account that the variables are changed according to the simulation.

```
%L
%E
!INDENT M4; "indent each mortran nesting level by 4"
!INDENT F2; "indent each fortran nesting level by 2"

$IMPLICIT-NONE;
$INTEGER I,J,K,L,NCASES,IQIN,IRIN,NHISTORIES;
$REAL XIN,YIN,ZIN,EIN,WTIN,UIN,VIN,WIN;


"------------------------------------------------------------"
"STEP 1:  USER-OVERRIDE-OF-EGSnrc-MACROS                     "
"------------------------------------------------------------"

"MACROS"
REPLACE{$CALL-HOWNEAR(#);}WITH{;CALL
HOWNEAR({P1},X(NP),Y(NP),Z(NP),IRL);}
"subroutine Hownear"

REPLACE {;COMIN/DATAOUT/;}WITH{;COMMON/DATAOUT/OUTDATA(1001,12),
ISAVE,ICOUNT,PHOTOELE,COMPTON,PAIRPROD;
$REAL OUTDATA;
$INTEGER ISAVE,ICOUNT,PHOTOELE,COMPTON,PAIRPROD;}
"common block to store the data in array with"
"1000levels & 11parameters in the disk"

REPLACE{;COMIN/SCORE/;}WITH{;COMMON/SCORE/PHI,HISTNUM,TOTALELEC,
SPECTENYT(3500),SPECTNUMYT(3500),
SPECTENPH(3500),SPECTNUMPH(3500),
ABSORBED,TOTALBREMESCAP,ANGLETOTAL(400),TOTALBREMPROD,
SPECTBREMESCAP(3500),SPECTBREMPROD(3500),EMSPECT(3500);

$INTEGER SPECTBREMESCAP,EMSPECT,TOTALBREMESCAP,TOTALBREMPROD,
SPECTBREMPROD,ABSORBED,ANGLETOTAL;
REAL*8
HISTNUM,TOTALELEC,PHI,SPECTENYT,SPECTNUMYT,SPECTENPH,SPECTNUMPH;
}

"REPLACE {;COMIN/BREMPR/;}WITH{;COMMON/BREMPR/" "Macro to
Bremsstrahlung photons"
"$LGN(DL(8,$MXMED)/1,2,3,4,5,6/),"
"$LGN(ALPHI,BPAR,DELPOS(2,$MXMED)),"
"$LGN(WA,PZ,ZELEM,RHOZ($MXMED,$MXEL)),PWR2I($MXPWR2I),"
"$LGN(DELCM,ZBRANG,LZBRANG,NNE($MXMED)),"
"IBRDST,IPRDST,ibr_nist,pair_nrc,itriplet,ASYM($MXMED,$MXEL,2);"
"$TYPE ASYM;"
"$REAL $LGN(DL/1,2,3,4,5,6/)," "Parameter for the fit of the
screening"
"ALPHI,"  "Prob. for the (1-BR)/BR part in BREMS, eq. (2.7.64)"
"BPAR, "  "Prob. for the 12*(BR-1/2)**2 part in PAIR, eq.
(2.7.105)"
"DELPOS, ""maximum delta, eq. (2.7.31)"
```

```
"WA,   "  "atomic weight"
"PZ,   "  "atomic fraction of an element in a compound"
"ZELEM, " "Z for a given component"
"RHOZ, " "density of an element in a compound"
"PWR2I, " "powers of 1/2 (used for sampling (1-BR)/BR"
"DELCM, " "136*m*exp(Zg), eq. (2.7.51)"
"ZBRANG, ""composite factor for angular distributions"
"LZBRANG;""-Log(ZBRANG)"

"$INTEGER NNE,"   "number of elements/compound"
"IBRDST," "flag to switch on bremsstrahlung angular
distributions"
"IPRDST, ""flag to switch on pair angular distributions"
"ibr_nist, " "use the NIST bremsstrahlung cross sections"
"itriplet, " "if set to 1, explicitely simulate triplet events"
"pair_nrc; " "=0 => use Bethe-Heitler pair cross sections"
"=1 =>" "use the NRC pair cross sections" }"

"REPLACE{$ibr_nist}WITH{1}"

REPLACE {;COMIN/ET-
Control/;}WITH{;COMMON/ET_Control/smaxir($MXREG),estepe,
ximax,skindepth_for_bca,transport_algorithm,bca_algorithm,exact_
bca,
spin_effects;
$REAL smaxir,estepe,ximax,skindepth_for_bca;
$INTEGER  transport_algorithm,bca_algorithm;
$LOGICAL exact_bca,spin_effects;}

"define a common to pass information about geometry to the
subroutine Howfar"
REPLACE{$MXMED}WITH{2}      "2 medium in the problem"
REPLACE{$MXREG}WITH{8}      "only 8 geometric regions"
REPLACE{$MXSTACK}WITH{15}   "15 particles on stack at once"

"ELECTRONS TRANSPORT"
REPLACE {$TRANSPORT-ALGORITHM-DEFAULT} WITH {$PRESTA-II}
REPLACE {$BCA-ALGORITHM-DEFAULT} WITH {0}
REPLACE {$SKIN-DEPTH-FOR-BCA} WITH {3}
"value in elastic mean free paths and not in length units"

"PARTICLE PARAMETERS"
REPLACE{$ZIN}WITH{0}  "position of the particle: midle of the
sphere"
"REPLACE{$ENERGYPART}WITH{2.011}" "energy of the particle
100kev+511kev [MeV]"
REPLACE{$CHARGEPART}WITH{-1} "Charge of the particle:electrons"
REPLACE{$MAXENERGY}WITH{3500}  "max energy of the spectra"

"REGION_SPHERE"
REPLACE{$MXSPHE}WITH{1} "Max.Number of spheres"
REPLACE{$DELSPH}WITH{0.0001}

REPLACE{$RADIUS}WITH{1} "square radius of the sphere
```

```
"Num. of levels to generate random numbers"
REPLACE{$luxury_level}WITH{2}
REPLACE{$iseed}WITH{314159265}

;COMIN/BOUNDS,MEDIA,MISC,THRESH,SCORE,EPCONT,STACK,
RANDOM,UPHIOT,DATAOUT,SPHDTA,ET-Control/;

"The above expands into a series of COMMON statements;"
"call all the common blocks used with properly parameters"


"-------------------------------------------------------------"
"STEP 2 PRE-HATCH-CALL-INITIALIZATION                        "
"-------------------------------------------------------------"

CHARACTER*4 MEDARR(24);
DATA  MEDARR /$S'SOFT_TISSUE',13*' '/;

call egs_init;

NMED=1;
DO I=1,24[MEDIA(I,1)=MEDARR(I);]
"this is to avoid a DATA STATEMENT for a variable in COMMON"

MED(1)=1;
MED(2)=0;

%E
ECUT(1)=0.521;
PCUT(1)=0.01;

ECUT(2)=0.521;
PCUT(2)=5;
"the high value is to stop the photons outside the sphere"


"-------------------------------------------------------------"
"STEP 3   HATCH-CALL                                         "
"-------------------------------------------------------------"

;OUTPUT;('\f Start Test1'//'CALL HATCH to get cross-section
data'/);

CALL HATCH;   "pick up cross section data for NaI"
              "data file must be assigned to unit 12"

;OUTPUT AE(1)-0.511, AP(1);
(/'knock-on electrons can be created and any electron followed
down to:'
,F8.3,'MeV kinetic energy'
/'brem photons can be created and any photon followed down
to:',F8.3,'MeV');

"Compton events can create electrons and photons below these
cutoffs"
```

```
"-------------------------------------------------------------"
"STEP 4  INITIALIZATION-FOR-HOWFAR and HOWNEAR                "
"-------------------------------------------------------------"

"define volume of the cube"
SPRAD2(1)=$RADIUS; "RADIUS(square)"


"-------------------------------------------------------------"
"STEP 5  INITIALIZATION-FOR-AUSGAB                            "
"-------------------------------------------------------------"

$INITIALIZE RNG USING $luxury_level AND $iseed;
"Random number generator, with 2 luxury levels"
"luxury levels are from 0 to 4 and a period of greater than
10^165"

IAUSFL(7)=1; "a bremsstrahlung interaction is to occur"
"and a call to BREMS is about to be made in ELECTR"

IAUSFL(8)=1; "returned to ELECTR after a call to BREMS was made"

IAUSFL(16)=1; "a pair production interaction is to occur and"
"a call to PAIR is about to be made in PHOTON"
IAUSFL(17)=1; "returned to PHOTON after a call to PAIR was made"

IAUSFL(18)=1; "a Compton interaction is to occur and a call"
"to COMPT is about to be made in PHOTON"
IAUSFL(19)=1; "returned to PHOTON after a call to COMPT was
made.

IAUSFL(20)=1; "a photoelectric interaction is to occur and"
"a call to PHOTO is about to be made in PHOTON"
IAUSFL(21)=1; "returned to PHOTON after a call to PHOTO was
made"


"-------------------------------------------------------------"
"STEP 6   DETERMINATION-OF-INICIDENT-PARTICLE-PARAMETERS      "
"-------------------------------------------------------------"

IQIN=$CHARGEPART; "charge of the incident particle - electron"

"MONOENERGETIC: energy of the incident particle"
"EIN=$ENERGYPART;" "energy of the particle"

/YIN,XIN/=0; "incident particle at origin: particle position"
ZIN=$ZIN; "be sure that we start inside the region 7"
"our particle is inside of the cube - middle of the cube"

"/UIN,VIN/=0; WIN=1;"
"particle moving along Z axis;"
"we won't need if we use isotropic emission"

IRIN=1; "start in the middle of the cube"
WTIN=1; "weight = 1 since no variance reduction used"
```

```
NCASES=100; "number of the loops for the histories"
NHISTORIES=100000;
"number of the histories inside each loop-more n°quickly"

"90Yttrium equation - polyenergetic spectra"
SPECTNUMYT(1)=0;
DO I=1,223
     [SPECTENYT(I)=I*0.01;
     SPECTNUMYT(I)=0.01458*(SPECTENYT(I))*(SPECTENYT(I))*
(SPECTENYT(I))*(SPECTENYT(I))*(SPECTENYT(I));
     SPECTNUMYT(I)=SPECTNUMYT(I)-0.07973*(SPECTENYT(I))*
(SPECTENYT(I))*(SPECTENYT(I))*(SPECTENYT(I));
     SPECTNUMYT(I)=SPECTNUMYT(I)+0.16173*(SPECTENYT(I))*
(SPECTENYT(I))*(SPECTENYT(I));
     SPECTNUMYT(I)=SPECTNUMYT(I)-0.19089*(SPECTENYT(I))*
(SPECTENYT(I));
     SPECTNUMYT(I)=SPECTNUMYT(I)+0.12946*(SPECTENYT(I));
     SPECTNUMYT(I)=SPECTNUMYT(I)+0.03522; ]

"90Yttrium cumulative probability"
DO I=2,223
     [SPECTNUMYT(I)=SPECTNUMYT(I)+SPECTNUMYT(I-1);]

DO I=1,222
     [SPECTNUMYT(I)=SPECTNUMYT(I)/SPECTNUMYT(223);]
SPECTNUMYT(223)=1;


"32Phosphorous equation - polyenergetic spectra"
"SPECTNUMPH(1)=0;"
"DO I=1,167"
     "[SPECTENPH(I)=I*0.01;"
     "SPECTNUMPH(I)=0.05063*(SPECTENPH(I))*(SPECTENPH(I))*"
"(SPECTENPH(I))*(SPECTENPH(I));"
     "SPECTNUMPH(I)=SPECTNUMPH(I)-0.10889*(SPECTENPH(I))*"
"(SPECTENPH(I))*(SPECTENPH(I));"
     "SPECTNUMPH(I)=SPECTNUMPH(I)-0.06523*(SPECTENPH(I))*"
"(SPECTENPH(I));"
     "SPECTNUMPH(I)=SPECTNUMPH(I)+0.16286*(SPECTENPH(I));"
     "SPECTNUMPH(I)=SPECTNUMPH(I)+0.02385; ]"

"32Phosphorous cumulative probability"
"DO I=2,167 "
     "[SPECTNUMPH(I)=SPECTNUMPH(I)+SPECTNUMPH(I-1);]"
"DO I=1,166"
     "[SPECTNUMPH(I)=SPECTNUMPH(I)/SPECTNUMPH(167);]"
"SPECTNUMPH(167)=1;"


"------------------------------------------------------------"
"STEP 7   SHOWER-CALL                                        "
"------------------------------------------------------------"
"Fortran language; to write something in text files;"
"we need to place * in 5 position to change the line"

%NL
```

```
%F
      OPEN(UNIT=7, FILE='BREMESCAPED_EN_X_Y.txt',
     *STATUS='UNKNOWN')
C     star continuation line before


      OPEN(UNIT=12, FILE='BREMESCAPE.txt',
     *STATUS='UNKNOWN')

      OPEN(UNIT=14, FILE='EMISSIONSPECT.txt',
     *STATUS='UNKNOWN')

      OPEN(UNIT=16, FILE='BREMPROD.txt',
     *STATUS='UNKNOWN')

%M

HISTNUM=0.0;

ISAVE=1; "array to store interest parameters-position 1"

TOTALBREMPROD=0;
TOTALBREMESCAP=0;
PAIRPROD=0;
COMPTON=0;
PHOTOELE=0;

DO K=1,$MAXENERGY  [EMSPECT(K)=0; SPECTBREMESCAP(K)=0;
SPECTBREMPROD(K)=0;]
"array to count the number of photons with some specific energy"

"initiate the shower NCASES with NHISTORIES each time"
DO I=1,NCASES [ "OUTPUT I;(//'START LOOP BLOCK',I8,':');"
  DO J=1,NHISTORIES [ "OUTPUT J;(/'EMISSION',I8);"

ABSORBED=1;

"Generate random energy - polyenergetic [MeV]"
$RANDOMSET COSTHE;
WHILE SPECTNUMYT(ABSORBED)<COSTHE[ABSORBED=ABSORBED+1];
EIN=(ABSORBED*0.01)+0.511; "energy of the particles"

"Determining ISOTROPIC EMISSION"
$RANDOMSET COSTHE;
COSTHE=2.*COSTHE-1;
SINTHE=SQRT(1.0-COSTHE**2);
$RANDOMSET PHI;  "Direction cosines with randomly angles"
PHI=TWOPI*PHI;
UIN=SINTHE*COS(PHI);
VIN=SINTHE*SIN(PHI);
WIN=COSTHE;

";OUTPUT;(T2,'CH',T7,'ENERGY',T18,'XPOS',T27,'YPOS',T35,"
"'ZPOS',T46,'U',T54,'V',T62,'W',T69,'IR');"

HISTNUM=HISTNUM+1;
```

```
EMSPECT(INT((EIN-0.511)*1000+0.5))=EMSPECT(INT((EIN-
0.511)*1000+0.5))+1;

CALL SHOWER(IQIN,EIN,XIN,YIN,ZIN,UIN,VIN,WIN,IRIN,WTIN);

   ]
]


"------------------------------------------------------------"
"STEP 8   OUTPUT-OF-RESULTS                                  "
"------------------------------------------------------------"

"total number of histories"
OUTPUT NCASES*NHISTORIES;('NUMBER OF EMISSIONS:',I20);

"total absorbed photons"
DO I=1,$MAXENERGY  [
TOTALBREMESCAP=TOTALBREMESCAP+SPECTBREMESCAP(I);]

;OUTPUT TOTALBREMESCAP;('TOTAL ESCAPED BREMSSTRAHLUNG:',I20);

DO I=1,$MAXENERGY  [
TOTALBREMPROD=TOTALBREMPROD+SPECTBREMPROD(I);]
;OUTPUT TOTALBREMPROD;('TOTAL PRODUCED BREMSSTRAHLUNG:',I20);

;OUTPUT TOTALELEC;(/,'NUM. ELECTRON INTERACTIONS:',F20.0);

;OUTPUT PHOTOELE;(/,'NUM.PHOTOELECTRIC INTERACTIONS:',I20);
;OUTPUT COMPTON;(/,'NUM.COMPTON INTERACTIONS:',I20);
;OUTPUT PAIRPROD;(/,'NUM.PAIR PRODUCTION INTERACTIONS:',I20);

"newline format"
%NL
%F
      DO 90 L=1,ISAVE-1
      WRITE(7,91)OUTDATA(L,1),OUTDATA(L,2),
     *OUTDATA(L,3),OUTDATA(L,4),OUTDATA(L,5),
     *OUTDATA(L,6),OUTDATA(L,7),OUTDATA(L,8),
     *OUTDATA(L,9)
90    CONTINUE
91    FORMAT(9F15.4)
      CLOSE(7)

      DO 70 L=1,3500
      WRITE(12,71) L,SPECTBREMESCAP(L)
70    CONTINUE
71    FORMAT(2I10)
      CLOSE(12)

      DO 60 L=1,3500
      WRITE(14,61) L,EMSPECT(L)
60    CONTINUE
61    FORMAT(2I10)
      CLOSE(14)
```

```
      DO 50 L=1,3500
      WRITE(16,51) L,SPECTBREMPROD(L)
50    CONTINUE
51    FORMAT(2I10)
      CLOSE(16)

%M
"-------------------------------------------------------------"
"STEP 9   finish run                                         "
"-------------------------------------------------------------"
call egs_finish;
STOP;
END; "end of the Main Program routine"


%M
"*************************************************************"
"                   SUBROUTINE AUSGAB                         "
"*************************************************************"
%E
SUBROUTINE AUSGAB(IARG);
$IMPLICIT-NONE;
$INTEGER IARG,IRL;
$REAL ANGLE;

COMIN/STACK,EPCONT,SCORE,UPHIOT,DATAOUT,BREMPR/;

IF (IARG=16) [PAIRPROD=PAIRPROD+1;]
IF (IARG=18) [COMPTON=COMPTON+1;]
IF (IARG=20) [PHOTOELE=PHOTOELE+1;]

IF(IR(NP)=1 & IQ(NP)=-1) [TOTALELEC=TOTALELEC+1;]
"number of electron interactions"

IF(IARG=1 & IR(NP).NE.1 & IQ(NP)=0)[

SPECTBREMESCAP(INT(E(NP)*1000+0.5))=SPECTBREMESCAP(INT(E(NP)*100
0+0.5))+1;

OUTDATA(ISAVE,1)=HISTNUM;
OUTDATA(ISAVE,2)=INT(E(NP)*1000+0.5);
OUTDATA(ISAVE,3)=X(NP);
OUTDATA(ISAVE,4)=Y(NP);
OUTDATA(ISAVE,5)=Z(NP);
OUTDATA(ISAVE,6)=U(NP);
OUTDATA(ISAVE,7)=V(NP);
OUTDATA(ISAVE,8)=W(NP);
OUTDATA(ISAVE,9)=ANGLE;

ISAVE=ISAVE+1;]

IF(IARG=7) [

SPECTBREMPROD(INT(E(NP)*1000+0.5))=SPECTBREMPROD(INT(E(NP)*1000+
0.5))+1;
"store the spectrum"
```

```
"COSTHE=(U(NP)*U(NP-1)+V(NP)*V(NP-1)+W(NP)*W(NP-1))/"
"((SQRT(U(NP)**2+V(NP)**2+W(NP)**2))*(SQRT(U(NP)**2+V(NP)**2+W(N
P)**2)));"

"ANGLE=ACOS(COSTHE)*180./3.14159;" "angle w.r.t. Z axis in
degrees"

"ANGLETOTAL(INT(ANGLE+0.5))=ANGLETOTAL(INT(ANGLE+0.5))+1;"

"OUTPUT U(NP),V(NP),W(NP);"
"('UBREM',F10.4,'VBREM',F10.4,'WBREM',F10.4);"

"OUTPUT COSTHE, ANGLE;('COSTHE',F10.4,'ANGLE',F10.4);"

"newline format"
%NL
%F
      IF ((ISAVE.EQ.1001)) THEN
      DO 80 ICOUNT=1,1000
      WRITE(7,81) OUTDATA(ICOUNT,1),OUTDATA
     *(ICOUNT,2),OUTDATA(ICOUNT,3),OUTDATA(ICOUNT,4),
     *OUTDATA(ICOUNT,5),OUTDATA(ICOUNT,5),
     *OUTDATA(ICOUNT,7),OUTDATA(ICOUNT,8),
     *OUTDATA(ICOUNT,9)
80    CONTINUE
81    FORMAT(9F15.4)
      ISAVE=1
      END IF

%M
 "close the first IF of the Ausgab"

]

RETURN;
END; "end of ausgab"


"************************************************************"
"                     SUBROUTINE HOWFAR                      "
"************************************************************"

%E
SUBROUTINE HOWFAR;
$IMPLICIT-NONE;
$REAL ASPH,BSPH,CSPH,ARGSP,ROOTSP,TVALS;
$INTEGER IHIT;
COMIN/EPCONT,SPHDTA,STACK,ET-Control/;
"the arrays PCOORD and PNORM are contained in COMMON/PLADTA"

IF(IR(NP).NE.1) [IDISC=1;]"Discard particles outside the cube"

ELSE[
    $SPHERE(1,1,IHIT,TVALS);
```

```
"First: number of sphere; second: inside/outside; third:ihit;
fourth:distance"
    "OUTPUT TVALS; ('TVAL', F20.3);"

    IF(IHIT.EQ.1) [$CHGTR(TVALS,2); ]
"First value:distance sphere; seconf: new region"

]

RETURN;
END; "end of HOWFAR"


"************************************************************"
"                      SUBROUTINE HOWNEAR                    "
"************************************************************"

%E
SUBROUTINE HOWNEAR(tperp, a, b, c, irl);

$IMPLICIT-NONE;
$REAL tperp,a, b, c,ASPH,BSPH,CSPH,ARGSP,ROOTSP,TVALS;
$INTEGER  irl,IHIT;
COMIN/ET-Control,SPHDTA,STACK/;

IF(irl = 2) [RETURN;]
ELSEIF(irl = 1)[ $SPHERE(1,1,IHIT,tperp);]

"tperp is the closest distance to any boundary;"
"we defined it as zero to avoid that EGS condense some"
"histories after the boundary"

"SKIN-DEPTH-FOR-BCA: specify the distance from a boundary"
"distance from a boundary (in elastic MFP) at which to"
"switch to one of the boundary crossing algorithms(BCAs)"

RETURN;

END;"end of subroutine HOWNEAR"

"======================end of tutor.mortran================="
```

APPENDIX 5. Matlab code to create a binary image from the list mode data (processed list-mode data obtained from the decoding program)

It is necessary take into account that the text name and the title changed according to the measurement name.

```
%"FRAMING UP" LIST MODE DATA

en_peak=140.5;
en_window=0.2; %20% of energy window
en_low=en_peak-((en_peak*en_window)/2); %126.5keV of minimum energy
en_high=en_peak+((en_peak*en_window)/2); %154.5keV of maximum energy
matrix_size=257; %matrix with 256x256 pixels after remove first row
and column
FOV=565.347; %[mm] values based in the GE NM/CT 670
pix_size=FOV/matrix_size; %[mm] 2.2mm pixel size

A=dlmread('99mTc_1EnerWind_09032012_SPLIT.txt'); %read the text files
[m,n]=size(A);

image=zeros(matrix_size); %0 black; 255 white

energy=round(A(:,1));
x_pos=A(:,2);
y_pos=A(:,3);
uniformity=A(:,4);

for i=1:m
    if (energy(i)>=en_low && energy(i)<=en_high)
        x_pixel(i)=uint16(x_pos(i)/pix_size)+0.5;
        y_pixel(i)=uint16(y_pos(i)/pix_size)+0.5;
    else
        x_pixel(i)=1;
        y_pixel(i)=1;
    end
end

x_pixel=x_pixel';
y_pixel=y_pixel';


for i=1:m
    if (x_pixel(i)<=matrix_size && y_pixel(i)<=matrix_size)
        image(x_pixel(i),y_pixel(i))=image(x_pixel(i),y_pixel(i))+1;
    end
end

image=uint16(image); %converts the elements of the array into unsigned
16-bit (2-byte) integers
image(1,:)=[];
image(:,1)=[];

imshow(image,[]); %without uniformity correction
title ('LIST MODE: 99mTc CENTRE (140.5keV +/-10%)');
```